Magnetic Tensor Spectroscopy for Humanitarian Anti-Personnel Landmine Detection

A thesis submitted to the University of Manchester for the degree of

Doctor in Philosophy

in the Faculty of Engineering and Physical Science

2015

Omar AbdelRehim AbdelKerim

School of Electrical and Electronic Engineering

Table of Contents

Word Count: 38,052

List of Figures

List of Tables

Abstract

The following abstract is for a thesis submitted to the University of Manchester for the degree of Doctor in Philosophy by Omar AbdelRehim AbdelKerim in 2015.

Anti-personnel (AP) mines remain a global problem that affects communities around the world, with 110 million active landmines still present. Landmines are a particularly callous and indiscriminate type of weapon detonating irrespective of presence of an enemy soldier or a child. Their devastating effect on communities has led to their ban through the 1997 Mine Ban Treaty. Current detectors used for mine clearance operations have an impeding weakness that has prompted this research; metal detectors used in humanitarian demining suffer from a high False Alarm Rate (FAR) prompting regular excavation of metallic clutter. The research presented aims to develop a detector capable of discriminating between metallic clutter and mines through the use of the magnetic polarizability dyadic tensor to reduce FARs, increase demining efficiency and improve deminer's safety.

A measurement apparatus was designed and constructed to perform spectroscopic magnetic measurements of small symmetrical metallic objects and produce for the first time unscaled accurate tensor values. The tensors deduced from the measurements were validated against analytical and simulated results and were found to be within 5% of measured tensors. The tensors of minimum metal AP mine surrogates and metallic clutter of symmetrical shape were measured and formed part of a tensor library to be used later by future research. This is in addition to a set of un-circulated US coinage which could be used as a calibration metric and a comparison piece for future work in this area.

A detailed description of the coil design and manufacturing process is presented to develop a coil array capable of inverting buried metallic object tensors. The selection criterion was poised to identify an array that was best suited to perform the correct measurements in order to invert to an accurate tensor. The manufactured coil exhibited strong mutual coupling between the receive coils deeming it unfit for the portable detector; however, the findings of the work presented and the selection criterion developed has aided the future design of a suitable coil array. Expected signal levels from minimum metal mine detection were calculated and helped aide in the design of future detectors to ensure suitable SNR performance is achieved.

A portable detector has been developed using the sensor head presented within this thesis. Work still lies ahead to achieve the complete detector capable of performing target characterisation and clutter elimination; however, significant advances have been made and are presented throughout this thesis.

Declaration

No portion of the work referred to in the thesis has been submitted in support of an application for another degree or qualification of this or any other university or other institute of learning.

Copyright

Glossary of Terms

ADC	Analogue to Digital Converter
AP	Anti-Personnel
APG	Aberdeen Proving Ground
AT	Anti-Tank
ATR	Aided Target Recognition
BAM	Bundesanstalt für Materialforschung und prüfung
CWA	European Committee for Standardization Workshops
EIT	Electrical Impedance Tomography
EMI	Electromagnetic Induction
ERW	Explosive Remnants of War
ES	Electrode Spacing
FABW	Find a Better Way charity
FAR	False Alarm Rate
FEM	Finite Element Method
FFT	Fast Fourier Transform
GC	Ground Compensation
GICHD	Geneva International Centre for Humanitarian Demining
GPR	Ground Penetrating Radar
GRP	Glass Reinforced Plastic
HMM	Hidden Markov Models
ICBL	International Campaign to Ban Landmines
IMAS	International Mine Action Standards
ITOP	International Test Operations Procedure
JRC	Joint Research Centre
KNN	K-Nearest Neighbour
LDV	Laser Doppler Vibrometers
MAG	Mines Advisory Group
MD	Metal Detection
MDD	Mine Detection Dogs
MDF	Medium Density Fibre
MFIA	Multi-Frequency Impedance Analyser
MPV	Man-Portable Vector Sensor

OTL	Organised Technology Ltd
PCB	Printed Circuit Board
P_d	Probability of Detection
PEDMIS	Portable Decoupled Electromagnetic Induction Sensor
PFA	Probability of False Alarm
PTFE	Polytetrafluoroethylene
R&D	Research & Development
RTI	Respect to Input
SNR	Signal-to-Noise Ratio
UNMAS	United Nations Mine Action Standards
UXO	Unexploded Ordinance
WTMD	Walk-Through Metal Detector
WWI	World War I
WWII	World War II

List of Symbols and Constants

The following constants are used in this thesis:

Symbol	Description	Value
π	Pi	3.14159…
μ_0	Permeability of free space	$4\pi \times 10^{-7}$ m·kg·s^{-2}·A^{-2}
k	Boltzmann's constant	1.38×10^{-23}m^{2}kgs^{-2}K^{-1}

The following symbols are used in this thesis:

Symbol	Description	Defined in Section
$\boldsymbol{B}$	Magnetic flux density	3.1
$\boldsymbol{H}$	Magnetic field strength	3.1
I	Filamentary current at passing through wire segment	3.1
$\boldsymbol{dl}$	Segment of current carrying wire	3.1
$\hat{\mathbf{r}}$	Unit vector from the wire to the point of observation	3.1
r	Magnitude of the Euclidian distance from wire to observation point	3.1
$\boldsymbol{dH}$	Differential magnetic field strength	3.1
$\hat{\Phi}$	Unit vector aligned in the azimuth direction	3.1
$\boldsymbol{B}_z$	Magnetic flux density along the axis of a circular loop	3.1
a	Radius of sphere or circle	3.1
V	Voltage	3.2
$\boldsymbol{E}$	Electric field	3.2
ds	Surface element	3.2
t	Time	3.2
$\boldsymbol{m}$	Magnetic dipole moment	3.3
S	Area of current loop	3.3
$\mathbf{r}$	Position vector	3.3
$\boldsymbol{J}$	Current Density	3.3
dv	Volume element	3.3
ω	Angular frequency	3.3
$\overleftrightarrow{\mathbf{M}}$	Magnetic dipole polarizability tensor	3.4
d	Maximum object dimension	3.4
$\boldsymbol{\Lambda}$	Eigenvalue matrix of tensor	3.4
R	Rotational matrix	3.4
δ	Skin depth	3.4
μ	Permeability of medium	3.4
σ	Conductivity of medium	3.4
f_R	Resonance frequency	5.3
L	Inductance	5.3
C	Capacitance	5.3
M_I	Mutual Inductance	5.3

Symbol	Description	Defined in Section
en	Op-Amp Voltage noise source	5.4
inn/inp	Op-Amp current noise source for inverting and non-inverting terminals	5.4
G	Amplifier gain	5.4
R	Resistance	5.4
T	Temperature	5.4
e_{amp}	Amplifier noise density	5.4
E_{amp}	Amplifier noise	5.4
$\mathrm{V}_{\mathrm{LSB}}$	Representative voltage of least significant bit	5.4
V_{FS}	ADC full-scale voltage	5.4
N_{levels}	Number of ADC levels	5.4
f_B	Bandwidth frequency	5.4
f_S	Sampling frequency	5.4

Preface

Omar AbdelKerim was born in Alexandria, Egypt in 1989. He studied for an MEng in ‘Electronic Systems Engineering’ at the University of Manchester, UK, and was awarded a first class degree with honours in July 2011. During this period he undertook two major projects with the Sensing, Imaging and Signal Processing Group, one at a BEng level and another at MEng level, under the supervision of Professor Hugh McCann and Professor Anthony Peyton respectively. His MEng project ‘Intelligent Discriminating Sensor System for Landmine Detection’, which was undertaken as part of a team of five individuals, provided an introduction to electromagnetic tomography and led directly to the research presented in this thesis. He began studying for the degree of ‘Doctor of Philosophy’ at the University of Manchester, UK, in October 2011 with the project title ‘Magnetic Tensor Spectroscopy for Humanitarian Demining’ under the supervision of Professor Anthony Peyton.

Acknowledgements

I would like to take this opportunity to express my thanks to all those who have helped me throughout my PhD.

To my supervisor Professor Tony Peyton, thank you for your continual help and guidance throughout my studies. Thank you for giving me the opportunity to become involved in such a worthwhile research that has helped me develop rapidly as an engineer and a person. It has been a true privilege to have worked with such a dedicated person to research.

To my parents, Nihad and Ahmed, and to my brother, Aly, another achievement which reflects upon all you have done for me. I have been blessed with parents whom have continually sacrificed their wellbeing in favour of mine and Aly's. You have been and always will be the strongest role models I turn to. Aly, you have been a strong motivator in my life that I have continually tried to better but gladly never have. Thank you for all your help in relieving the stressful times and enjoying the good ones.

To my girlfriend, Lisa, you have been by my side during every step of this PhD and have shared much of the burden leading up to submission. Thank you for being so understanding, patient and loving. Thank you for helping in every possible way to ensure I am able to achieve this long standing goal of mine.

To Dr. Liam Marsh, your help has been of vital importance to this thesis. Thank you for all your assistance and technical guidance during the duration of this PhD.

To Dr. John Davidson, thank you for your help on tensor simulation. Your contribution has been essential to present a strong tensor study.

To Find a Better Way (FABW) charity (http://www.findabetterway.org.uk/), thank you for the financial support of this research under the research programme.

To any others I may have omitted I offer my apologies.

1 Introduction

The presence of anti-personnel (AP) landmines impacts many communities and countries as an enduring legacy of numerous conflicts worldwide. AP landmines can be described as munitions designed and deployed to detonate as a result of the presence, proximity or contact of personnel [1, 2]. The indiscriminate nature of AP mines has made them devastating to communities decades after they have been laid [1].

This thesis describes efforts to develop an intelligent landmine detector to aid the operation of humanitarian demining. This first chapter describes the aims and objectives of the research, includes a statement of originality highlighting aspects of the research to be considered novel and finally explains the structure of the thesis.

1.1 Aims and Objectives

One of the most significant weakness of current detectors is their high false alarm rate (FAR). The large number of false positives encountered during demining operations seriously impacts the time and cost required to clear mined areas as well as compromising the safety of deminers, who must spend time excavating the innocuous items. The burden of unnecessary excavation can result in complacency when faced with a real threat and can lead to the injury of the deminer [3]. Thus, the production of a detector capable of reducing the FAR acts as the main motivation of this research.

The provision of a means of discriminating between innocuous objects and threats (anti-personnel mines) would allow a significant increase of clearance rates, reduction of cost and save injury and loss of life. The wider research at the University of Manchester aims to combine enhanced metal detection with ground penetrating radar (GPR) in order to reduce the false alarm rate. This thesis will focus only on the development and enhancement of the inductive metal detection. The enhancement is in the form of the inversion of multi-frequency measurements of detected objects to provide spectral information of the target's electromagnetic characteristics. The response can give indication of the target's material, size, shape and orientation through an object specific property known as the electromagnetic polarizability tensor (termed tensor for short through the remainder of this thesis). Mines contain a standard set of metallic components and so their electromagnetic response is repeatable from device to device for a particular type of mine. Furthermore, this response is different to that of other metallic items found in a minefield, known as clutter, which allows the tensor to act as a discriminating property. With the further addition of GPR, the future detector will allow for a significant elimination of false positives and the reduction of the FAR.

This research applies such technology in a lab environment with transferable components to a preliminary field instrument. The following form the main objectives of the research and that reported within this thesis.

- A measurement apparatus capable of measuring the non-scaled tensor values for low metal mines and small metallic clutter.
- A library of the tensors for low metal mine parts and typical clutter items to help in the development of the enhanced metal detector.
- A sensor head optimised for inversion that is capable of detecting anti-personnel mines to depths required by mine clearance standards.

In addition to the main objectives above, secondary objectives also include:

- design and implementation of front-end amplification capable of amplifying the detector signal and providing acceptable signal to noise.
- production of a multi-frequency data acquisition system.
- implementation of an auto-nulling procedure capable of minimising the contribution of the background signal to the measured receive signal.

1.2 Statement of Originality

The main original aspect of the research described in this thesis lies within the utilisation of the tensor to discriminate between metallic clutter and AP mines. Almost all portable metal detectors used for demining provide an audio indication that represents the magnitude and phase of the signal measured through the adjustment of volume and pitch. It is to the writer’s knowledge that there is no hand-held anti-personnel landmine detector that performs the tensor analysis on the electromagnetic signal of the detector in real-time.

The thesis reports on an experimental lab apparatus developed to systematically obtain unscaled tensor values for low-metal anti-personnel mines and small items of metallic clutter. There has been no reported literature that presents the measurement of absolute tensor values in correct units, such as m^3. Literature has only reported scaled relative tensors for unexploded ordinances (UXOs) and clutter. In addition, anti-personnel mine tensors have never been reported, scaled or unscaled in the open literature. The tensors obtained from the apparatus are validated against independent simulation and analytical solutions. This exercise is another novel facet, building confidence in the apparatus and the measurement methods. The validation confirmed the experimentally obtained tensor to be the correct representation of the measured object.

The thesis also presents an optimal sensor head for tensor inversion of metallic objects detected during humanitarian demining. A number of studies were performed in the selection process; sensitivity analysis and investigation of the invert-ability of the measured data acquired from a particular coil geometry. The study and selection criteria are novel approaches that have not been reported previously.

Finally, a number of novel aspects lay within the development of the full landmine detection system. These include the excitation of the detector head with more than one continuous frequency. Continuous wave detectors tend to operate at a single frequency; none display the extensive frequency range and spectral analysis displayed by the detector developed in this research. It can be argued that pulsed detectors do provide a greater range of frequencies, however there is no evidence of an FFT performed on the detected signal or any spectral analysis of the object response. Pulsed systems also suffer from a poorer SNR with regards to the individual frequencies, making pulsed systems unsuitable for the spectroscopic analysis performed in this thesis. The prototype system developed as a result of this research also performs an auto-nulling procedure that minimises the background signal to a minimum, allowing for greater front-end amplification and in turn better signal to noise performance. This again is a novel aspect to the writer’s knowledge.

1.3 Organisation of the Thesis

The thesis sets out with a background chapter, Chapter 2, which describes the main challenges facing humanitarian demining and the current operational practice in the field. The chapter goes on to review current inductive metal detectors in use and provides a review of research efforts to develop landmine detection technology. The chapter also includes a section describing the partners and bodies working on the wider project of landmine detection at the University of Manchester.

The thesis then follows with a chapter on the theory behind the tensor response and how it can be deduced from voltage measurements of a sensor head. It defines what the tensor represents and what properties of the metal can be deduced from it. The chapter closes with a literature review that presents research efforts to utilise the tensor for locating metallic items and performing classification.

Chapter 4 describes the experimental set-up used to measure the tensor values of several mine surrogates, as well as items of clutter. The chapter describes the apparatus used, the method and the validation exercises performed to ensure the tensors measured are truly representative of the objects. The chapter then reports the measured tensors of clutter and mine surrogates, with a discussion on the features observed highlighting the discriminatory potential of the tensor.

Chapter 5 focuses on the development of a preliminary sensor head. It describes the selection process, design and manufacturing of a coil array capable of providing measurements suitable for inversion. The selection process involved the assessment of several coil geometries; comparing their sensitivities and their ability to invert tensors at different locations and under different noise conditions. The chapter continues to describe the manufacturing process and reports on the impedance characteristic for the final coil. Finally, the chapter concludes with a calculation of the expected signal levels from the targets measured in chapter 4 and predicts SNR performance and maximum depths at which inversion of measurements is possible.

Chapter 6 completes the description of the research work with a summary of the work completed. The chapter also describes the remaining field device components such as the data acquisition system, front-end amplification and auto-nulling procedure. Finally, the chapter concludes the thesis by presenting the key areas for future work.

2 Background

In order to highlight and identify the benefits of this research in humanitarian demining, this chapter provides the necessary background to understand the global landmine challenge. At the outset of the chapter, an introduction to the landmine problem is provided, identifying the impact it has on many communities world-wide. The chapter moves onto introducing the main partners within the work and key funders of the research. The chapter continues with the procedure followed by humanitarian demining drawing attention to the current standards set. Finally, the chapter concludes with a review of modern detectors and research efforts to improve the technology.

2.1 Global Landmine Challenge

Landmines were initially developed during World War One (WWI), and were widely used in World War Two (WWII) and following conflicts. They were initially viewed as ‘force multipliers’ and were laid with the intent to [4]:

- provide a defensive barrier around vulnerable/important sites and utilities.
- channel enemy troops and vehicles into a vulnerable area.
- act as a surprise attack.
- deny the enemy safe access to utilities post withdrawal.

Some of the mined areas were clearly marked when planted, depending on the intent for which they were laid. However, the mines laid with the intent of surprising the enemy are typically concealed. This ‘surprise’ intent is usually maximised by poorly equipped sides and those that do not desire to permanently occupy the territory [4].

Landmines are a particularly callous and indiscriminate type of weapon detonating irrespective of presence of an enemy soldier or a child. The impact of landmines is even more shocking as only a fraction of mines are detonated during conflict, leaving a legacy that continues to kill and maim civilians generations later. It is estimated that around 110 million active landmines are present [5] in 59 states; Figure 2-1 shows the states affected. The resulting impact is that the majority of casualties from mine and explosive remnants of war (ERW) are civilians (accounting for 78% of all casualties in 2012 where civilian/military status was known), as illustrated graphically in Figure 2-2. Children form a large part of the civilian casualty as they are most vulnerable [6], with 1,168 child casualties in 2012 amounting to 47% of civilian casualties, see Figure 2-3. UNICEF estimates one third of all landmine victims are children under the age of fifteen [7].

Figure 2-1: Countries affected by landmines or explosive remnants of war, derived from [8].

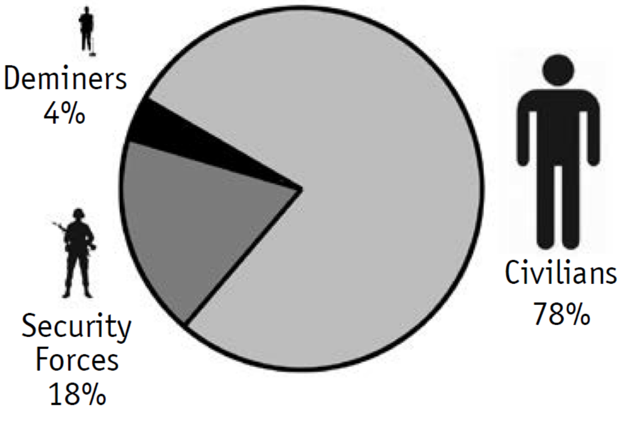

Figure 2-2: Percentage of civilian casualties where civilian/military status was known [8].

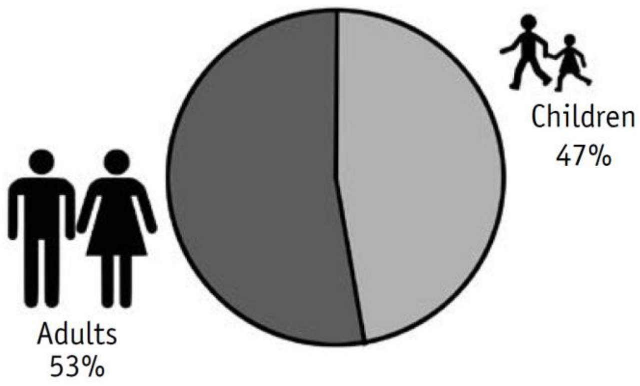

Figure 2-3: Percentage of children casualties [8].

2.2 Global Efforts to Tackle the Landmine Challenge

The horrific nature of landmines has triggered strong efforts to ban their use. The most successful effort that has emerged is the International Campaign to Ban Landmines (ICBL), that sets out to prohibit the use of landmines, their production, stockpiling and transfer [9]. The effort resulted in the 1997 Mine Ban Treaty and proved to be the most comprehensive international instrument for ridding the world of the scourge of mines [9]. States abiding to the treaty commit to:

- never use anti-personnel mines, nor to "develop, produce, otherwise acquire, stockpile, retain or transfer" them.
- destroy mines in their stockpiles within 4 years.
- clear mined areas in their territory within 10 years.
- conduct mine risk education and ensure that mine survivors, their families and communities receive comprehensive assistance.
- offer assistance to other States or Parties, for example in providing for survivors or contributing to clearance programs.

More than 80% of the world's states have joined the treaty, curbing the number of newly laid mines and in turn casualties. Even those outside the treaty mostly abide by its key provisions, indicating near-universal acceptance of the landmine ban [8]. The treaty does not include USA, China and Russia. However, some of the countries are responding to pressures to comply with the treaty despite not legally abiding to it. The USA is the world's largest individual contributor to mine clearance efforts, has not used mines since 1991 nor exported since 1992 [10]. Despite these efforts landmines are still being laid by countries outside the treaty and even by countries part of the treaty that have experienced recent conflicts. The ICBL has recently confirmed new use of mines in Israel (not part of the treaty) and Libya (part of the treaty) in recent events during 2010-2011 [11].

The ICBL continues to monitor the compliance of countries, who are part of the treaty, while applying added pressure to those who are not. However, even without the laying of new mines the 110 million active mines already present would require USD30 billion to safely excavate and disarm and would take more than 1,000 years [7]. As a result the need for technological development becomes apparent to increase the productivity of humanitarian demining methods while maintaining or increasing deminers' safety. There have been numerous efforts to develop landmine detection techniques by humanitarian and military bodies as will be highlighted in section 2.6; however, there still remains a need for better detection equipment.

2.3 Partners and Collaborators

The research at The University of Manchester is mainly funded by the Find a Better Way (FABW) charity. Find a Better Way is a new charity founded by Sir Bobby Charlton in 2011 to develop new technologies to assist and accelerate the detection and removal of landmines globally. It has since launched a wide range of research projects into the development and integration of different detection techniques of which falls this project. FABW have worked with the Mines Advisory Group (MAG) to draw upon their field experience. MAG are a neutral humanitarian organization, working to reduce the impact of explosive remnants of conflict in current and former conflict zones [12]. They are heavily involved with operational humanitarian demining, training deminers, educating communities about the dangers and assisting the development of affected areas [12]. The group at The University of Manchester utilised the expertise of individuals at MAG to understand the conditions and procedures of humanitarian demining at the outset of the project to avoid pitfalls and ensure a suitable detection method is developed. The research group at The University of Manchester has also developed strong ties with the Croatian research group from Fakultet Elektrotehnike i Računarstva in Zagreb. This relationship has facilitated access to a test mine site for field trials of the preliminary prototype field device.

2.4 Demining Procedures and the Role of Metal Detectors

Metal detectors have been, and continue to be the primary detection tools used by deminers. Laid landmines are occasionally visible and the deminer is capable of locating the mines through visual inspection [4]. However, this is regularly not the case; mines laid for extended periods can become difficult to locate and metal detectors become necessary. Metal detection (MD) is considered to be a mature technology that has developed over the years to tackle efforts by landmine manufacturers to produce low metal hard-to-detect mines.

2.4.1 Background on Demining

Humanitarian demining and military demining are considerably different in several aspects, most notably the acceptance of casualties and the procedures followed for detection and clearance. Military mine clearance has been performed for more than 80 years while humanitarian demining of all ERW only began in the late 1980s in Afghanistan and Cambodia by civilian organizations [4, 13]. The major difference in procedure is that humanitarian demining sets out to detect, remove and destroy all ERW in a non-military area, whereas military procedures are more strategic; for example only clearing a path through a mine field with pressure to work quickly [13]. Until recently humanitarian demining used detectors designed for military use, as the market for humanitarian demining did not justify the investment to specialise for humanitarian procedures [4, 13]. Detector designers have increasingly considered the needs of humanitarian demining, but the commercial reality still requires they also appeal for military use.

International standards for humanitarian demining were first proposed in 1996 during a technical conference in Denmark, highlighting the need for a standardised protocol to be followed world-wide [14]. A UN-led effort arrived with a first edition of standards a year later, namely the UN Mine Action Standards (UNMAS). The scope then expanded to encompass other components of the demining operation. The standards were renamed to International Mine Action Standards (IMAS) and were developed with the assistance of the Geneva International Centre for Humanitarian Demining (GIHCD). These standards are continually reviewed and amended by technical committees involving international, governmental and non-governmental organizations to include procedural developments and the inclusion of arising aspects [14]. An example of such adjustment is the current review and development of manual detection procedures for dual sensors.

IMAS provides a framework of international standards and guidelines for more than just the demining activities such as mine risk education, survey, mapping and clearance. Due to the overlap between complementary humanitarian and development plans, IMAS provides a general framework that allows the efforts of different organizations and agencies to be aligned by providing a protocol for data collection, operation management, handover documentation and much more [14]. IMAS acts as the protocol for demining world-wide unless there is a national standard in the country of operation. This thesis will only highlight a few key aspects of the standards, focusing on the assessment and clearance process.

Figure 2-4 describes the full demining process as specified by IMAS. Metal detectors are usually the main tool used during the surveying and clearance of mines and ERW. The process is viewed as a continuous assessment process where information about the area is continually developed and strategies reassessed at every stage.

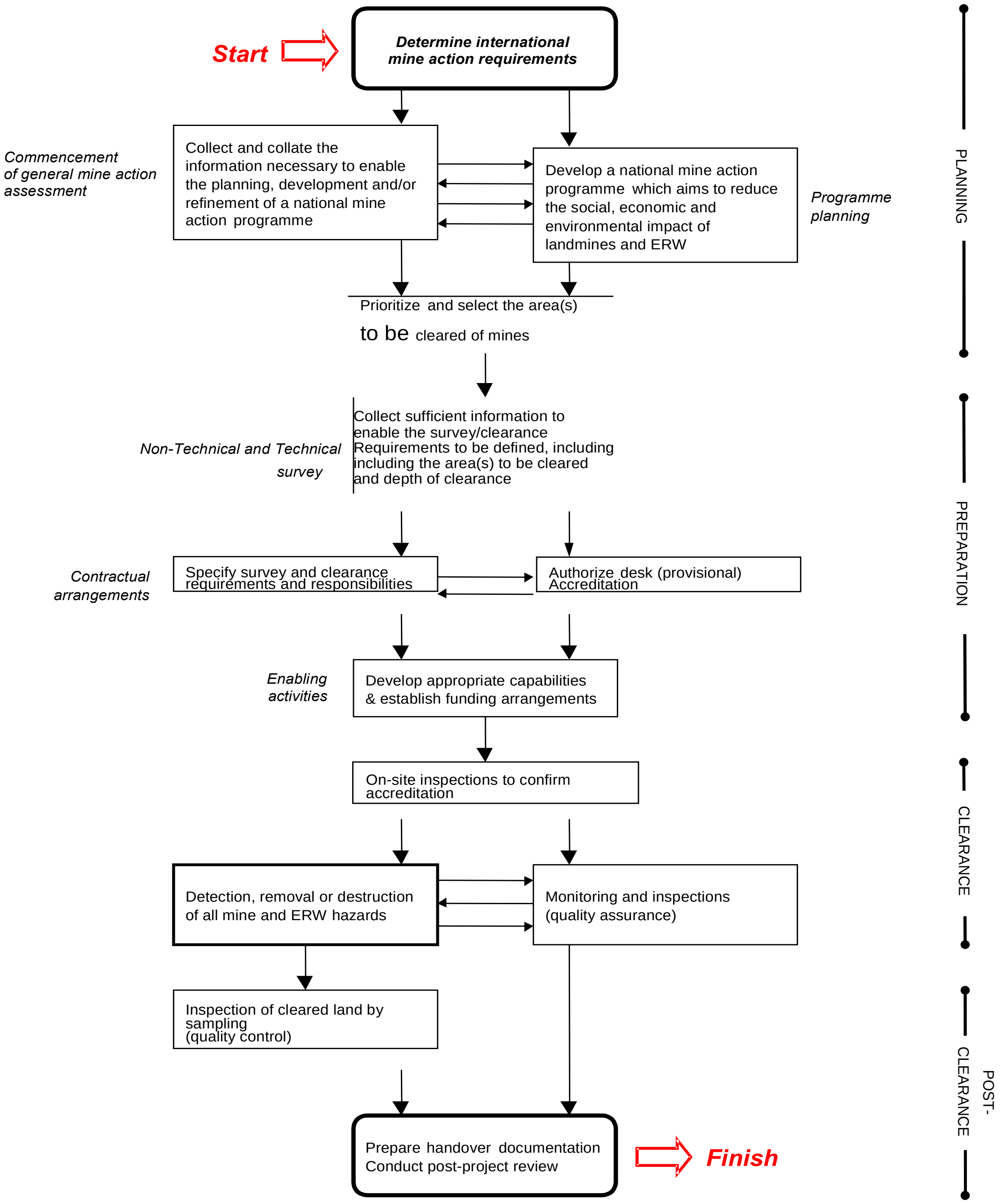

Figure 2-4: The full demining process as specified by IMAS [15].

One of the most important pieces of information that IMAS provides for this project is the specified depth of clearance as this acts as the specification required for the metal detector developed within the research. The clearance depth is usually determined during the technical survey or from other reliable information (e.g. documentation identifying depth of mines and ERW) [16]. However, if the survey fails to identify the anticipated depth of mines and there is no information aiding the process, a default depth is specified. For minimum metal mines the depth is based on the effective detection depth of the state of the art metal detectors [16]. Modern metal detectors have displayed detection of minimum metal mines at a search depth of 130 mm below the original surface level and hence the standard depth should not be less if there is no anticipated depth specified [16]. It is important to realize that the default depth is specified by the performance limitation of metal detectors and not the mine properties. If mines could be reliably detected at greater depths by metal detectors or alternative/combined methods then the greater depth is selected [16].

Detection and clearance are currently carried out by one of four methods [13]:

- manual clearance using metal detectors.
- manual clearance using excavation.
- dogs and manual.
- mechanical and manual.

The different methods are used during different scenarios and terrain conditions as will be explained in the following sections. The main factors that influence the decision are the amount of metal present in the soil commonly known as metal contamination, the soil type and the preservation of the land. Manual deminers are part of every category as the industry is yet to accept a fully mechanised method [13]. The remainder of section 2.4 is derived from [13] unless stated otherwise. Note that the standard operating procedures for the use of dual sensors (GPR and MD) for clearance operations have not yet appeared in literature but are expected to be included in the near future. As a result this had been omitted from this section and an explanation of individual dual detector operating procedure is included in section 2.7.

2.4.2 Manual Clearance Using Metal Detectors

Manual detection using metal detectors is exercised when the ground is not too naturally magnetic or contaminated with excessive metallic scrap or clutter items. AP mine locations can be evident after the removal of undergrowth and vegetation, especially for recently placed mines. However, as time passes mines can become more deeply concealed, sometimes changing orientation and can also become discoloured and weathered making it much harder to spot using the naked eye. Consequently metal detectors are required. The realisation that there might be deeply buried mines results in a significant overhead to clearance operation as it is more time-consuming to detect and excavate deeply buried mines.

Metal detectors are used by deminers to identify mine locations through the electromagnetic induction (EMI) of their metallic content. Fragmentation mines contain a significant amount of metal and are usually buried with their fuse mechanism above ground and so are relatively easy to detect and can be visually apparent.

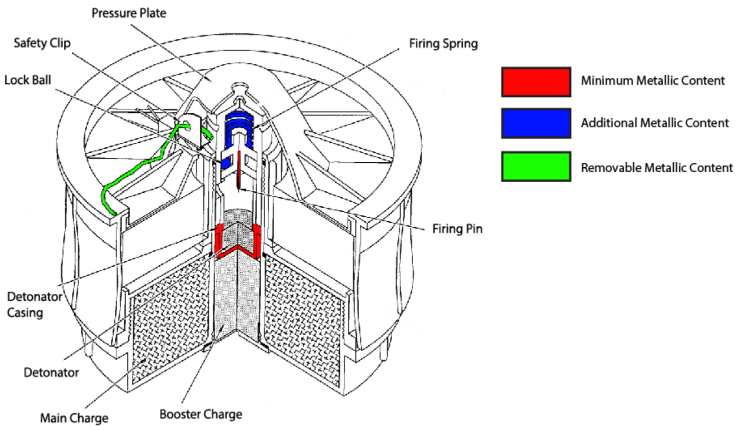

Figure 2-5: Metallic content in anti-personnel mines. Figure adapted from [17].

Some anti-personnel mines have been designed to use the smallest amount of metal in their construction to impede their detectability. These types of mines are known as *minimum metal mines* and typically contain only a few metallic components limited to the necessary parts. Figure 2-5 shows a cross-sectional schematic view of a typical anti-personnel mine with the metallic components highlighted in red, green and blue. While some anti-personnel mines can contain a spring and lock ball arrangement to form the detonation mechanism, highlighted in blue, minimum metal mines substitute these components and may utilise a non-metallic diaphragm to reduce their metallic content. As a result, minimum metal mines can contain metallic content that is composed of only a firing pin and the detonator casing, highlighted in red in Figure 2-5. The safety pin is removed when arming the mine and so does not contribute to the EMI response measured by metal detectors. The reduction of metallic content has been the main drive by mine manufacturers to make mines harder to detect with a small number of zero metal content mines developed over the years. However, very few of the no metal mines have made it through manufacturing and sales and are now restricted by the 1997 Mine Ban Treaty. These mines have been found either using dogs or manual excavation, however no metal mines were found to be non-functional after a decade in the ground [13].

The safety of the deminer is of top priority and metal detectors need to be able to reliably detect and accurately locate the metal to ensure this. The metal detector needs to provide a signal by which the deminer can locate the centre of the metallic content and so create a safe perimeter. Once the metallic content is discovered the deminer then probes the ground sideways to avoid activating the pressure plate. This probing exercise allows the deminer to discriminate between clutter and mines. If the mines have been tilted then even a cautious deminer can set it off by lateral probing.

Figure 2-6: A deminer probing a potential threat located using a metal detector. Obtained from www.maginternational.org ©Sean Sutton.

Lateral probing has come under increasing scrutiny in recent years as studies revealed that significant force is required to probe the ground to depths greater than 5 cm [18]. The associated risks has resulted in the decrease of ground probing operations and the use of probing devices as standalone instruments for manual excavation is no longer common practice [18]. Accidents during excavation are most common in humanitarian demining and are often a result of inaccurate location marking or the change in mine orientation, Figure 2-7. However, if the deminer is adequately protected, he/she should survive the blast without disabling injuries [13, 19]. Thus, the potential to inform the deminer of the mine's accurate location and orientation prior to excavation could be of significant safety benefit during excavation.

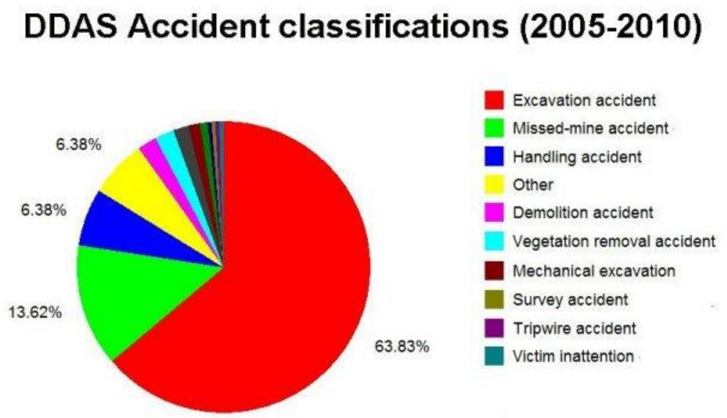

Figure 2-7: Humanitarian demining accidents between 2005 and 2010 based on DDAS accident records [20].

2.4.3 Manual Detection Using Excavation

This method is used when presented with soil which is either naturally magnetic or contains an artificially high metal content due to contamination. Such situations would give rise to continuous alarms from conventional metal detectors. Deminers then resort to manual excavation of the entire top-surface of the ground to the determined clearance depth. The contamination level at which deminers decide to revert to manual excavation is three pieces of metal per square meter according to [13]. Manual excavation at these levels becomes quicker than the detection and safe removal of individual metal pieces. This process is extremely time consuming with significant attempts towards reducing areas to which manual excavation has to be done. Dogs are regularly used to reduce the suspected areas. The identification of clutter would significantly enhance this form of demining or more accurately deem it unnecessary as manual clearance using metal detectors would be possible even in highly contaminated areas.

Figure 2-8: A deminer excavating a mine in Sri Lanka. Obtained from www.maginternational.org ©Sean Sutton.

2.4.4 Explosive Detecting Dogs and Manual Methods

The introduction of dogs in the demining process has proved to be successful and has mainly been used to reduce suspected areas prior to manual clearance. This has helped speed up the clearance process. Dogs are occasionally used for precise mine location when mines are significantly spaced out. However, they are ineffective for location in densely mined areas as scent from several sources may combine. At least two dogs are used to scan the same area to increase confidence. IMAS contains a section on the use of mine detection dogs (MDD). Dog usage has become more common as a result of the following [21]:

- MDD can be better and more cost effective if implemented correctly in comparison to manual demining.
- dogs are capable of detecting low-metal and no-metal mines and ERW in areas of high metal contamination.
- they tend to act in a complementary role with other mechanical and manual detection techniques.

Dogs are used in several situations including clearance verification, creation of safe lanes for clearance start points, searching railways, highly contaminated areas and land unreachable by mechanical demining equipment. However, dogs are considered most useful during initial technical survey where land areas could be quickly established to be free of mines and ERW. MDD are deployed for boundary detection as it is often the case that boundaries are low density and manual demining follows to clear the reduced area. Dogs are also more cost effective on roads as roads tend to be free of trip wires, vegetation and exhibit low density of mines [21].

2.4.5 Mechanical and Manual Methods

The use of machines to assist demining is becoming increasingly common [16]. There are three main types of machines involved in humanitarian demining. Each type of machine has a specifically defined function; ground preparation, hazard detection and hazard detonation. [22]. Ground preparation machines are the most commonly used machines and provide vegetation cutting, soil loosening and processing, and the removal of weakly-magnetic metal contamination [16, 22]. Hazard detection machines can carry an array of detectors potentially increasing the speed, whilst others perform physical detection as with sifting machines and rollers. Finally detonating machines such as flails and rollers (known as ground milling machines) are sometimes used to clear hazardous areas, however their effect on the soil is usually undesirable and sometimes avoided.

2.4.6 Demining Procedures using Metal Detectors

Metal detectors are used during several stages of the demining process; assessment, surveying, clearance and confirmation of cleared land. During the day a number of tests are performed prior to, during and after the use of metal detectors. These tests involve checking the detector’s general condition and functions at the start of the day, adjusting the detector to the ground conditions and to the target, repeating set-up for changed conditions and end of day check. These checks are vital to ensure correct operation of the detector and the safety of the deminers. The detectors tend to have a number of safety features installed such as battery checks and system fail circuitry to highlight any issues with the detector. Confidence clicks in the audio signal help ensure the detector is switched on and operating correctly.

Currently, every response made by a metal detector must be assumed to be an indication of a mine regardless of any discriminatory signal characteristics. The signal strength tends to vary; however, it is not used to discriminate between items such as crushed cans, grenades, ring-pulls or minimum metal mines. This shortfall has been highlighted as the prime weakness of metal detectors as it does not only add a significant cost and time overhead but it is also results in decreased deminer caution as they spend most of their time locating metal of non-hazardous objects.

A crude average has been given in [16], that 50% of the signal sources are visible during demining. If the detected metal is not visible, an excavation process follows the detection. Before excavation, the deminer performs a more accurate scan of the area; consisting of a greater number of measurements over a smaller area, to pinpoint the metal object. This extra resolution can significantly reduce the time of the excavation process [23]. If the metal object is located within a centimetre or better, the dangerous excavation process is made safer and false alarms are identified quicker [23]. To further increase the accuracy of location the deminer sweeps the detector at different angles and orientations approaching the object from different directions to infer as much information as possible about the location and size [23]. Figure 2-9 highlights the region which would typically produce a signal as the detector approaches the target.

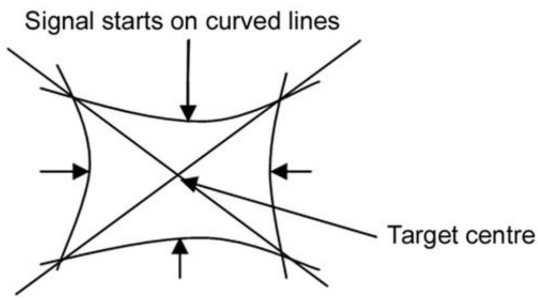

Figure 2-9: Typical signal producing region for metal detectors as the target is approached [23].

The deminer marks the closest boundary where the detector signals for excavation. The excavation process is then initiated as discussed earlier by excavating and/or probing the ground from the side; digging and advancing sideways towards the mark until the mine is exposed from the side to confirm its nature. Identifying the orientation of the mine prior to excavation could considerably reduce the risk of detonating on excavation, a risk currently considered as unavoidable [19]. Once exposed the supervisor is then called to decide on the safe and effective demolition/disarming option.

2.5 Metal Detection Performance

At the outset of the research an evaluation through literature review was carried out to identify metal detectors used in humanitarian demining and determine typical performance metrics, such as sensitivity, weight and battery life. Literature in this area is rather limited, however a review of current metal detectors was performed by The Institute for the Protection and Security of the Citizen, European Commission Joint Research Centre [23] and provided insight into the performance of the detectors against one another. The review involved a set of laboratory tests performed by the Joint Research Centre (JRC) in 2003 to help compare the performance of detectors. These trials aimed to provide information on metal detectors to assist users for identifying a suitable detector for their use, help development by manufacturers and support European Committee for Standardization Workshops (CWA). The majority of the information presented in section 2.5 is extracted from the study [23] unless stated otherwise.

The trialled detectors included both static and dynamic detectors. To ensure the tests were not biased to a type of detector, metrics were always determined during sweeping motion and not static measurement. The detectors trialled as part of these test were the following:

- CEIA S.p.A. – MIL-D1 and MIL D1 DS
- Ebinger GmbH – Ebex 421 GC, Ebex 420 H-Solar, Ebex 421 GC/LS
- Guartel Ltd. – MD 8+
- Inst. Dr. Foerster GmbH and Co. KG – MINEX 2FD 4.500.01
- Minelab Pty. Ltd. – F3, F1A4 and F1A4 UXO
- Schiebel Elektronische Geräte GmbH - ATMID
- Shanghai Research Institute of Microwave Technology – Model 90
- Vallon GmbH – VMH3, VMH3C with UXO head

with the addition of the following for some tests and not all:

- Adams Electronics International Ltd AX777
- Beijing Geological Instrument Factory - GTL 115-2
- Schiebel Elektronische Geräte GmbH - AN 19/2

The tests conducted included detection capability of targets in air and in soil, immunity to environmental and operational conditions and an evaluation of ergonomic and operational aspects. The review includes a large number of detailed tests highlighting numerous aspects of the detectors. The following sections will report on a few of these tests which are thought to be of most relevance to this research.

2.5.1 Speed Tests

The initial tests performed were in air tests to identify the optimal sweep speed for each detector; slow and fast sweeps were found to result in loss of sensitivity for some detectors. Table 2-1, reports the results of the optimal speeds along with the effects of performing sweeps at low and high speeds. The detection object used in the test was a 100 mm 100Cr6 (a widely available ferromagnetic steel) sphere.

Table 2-1: Effect of sweep speed on sensitivity [23].

Detector	Optimum speed (m/s)	Loss of sensitivity at low speed 0.1 m/s	Loss of sensitivity at high speed - 1 m/s
Adams AX777	≥1.0	28%	0
CEIA MIL D1	0.1 to ≥1.0	0	0
Ebinger 420HS	0.45-0.65	61%	2%
Ebinger 421GC	0.6	30%	20%
Foerster 2FD 4.500	0.1	0	14%
Guartel MD8+	0.1	0	16%
Minelab F1A4	0.6 to ≥1.0	22%	0
Minelab F3	0.9	9%	8%
Schiebel ATMID	0.5	11%	2%
SHRIMT Model 90	≥1.0	33%	0
Vallon VMH3	0.5-0.6	19%	3%
CEIA MIL D1 DS	0-0.5	0	5%
Ebinger 421GC LS	0.4-0.8	30%	20%
Minelab F1A4 UXO	0.6	50%	10%
VMH3C UXO	≥0.9	30%	0

It is evident that most detectors have an optimum speed less than 0.7m/s and have measurably lost sensitivity by 1m/s. The SHRIMT Model 90, Adams AX777, both Edingers and the F1A4 suffered a significant sensitivity loss for slow sweeps as they are dynamic detectors. Dynamic detectors are designed to go silent if they are held stationary over a target, which is done by some manufacturers with the intention of improving pinpointing. CEIA MIL D1 displays the strongest performance in this criteria as it is unaffected by sweep speeds in the entire range of 0.1-1 m/s. Detectors displaying an optimal sensitivity of greater than or equal to 1 m/s continued to show improved sensitivity as the speed was increased to the maximum apparatus speed.

2.5.2 Repeatability on Set-up

Repeatability on set-up is an important factor as detector sensitivity can vary when repeatedly switched on and setup in the same way. This could be potentially dangerous if the detector is switched off during a break and reused without a re-check after. To determine the repeatability, detectors were set to maximum sensitivity and left for three minutes to settle. The maximum detection height of the 100 mm 100 Cr6 sphere was then recorded. The measurement was repeated 5 times for each detector and Table 2-2 reports on the variability between each run for the detectors.

Table 2-2: Repeatability on set-up [23].

Mnftcr.	Model	Meas. No.	Max. height (mm)	Diff. from average	Mnftcr.	Model	Meas. No.	Max. height (mm)	Diff. from average
CEIA[1]	MIL-D1	1	165	0.00%	SHRIMT	Model 90	1	205	-12.02%
		2	165	0.00%			2	170	7.10%
		3	165	0.00%			3	170	7.10%
		4	165	0.00%			4	185	-1.09%
		5	165	0.00%			5	185	-1.09%
Ebinger	Ebex	1	195	-4.28%	Vallon	VMH3	1	300	-6.76%
	420 HS	2	185	1.07%			2	285	-1.42%
		3	175	6.42%			3	270	3.91%
		4	190	-1.60%			4	280	0.36%
		5	190	-1.60%			5	270	3.91%
Ebinger	Ebex	1	160	2.44%	Vallon[2]	VMH3 M	1	270	-1.89%
	421 GC	2	165	-0.61%			2	265	0.00%
		3	165	-0.61%			3	265	0.00%
		4	165	-0.61%			4	265	0.00%
		5	165	-0.61%			5	260	1.89%
Foerster	Minex	1	205	-0.49%	BGIF	GTL-115	1	125	0.79%
	4.500	2	205	-0.49%			2	110	12.70%
		3	205	-0.49%			3	135	-7.14%
		4	200	1.96%			4	130	-3.17%
		5	205	-0.49%			5	130	-3.17%
Guartel	MD8+	1	120	0.00%	CEIA[3]	MIL D1 DS	1	480	-1.27%
		2	120	0.00%		(UXO)	2	465	1.90%
		3	120	0.00%			3	485	-2.32%
		4	120	0.00%			4	470	0.84%
		5	120	0.00%			5	470	0.84%
Minelab	F1A4	1	200	0.00%	Ebinger	421GC LS	1	95	3.06%
		2	200	0.00%		(UXO)	2	85	13.27%
		3	205	-2.50%			3	75	23.47%
		4	200	0.00%			4	100	-2.04%
		5	195	2.50%			5	135	-37.76%
Minelab	F3	1	170	0.00%	Minelab	F1A4	1	205	0.97%
		2	170	0.00%		(UXO)	2	210	-1.45%
		3	165	2.94%			3	205	0.97%
		4	175	-2.94%			4	205	0.97%
		5	170	0.00%			5	210	-1.45%
Schiebel	ATMID	1	225	6.64%	Vallon	VMH3 CS	1	185	-3.93%
		2	225	6.64%		(UXO)	2	175	1.69%
		3	260	-7.88%			3	175	1.69%
		4	225	6.64%			4	175	1.69%
		5	270	-12.03%			5	180	-1.12%

Detectors that do not allow fine sensitivity adjustment have displayed stronger repeatability. The authors of the laboratory test report, [23], viewed this to be a trade-off between offering fine sensitivity adjustment and detector repeatability.

2.5.3 Sensitivity Drift

Sensitivity drift is a common feature of metal detectors, however if the detection capability changes significantly over time the operator is required to repeatedly re-adjust the detector sensitivity. Regular sensitivity measurement of an appropriate target was conducted to determine the sensitivity drift of detectors and the outcome is shown in Figure 2-10.

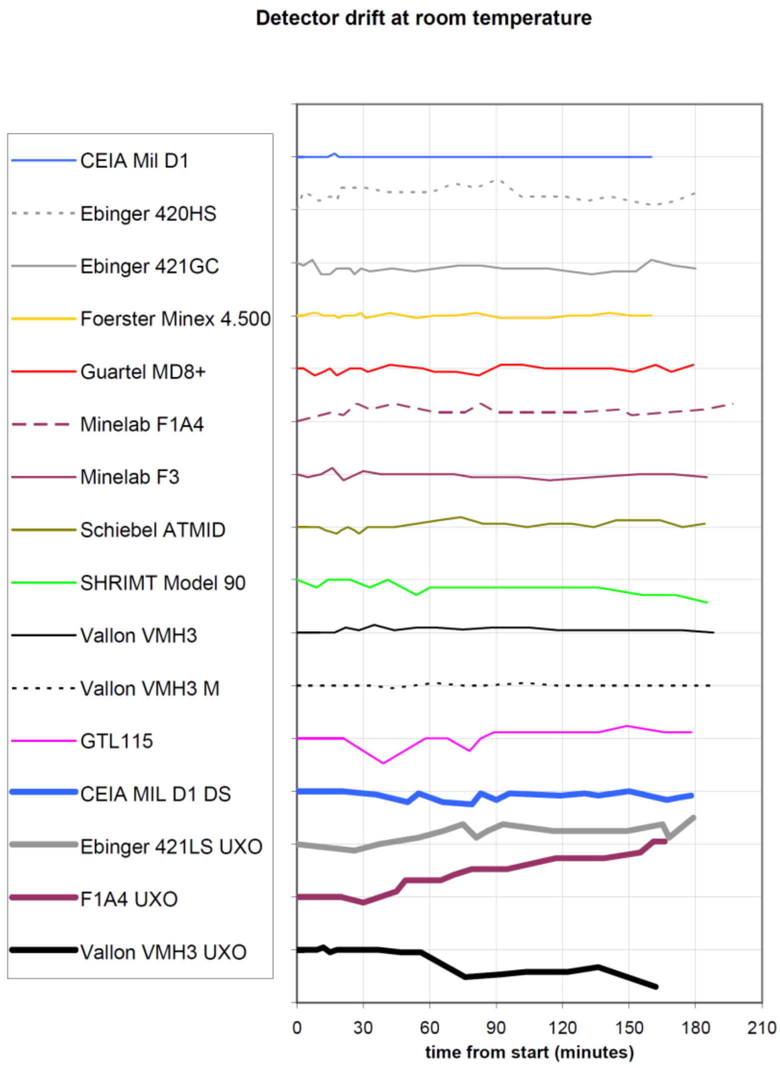

Figure 2-10: Chart of detector sensitivity drift. The sensitivities are normalised to their starting values. For all plots, one vertical division represents 50% increase (or decrease) in the maximum detection height of the target [23].

The CEIA MIL D1, Foerster Minex and Vallon VMH3M displayed the steadiest sensitivity variation during the course of the test. It is important to note that the drift measurements displayed in Figure 2-10 are affected by variations of power delivered by power regulators and hence encompass . However, the information displayed is still beneficial to the end user as it displays the overall sensitivity fluctuation.

2.5.4 Minimum Target Detection Curves In-Air

The following subset of tests addresses the minimum sphere size that the detectors were capable of detecting in air for different sphere materials. The spheres were held in place and the detectors were swept over the targets manually at different heights at their optimum setting and speed to determine their performance. Figure 2-11 to Figure 2-13 report on the detetcor performance using 100Cr6, AISI 316 (stainless steel) and aluminium spheres respectively.

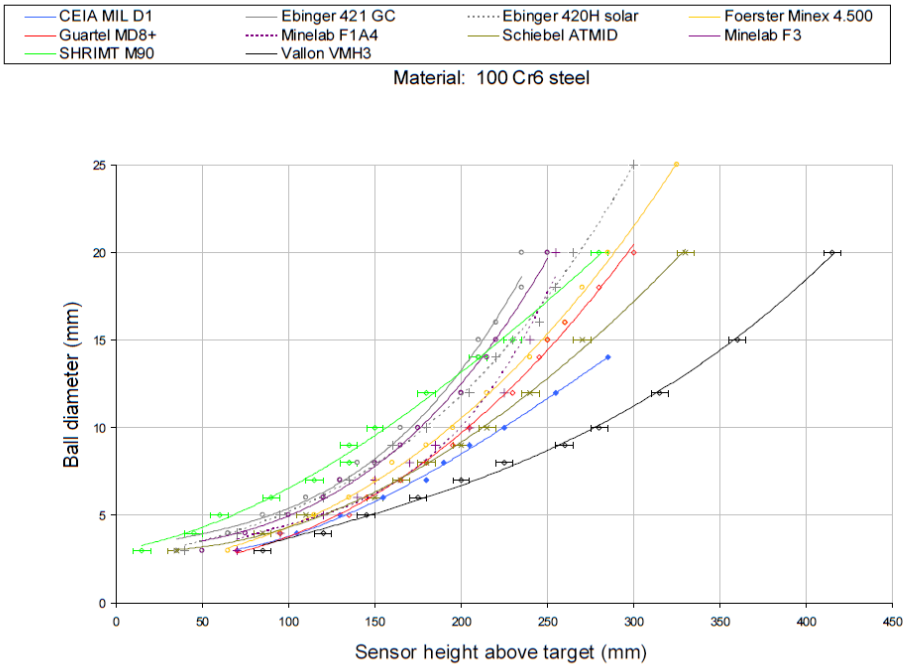

Figure 2-11: Minimum detectable sphere diameter versus sensor height above 100Cr6 steel spheres in air [23].

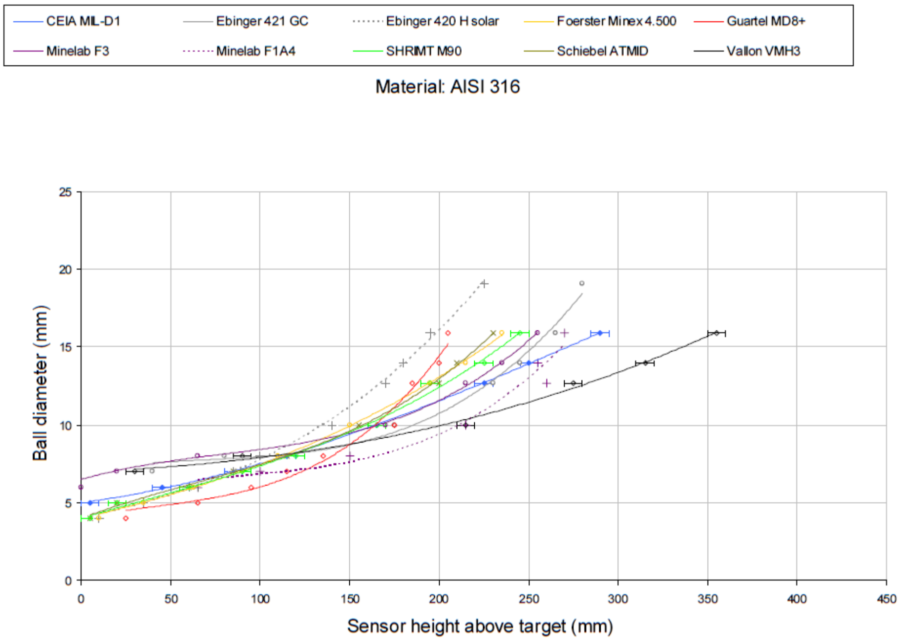

Figure 2-12: Minimum detectable sphere diameter versus sensor height above AISI 316 steel spheres in air [23].

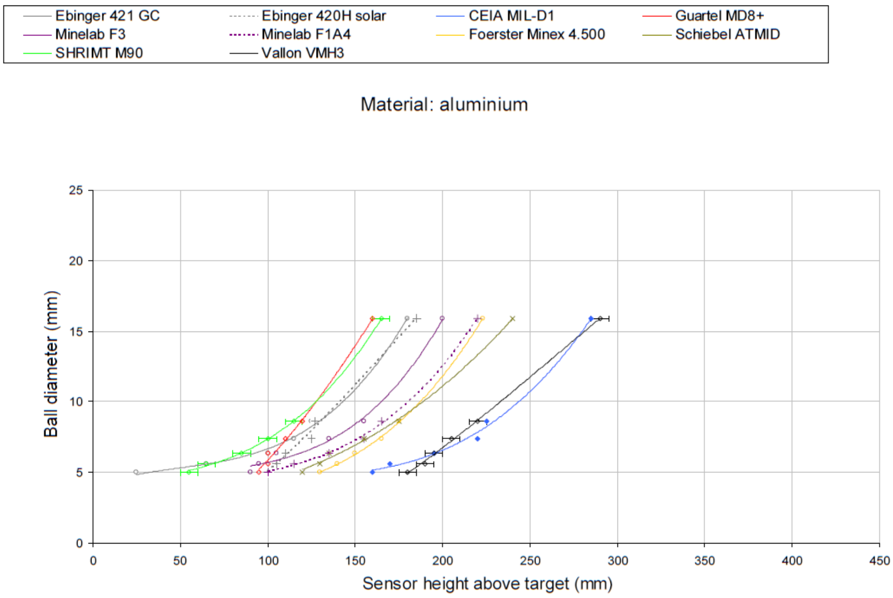

Figure 2-13: Minimum detectable sphere diameter versus sensor height above aluminium spheres in air [23].

For all materials the minimum sized sphere detectable was around 1 to 3 mm. The sensitivity of the detectors varied significantly with the height variance. The Vallon VMH3 displayed outstanding sensitivity in air for all targets followed by the CEIA MIL D1. Detectors proved to be generally less sensitive to AISI 316. This is expected and is a direct result of the reduced conductivity and magnetic permeability of the AISI 316. The AISI 316 is a class of steel that is completely non-magnetic in spite of the iron being the largest alloy and is known as austenitic. The effects of the material on the object detectability will be discussed further in section 3.4.2.

2.5.5 Detection Capability of Specific Targets In-Air

A similar test was then performed using targets from two standardised demining sets; the International Test Operations Procedure (ITOP) fuze inserts identified by CWA and simulated fuzes made by CEIA SpA. These targets emulated the responses of real mines and helped identify the detection capability corresponding to relevant targets. The ITOP fuzes C0-O0 are fuze simulants of increasing difficulty of detection from O0 to C0; C0 to K0 are AP simulants and M0 and O0 are anti-tank (AT) simulants. The CEIA simulated fuzes were placed in Perspex holders designed to emulate the different mine casings.

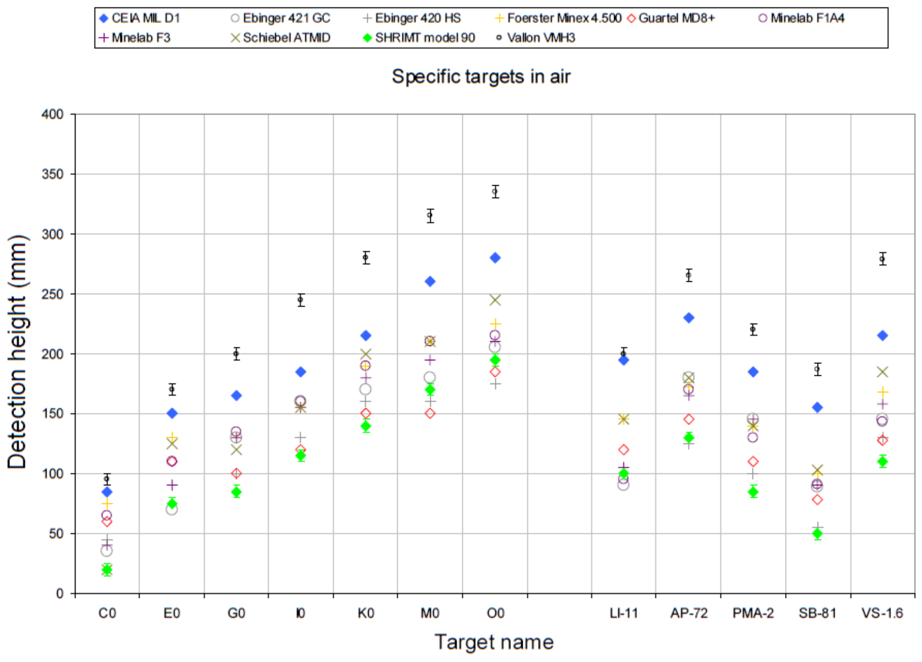

Figure 2-14: Detection heights for specific targets measured in air [23].

Figure 2-14 represents the test result of the in-air scanning of the fuzes from the two sets of mine simulants. Again, the Vallon VMH3 demonstrated the strongest performance, followed by the CEIA Ml D1.

2.5.6 Minimum Target Detection Curves In-Soil

The test described in Section 2.5.4 was repeated but placing the metallic spheres in different magnetic soil types to determine the detector susceptibility to the magnetic content of the soil. However, the test was only performed for the 100Cr6 sphere. Two soil types were used; Napoli volcanic soil and Montagnola Terra Rossa soil. The magnetic susceptibility of the soils were classified by CWA as “severe” and “moderate to severe” respectively. The Napoli soil has geologically recent volcanic activity and the soil tests reported a relatively high magnetic susceptibility of around 600 x 10^{-5} $m.kg^{-1}$ at frequencies from 0.5 kHz to 5 kHz (higher frequencies were not reported). The Terra Rossa however, was found to have high magnetic susceptibility at 0.5 kHz but decreased as the frequency increased to 5 kHz.

The detectors were adjusted for the different soils and swept over the buried sphere to determine the maximum detection height. Figure 2-15 and Figure 2-16 display the results obtained from the two soil types.

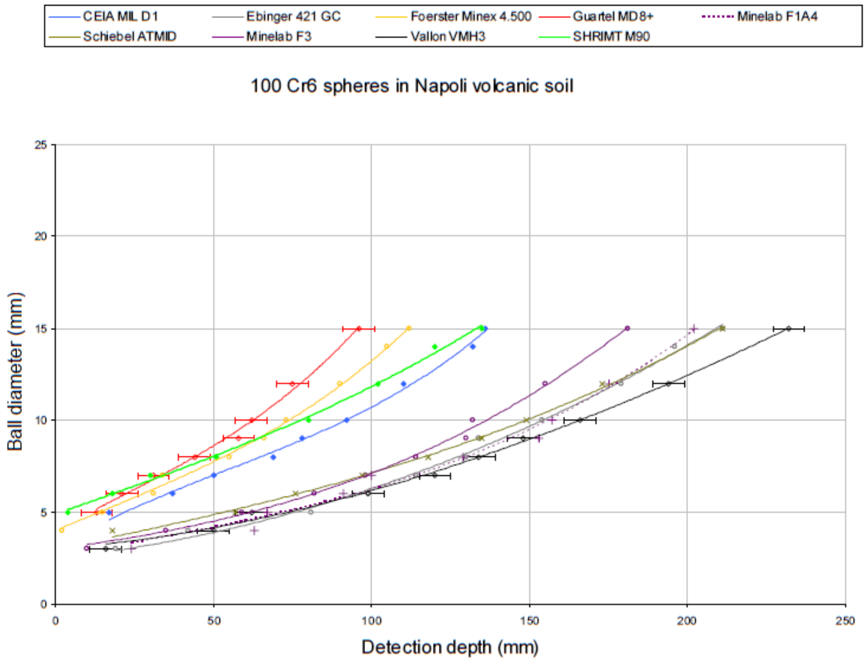

Figure 2-15: Minimum detectable 100Cr6 steel sphere diameter versus depth below soil surface for in Napoli volcanic soil. The detector Ebinger 420HS is not shown as it was unusable on this soil [23].

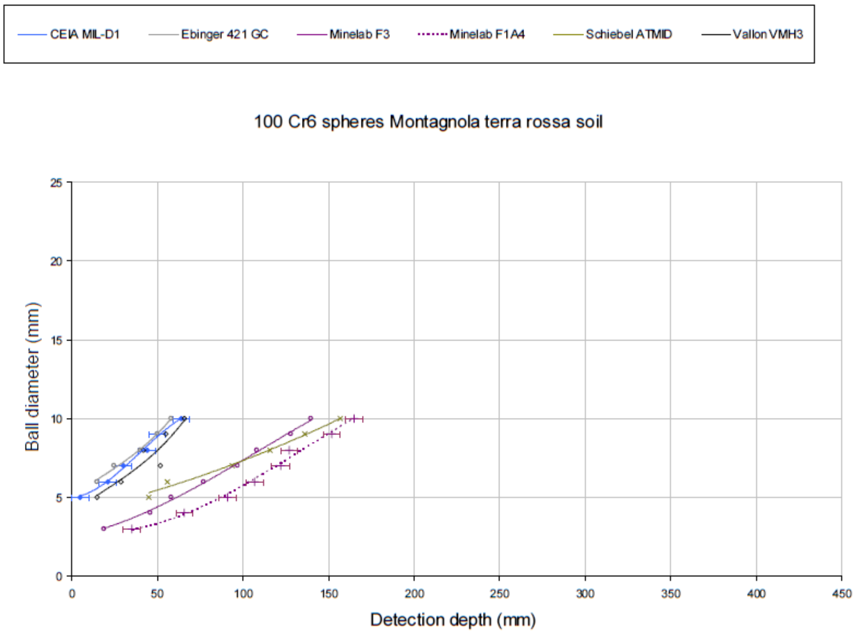

Figure 2-16: Minimum detectable 100Cr6 steel sphere diameter versus depth below soil surface for in Montagnola terra rossa soil. Detectors Minex 4.500, 420HS, Model 90 and MD8+ were unusable on this soil [23].

The figures show the Vallon VMH3 was the strongest performer in Napoli volcanic soil while the Minelab F1A4 was the strongest in the Montagnola Terra Rossa soil. However, all detectors displayed a significantly reduced detection height for the spheres highlighting the impeding property of a soil with magnetic content.

2.5.7 Weight and Power Consumption

The authors of [23] continued the review by discussing the importance of a good design of the detector to reduce fatigue experienced by deminers. Deminers use metal detectors for up to 6 hours a day, months at a time. The weight of the detector is an important factor as well as the position of centre of gravity. The closer the centre of gravity is to the operators hand the easier the detector is to handle and the less effort is excreted by the deminers during the course of the day. Figure 2-17 displays the weight of the different detectors and highlights the acceptable range is between 1.5-3 kg.

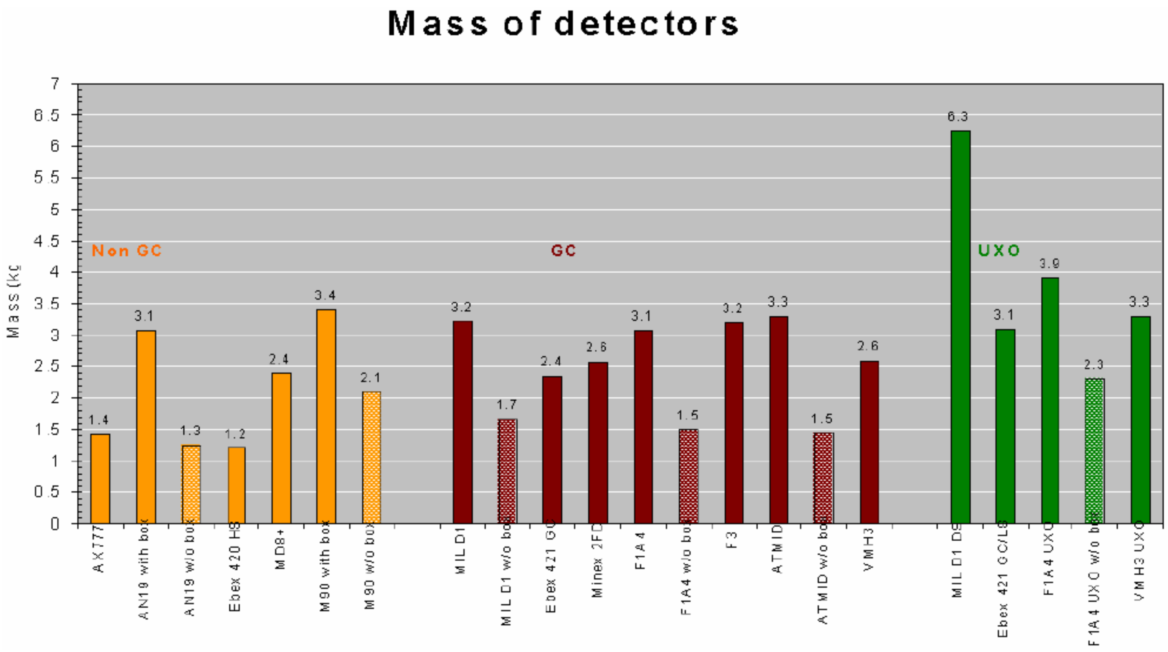

Figure 2-17: Total masses of the detectors as operated. In cases where the control box is detachable, the mass without it is shown as a hatched bar. For the Model 90 this is the only configuration possible. Detectors are divided into detectors with ground compensation (GC), without ground compensation (Non GC) and UXO detectors [23].

Finally, the lab trials investigated the performance of the batteries and the performance of the detectors with dropping battery voltage. Figure 2-18, displays the effect of reducing the supply voltage to the Minelab F1A4 and measuring the sensitivity (detection depth for a specific target).

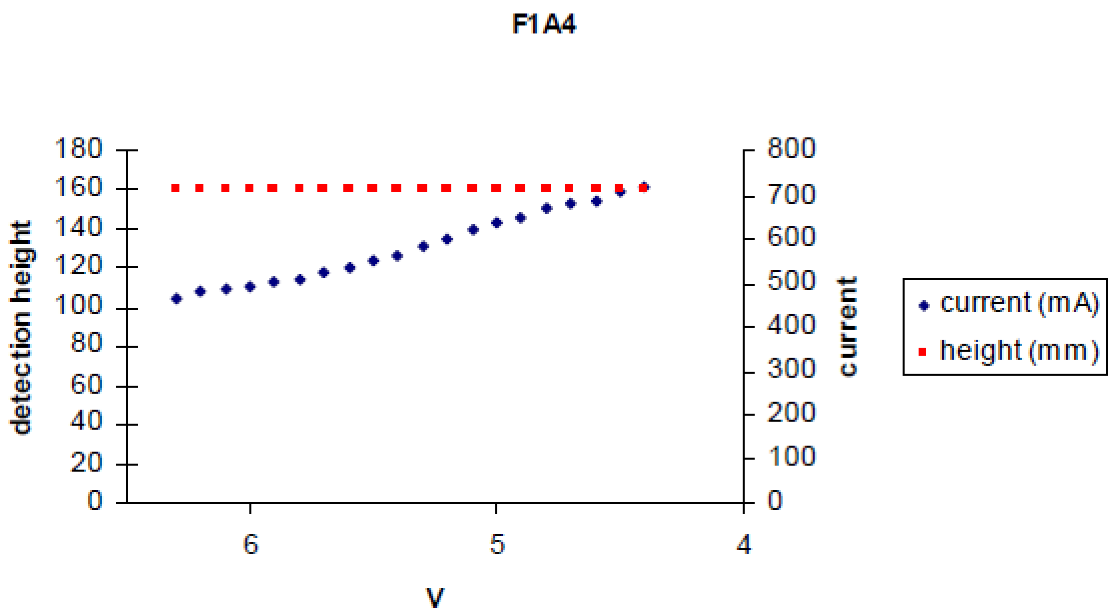

Figure 2-18: Effect of reducing supply voltage for the Minelab F1A4. This detector takes four alkaline cells of size “D” (LR20 or MN1300) [23].

The current drawn from the batteries increased as the battery discharged and the voltage dropped. This is the common trend in metal detectors tested where the internal power regulators approximately draw constant power rather than constant current. The sensitivity for most detectors was found to be unaffected by the battery discharge highlighting the quality of the internal power regulators. In order to test the battery consumption of the detectors a set of fresh consumer grade alkaline batteries were connected to the detectors. The detectors were switched on and left to run until the battery discharged. Figure 2-19 displays the time it took for each detector to reach an unusable state.

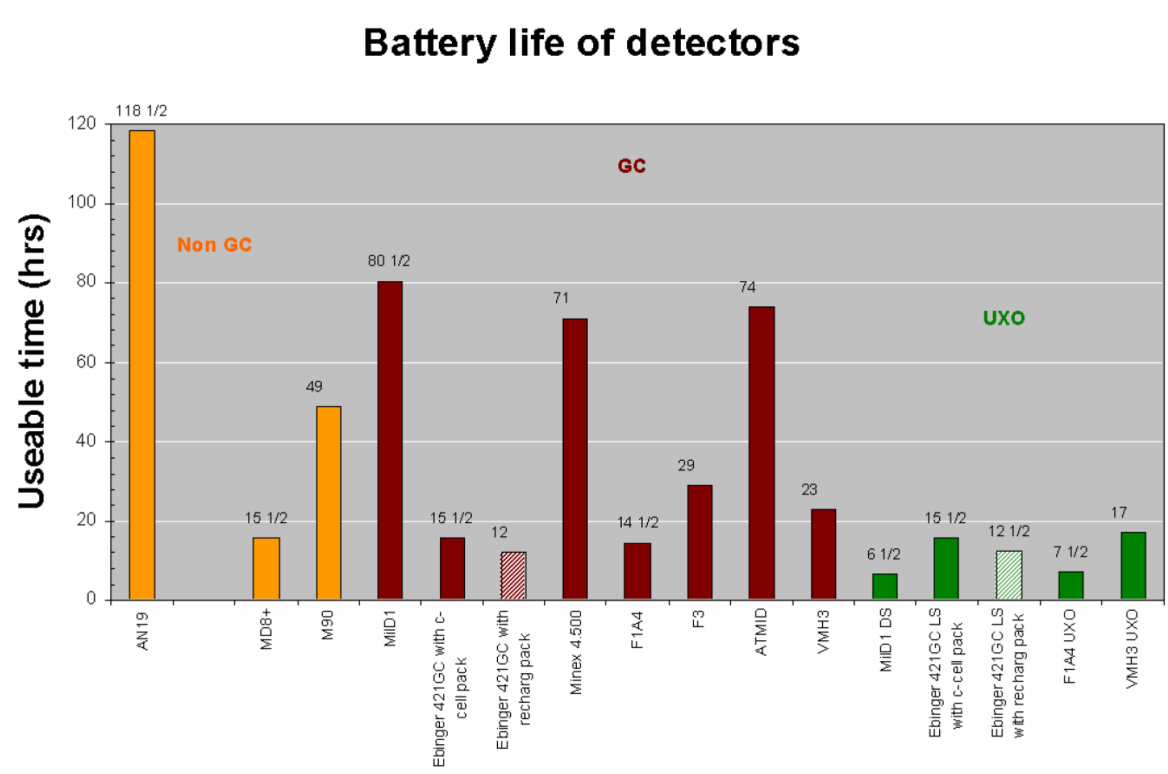

Figure 2-19: Ultimate battery life for detectors, continuing beyond the initial alarm until detector unusable. Detectors are divided into detectors with ground compensation, GC, without ground compensation, Non GC and UXO detectors [23].

Continuous wave detectors displayed a longer battery life in comparison to pulsed induction with the exception of the AN19 which displayed a significantly longer battery life. The Ebinher 420 HS was not included in the results above as it constantly recharges its battery under normal battery use using solar panels.

2.6 Review of Research Efforts

Following the review of metal detectors a secondary review followed to identify the current and previous research efforts to enhance detection technologies. The review was important in understanding the pitfalls of previous research. This was again aided by a major review carried out in 2006 by the Geneva International Centre for Humanitarian Demining [24]. The report summarises previous and current attempts to enhance detection apparatus as well as current systems in use. The Geneva report highlights the fact that a considerable funding and effort has been made since the mid-1990s to develop new systems for humanitarian and military demining. A key point raised by the review is the low portion of technologies that have progressed from research and development (R&D) to field use. The report concluded three main reasons for such an ineffective conversion into field instruments [24];

- most R&D has focused on the technology development and overlooked the complexity of the environmental and field use conditions.
- the mismatch between research ideas and application requirements in the field.
- the significant non-technological problems in funding the resources to turn prototypes into fully tested commercial products ready to use in the field.

To avoid such scenarios, the group at the University of Manchester consulted MAG at the start of the research to draw upon their operational knowledge and help identify any constraints that may have been overlooked by the group.

A host of different physical principles have been investigated over the past years with the aim to improve detection apparatus. There are two main parameters that detection tools are measured by; probability of detection (P_d) and probability of false alarms (PFA), prompting two main areas for development. Metal detectors are viewed as a mature technology in the field with already a high P_d, only struggling with the low metal mines at depths [24]. Hence, the major focus has been directed at reducing PFA or FARs. Metal detectors could typically uncover 100 to 1000 inert metal objects for every mine [25]. Several attempts have been made to reduce FARs with suggestions of having separate confirmatory detectors. However, only one recent approach has proved fruitful; the development and deployment of dual sensor systems [26]. The combination of ground penetrating radar and metal detection in particular has provided promising results; enhancing detection of low metal mines and extensively reducing FARs (up to 86% reduction) [26].

Metal detection has gone through little development in recent years. Development of inductive metal detectors has mainly focused on increasing sensitivity and cancelling ground effect up until recently. Recent research efforts have investigated the potential to characterise detected objects in line with the goals and objectives of this research. A summary of the literature review relating to metal characterisation is present in section 3.5 once the tensor is introduced. The remaining sections in this chapter will provide a summary of the literature review of research performed to develop mine detection through alternate technologies; Electrical Impedance Tomography (EIT), acoustic and GPR. GPR is reviewed more extensively as it is the single technology that has managed to be deployed successfully in the field with immediate reduction of FARs.

2.7 Ground Penetrating Radar (GPR)

The success of GPR can be linked in part to the much greater funding it has received when compared to other technologies [27]. GPR has been developed over the past 20 years for numerous applications to detect buried objects and for soil study [27]. As a result it is considered a mature technology with numerous applications in the fields of civil engineering, geology and archaeology to locate objects ranging from utility pipelines to archaeological artefacts [27, 28]. However, GPR had struggled to meet performance targets for landmine detection due to lack of understanding of how different environmental factors and mine characteristics affect its performance [28]. GPR's potential of detecting plastic-cased mines of low metal content has added considerable interest for further research and as a result has developed to recently feature in a number of new detectors. The use of GPR has been deployed alongside traditional MD in dual sensors, promising a significant reduction in false alarm rates and enhanced capability to detect low metal mines [26].

The operating principle is very similar to that of radar, where an electromagnetic wave is emitted and the reflected wave is measured. However, the wave is emitted into the ground rather than air using an antenna that does not require ground contact. Buried objects and air-ground interface cause reflections due to different electrical properties resulting in different refraction indexes at material boundaries [27, 29]. These reflections are picked up by the receive antenna(s) and processed to produce an image such as in Figure 2-20 or an audio signal that indicates detection of a mine-like object (by comparing the signal with a mine reference library) [29]. The majority of handheld detectors present the GPR data in the form of an audio signal; however, recent versions are starting to present an image form of the GPR signal. The frequency used determines the spatial resolution of the radar system, where higher frequencies provide higher resolution. However, higher frequencies limit the penetration depth [27], which presents the designer with a trade-off between quality of the image and penetration depth [29].

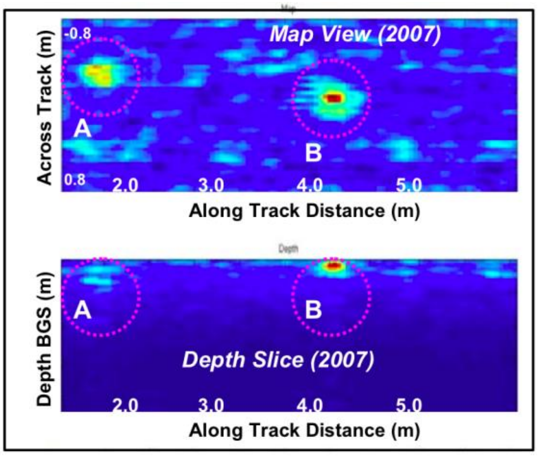

Figure 2-20: GPR image of a plastic cased (A) and a metal cased (B) landmine targets [30].

The magnitude of reflections depends on the contrast of electric properties, in particular the dielectric constant, as well as the size and shape of the object [27]. This presents a number of challenges for the use of GPR for humanitarian demining. The contrast between a metal mine in the presence of a far-less conducting soil would present a significant signal, whereas a plastic mine would be a much more difficult target to detect specially in mediums such as sand [29], which has a similar electrical permittivity to the mine. Sensing is further complicated by the multiple dielectrics present within a mine [29]. Another challenge is the significant reflection received from the ground surface, normally the area of greatest dielectric contrast, otherwise known as large "ground bounce" [29]. If the GPR bandwidth results in low resolution, then a reflection from a mine placed at a shallow depth would be swamped by the large ground reflection [29]. Finally, clutter is also an issue for GPR. GPR clutter is regarded as spurious reflections from subsurface inhomogeneities such as rocks, roots, pockets of water…etc. [29]. These represent the principal source of false alarms for GPR [29].

It is noted that four main properties define GPR systems; path loses that are mainly a result of soil attenuation, target radar cross section, surface clutter and buried clutter [27]. Signal processing and antenna design significantly influences these factors. Signal processing algorithms play a vital role in the effectiveness of GPR. GPR previously produced an unacceptable FAR), however algorithms such as hidden Markov models (HMM) used in HSTAMIDS, significantly aided the filtering out of clutter signals [29, 31]. These algorithms continue to be developed to further enhance the performance of GPR [29]. The GPR antennas need to be able to provide the required signal to noise to detect mines after the large ground bounce and are designed to have [32]:

- low gain.
- minimum sidelobes and backlobes.
- specific requirements in terms of bandwidth.
- specific requirements in terms of impulse response.
- linear phase for time domain systems.

With GPR being the most successful technology, a number of detectors have now started to be commercially sold for field use; namely the US Army Handheld Standoff Mine Detection System (HSTAMIDS) and MINEHOUND. The following sub-sections will report on the detectors currently deployed in the field and being researched. The amount of information provided is somewhat varied as different groups opt for different levels of transparency. As mentioned earlier, operating procedures for each detector are reported if available in current literature.

2.7.1 The AN/PSS-14 (HSTAMIDS)/AMD-14

CyTerra developed the Handheld Standoff Mine Detection System (HSTAMIDS) on behalf of the US Army. CyTerra claim the HSTAMIDS to be a revolutionary detection tool that uses advanced data fusion algorithms to combine the signals from a highly sensitive metal detector and GPR enabling a reliable and consistent detection of low-metal anti-personnel and anti-tank mines [33]. CyTerra also claims the performance to be maintained in variable soil types; wet, dry frozen, iron-rich, clay and sand [33, 34].

Figure 2-21: The HSTAMIDS in operation during field tests by MAG[34].

The MD signal is provided in the traditional format where the volume and pitch of the audio signal vary depending on the magnitude and phase [33]. The second signal is the output from the data fusion algorithm, Aided Target Recognition (ATR), that provides a sharp beep when the MD and GPR data indicate the presence of a mine like object [33]. The operator could choose to switch either of them off. This allows the operator to focus on one signal, which becomes useful if one signal is producing a constant high volume that could distract the operator (e.g. a high metal anti-tank mine) [33].

There have been a number of tests performed both by the US army and by humanitarian organizations in both controlled environments and field tests. The US Army Operational Test Command performed operational tests to compare the performance of the HSTAMIDS with conventional detectors. The operators received a 40-hour training course and were asked to perform scans of test lanes. The authors of the trial report claim a reduction in FAR by a factor of 5 (77% of false alarms were rejected) and an increased detection probability. This FAR reduction was calculated to equate to a time saving of over 250 hours for the 800 clutter items rejected [35].

2.7.2 VMR-3(G) MINEHOUND

Figure 2-22: The MINEHOUND system in operation [36].

MINEHOUND is the second handheld detector that integrates both MD and GPR, again with the aim to reduce FARs. It combines custom-designed GPR developed by ERA (UK) with a pulse induction metal detector, VMH3, by Vallon (Germany) [27].

MINEHOUND presents an audio signal for both the GPR and MD output [27]. There has been no mention of the MINEHOUND performing any means of data fusion of the signals and so is assumed not to do so. GPR responds to the smallest flush-buried mines but not too small metal fragments [37], which provides the basis of clutter rejection in MINEHOUND. It also allows an adjustable start search point for the GPR to remove noise from the soil surface/ground bounce and an adjustable stop point limits to define a maximum depth to remove noise from bedrocks and water tables [36]. The GPR provides accurate position and depth along with the radar cross-section of the mine target [37]. To do so the MINEHOUND utilises a single receiver and transmitter antennas, mounted on a purpose designed printed circuit board that deals with the associated control [27].

A number of field trials were performed using the final prototype of the MINEHOUND during 2005-2006 in Cambodia, Bosnia and Angola and further field trials were performed during 2010-2013 using the production model in Cambodia and Afghanistan. In all trials MINEHOUND was used as a follow up to conventional metal detectors investigating marked detections [38, 39]. Conventional metal detectors would initially scan an area or lane and mark all targets with a red wooden disc. The MINEHOUND then followed to interrogate the marked targets using MD and GPR and a blue mark was placed if it rejected the target as clutter [39]. The final production MINEHOUND trials in Cambodia encountered 661,890 metal signals out of which 92% were correctly deemed as clutter [39]. The 845 true treats were also correctly identified however since the MINEHOUND simply followed and only investigated conventional detector marks, it is hard to accurately determine the MINHOUND's P_d. The trials claimed a clutter rejection rate of 72% at the start and increasing to 95% by the end of the trials in 2013 as the operators became more familiar with the device [39]. The clutter rejection rate was much higher in Afghanistan, 99%; however, those trials were investigating AT mines with larger radar cross section and hence a lower probability of GPR false alarms [39].

2.7.3 Advanced Landmine Imaging System (ALIS)

ALIS, Advanced Landmine Imaging System, is a third hand-held detector that provides dual sensing; however, has been conducting several field evaluations over the last decade and has not quite reached the level of deployment as the previous detectors. The key difference between ALIS and the other detectors is the ability to provide images of the MD and GPR signals [27]. The sensor position is recorded using a CCD camera mounted on the sensor handle [40], allowing the system to provide real-time MD imaging and post processing GPR [40]. The system can present the MD sensor output in real-time on a head mounted PC display [41]. This is considered to be an advantage as ALIS claims to help deminers scan only regions of interests once a target has been identified[42].

Figure 2-23: ALIS system in operation with control unit (back) and palmtop PC on flexible arm [42].

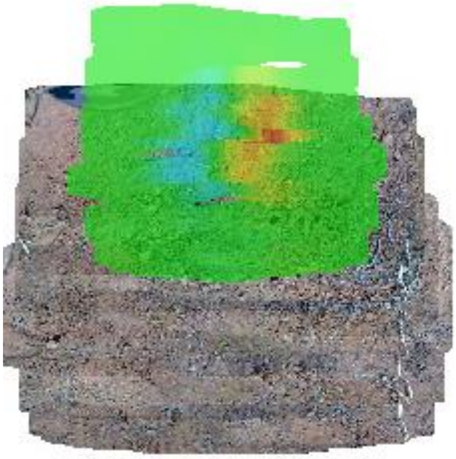

Figure 2-24: Visualised metal detector data [42].

The ALIS is initially used as a standard metal detector, where the deminer scans an area of 1x1 m, locating any buried metallic targets [42]. Once a target is located, the deminer then narrows the search down to an area of about 40 cm^2 performing a slower scan to aid the quality of GPR images [42]. The ALIS system then spends 5-10 seconds processing the captured data and provides images of the metal detector signal and the GPR image as displayed in Figure 2-25 [42]. The operator is able to observe the images on the display provided and step through the different depths of the GPR image slices [42]. The group developing ALIS have indicated to future research aimed at developing a semi-automatic detection algorithm that would aid ALIS operators in identifying threat objects [42], however no data fusion has been reported thus far.

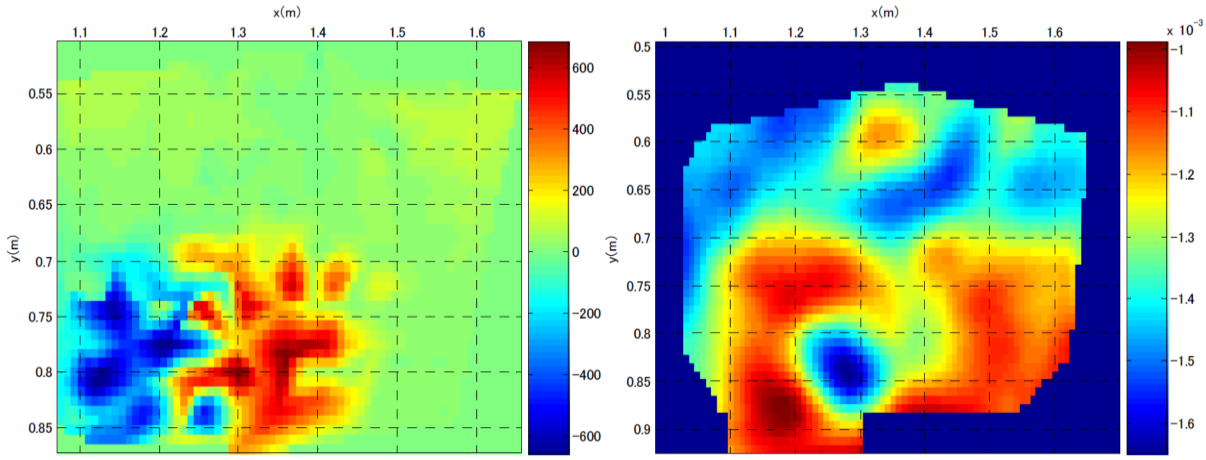

(a) (b)

Figure 2-25: (a) Metal Detector image and (b) GPR image from ALIS tests in Croatia [42].

Two field evaluations were performed in Afghanistan in December 2008; a controlled flat test site for the evaluation of landmine sensors and a real landmine field on a small hill

[41]. At the first site, real PMN-2 and Type 72A mines were buried without the booster charge. The metal detector was able to detect landmines up to a depth of 15 cm and the GPR was able to display clear images of landmines buried up to 20 cm [43]. Metal fragments did not show clear GPR response allowing the elimination of clutter [41]. However, these trials seem to lack the definitive performance figures produced by MINEHOUND and HSTAMIDS in relation to percentage of clutter pieces rejected.

2.7.4 Summary Evaluation

GPR has numerous advantages that encouraged funding, advancing the technology to become the most successful alternative/addition to metal detection. It complements metal detection by sensing the variation of the dielectric constant of the mine casing and not the metallic content. It does not respond well to metallic clutter and hence assisting in its disregard. It provides the possibility of imaging mines or other buried objects while maintaining reasonable penetration depth [28]. Most GPR mine detection systems use very low power and do not present any radiation hazard, allowing for sustained battery life [27]. Finally, it is a relatively mature technology that has been well researched in numerous other applications [27, 28]. This may have been a large contributor to its successful introduction to demining operations.

GPR responds to natural subsurface inhomogeneities, such as roots, rocks and water pockets resulting in mine-like signals and false alarms [28]. GPR struggles to operate in wet soils as its penetration suffers and attenuation increases with increased moisture; wet clay particularly provides extremely challenging conditions [27, 28]. Contrastively, very dry soils also present a challenge as the dielectric contrast is reduced making it hard for plastic objects to be detected [27]. An additional limitation is that GPR systems may miss very small plastic mines buried at shallow depths because the signal at the ground surface can mask the return signal from the mine unless it is tuned to a sufficiently high frequency [28]. An issue which results in a trade-off/balance between higher resolution (higher frequencies) and further penetration depth (lower frequencies) [27, 28]. GPR can also struggle in terrains with very rocky ground as it is not always possible to find space to swing the detector head close to the ground surface [39]. Same applies to very uneven grounds such as old ploughed fields as tuning the GPR response to reject the ground bounce can be difficult [39]. Finally, GPR has also been criticised to actually reduce P_d rather than enhance it [44]. GPR is almost always used as secondary detection to reject clutter and as a result is not used to detect a mine missed by the metal detector. This along with the fact that GPR does not have a probability of detection of 100% can be viewed to result in more missed mines [44]. However this argument has been rejected in [44], and evidence weighs against this view [39]. Deminers have been found to reduce the sensitivity of metal detectors as a means of reducing some clutter signals. The introduction of GPR would allow deminers to use metal detectors at higher sensitivities and have more confidence in indications presented and hence increasing P_d [44].

The combination of GPR and MD has produced the most promising results in reducing FAR and enhancing the performance of mine clearance. It is the most mature alternative technology with continued research to process individual signals to perform data fusion for enhanced mine detection. The varied performance of GPR has previously hindered its adoption into landmine detection, however recent research in advanced modelling of GPR and enhanced signal processing is proving to eliminate a lot of those issues [28].

2.8 Electrical Impedance Tomography

Electrical impedance tomography (EIT) is a soft field modality that has been used in several industry sectors to image inaccessible regions of interest. By interrogating and reconstructing the distribution of conductivity for a region using periphery measurements non-intrusive imaging can be achieved [45]. Since the ground is slightly conductive, the technique could be used to map the subsurface strata by probing the surface with electrodes [46]. This has a direct application for landmine detection where buried objects and mines could be mapped as mines are buried at shallow depths and cause discontinuity in the soil conductivity [47].

EIT relies on measuring electrical potentials across a series of electrodes for different current injection sites. Pairs of electrodes are excited passing current through the medium, soil, while other pairs of probes are used to measure potential. Through a series of applied excitation currents, the measurements are collected and used to solve the quasi-static inverse problem to produce a map of conductivity that could have resulted in these measurements [48]. Both metallic and non-conductive mines will disturb the conductivity in the soil and provide anomalies in the measurement which vary based on the size, shape, conductivity and depth of the buried mine [47]. The main advantage is that EIT provides superior performance when dealing with wet environment and soil, rather than dry conditions; a condition where both metal induction and radar struggle. As a result it is viewed as an attractive technology to research as it complements GPR and EMI in wet conditions.

A group in Canada has performed the majority of research regarding the application of EIT to detect landmines. Recent efforts by Church *et al.* [48] report on results of applying EIT outside the lab environment to detect buried landmines. The instrument used is displayed in Figure 2-26 and highlights an 8x8 electrode array, spring loaded to accommodate for terrain variations.

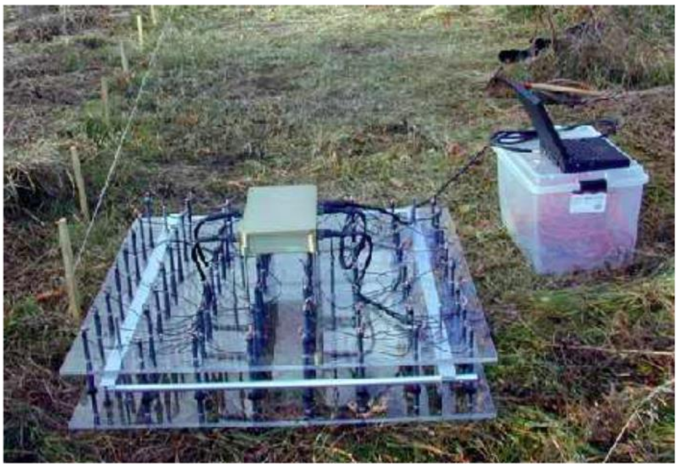

Figure 2-26: The EIT instrument performing measurements at a test site at DRDC Suffield. The data acquisition system is the rectangular box above the electrode array, connected to the laptop (data processing) [48].

Church *et al.* [48] provided field test results for anti-tank mine surrogates over grassy terrain with sandy soil. The tests displayed reasonable reconstructions for non-metallic objects of a diameter of 2 Electrode Separation (ES), buried up to a depth of 1.75 ES and a thickness less than 1 ES [48]. The results below display the inverse solution calculated at 14 cm when using a mine-like object with a diameter of 28 cm and a thickness of 12 cm.

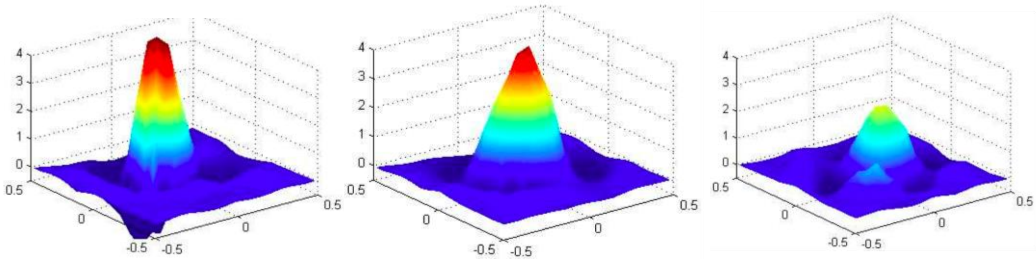

(a) (b) (c)

Figure 2-27: Results obtained for a mine like object buried in sandy soil at depths of 7, 14 and 21 cm respectively [48]. Horizontal axis units are horizontal distance from centre of object (0,0) in meters. Vertical axis is detector response in arbitrary units.

The ability of the detector to detect two identical targets in close proximity was also investigated. Figure 2-28, displays a contour map of EIT detector response at a depth of 14 cm and 21 cm for two identical targets 7 cm and 14 cm apart respectively.

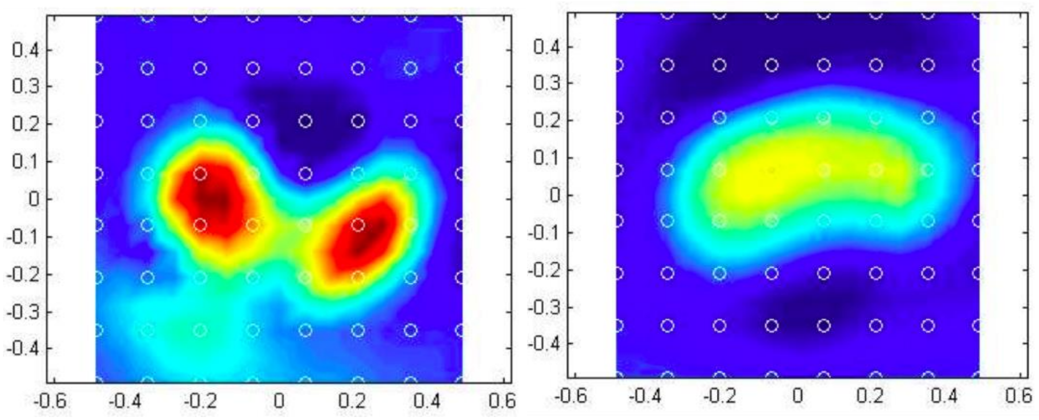

(a) **(b)**

Figure 2-28: Results for identical objects buried at 14 cm and 21 cm in sandy soil, separated by (a) 7 cm and (b) 14 cm [48].

The work by Church *et al.* does not report on any results for anti-personnel mines which leads the writers to believe EIT struggled with such small targets. Further research has been performed to assess the performance of EIT to detect mines underwater, especially in sea water, which is an environment where EMI and GPR are inoperable. EIT displayed potential of detecting mines underwater, however still required contact with the ground surface as its performance dropped off quickly when not in contact with the sand surface [48, 49]. These tests placed the object just under the sand surface and do not identify the breakdown depth at which the detector failed to identify buried mine like objects.

2.8.1 Summary Evaluation

Both metallic and non-metallic objects disrupt the soil conductivity, which makes EIT theoretically suitable for all types of mines. It also demonstrates a niche in wet environments and so could be suitable for detection in beaches or marshes [28]. EIT equipment is relatively simple and inexpensive which is an added positive to the approach [28].

However, a significant disadvantage of the technology is that it requires physical contact with the ground, which could potentially detonate a mine. EIT also struggles in dry conditions requiring excessive insertion pressure in non-conductive environments such as deserts and rocks [28]. The system is also highly susceptible to noise [28], becoming more susceptible as the depth increases [49]. This makes the system only feasible for shallow buried objects, where both GPR and MD are capable of detecting low metal mines. Finally, the resolution is not as fine as that provided by other technologies such as GPR [28].

It has been concluded that EIT is not broadly suited for humanitarian demining [28]; however, displays a potential use when detecting non-metallic mines in wet environments, a property which has evaded other detectors. Even in these conditions it has a very limited depth range and mines in those conditions are usually buried much deeper than usual [28].

2.9 Acoustic/Seismic Detection

Seismo-acoustic methods detect mines by causing vibration using acoustic or seismic waves sent through the ground [28, 50]. The waves are generated and received by either non-contact or contact transducers for acoustic and seismic systems respectively [50]. The detection method is unique as it interrogates the mechanical properties of the mine and not the electromagnetic properties [28]. Compliance is the property that specifies the deflection of an elastic body by an applied force and is the mechanical property used to differentiate between mines (compliant) from other buried objects or false alarms (usually non-complaint) such as rocks, tree roots, metallic clutter, bricks…etc. [50].

The mine casing provides a high vibration contrast, as it is acoustically compliant and noticeably different from the surrounding soil [50]. The mine is also non-porous whereas the soil is porous providing additional contrast in the presence of coupled sound. The complaint mine container dynamically interacts with the soil on top of it leading to specific linear and nonlinear effects aiding detection and discrimination [50]. Buried landmines will resonate under an excitation by the acoustic/seismic coupled energy. These resonances are due to the bending resonances of the mine casing’s upper diaphragm [28]. The mass of the soil on top of the mine creates a mass-spring system which affects the resonance resulting in a well-defined resonance response, which forms the vibration signature [50]. These signatures have been measured in numerous laboratories and field tests to assess the capability of detection and discrimination [50].

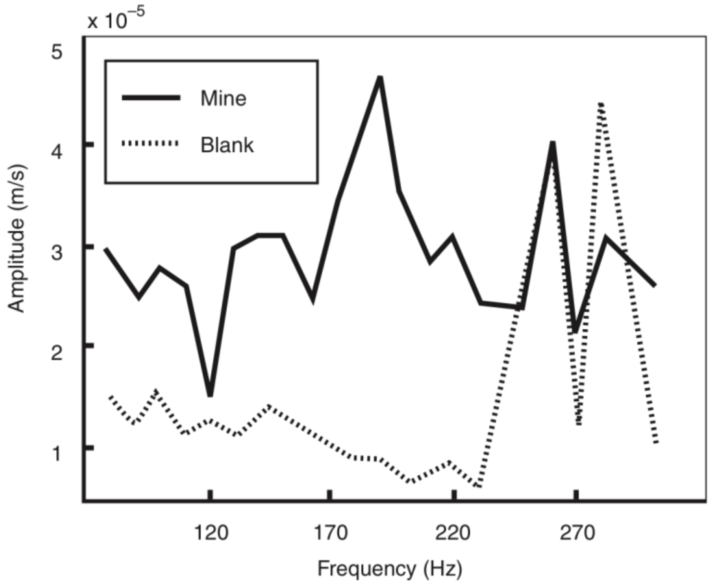

Figure 2-29: Amplitude of surface vibration of ground over a mine (solid line) and a blank (dashed line) in response to sound waves [28].

For mine detection literature reports on mainly the use of acoustic energy to induce mine vibration. [50]. Acoustic energy is emitted into the ground by a powerful loudspeaker of which a large fraction is reflected by the ground surface and the rest penetrates into the soil as a form of seismic bulk wave. The wave propagates through the soil and insonifies the buried mine causing a tiny but detectable vibration at the ground surface (typically less than 1 μm). Sound produced in the air efficiently couples into the first 0.5 m of the soil because of the porous nature of weathered ground resulting in acoustic vibrations that are sensitive to the presence of buried mines [28]. Remote sensors (vibrometers) are the typical choice to detect the induced vibrations at the ground surface with Laser Doppler Vibrometers (LDV) being the typical choice.

Literature reports on at least two research efforts to develop detectors capable of detecting mines using acoustic\seismic techniques; the Multi-Beam Laser Dopler Vibrometer and the Scanning Laser Doppler Vibrometer. Once again, these detectors only performed field trials with no reported field devices used by humanitarian or military demining.

2.9.1 Multi-Beam Laser Dopler Vibrometer (MB-LDV)

Figure 2-30: The LDV based mine detection system during a field measurement. The LDV unit was mounted onto a vehicle-based platform. The laser beam of the LDV sensed the ground surface in a remote, raster-scanned manner [51].

The MB-LDV is an applied research project conducted by the University of Mississippi to utilise acoustic-to-seismic coupling in landmine detection. The principle of the system relies on the contrast of acoustic compliance as mentioned previously; greater compliance of mines in comparison to soil results in better detection signals. The system excites ground vibrations and measures the surface vibration using a Laser Doppler Vibrometer (LDV). The LDV exploits the Doppler frequency shift as a result of surface vibrations by emitting a laser beam onto the vibrating surface and measuring the reflected laser light. The system takes spot measurements of surface velocity scanning in search of a mine

The group identified that pseudo random noise in the range between 100 Hz and 680 Hz is optimal for AP mine detection and 100 Hz to 250 Hz is optimal for AT mines buried no deeper than 20 cm [51, 52]. The instantaneous seismic velocity of the ground surface was sampled at grid point, Fourier transformed and averaged over several periods in the complex frequency domain, producing a velocity function at each grid point [52]. The velocity function was then integrated over the frequency band chosen to obtain the final results. Example results obtained by MB-LDV are presented in Figure 2-31. Figure 2-31 presents the output obtained when scanning a 30x30 cm region with a PMA-3 AP mine buried 2.5 cm deep [52].

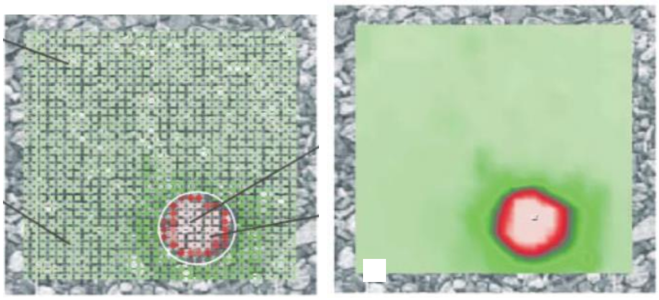

(a) (b)

Figure 2-31: (a) Spot measurements for the PMA3 AP mine buried at 2.5cm, producing a color map (b) clearly indicating a threat.

The reported results in [52] do not provide any measurements for objects buried more than 5cm deep nor does it highlight the system P_d. The report also fails to highlight the effect of vegetation or moisture on the system.

2.9.2 Scanning Laser Doppler Vibrometer (SLDV)

The second device reported in literature is the Scanning Laser Doppler Vibrometer. Like the MB-LDV, the SLDV combines acoustic and optical measurements to analyse the soil vibrations induced by its internal acoustic transmitter [50]. The sensor performs 2D surface imaging using its optical receiver and preforms detailed frequency analysis to identify buried mines [50]. The data is then processed to produce vibration images such as that displayed in Figure 2-32.

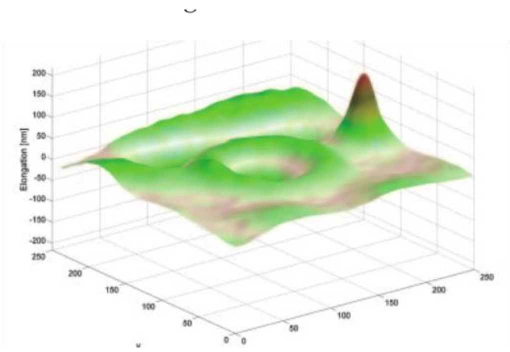

Figure 2-32: Amplitude of soil vibration caused by a mine and a clutter object nearby [50].

Results from field tests have not been readily available, however as part of a multi-sensor review, [53], a brief summary of the performance was provided. The report highlighted a few limitations of the SLDV, with no performance figures similar to those presented for GPR dual sensors [53]:

- Data quality depended on soil type where dry soils provide optimum results. However, extremely dry conditions and heavy vegetation resulted in clutter signals.
- Deep and narrow cracks in soil crust created parasitic resonance and soil partly covered by weeds created “false” signatures of potential mine locations.
- Thermal management is a critical design factor as it affected the performance of the instrument signal strength during the field trials.

2.9.3 Summary Evaluation

The main strength of acoustic/seismic sensing is the mechanical interrogation of the mine as opposed to sensing the electromagnetic properties as with MD, GPR and EMI [28]. Literature reports on low false alarms as spectral analysis assists in eliminating most of the clutter signals experienced [50, 51]. Another feature is that sensing could be performed outside the mined area [50]. Finally, acoustic/seismic sensing is unaffected by moisture and weather, unlike GPR, although frozen ground may limit the sensor’s ability [28].

Acoustic/seismic sensing struggles with deeply buried mines; struggles to detect mines deeper than one mine diameter as the resonance response attenuates rapidly with depth [28]. Moreover, the system tends to be slow due to grid sensing; however, introduction of array sensing could speed the process [28]. Moderate to heavy vegetation hinders the performance of the sensor, mainly due to the dependency on LDV to measure surface vibrations [28, 50]. Acoustic/seismic sensing tends to be more sensitive to non-metallic mines as it is more sensitive to dynamically compliant mines [50]. This could be argued to be a potential advantage, as low metal mines present a challenge to current EMI detectors.

Significant progress has been made towards the understanding and modelling of mine interaction with the soil allowing for enhanced data processing [28]. However, the technology is mainly limited by the existing sensing technology [50]. Development of a faster sensing element, that penetrates vegetation and copes well with the adverse conditions in minefields would allow this technology to progress further [28].

3 Magnetic Polarizability Tensor

This chapter provides an elucidation of what the magnetic polarizability dyadic tensor is, what this quantity represents and how it can be used as a classification attribute to identify threat objects and disregard innocuous ones. To do so, the chapter introduces a number of key physical principles utilised throughout the research. The Biot-Savart Law is introduced with some discussion about how it can be used to determine the magnetic field created by a coil configuration, an arrangement typically used in inductive metal detectors. This is followed by a description of Faraday's Law and the notion of the magnetic dipole moment. The chapter continues to introduce the tensor with a clarification of its composition, how it can be deduced from a measured response and what information about the object can be gathered. Finally, the chapter concludes with a literature review summarising efforts in research to use the property for UXO and mine classification and clearance. For the sake of brevity, the magnetic polarizability tensor will be referred to as simply the tensor.

3.1 Biot-Savart Law

The Biot-Savart Law is used to calculate the magnetic flux density ($\boldsymbol{B}$) or the magnetic field strength ($\boldsymbol{H}$) at any point in space as a result of a current flowing through a wire. The native form of the law, in differential form [54] , can be represented as

$$\boldsymbol{dH} = \frac{I\, \boldsymbol{dl} \times \hat{\mathbf{r}}}{4\pi r^2} \qquad (\mathrm{A} \cdot \mathrm{m}^{-1}) \tag{3-1}$$

where

I = filamentary current at passing through a wire segment at P_1 (A)

$\boldsymbol{dl}$ = segment of current carrying wire (m)

$\hat{\mathbf{r}}$ = unit vector from the wire to the point of observation P_2

r = the magnitude of the Euclidian distance from the wire segment (P_1) to the point of observation (P_2) (m)

$\boldsymbol{dH}$ = the differential magnetic field strength generated as a result of I flowing through $\boldsymbol{dl}$ $(\mathrm{A} \cdot \mathrm{m}^{-1})$

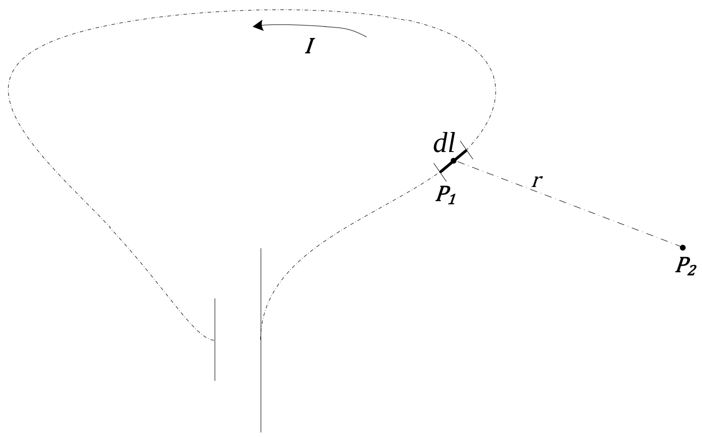

Figure 3-1: The differential magnetic field strength, $\boldsymbol{dH}$ generated at P_2 as a result of wire segment $\boldsymbol{dl}$ at P_1 with a current of I flowing through it.

The law makes a number of assumptions; the wire is filamentary, exists in vacuum and $\boldsymbol{dl}$ is negligibly small. The current form of the equation is an unrealisable case, as it is impossible to have an isolated segment with current flowing and the wire segment in reality is part of a closed current loop. The principle of superposition applies to magnetic fields [55] and thus the law can be re-written in its better known integral form that allows for experimental application [54]

$$\boldsymbol{H} = \frac{I}{4\pi r^2}\oint_c \boldsymbol{dl} \times \hat{\mathbf{r}} \qquad (\mathrm{A \cdot m^{-1}}) \tag{3-2}$$

Using the above equation the magnetic field generated by the presence of any arbitrary circuit/coil at any point in 3D space can be calculated. This can be used to determine the value of $\boldsymbol{H}$ generated by the coils in an inductive metal detector. The equation can be applied for numerous observation points to build an image of the magnetic field strength through a volume at discrete points. Biot-Savart Law can also be used to calculate the magnetic flux density, $\boldsymbol{B}$, through the multiplication with the magnetic permeability of free space as shown below

$$\boldsymbol{B} = \mu_0 \boldsymbol{H} \qquad (\mathrm{T}) \tag{3-3}$$

The Biot-Savart Law has derived forms for several standard shapes (e.g. circular loop, solenoids…etc.). One format of interest to this research is that of a finite length of straight wire. Equation (3-4) can be used to calculate the field strength at observation point P_2 due to a finite length of current carrying wire [56], Figure 3-2.

$$\boldsymbol{H} = \frac{I}{4\pi r}(\cos\theta_1 - \cos\theta_2)\widehat{\Phi} \qquad (\mathrm{A \cdot m^{-1}}) \tag{3-4}$$

where $\widehat{\Phi}$ is a unit vector aligned with the azimuth direction.

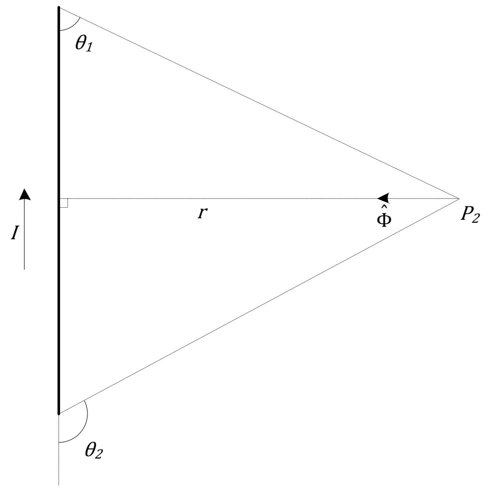

Figure 3-2: ***H*** for any extended line segment.

The sensor used within this research is composed of a number of square coils, discussed further in chapter 5. The square coils can be broken down into a number of straight wire segments and the total field generated can be summed to calculate the field experienced at the point of observation due to current flowing through the entire coil arrangement.

$$\boldsymbol{B}_z = \frac{\mu_0 I a^2}{2(a^2 + r^2)^{3/2}} \text{ (T)} \tag{3-5}$$

Another important derivation is the magnetic flux for a circular loop along the axis of the loop. While this is not necessarily used for the calculation of the field in this thesis, it highlights an important characteristic of the magnetic field strength for a current loop. Equation (3-5) displays the derived form and highlights the fact that $\boldsymbol{B}_z$ decays at a rate of $1/r^3$as you move away from the loop. This remains valid given the condition $r^2 \gg a^2$. Thus the field of view is limited as the magnetic field decays rapidly with depth. The full derivation exists in [55].

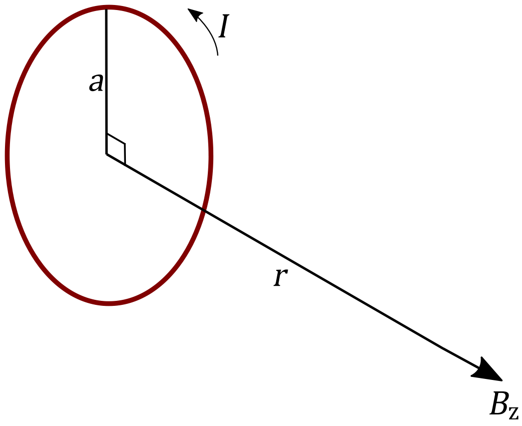

Figure 3-3: Decaying $\boldsymbol{B_z}$ as point of observation moves away from current carrying loop $\boldsymbol{I}$

3.2 Faraday's Law

Faraday's Law states that in the presence of a varying magnetic flux density $\boldsymbol{B}$ through a closed loop, a voltage, V, will be induced across the terminals as in Figure 3-4.

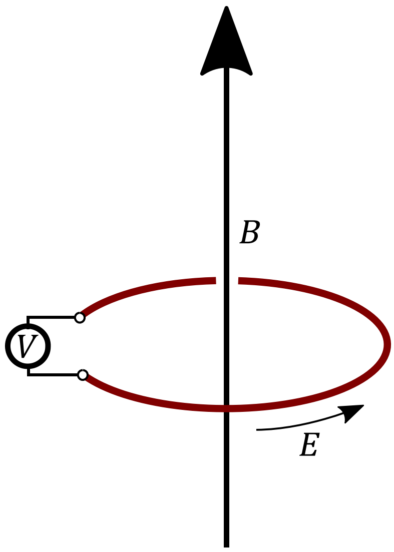

Figure 3-4: Voltage induced ($\boldsymbol{V}$) across the terminals of a loop due the varying magnetic flux density ($\boldsymbol{B}$) generating a changing electric field ($\boldsymbol{E}$)

This relationship is identified by Faraday's Law as [57]

$$V_{ind} = \oint_c \boldsymbol{E} \cdot \boldsymbol{dl} = -\iint \frac{\partial \boldsymbol{B}}{\partial t} \cdot \boldsymbol{ds} \ \text{(V)} \qquad (3\text{-}6)$$

where

V_{ind} = induced emf in the loop/circuit (V)

$\oint_c \boldsymbol{E} \cdot \boldsymbol{dl}$	=	line integral around the loop/circuit c (V)
$\iint \frac{\partial \boldsymbol{B}}{\partial t} \cdot ds$	=	surface integral of $\frac{\partial \boldsymbol{B}}{\partial t}$ over loop area (V)
$\boldsymbol{E}$	=	Electric field around the loop ($V \cdot m^{-1}$)
$\boldsymbol{B}$	=	magnetic flux density (T)
ds	=	surface element (m^2)
t	=	time (s)

Thus if a coil pair is present and a varying current is flowing through one coil, a varying induced voltage will be induced in the second. This form of the law is sometimes known as the transformer induction equation and presents the induced emf due to a varying $\boldsymbol{B}$ at a specific time rate for a circuit or loop that is fixed with respect to the observer [57].

A number of points need to be addressed before moving on to the magnetic dipole moment. Firstly, the presence of a negative sign in equation (3-6). This is to highlight the fact that the voltage is induced such that it opposes the changing field in accordance with Lenz's Law [58]. Secondly, the chapter will continue to reference a transmit and receive coil; this refers to the coil pair of an inductive metal detector. Due to the principle of mutual inductance the transmit and receive coils are interchangeable, meaning that a varying current could be flowing through either coil and the same voltage would be induced in the other [57]. This form of the law applies to the case when the closed loop is stationary, which is true for this research. Even though the coil is scanned over a target, the induced emf measured is a momentary value representing the stationary interaction between the transmit coil, receive coil and detected object.

3.3 Magnetic Dipole Moment

The final principle required to arrive at the tensor is that of a magnetic dipole moment. A magnetic dipole moment can be described as a plane current-loop. The dipole moment is used to symbolise an object's response, hence this section will identify how a magnetic dipole moment would result in an induced voltage. For an arbitrary plane loop carrying a current I, the magnetic dipole moment can be described as [55]

$$\boldsymbol{m} = SI \quad (\mathrm{A} \cdot \mathrm{m}^2) \tag{3-7}$$

where S is the area of the current loop.

Equation (3-7) is only for a planar representation and the equation can be extended to represent volumes through a generalised form of an arbitrary current distribution occupying a volume [55]

$$\boldsymbol{m} = \frac{1}{2}\int_{v} \mathbf{r} \times \boldsymbol{J}\, dv \; (\mathrm{A \cdot m^2}) \tag{3-8}$$

where

$\mathbf{r}$	=	position vector (m)
$\boldsymbol{J}$	=	current density $(\mathrm{A \cdot m^{-2}})$
dv	=	volume element $(\mathrm{m^3})$

The presence of a magnetic dipole results in a vector potential in the surrounding vicinity. This vector potential, $\boldsymbol{A}$**,** can be approximated to be [55]

$$\boldsymbol{A} \approx \frac{\mu_0}{4\pi}\frac{\boldsymbol{m} \times \hat{\boldsymbol{r}}}{r^2} \ \ (\mathrm{V \cdot s \cdot m^{-1}}) \tag{3-9}$$

Faraday's Law states that in order for an emf to be induced on a sensing loop, the magnetic flux density needs to be time varying in nature. Since the flux density $\boldsymbol{B}$ can be expressed in terms of $\boldsymbol{A}$, as shown in equation (3-10) [59], then the vector potential and consequently the dipole moment need to be varying in nature in order for a voltage to be induced as a result of the magnetic dipole moment.

$$\boldsymbol{B} = \nabla \times \mathbf{A} \ \ (\mathrm{T}) \tag{3-10}$$

By substituting for $\boldsymbol{B}$ in Faraday's Law, (3-6), we can describe the induced voltage in terms of $\boldsymbol{A}$ [59]

$$V_{ind} = \oint \boldsymbol{E} \cdot \boldsymbol{dl} = -\oint_c \frac{\partial \boldsymbol{A}}{\partial t} \cdot \boldsymbol{dl} \ \ (\mathrm{V}) \tag{3-11}$$

Equation (3-11) demonstrates that the time derivative of $\boldsymbol{A}$ would result in an induced emf as it would be responsible for a time varying magnetic flux density. Now if we consider a time varying magnetic dipole moment at a sinusoidal rate resulting in a varying vector potential $\boldsymbol{A}$, the time derivative of the vector potential can be simplified to

$$V_{ind} = -\oint_c j\omega \boldsymbol{A} \cdot \boldsymbol{dl} \ \ (\mathrm{V}) \tag{3-12}$$

By substituting equation (3-9) for $\boldsymbol{A}$

$$V_{ind} = -j\omega \oint_c \frac{\mu_0}{4\pi}\frac{\boldsymbol{m} \times \hat{\boldsymbol{r}}}{r^2} \cdot \boldsymbol{dl} \ \ (\mathrm{V}) \tag{3-13}$$

Finally, substituting for $\boldsymbol{H}$ using Biot-Savart Law, (3-2),

$$V_{ind} = -j\omega \frac{\mu_0}{I_R} \boldsymbol{m} \cdot \boldsymbol{H}_R \ (\mathrm{V}) \tag{3-14}$$

The terms $\boldsymbol{H}_R$ and I_R here refer to that of the loop on which the induced voltage is presented across its terminals, Figure 3-4. This is effectively the receive coil in the detector which is why subscripts of R are present. The expressions for the magnetic dipole moment are valid for $r^3 \gg a^3$ where a is the radius/longest dimension of the current loop [55].

This section identified the relationship between the magnetic dipole moment and an induced voltage on a receive coil. As mentioned at the start of the section, the magnetic dipole moment is used to represent the object's response in this research. Thus the final detail in order to describe the induced voltage in terms of the object (the tensor) is the representation of the tensor through the dipole moment model.

3.4 Magnetic Polarizability Tensor

The object's response to an incident magnetic field can be represented by that of an induced dipole moment, such that the object specific response is embedded within the moment, $\boldsymbol{m}$. The moment created then becomes a linear function of the tensor and the incident field as displayed below [60].

$$\boldsymbol{m} = \overleftrightarrow{\mathbf{M}} \cdot \boldsymbol{H}_T \ (\mathrm{A} \cdot \mathrm{m}^2) \tag{3-15}$$

where

$\overleftrightarrow{\mathbf{M}}$	=	magnetic polarizability tensor (m^3)
$\boldsymbol{H}_T$	=	incident field ($\mathrm{A} \cdot \mathrm{m}^{-1}$)

The incident field would be generated by a transmit coil and thus a subscript of T is present. By substituting for $\boldsymbol{m}$ in equation (3-15)

$$V_{ind} = -j\omega \frac{\mu_0}{I_R} \boldsymbol{H}_T \cdot \overleftrightarrow{\mathbf{M}} \cdot \boldsymbol{H}_R \ (\mathrm{V}) \tag{3-16}$$

Equation (3-16) describes the voltage induced on a receive coil due the response of an object to an incident field. By observing equation (3-16), it becomes apparent that $\overleftrightarrow{\mathbf{M}}$ is the only parameter which cannot be pre-determined for a detector with a known coil geometry and electrical characteristics and can be treated as the only variable that refers to the object. Therefore if we re-arrange (3-16) such that the relation is expressed in terms of $\overleftrightarrow{\mathbf{M}}$ we arrive at

$$\overleftrightarrow{\mathbf{M}} = \frac{I_R}{-j\omega\mu_0} V_{ind} (\boldsymbol{H}_T \cdot \boldsymbol{H}_R)^{-1} \ (\mathrm{m}^3) \tag{3-17}$$

Equation (3-16) and (3-17) form the key computation throughout this research, they are representative of the forward and inverse problems respectively in tomographical terms. Equation (3-16) can be used to describe the entirety of the system and detection process; an arbitrary current carrying coil generates a varying magnetic field known as the primary field, which in turn results in an induced field, secondary field, due to the object interaction which is measured by a receive coil where a voltage is induced. Equation (3-17) can be used to extract the object properties through the tensor to provide a classification parameter while equation (3-16) is used heavily to determine detectors with suitable sensitivity. This will be discussed further in chapter 4 and chapter 5 respectively.

A number of assumptions are made in order for the approximation of the object response to be represented by a dipole approximation. Firstly, the distance between the object and the coils, r, is assumed to be much larger than the longest dimension of the object, d, to abide by the statement made earlier $r^3 \gg d^3$. The field lines through the object are also assumed to be parallel, although this is simply a consequence of the previous statement. Secondly, the transmit and receive coils are assumed to be composed of filamentary wires so that the derived forms of Biot-Savart Law, equation (3-4) can be used to determine the field strength.

3.4.1 Tensor Composition

The tensor is composed of a 3x3 matrix displayed in equation (3-18) that is frequency dependent. It describes the object response to an incident primary field in all axial directions and cross-diagonals as displayed in Figure 3-5.

$$\overleftrightarrow{\mathbf{M}} = \begin{bmatrix} M'_{xx} + jM''_{xx} & M'_{xy} + jM''_{xy} & M'_{xz} + jM''_{xz} \\ M'_{yx} + jM''_{yx} & M'_{yy} + jM''_{yy} & M'_{yz} + jM''_{yz} \\ M'_{zx} + jM''_{zx} & M'_{zy} + jM''_{zy} & M'_{zz} + jM''_{zz} \end{bmatrix} (\mathrm{m}^3) \qquad (3\text{-}18)$$

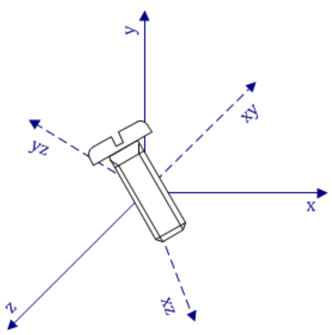

Figure 3-5: Graphical representation of individual tensor components of a screw.

The interchangeable nature of the transmit and receive coil pair due to electromagnetic reciprocity gives rise to symmetry within the tensor $\overleftrightarrow{\mathbf{M}}$; $M_{xy} = M_{yx}$. It also means that the order of the multiplication in equation (3-16) is irrelevant and will yield the same result. Consequently $\overleftrightarrow{\mathbf{M}}$ has only 6 complex unique values. The frequency dependency is implicitly represented through the complex nature of the tensor and reflects the phase shift between the primary field (transmit field) and the induced or secondary field [60]. Finally, the doubled arrow accent represents the dyadic nature rather than a matrix or vector quantity [61].

3.4.2 Object Properties and the Tensor

A number of object properties can be inferred by reviewing the spectroscopic tensor. Figure 3-5 represents the individual tensor components represented in equation (3-18) for a metal object, shown here as a bolt, in an arbitrary position. The individual tensor component values vary depending on the object response in each direction.

On examining Figure 3-5, it is clear that a change in orientation of the screw would result in different tensor values making the tensor orientation dependent. This may seem as a favourable property, however in order to perform classification of objects, orientation independence is required to ensure that the same tensor would be obtained for an object regardless of its angle of presentation. Therefore, the eigenvalue matrix of the tensor, $\mathbf{\Lambda}$, is used instead for classification. The eigenvalues are the responses induced when the primary field is aligned with each principle axis of the object in turn [62]. The principal axes for an object are orthonormal to one another and an external magnetic field pointing along one of the axis would induce a steady-state dipole moment parallel to it [63]. However, the orientation information can be retained through the rotational matrix R as displayed in equation (3-19)

$$\overleftrightarrow{\boldsymbol{M}} = R \cdot \mathbf{\Lambda} \cdot R_T \;\; (\mathrm{m}^3) \qquad (3\text{-}19)$$

where $\mathbf{\Lambda}$ is a diagonal matrix:

$$\mathbf{\Lambda}(f) = \begin{bmatrix} \mathbf{\Lambda}'_{xx} + j\mathbf{\Lambda}''_{xx} & 0 & 0 \\ 0 & \mathbf{\Lambda}'_{yy} + j\mathbf{\Lambda}''_{yy} & 0 \\ 0 & 0 & \mathbf{\Lambda}'_{zz} + j\mathbf{\Lambda}''_{zz} \end{bmatrix} (\mathrm{m}^3) \qquad (3\text{-}20)$$

Figure 3-5 also reveals that the shape of the object would result in stronger responses in some directions which would result in larger tensor components in relation to others depending on the shape of the object. This shape dependent variance is further clarified through Figure 3-6, where the eigenvalue tensor is represented for different object shapes.

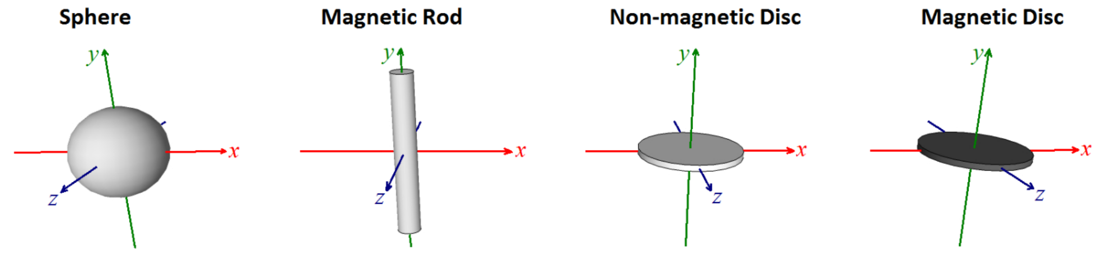

$$\overleftrightarrow{\mathbf{M}} = \begin{bmatrix} k_1 & 0 & 0 \\ 0 & k_1 & 0 \\ 0 & 0 & k_1 \end{bmatrix} \quad \overleftrightarrow{\mathbf{M}} = \begin{bmatrix} 0 & 0 & 0 \\ 0 & k_2 & 0 \\ 0 & 0 & 0 \end{bmatrix} \quad \overleftrightarrow{\mathbf{M}} = \begin{bmatrix} 0 & 0 & 0 \\ 0 & k_3 & 0 \\ 0 & 0 & 0 \end{bmatrix} \quad \overleftrightarrow{\mathbf{M}} = \begin{bmatrix} k_4 & 0 & 0 \\ 0 & 0 & 0 \\ 0 & 0 & k_4 \end{bmatrix}$$

Figure 3-6: Variance of tensor depending on object shape and material where *k* is a complex scalar [61]

A uniform object such as a sphere would respond equally in the x, y and z-direction and hence the tensor component is equal in all three directions. It also means that the response is invariant to rotation of the object. A non-uniform directional object, such as a magnetic rod would concentrate the field in one direction and have little effect in the other two directions. In the above example the tensor assumes the rod is negligibly small in the x and z-directions. In the case of the thin magnetic disc, the field would be concentrated in the x and z-direction and not in the y (assuming the object's y-dimension is negligible). Finally, the conducting disc would result in eddy currents induced in the object, which would circulate in the dominant xz-plane which in turn would result in a secondary field in the y-direction, hence producing the tensor shown. This secondary field generated results in a phase shift in the response and contributes to a complex imaginary value of the tensor component *k*.

The shape analysis presented so far only considers the tensor at a single frequency. The spectroscopic tensor can reveal significantly more information about the object's material and size. The complex nature of the tensor describes implicitly the phase shift experienced between the primary (transmit) field and the induced dipole or secondary field. This phase shift is a consequence of the object's electromagnetic properties [62] as the real and imaginary tensor components represent the reactive and resistive response of the object. Figure 3-7 represents a typical spectroscopic eigenvalue tensor and the effects of varying the object properties.

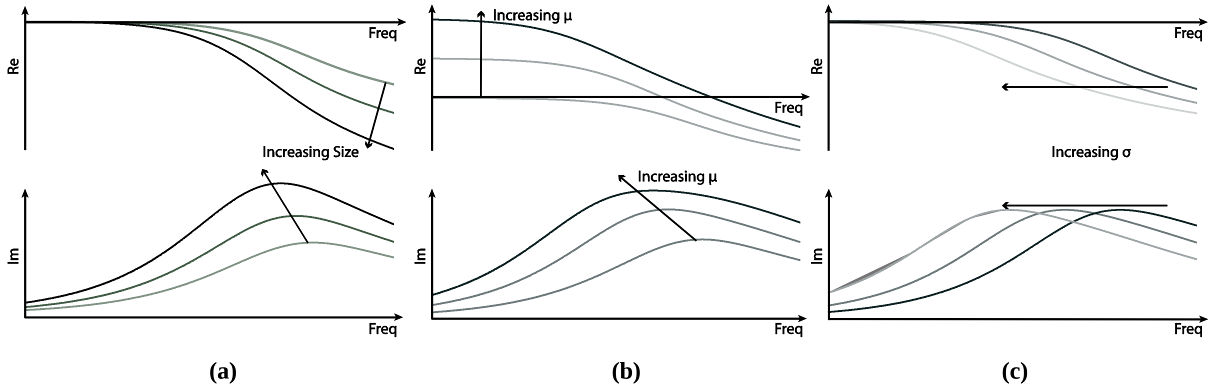

Figure 3-7: The variance in the spectroscopic complex tensor with a change in object properties; increasing size (a), increasing permeability (b) and increasing conductivity (c).

There are two distinct features that identify the tensor shapes and reveal object information. Namely, the peak frequency displayed by the imaginary tensor and the asymptotic levelling of the real tensor at low and high frequencies. The peak imaginary frequency can be explained by reviewing the eddy currents induced in a non-magnetic conducting sphere as the primary field frequency increases. Figure 3-8, displays the eddy currents circulating through a sphere as the frequency of the primary field increases from 100 Hz to 100 kHz.

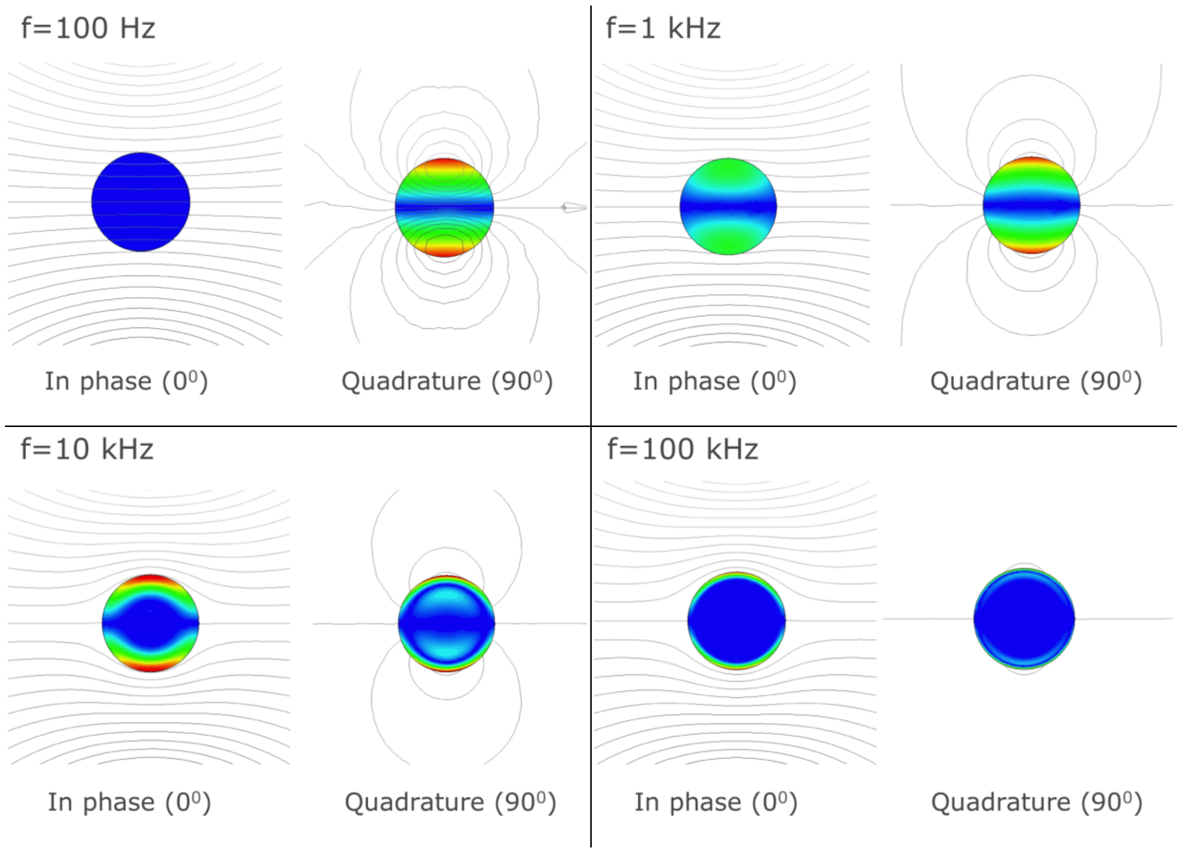

Figure 3-8: The effect of increasing the primary field frequency on the Eddy currents induced inside a non-magnetic conducting sphere [64].

At low frequencies, eddy currents circulate through the majority of the sphere creating a weak secondary field. The field lines flow through the object unhindered and hence the real component is around zero for low frequencies. As the frequency increases, the eddy currents start to get pushed to the edges, circulating at a higher current to oppose the increasing rate of change of the primary field. This results in a greater secondary field which is in turn results in an increase in the imaginary component as the frequency increases. The eddy current circulating through sphere make the sphere less permeable and consequently, the field lines start to diverge round the object. This is the cause for the negative gradient represented in the real component of the tensor in Figure 3-7. As the frequency increases further the eddy currents are pushed to the extremity of the object and the generated secondary field is weakened due to the reduced effect of the sphere and the eventual reduction of the imaginary tensor component is observed. Finally, the boundaries of the object determine the path of the eddy currents and subsequently the deviation of the field lines round the object at high frequencies.

This variance of the eddy current distribution is commonly known as the skin or diffusion effect. The skin depth, δ, is a characteristic of the medium and determines how deep an electromagnetic wave can penetrate into the conducting medium. It is a function of frequency, permeability and conductivity and can be defined as [56]

$$\delta = \frac{1}{\sqrt{\pi f \mu \sigma}} \quad (\mathrm{m}) \tag{3-21}$$

where

f	=	frequency of electromagnetic wave (Hz)
μ	=	permeability of the medium ($\mathrm{H\ m-1}$)
σ	=	conductivity of the medium ($\mathrm{S\ m-1}$)

Equation (3-21) highlights how the object's material has a strong influence on the response as it commands the depth at which eddy currents circulate. A more conductive sphere would result in a lower skin depth and as a result would result in a shift of the spectroscopic tensor to lower frequencies.

Both the real and imaginary components of the response in Figure 3-7 vary with the object's size; permeability and conductivity. As the object size increases, both tensor components increase. This is accompanied by a shift of the imaginary peak frequency to lower frequencies. The real tensor component also experiences an increase in gradient. An increase in size would result in an increased magnitude of tensor components as the increased size would interact with more primary field lines. However, this would also mean greater deviation of the lines as effects of the eddy currents are witnessed, resulting in a lower frequency at which the imaginary components experiences a reduction. An increase in material magnetic permeability results in the field lines concentrating through the object as represented in Figure 3-9. This shifts the real response up, resulting in a positive real tensor at lower frequencies and crossing over to negative values at higher frequencies, reaching an asymptote that is dependent on the outer shape of the object. For ferrous objects this asymptote occurs at very high frequencies, well above MHz, which are generally beyond the range of practical measurement. The imaginary tensor exhibits an increase in magnitude as well as a slight shift in the peak frequency to lower frequencies due to the increased field interaction with the object material. The increased field strength through the object results in stronger eddy currents at lower frequencies. An increased permeability would result in a shift to lower frequencies due to the reduced skin effects, equation (3-21). However, it would also concentrate the magnetic field lines through the sphere; strengthening the primary field and the secondary field in turn.

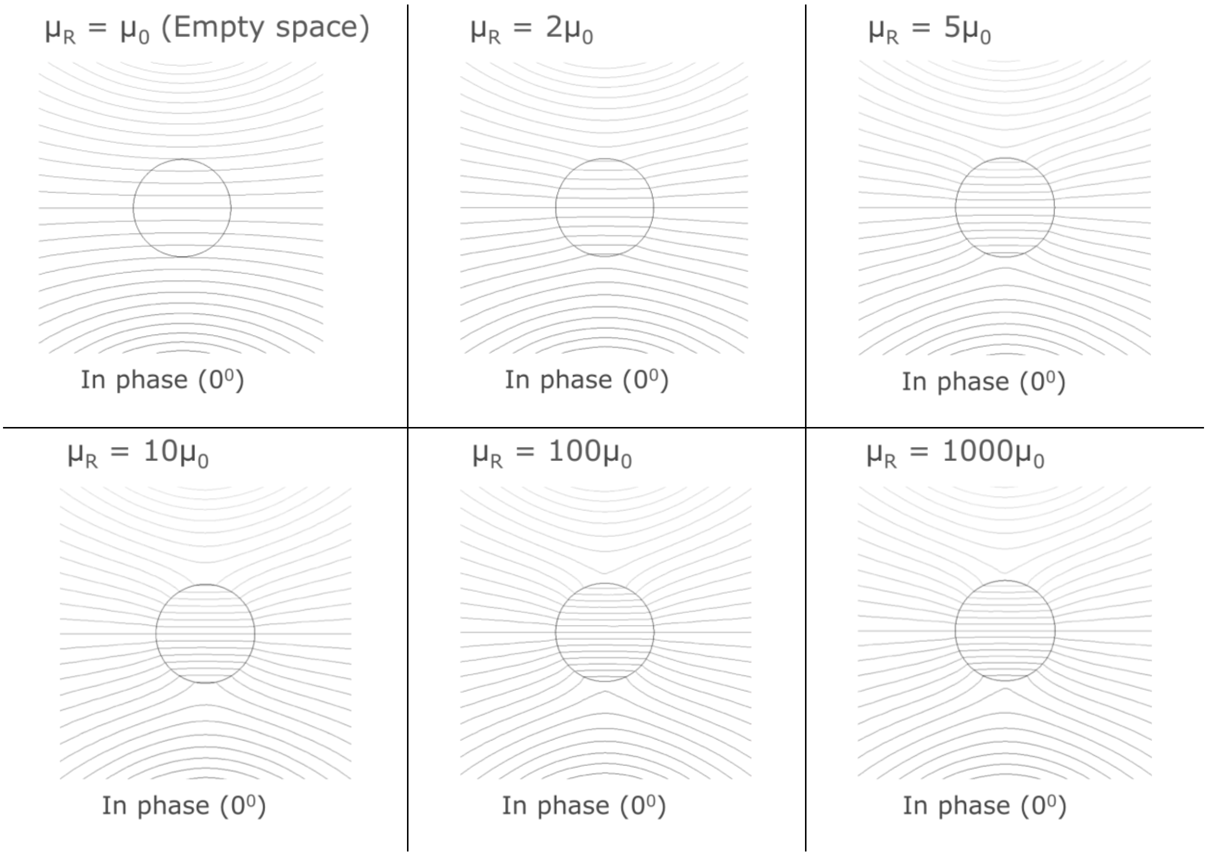

Figure 3-9: The effect of increasing permeability on field lines [64].

Finally, an increase in object conductivity results in the shift of the imaginary tensor to a lower frequency. The shift to lower frequency is also displayed by the real tensor. These linked variations of the tensor to the object properties, make the tensor a capable property for characterisation and discrimination. To conclude, there are four key features within the spectroscopic tensor; the peak imaginary component, the sign of the real component at low frequencies, the magnitude of the tensor and the asymptote frequency of the real component.

Through the discussion within this section it becomes clear how the tensor can become an object signature and a means of characterising the detected object; inferring information about its material, shape and orientation. The measured induced voltage can be used as inputs to the inverse problem to obtain the spectroscopic graphing of the detected object. This can be used along with knowledge libraries to identify the object detected. To conclude this chapter, a literature review is presented on work that has been done in this area of research to classify detected objects in UXO detection and other.

3.5 Tensor Literature Review

As previously discussed, there is little literature regarding commercial metal detectors with the exception of the European study presented in section 2.5. On the contrary, there have been a number of papers that discuss the use of tensors or object responses to classify buried targets.

Das *et al* [65] introduced the utilisation of the magnetic dipole moment to represent the object response. The paper introduces the calculation of the measured response of a sphere and a prolate spheroid on a square receive coil due to an induced dipole moment generated by a transmit coil interacting with the article. The calculated responses are compared only qualitatively to that measured by the experiment. The paper reports on the variations in the response due to the object's orientation, material, shape and depth. The paper is effectively investigating the tensor property, however in a different mathematical representation. The paper concludes with the summary that with prior object knowledge, the location of buried objects can be determined as the response can be compared to calculations.

Bell *et al* [60, 62] build upon the magnetic dipole moment approximation to represent the response of generic subsurface objects by introducing the notion of the magnetic polarizability tensor. A complex, 3x3 symmetrical matrix that is object specific and is used in conjunction with the transmit and receive coil fields to determine the induced voltage on the receive coil in time and frequency domain systems. The tensors for a number of objects are measured and then used to predict the induced voltage as the coils are swept over the object. The paper tests the legitimacy of using the dipole approximation by deducing the tensor at different depths and comparing the results. The dipole model assumes distance to object much larger than object dimensions and Bell reports that the dipole approximation does break down when the object is placed close to the coil; however, this is only seen for relatively large objects in respect to the coil dimensions. The approximation remained valid for an antipersonnel mine (TS-50) placed as close as 0.5 cm. The rationale given behind these results is that the TS-50 metallic parts are fairly small and hence the dipole approximation is still capable of representing the object. This is of particular importance to the research presented here as the detector is looking to only detect anti-personnel mines, where the metallic content is typically minimal. The work also investigates the difference between the tensors of clutter objects and potential threat objects such as mortars and other unexploded ordnances, highlighting the potential discriminatory aspect of the tensor. It does not however provide the tensors for low metal mines, or provide unscaled tensor values. All tensor comparisons seem to be in relative values.

The most significant and extended effort for the use of the magnetic polarizability tensor to classify sub-surface detections comes from research supported by the U.S. Army Corps of Engineering. Fernández, Barrowes and Grzegorcyzky *et al* experiment with several detectors to identify the tensors and locations of buried UXOs. In [66], Fernández *et al* introduce the Man-Portable Vector Sensor (MPV), a detector used to infer the tensor from time-domain measurements. The complete system and associated coil arrangement is shown in, Figure 3-10.

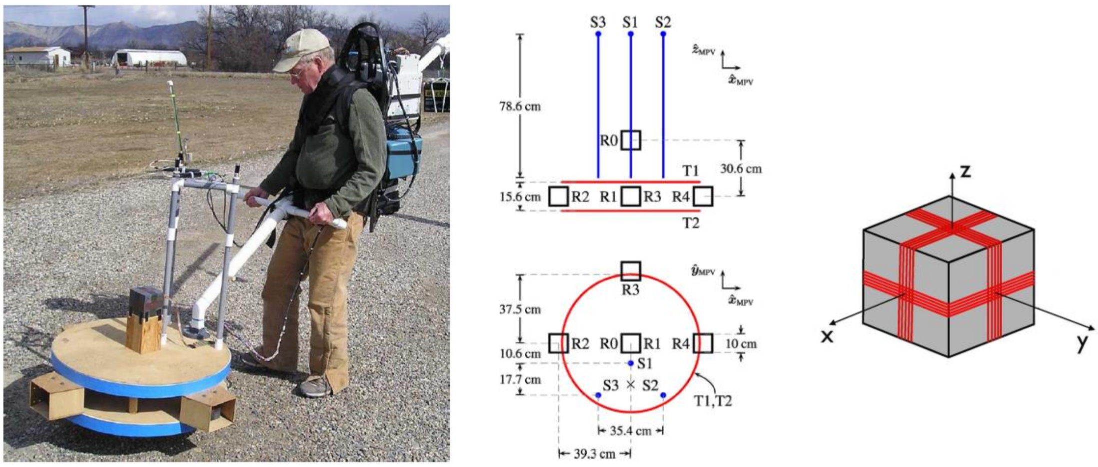

Figure 3-10: The MPV sensor (left), the coil arrangement (middle) and the receive sensor design (right) [66].

The sensor is composed of two circular transmit coils (37.5 cm radius) and five receive coils. The receive coils are slightly unusual in that they are constructed of a cube (10cm) with the coil wound in the x, y and z-direction. This provides the receive coils with good measurement capability of the secondary field in all field directions. The tensors of several projectiles and mortars are presented in the paper. The tensors offered are in the time-domain as opposed to the frequency domain presented within this thesis. Static measurements are performed along a set of locations and compiled to perform the inversion and deduce the tensor and object location. The paper discussed the possibility of performing dynamic measurement/inversion; however, it does not provide any of the results. The paper also displays successful multi-target inversion for a projectile and a box of nails significantly separated laterally. The paper concludes by identifying a number of limitations of the MPV and introduces a second generation of the detector, MPV-II [63], which is significantly lighter and provides better location measurements as well as better invertible data, Figure 3-11.

Figure 3-11: The MPVII

A second paper [67], presented by Grzegorcyzky *et al* introduces the use of Kalman Filters to perform real-time inversion of the data as measurements are being performed. The paper uses the measurements obtained using the MPV-II and Metal Mapper (a vehicle mounted device) and updates inversion results as more measurements are performed. An immediate limitation conceded by the method is that the real-time results would only be capable of identifying the location of the detected target and would fail to provide full tensor information. This is due to the reduced measurement time, claiming that only a volumetric characterisation might be possible. Despite the MPV-II capable of performing dynamic measurements, the majority of the results reported for the MPV-II are that of truncated static measurements as the data quality (SNR) was deemed favourable. The article presents a number of tensors from dynamic measurements but highlights the lack of full tensor representation due to the short measurement window of dynamic measurement.

A third paper by Grzegorcyzky *et al*, [68], reports on the capability of simultaneous multiple tensor inversions using MPV and TEMTADS (another vehicle-mounted time-domain sensor). They experiment with two and three simultaneous inversions at several relative locations. Again, the focus of this paper is mainly the location of detected objects as a measure of the quality of results with little quantitative analysis of tensor degradation. It identifies two scenarios where the inversion struggles to provide satisfactory locations; when targets are directly above one another and when targets are far apart that one object is on the boundaries of detection. The second scenario is not so much a problem for the case of anti-personnel mine clearance. As highlighted earlier in section 2.4.2, once a detector has picked up a target, localised scans are performed and hence eliminating the scenario. Therefore, the first scenario is one that this research is likely to be faced with. The paper also reports on encouraging signs of detectors being capable of determining several target locations without prior knowledge of the number of targets being measured.

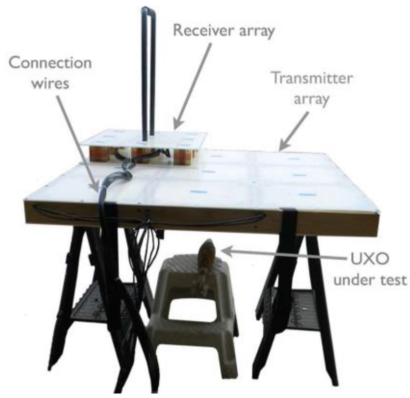

Figure 3-12: The Pedemis sensor in a laboratory setting [69].

Finally, Grzegorcyzky *et al* [69] introduce a new detector, the Portable Decoupled Electromagnetic Induction Sensor or Pedemis. The Pedemis features decoupled transmit and receive coils which is different from all the other detectors presented so far. This allows the receive coils to be moved around with respect to the transmit and thus providing more fields of view of the object by altering the relation between the transmit and receive fields. The paper reports on the test performed at Aberdeen Proving Ground (APG), highlighting the enhanced quality of tensor inversion from the new detector and the enhanced multi-target detection capability (up to five simultaneous objects). However, this improvement seems to be as a result of an effective increase in transmit-receive coil combinations. The Pedemis system has nine transmit coils which are excited sequentially and nine receive coils (same shape as the MPV), which are moved between five locations. Thus the improvement is not so much as a result of the decoupling but more the increase of the effective transmit-receive channels. Every time the receive array is moved with respect to the transmit array an equivalent nine more receive coils are introduced to the system. It is likely this approach was chosen since creating 35 fixed receive coils would introduce a significant weight addition as well as strain on real-time computation.

A final detector reported in literature that performs characterisation of subsurface metallic targets is presented by Huang and Won in [70]. GEM-3 performs inversion of the electromagnetic spectral measurements to provide sphere equivalent parameters such as equivalent sphere radius, depth, conductivity and permeability. Huang and Won argue that this information can be used to characterise and distinguish between detected objects. The paper displays results of several test spheres buried in dense red clay of 90 Ω.m resistivity. The work uses the GEM-3 detector to determine the resistivity and conductivity of different targets prior to burial (in air). Targets are then buried and the obtained values are compared to those previously measured. This poses a question as to whether this provides an independent means of determining percentage errors of the electrical properties as both compared values are obtained using GEM-3 inversions. The paper reports a significant discrepancy between the in air and buried results, particularly struggling with small spheres and objects. The paper also presents the inverted results for buried pipes in the same soil. The equivalent sphere radius and depth reported display a potential for discrimination between targets. However, due to the varied error percentages it is in the author’s view that it would be difficult to confidently dismiss clutter values obtained from such a system.

Figure 3-13: The mapping of the detected object on the passing individual using the walk-through metal detector developed at the University of Manchester [71].

Along with all the work carried out on UXOs, there has been extensive research work carried out within the group at the University of Manchester to use the tensor theory to classify metallic targets using a walk-through metal detector (WMTD). Work carried out by Marsh *et al* [71], display an airport style walk-through metal detector capable of presenting the relative tensor and location of the object detected (superimposed on individual's body as they walk-through the detector). The detector was also showcased to be able to provide information on multiple objects passing through the detector in [72]. It is capable of performing the inversion and identifying two objects, however struggles when it attempts to perform the inversion for three objects at similar heights. The paper does highlight that the system would flag a poor inversion result in the case of three targets, which would warrant a body search. Makkonen *et al*, builds on the tensor work performed by applying a K-Nearest Neighbour (KNN) classification to the tensors obtained by the detector in order to provide target classification [73]. The paper looks at a number of threat and innocuous targets and attempts to classify the objects by building a library of tensor values and using them to identify similar objects. The paper reports a success rate of over 95% in recognizing and identifying the target. The work performed on the walk-through metal detector only utilises single frequency analysis of the tensor, limiting the amount of information gathered about the object; mainly information about the shape and some aspects about the material. The landmine detection work presented in this thesis is an extension of the walk-through detector research. It aims to build on the research and perform spectroscopic inversion as opposed to delivering single frequency tensors, providing a significant increase in object specific data for characterization. This classification work performed by Makkonen *et al* gives confidence in the possibility of developing a detector capable of identifying threat objects and dismissing innocuous ones.

In line with the Statement of Originality, section 1.2, it is to the author's knowledge that no research presented the unscaled spectroscopic tensor values for small metallic objects and anti-personnel mines. Neither have there been any reports regarding a detector that is capable of providing these tensors for such small objects. The detector developed in this research is a frequency domain detector and the 3x3 tensor values reported are also functions of frequency. The latter is not so much a statement of originality but more fittingly a different approach to the time domain measurements and tensor reporting presented in literature.

4 Measuring Object Tensors

This chapter forms one of the fundamental original aspects presented within this thesis. The chapter describes a methodology by which the true tensor values of small metallic objects and low-metal anti-personnel mines can be obtained in SI units. The chapter begins by describing the apparatus used to perform the measurement and the experimental procedure followed to obtain the tensors. The experimental tensor was verified against simulation and analytical solutions to confirm that the obtained tensors are the true unscaled object tensors. The chapter then presents the tensors obtained for the full set of uncirculated US coinage and a number of typical clutter items, discussing the differences observed and interpreting the object properties embedded within the tensor. The chapter continues to present the tensors for low-metal antipersonnel mine surrogates, with a description of the differences observed. The chapter then concludes with a discussion on the feasible use of the tensor to discriminate between mines and clutter and its capability to provide information to reject innocuous objects and reduce FARs.

It is to the author’s knowledge that the tensors for low-metal anti-personnel mines have not been reported in any literature. As well as the novel measurements, the tensors are presented for the first time in SI units. Previous work has only presented measured tensors in relative terms. Finally, the verification process against simulation and analytical solution from first principles is an additional original aspect that has not been performed before.

4.1 Purpose of the Measurement

Tensor measurements provide a number of benefits to the project. Firstly, as mentioned earlier, it provides a library of spectral signatures to be later used by detectors to identify threat objects and discard innocuous ones. The following tensor measurements also provide an in depth understanding of the response of anti-personnel landmines. The response provides more knowledge about the metallic nature within the mine (magnetic/conductive content) and the way it responds. It also confirms the difference between mine tensors and clutter items as will be displayed shortly.

4.2 Measurement Apparatus and Methodology

The primary instrument used to perform the measurements was an impedance/gain phase analyser, SI 1260. The SI 1260 impedance analyser excited the measurement coil with discrete fixed frequencies, stepping through the desired range to provide the spectroscopic measurement.

The excitation signal was passed through front-end amplification to achieve a stronger drive current to the coil (≈1.2 A). The induced voltage across the receive coil was also passed through front-end amplification to increase the signal around 50-100 times depending on the size of the measured object. The current passing through the transmit coil was captured through the measurement of the voltage across a 1 Ω current sensing resistor in series. The impedance analyser post-processed the voltages across the current sensing resistor and the receive coil, presenting the phase and magnitude of the trans-impedance measured across the transmit / receive coil pair. A bespoke LabVIEW code controlled the measurement process; stepping through the desired frequencies, providing the required excitation values and storing the trans-impedance measured by the impedance analyser. This data was then further processed using a MATLAB programme to perform the calibration, inversion and tensor calculation described in equation (3-17). A system schematic is represented in Figure 4-1.

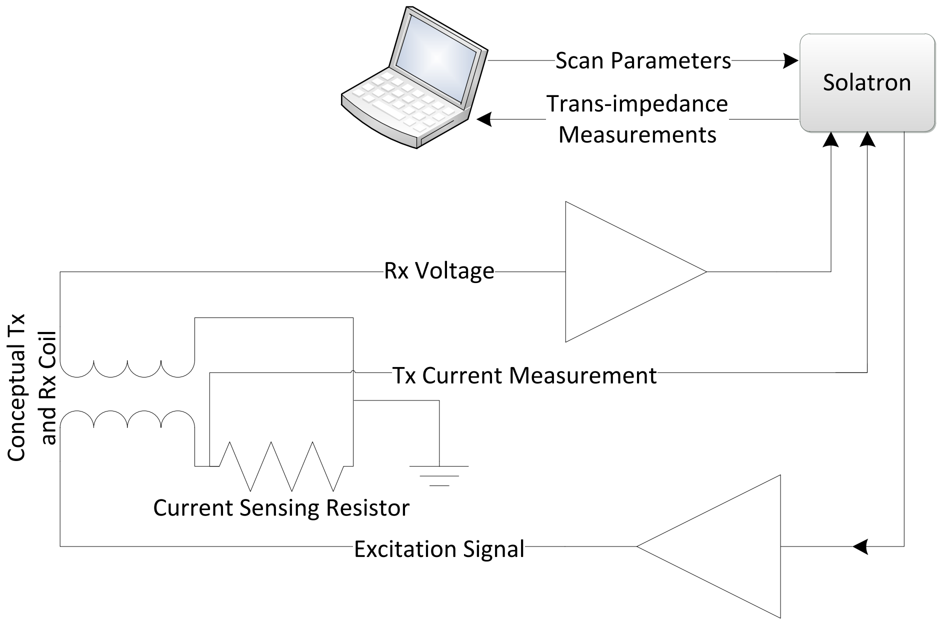

Figure 4-1: System schematic showing the flow of signals and measurements to and from the impedance analyser, front-end amplification and the sensing coil.

4.2.1 Measurement Coil

The measurement coil constructed to perform the tensor measurements was designed to provide a uniform parallel field required to permit the use of the magnetic dipole approximation for tensor calculation, section 3.4. The original coil design was developed by Dr. Bachir Dekdouk. Here, a solenoid coil was constructed to provide the parallel field and perform the measurements, pictured in Figure 4-1. The coil was composed of an inner 120 turn transmit coil, visualised in red in Figure 4-1 (a), and two outer 60 turn receive coils wound in a reverse opposition arrangement, displayed in green in Figure 4-1 (a) and red in Figure 4-1 (b). The coil dimensions were as follows; a=202 mm, b=105 mm, H=220 mm, d=107 mm and D=149 mm, with a wire wall thickness of 1.75 mm for the transmit coil and 1.66 mm for the receive coil. The z-axis is considered to be along the axis of the coil.

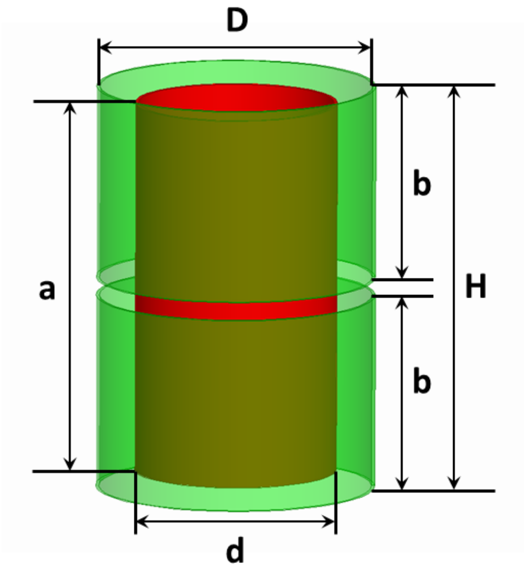

(a)

(b)

Figure 4-2: (a) Coil schematic, (b) constructed coil.

The coil was designed to provide maximum sensitivity through the maximum number of turns while ensuring the resonance of the coil was well above the region of interest. The frequency range investigated within this thesis is 1-100 kHz as this contains the majority of the useful information required for classification of low-metal mines. The frequency response of the transmit and receive coils are displayed below in Figure 4-3, where the resonance was measured to be around of 650 kHz and 950 kHz respectively.

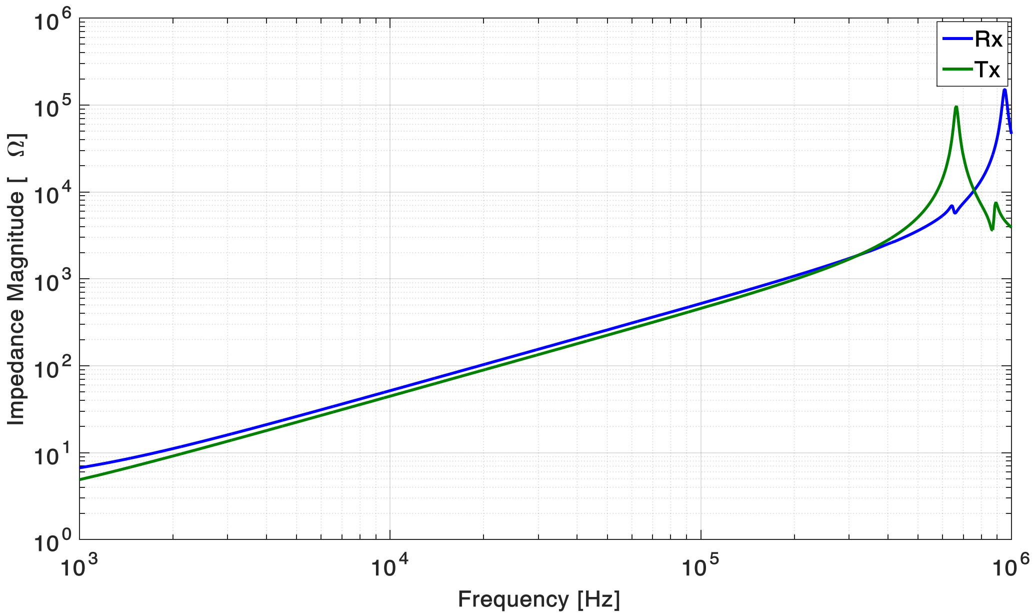

Figure 4-3: Frequency response of the transmit and receive coils in the test solenoid.

4.2.2 Experimental Procedure

A number of mechanical devices were used to position the small metallic objects and mines at the most sensitive part of the gradiometer along the z-axis. The arrangements enabled manual rotation for defined angular orientations. Rotations about the y-axis in 15° steps were performed to obtain the necessary data for the subsequent calculations to arrive at an accurate tensor. At each angular orientation a full frequency sweep was performed from 1-100 kHz.

4.2.3 Background Cancellation and Calibration

The raw trans-impedance measurements required some post-processing to remove the background signal and any distortion introduced by the amplifiers. The results displayed throughout this section are not the trans-impedance measurements but are the mutual inductance or, more strictly speaking, the change in mutual inductance measured. This is simply achieved by normalising the trans-impedance measured by ω. An initial scan captured the background mutual inductance signal in the absence of the measurement object. The values obtained were subtracted from those measured when the object is present to extract the change in mutual inductance due to the object alone. The use of front-end amplification introduced small errors to the spectroscopic measurement in the form of an uneven phase shift and uneven amplification across the frequency range. To remove these effects a 6x20 mm NiZn ferrite rod was used to calibrate the instrument, Figure 4-4. This ferrite results in an increased mutual inductance measured for the coil pair with no phase shift over the measured frequency range, i.e., the change in mutual inductance measured should be a flat real response with no imaginary content. However, this was not the response obtained due to the amplification imperfections as displayed in Figure 4-5.

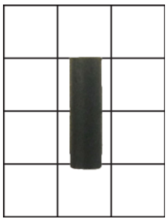

Figure 4-4: Ferrite calibration rod against a 1 cm grid.

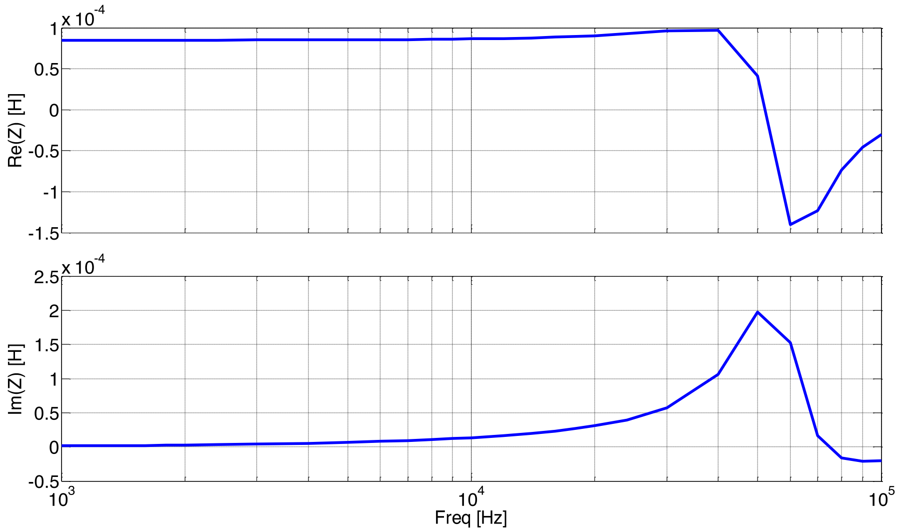

Figure 4-5: Un-calibrated mutual inductance measured for a 6x20 mm NiZn ferrite rod.

These measurements were used to cancel out the phase and magnitude errors introduced to produce the expected ferrite response. To do so the ferrite measurement at each frequency in Figure 4-5 was converted to its polar form. The magnitude and angle of the calibration readings were then subtracted from the following object measurements, to remove the imperfections. Finally, the measurements were returned to their Cartesian form. This operation is depicted in equation (4-1) and was capable of correctly removing the amplification imperfections as displayed in Figure 4-6.

$$M_c(r,\theta) = \left(M(r) - M_f(r), M(\theta) - M_f(\theta)\right) \quad (4\text{-}1)$$

where, M_c is the calibrated measurement, M_f is the ferrite measurement and M is the raw object measurement.

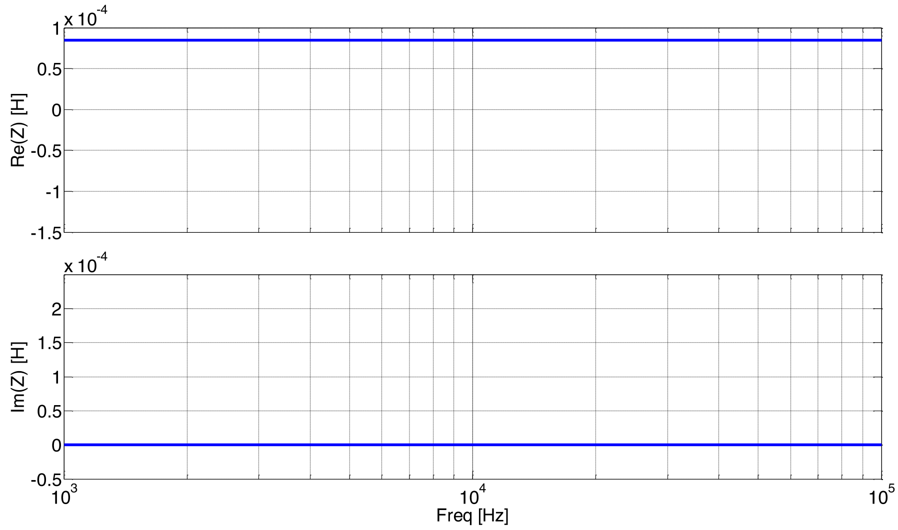

Figure 4-6: Mutual inductance of the 6x20 mm NiZn ferrite rod post-calibration. The measurement represents the expected response of a flat real component and the absence of imaginary response.

The background signal removal and ferrite calibration of measurements ensured that the values obtained are a direct result of the measured object only. Figure 4-7, represents an example change in mutual inductance measured when a unidirectional object was rotated by 360˚ within the coil.

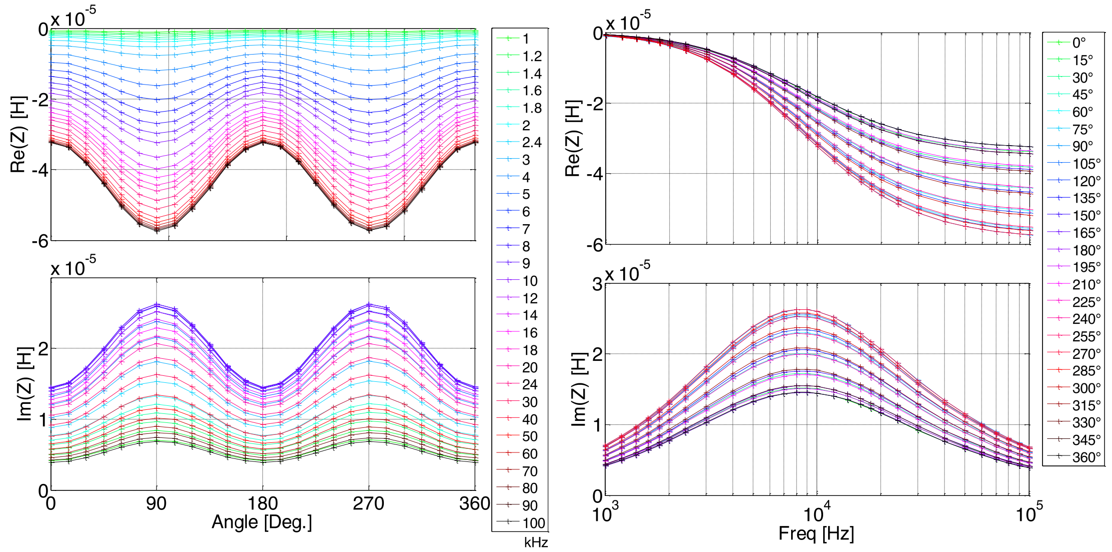

(a) (b)

Figure 4-7: Trans-impedance measurement divided by ω, displayed per frequency (a) and per angle of rotation (b)

The plots highlight expected results such as the sinusoidal shaped response in (a) which is a result of the geometrical unidirectional shape of the object. As the object is rotated through the parallel field it interacts more with the field as a larger part of the object is exposed until it reaches a horizontal position; 90 ˚. The signal then decreases again as the object is returned to a vertical position; 180 ˚. Despite the tensor not being deduced yet, the mutual inductance frequency response displayed in (b) already demonstrates characteristic features elucidating to the material and size of the object. The lack of a positive real response at low frequencies alludes to the lack of ferritic composition in the material and the location of the peak frequency of the imaginary response is a function of the object material and size as discussed in section 3.4.2. As will be revealed when comparing the eigenvalue tensors in section 4.5 these characteristics are maintained and the orientation variance displayed in Figure 4-7 (b) is removed to allow for further interpretation and characterisation. Finally, the smooth transition of measurement as the object is rotated can be viewed as a merit to the quality of measurements as they proved to be very reproducible, within 5%.

4.2.4 Post-Processing and Field Measurement

The experimental stored measurements were passed from LabVIEW to MATLAB to perform the post processing and calculate the eigenvalue tensor. Equation (3-17) was implemented to deduce the tensor values, and subsequently Λ through Equation (3-20). This operation required the field values for the transmit and receive coils, $\boldsymbol{H}_T$ and $\boldsymbol{H}_R$ respectively. These were derived from flux density measurements obtained using a Hall probe at the position of the measured object when a 1A current was passed through the transmit and receive coils in turn.

It is worth noting at this point the limitations of the measurement system presented here. The system and procedure only allow the correct tensor inversion for small symmetrical metallic objects. Asymmetrical objects would need to be rotated about two planes; (i) to establish a principle axis and (ii) to measure the tensor components perpendicular to this axis. Secondly, the system is only capable of measuring small metallic objects to uphold the uniform parallel field through the object.

4.3 Simulation

Simulations were performed using the commercial FEM (Finite Element Method) solver, Ansys Maxwell v16. The simulations were performed in partnership with a colleague, Dr John Davidson. The simulation geometry comprised of an outer free-space region, the coil arrangement as shown in Figure 4-2 (a) and the test object positioned nominally at the region of uniform sensitivity of the gradiometer. A series of simulations involved geometrical rotations of the test object about its centre in 15° increments from 0° to 345° over the frequency sweep range 1 kHz to 10 kHz in 1 kHz steps and thereafter in 5 kHz steps up to 100 kHz. In this case the test object was a .222 Remington cartridge case from a spent ammunition round. The geometry of the .222 Remington case was simplified by three stacked geometrical primitives; a long and thin tapered cone, a smaller fatter cone and a simple cylinder representing the outer main body, shoulder and neck respectively of the cartridge. Subtraction of smaller sized primitives enabled the creation of a simplified cartridge shell of 0.5 mm wall thickness. Typical total meshing levels was in the order of 700k tetrahedral elements and solution times for all frequencies and rotations was in the order of 72 hrs running on an Intel Xeon ES-2620 (2 GHz) and required approximately 40 GBytes of physical RAM. An example H-field plot of the cartridge shell in the coil arrangement for a simulation of 20 kHz excitation current and angular orientation of 0˚ to the z-axis is shown in Figure 4-8.

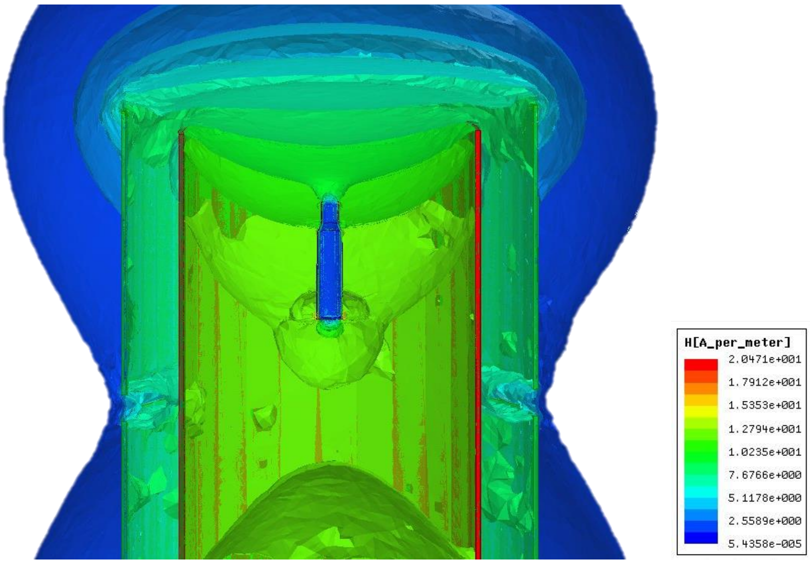

Figure 4-8: Cross-sectional upper half of gradiometer showing an example H field perturbation due to the modelled .222 Remington rifle cartridge. Midpoint of the cartridge is at the simulated rotational centre and the most sensitive part of the gradiometer.

4.4 Experimental Validation

Validation of the experimental procedure and tensor calculation methodology was initially achieved using the objects shown in Figure 4-9. The validation involved comparison of experimentally derived eigenvalue tensors with simulation and analytical solutions where possible.

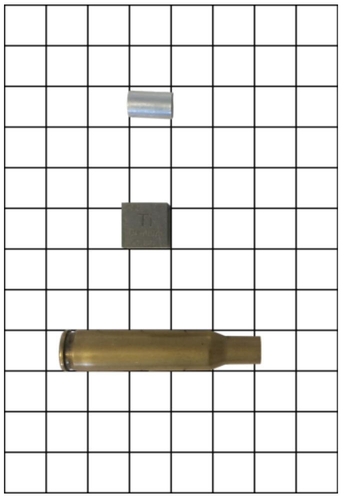

Figure 4-9: Validation objects used on a 1cm grid. The objects pictured from top to bottom are a Type-72A Chinese mine phantom for the detonator components, Titanium cube and .222 Remington shell

A 1 cm titanium cube was the first validation piece used as it is a well-defined object that can be accurately simulated. An analytical solution for the tensor can be calculated for the cube as it was deemed to have the same tensor structure of a sphere, Figure 3-6; composed of equal diagonal tensor components. This is a result of the symmetrical shape of the cube along all three axes. This was confirmed by rotating the cube through the coil and the response measured was found to be equal for all orientations. Consequently, a volume equivalent sphere was used to calculate the analytical solution for the tensor of the cube. There is an abundance in literature reporting the tensor for a sphere as in [65], [74] which can be calculated using equation (4-2) and (4-3)

$$\overleftrightarrow{\mathbf{M}} = -2\pi a^3(k' + jk'')\begin{pmatrix} 1 & 0 & 0 \\ 0 & 1 & 0 \\ 0 & 0 & 1 \end{pmatrix} \ (\mathrm{m}^3) \tag{4-2}$$

$$(k + jk'') = \frac{[\mu_0(1 + k^2a^2) + 2\mu]\, sinh(ka) - (2\mu + \mu_0)ka \cdot cosh(ka)}{[\mu_0(1 + k^2a^2) - \mu]\, sinh(ka) + (\mu - \mu_0)ka \cdot cosh(ka)} \ (\mathrm{m}^3) \tag{4-3}$$

Here, $\mu = \mu_0\mu_r$ is the magnetic permeability of the sphere, σ is the conductivity, ω is the angular frequency of excitation and $k = \sqrt{i\sigma\mu\omega}$.

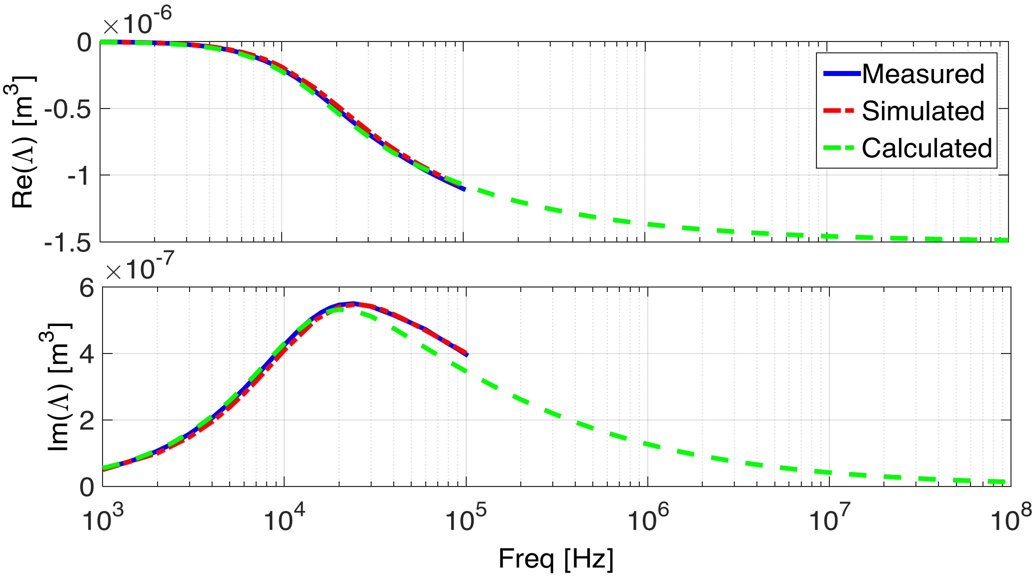

Figure 4-10: Validation of eigenvalue calculation and tensor methodology applied to titanium cube. The solid blue line is the eigenvalue of the tensor derived from experimental data, Measured, whereas the dashed lines are derived from simulation, Simulated, or analytical solution, Calculated.

Figure 4-10 displays the spectroscopic real and imaginary eigenvalue tensor for the cube. Note, only one eigenvalue is plotted as all three values were equal. The comparison shows good agreement for all three solutions. The measured and simulated tensors match, within 1.75%, for both the real and imaginary components, which is considered acceptable for the tolerances in the instrumentation, mechanical aspects of the experiment and the errors in the FEM models. The calculated tensor matches well for the real component, within 2.5%, however with a slight disagreement for the imaginary component at higher frequencies; increasing from 3% to 30% for frequencies above 20 kHz. This is likely to be due to the use of a spherical equation used to calculate the tensor. At high frequencies the eddy currents are pushed to the limits of the object and hence the precise shape has more influence on the eddy current distribution, the skin depth and ultimately the imaginary component of the tensor. Nevertheless, the strong agreement between all three solutions for the titanium cube gives confidence in the adopted method. In particular, the agreement with the analytical solution confirms that the obtained tensor is the absolute unscaled tensor value. Such absolute tensor calculation allows for the development of a tensor library which is transferrable between detectors and can act as a powerful calibration tool.

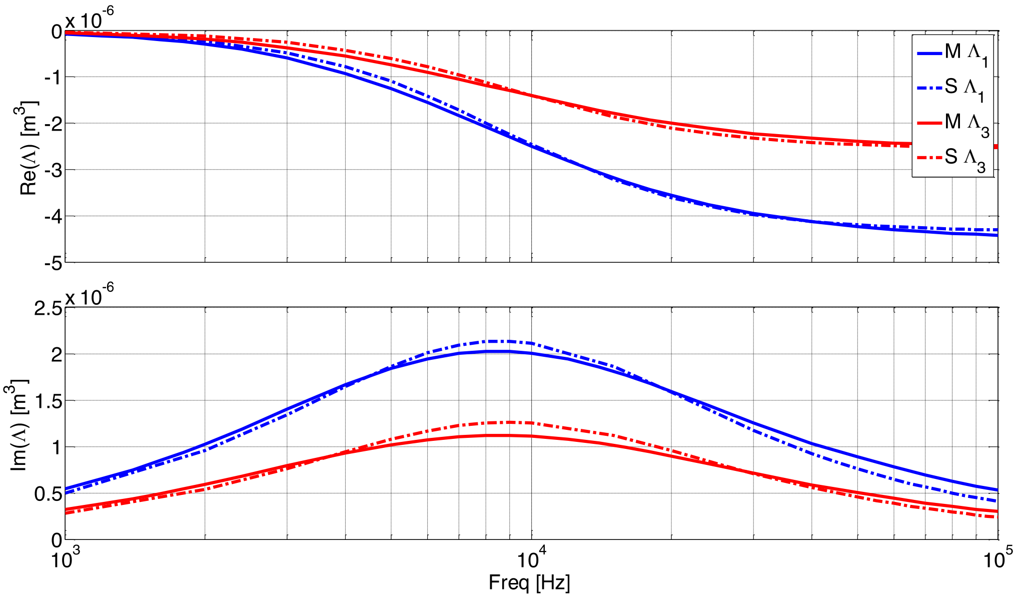

Figure 4-11: Validation of eigenvalue calculation and tensor methodology applied to .222 Remington cartridge. The solid lines are the eigenvalue tensors derived from experimental data, M, whereas the dashed lines are derived from simulation, S.

The apparatus was then validated for a .222 Remington cartridge shell to ensure the method holds for complex shapes. The Remington shell is representative of a typical clutter piece that could be found in a mined area of previous conflict. The measured tensor was compared to only that of simulation as an analytical solution does not exist for such a shape. Figure 4-11 represents the eigenvalues obtained from measurement and simulation. Note that two eigenvalues are reported here since the cartridge presents two equal smaller eigenvalues along the non-axial direction, Λ_3, with a dominant eigenvalue along the axial direction, Λ_1. This tensor structure re-affirms the possible shape characterization through the tensor as it is representative of the cartridge dimensional ratios. As for the titanium cube, a relatively good agreement is observed; within 2.5% for the real tensor and 7% for the imaginary. The small discrepancy between experimental and simulation can be attributed to a number of reasons. Firstly, the simulation was performed with typical values for a brass alloy and lacked exact material properties of the cartridge; mainly conductivity. The simulation also performed a number of subtle simplifications to the cartridge shape such as the absence of the extractor groove and primer. Finally, the wall thickness was simulated to be slightly thicker to reduce the required meshing.

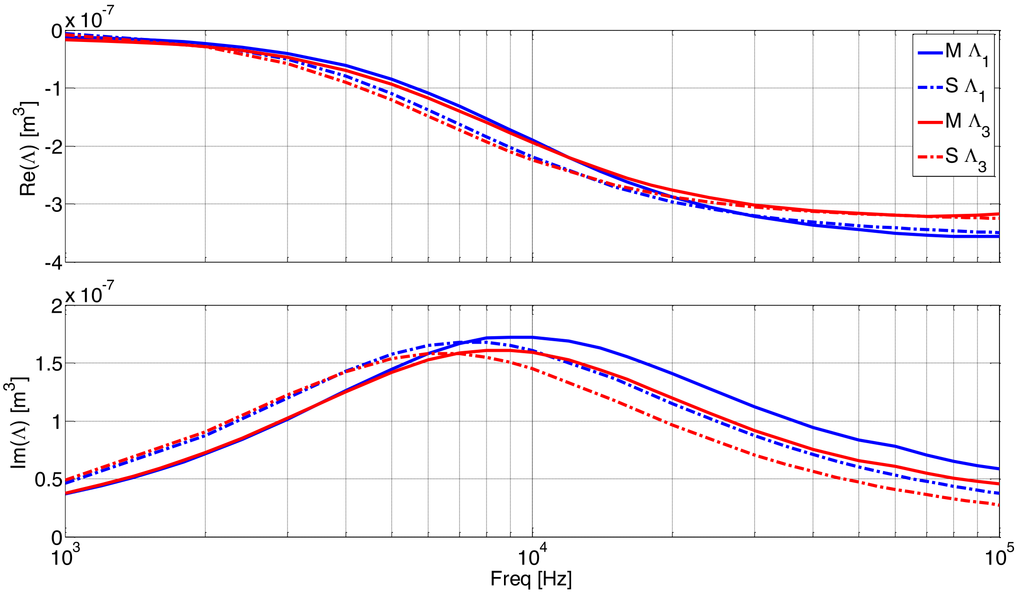

Figure 4-12: Validation of eigenvalue calculation and tensor methodology applied to a Type-72A phantom. The solid lines are eigenvalue tensors derived from experimental data, M, whereas the dashed lines are derived from simulation, S.

A third validation exercise followed, using a phantom piece for a Type-72A mine, Figure 4-12. The phantom piece is usually used in the field to calibrate metal detectors prior to clearance operations and was considered a suitable validation piece to represent a typical landmine tensor. Once again, agreement is observed, around 5% for the real response, but with some discrepancy of around 13% in the quadrature tensor. The exact material properties were again absent for the simulation. However, by observing the effects of increased conductivity in Figure 3-7 (c), the observed discrepancy can be attributed to a mismatch of conductivity between that used for simulation and that of the phantom.

A final verification exercise was performed to confirm the apparatus's ability to correctly deduce the tensors of uncirculated US coinage. To do so, a set of copper coins resembling the dimensions of a dime, quarter and half-dollar coins were manufactured, Figure 4-13.

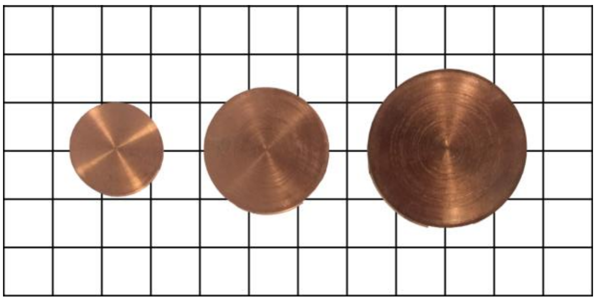

Figure 4-13: Copper coin validation pieces with dimensions of a dime (left), quarter (middle) and one dollar (right) against a 1cm grid.

The measured and simulated eigenvalue tensors were compared and are presented in Figure 4-14. A wider frequency range is represented for the simulated tensor for the sake of completeness as the peak frequency for the coins spanned outside the region of 1-100 kHz, the measured frequency range. Again, the coin validation exercise showed good agreement between the measured and simulated tensors; within 3% for the dime and quarter and 9% for the half-dollar. Please note that skin depth refinement was applied to the simulation of the larger quarter and half-dollar to increase the mesh density at the surface of the disks and correctly model the skin effects at high frequencies.

The validation exercise confirmed the apparatus is capable of accurately obtaining the unscaled tensor values for small metallic objects that embody coins, clutter and mine targets. The thesis now moves on to reporting the measured tensors for the uncirculated US coinage, a number of clutter items and mine surrogates.

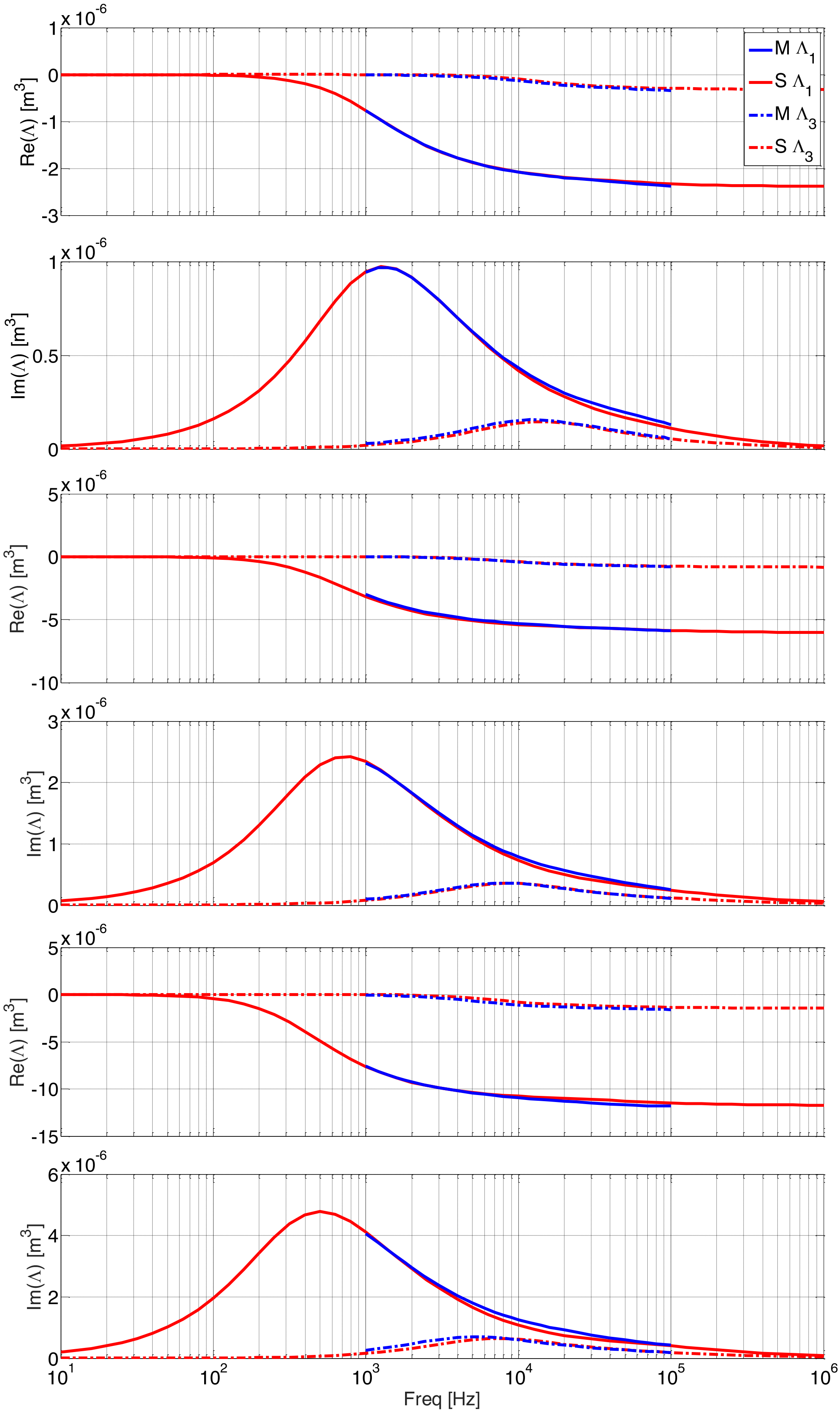

Figure 4-14: Coin verification for copper dime (top), quarter-dollar (middle) and half-dollar (bottom).

4.5 Tensor Measurements

4.5.1 US Coinage

A full set of uncirculated US coinage was obtained from the US Mint at Philadelphia. The coin responses were measured and the eigenvalue tensors are presented in Figure 4-15. Only two tensors are displayed here as the symmetry of the coin presented a repeated tensor; the minor eigenvalue tensor, $\Lambda 1$, is repeated. This tensor ratio is expected as the coins reflect the shape of the non-magnetic disc displayed in Figure 3-6.

The first difference noticed between the coin tensors is the variance in peak frequency of the imaginary tensors. This is heavily dependent on the coin composition; the higher the conductivity the lower the peak frequency, Figure 3-7. Table 4-1 summarises the characteristics and composition of the US coin set. The nickel, dime, quarter and half-dollar are all composed of Cupro-Nickel. The coin compositions for the dime, quarter and half-dollar are identical. However, the overall weights and sizes of the coins vary resulting in an expected lower peak frequency for larger coins. The lower copper percentage present in the nickel, 75% as opposed to 91.33%, is reflected by the higher peak frequency despite it being larger in size and weight than the dime.

The cent composition is considerably different as it is a Zn based coin. The peak frequency of the cent suggests that the overall conductivity of the cent is higher than that of the nickel but less than the dime. Zn is more conductive than Ni and as a result the overall conductivity of the nickel coin is less than the cent when the overall coin conductivity is considered due to the high Ni content. The dollar also has a lower copper content than the Cupro-Nickel coins; dime, quarter-dollar and half-dollar. As a result the peak imaginary frequency is expected to be lower. However, the dollar is relatively larger in size and weight than the dime and quarter. As a result the peak frequency appears to be higher than that of the dime and similar to the quarter. The differentiating factor is the larger tensor magnitudes, indicating it is an object of greater size of lower conductivity.

Finally, all the coin responses indicate no magnetic content is present as there is no positive real response at low frequencies. However, this can only be confirmed experimentally for the cent, nickel and dime as the low real frequency asymptote for the remaining coins is not within the measured frequency range.

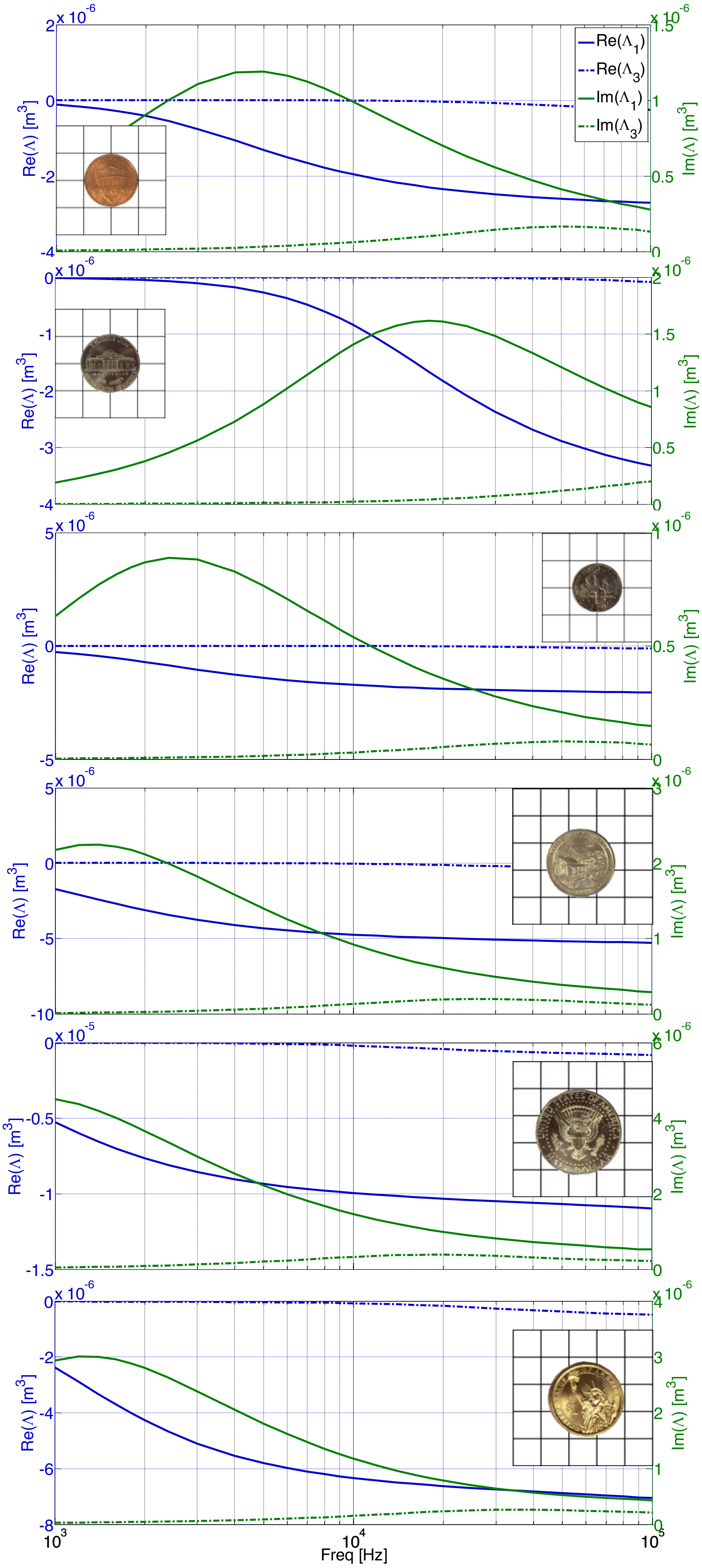

Figure 4-15: Tensors obtained for uncirculated US coinage; 1 cent, nickel, dime, quarter, half-dollar and dollar (top to bottom). Note that the indented coins are represented on a 1cm grid and are to scale with respect to one another. Blue plots are real tensor compoeenents plotted against the left axis and green plots are imaginary plotted against the right axis.

Table 4-1: US coinage characteristics [75]

Denomination	Cent	Nickel	Dime	Quarter Dollar	Half Dollar	Presidential $1
Composition	Copper Plated Zinc 2.5% Cu Balance Zn	Cupro-Nickel 25% Ni Balance Cu	Cupro-Nickel 8.33% Ni Balance Cu	Cupro-Nickel 8.33% Ni Balance Cu	Cupro-Nickel 8.33% Ni Balance Cu	Manganese-Brass 88.5% Cu 6% Zn 3.5% Mn 2% Ni
Weight	2.500 g	5.000 g	2.268 g	5.670 g	11.340 g	8.1 g
Diameter	0.750 in. 19.05 mm	0.835 in. 21.21 mm	0.705 in. 17.91 mm	0.955 in. 24.26 mm	1.205 in. 30.61 mm	1.043 in. 26.49 mm
Thickness	1.52 mm	1.95 mm	1.35 mm	1.75 mm	2.15 mm	2.00mm
Edge	Plain	Plain	Reeded	Reeded	Reeded	Edge-Lettering
No. of Reeds	N/A	N/A	118	119	150	N/A

4.5.2 Clutter Items

The second set of tensors presented in this thesis is those of typical clutter items. Figure 4-16 represents the clutter items measured along with the tensors obtained. The set of clutter items was chosen to represent potential clutter faced during demining operations. Even on a cursory examination of Figure 4-16, the difference between each item tensor is clear; the change in peak imaginary frequency, the positive or lack of real component and the variance in tensor ratios and values.

The first clutter tensor displayed is of a steel nail. A metallurgical assessment of the steel was not made, but by observing the tensor it is clear that the nail is composed of ferrous steel. This is deduced from the positive real component. The nail tensor also exhibits larger tensor values than most coins despite being smaller in size which can also be credited to the increased permeability as emphasised in Figure 3-7. The extreme unidirectional shape of the nail results in two near negligible tensors, $\Lambda 1$, in comparison to the dominant axial tensor, $\Lambda 3$. This is clearly shown by the near zero components for the real and imaginary eigenvalue tensor $\Lambda 1$. The tensor structure of the nail is representative of the magnetic rod discussed in Figure 3-6. Note if the nail was bent in one or two planes then only one or no near zero tensors would have been measured.

The .222 Remington cartridge shell is also unidirectional in shape as discussed earlier. However, ratio is not as extreme as the nail and the non-axial tensor, Λ3, is of some magnitude. The ratio of Λ1 to Λ3 is not linearly representative of the object's relative dimensions as the tensor ratio is roughly 2:1, whereas the object's relative dimensions are around 5:1. The lack of a positive real component indicates that the cartridge material is non-magnetic with relative permeability around 1. The material of the cartridge is known to be a brass alloy and hence the statement complies with brass properties.

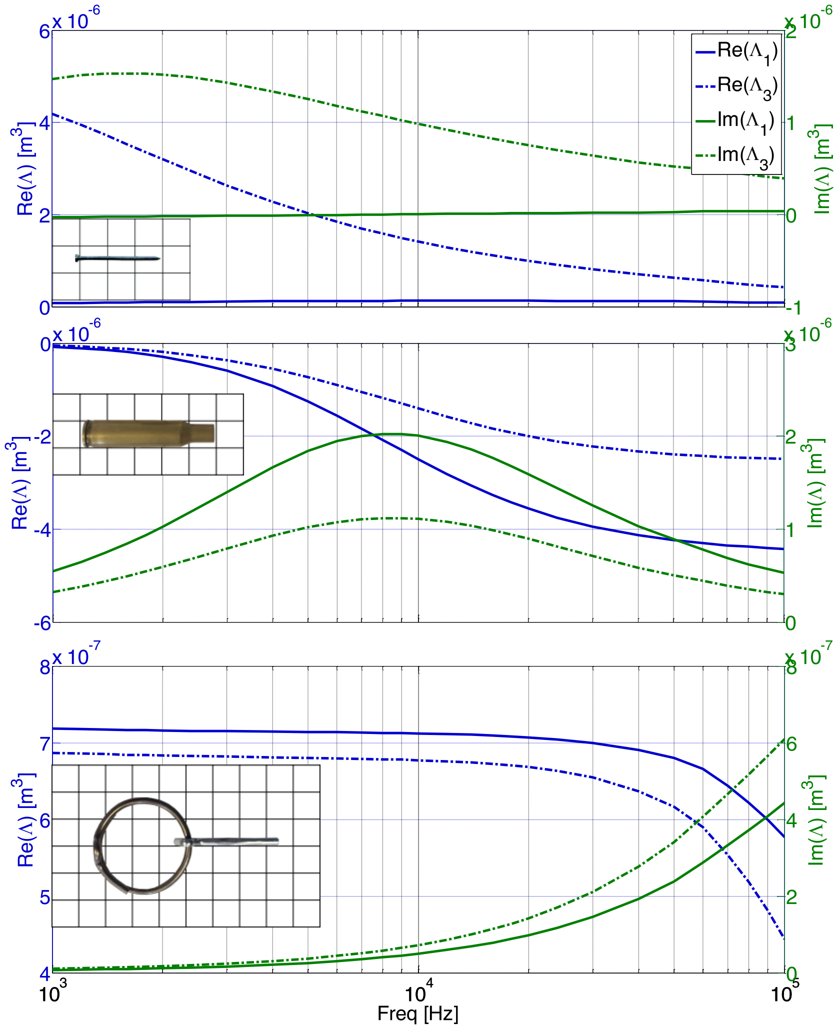

Figure 4-16: Tensors obtained for clutter items; a nail, .222 Remington cartridge shell and a grenade safety pin (top to bottom). Note that the clutter items are represented on a 1cm grid and are to scale with respect to one another. Blue plots are real tensor compoenents plotted against the left axis and green plots are imaginary plotted against the right axis.

The safety pin of an L109A1 grenade is the last clutter item presented in this thesis. The grenade pin was measured in the arrangement presented in Figure 4-16, with the pin and ring coplanar. Since the pin is able to freely move with respect to the ring, the tensor becomes variable in nature as it is will vary depending on the orientation of the pin with respect to the ring. However, the combined material will remain constant regardless of the arrangement. The metallic composition of the pin appears to be ferritic. The peak frequency is not visible in the frequency range measured, which indicates to a rather non-conducting material relative to the other objects. These tensor characteristics will be present regardless of the ring-pin arrangement, with only the tensor ratio varying as the pin is moved with respect to the ring. The pin should introduce a unidirectional property to the tensor increasing the ratio of the components, between $\Lambda 1$ and $\Lambda 3$. However, the tensor seems to not display a very unidirectional ratio, indicating that the ring is the dominant metallic component. This means that the tensor variation would be considerably less than if the ring and the pin were of similar magnitude of response. These aspects make the tensor presented still viable to characterise the pin.

4.5.3 Anti-personnel Mine Surrogates

A number of minimum metal anti-personnel landmine surrogates were obtained from Fenix Insight Ltd. to perform tensor measurements. Figure 4-17, reports on the tensors obtained from a Type-72A Chinese landmine, a Yugoslavian PMA-2 landmine, a South-African R2M2 landmine, a Belgian M409 and an Italian TS-50. The variance between mine types here is not as high as that displayed for clutter items. This is expected as mine parts are relatively similar with a similar set of components. However, there is still a significant amount of difference between the tensors to differentiate between the mines.

Comparing the magnitude of the tensors it is clear that the PMA-2 has the lowest metallic content followed by the Type-72A. These mines are generally considered to be amongst the most difficult mines to detect due to their low metallic content. The tensors of the Type-72A, R2M2, M409 and the TS-50 reveal a metallic composition of ferritic content. The M409 is slightly different as the ferritic component appears to have an influence in only one direction. This is interpreted from the positive real value for Λ_1 only and not for the repeated Λ_3. This can be attributed to the two cylindrical torsion springs highlighted in the plan X-ray scan of the M409 mine shown in Figure 4-18 (a). The spring material was confirmed to be ferritic by the manufacturer and so the two spring formations effectively act as two magnetic rods, strengthening the field in one direction significantly more than the other two. This type of spring arrangement is not included in other tested mines as displayed by the X-ray of the smaller PMA-2 presented in Figure 4-18(b).

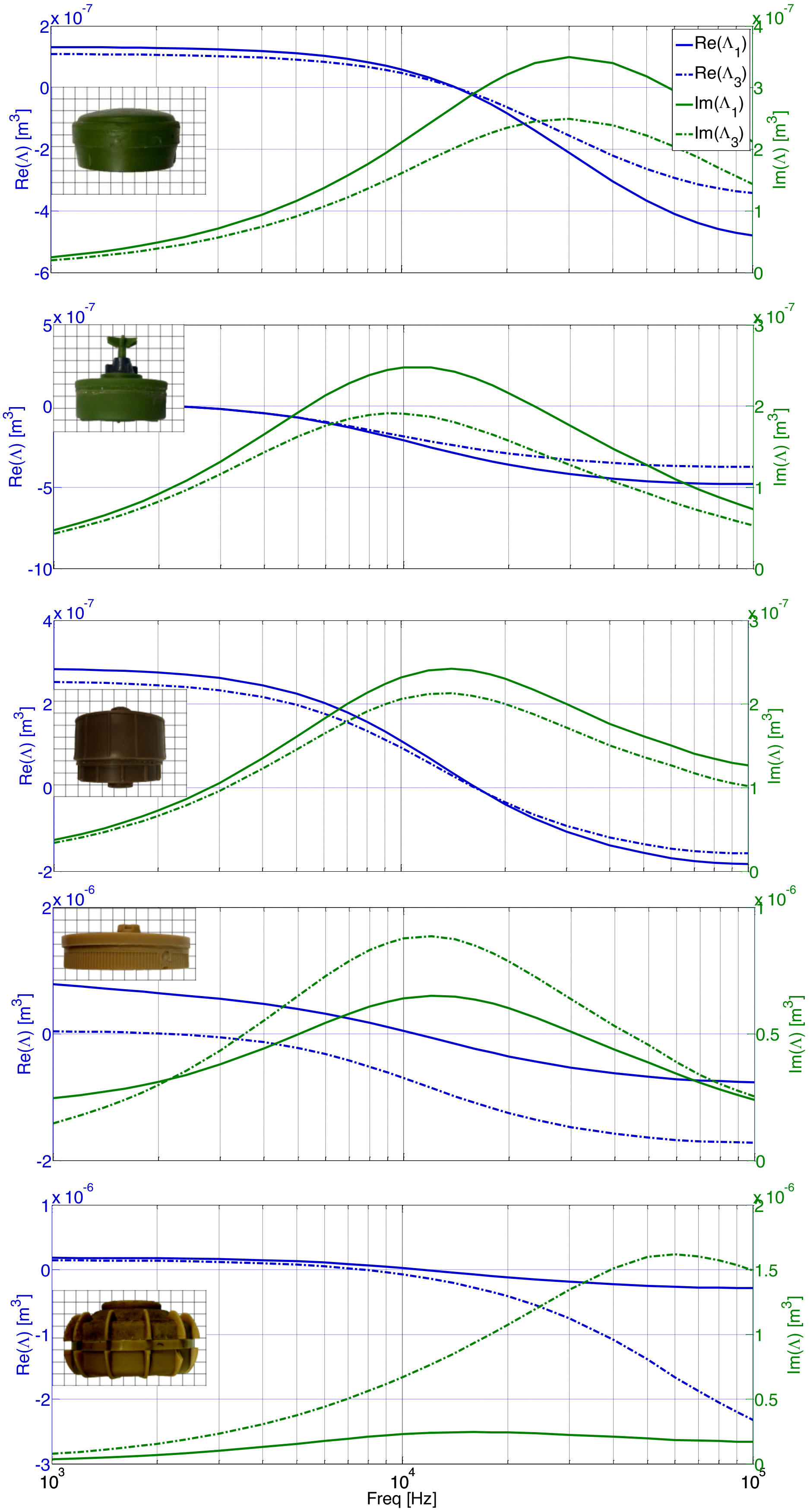

Figure 4-17: Tensors obtained for minimum metal mine surrogates; Type-72A, PMA-2, R2M2, M-409 and TS-50(from top to bottom). Note that the mines pictures are to scale with respect to one another and represented on 1 cm grid. Blue plots are real tensor components plotted against the left axis and green plots are imaginary plotted against the right axis.

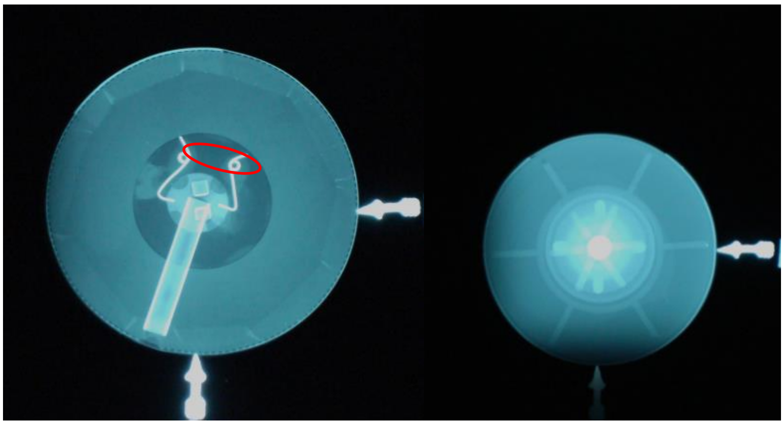

(a) (b)

Figure 4-18: Plan X-ray projections of (a) M409 and (b) PMA-2. Scaling between the two landmines is approximate.

The TS-50 mechanism for detonation is more complex, containing several additional metallic components. This is reflected in the larger values of the tensor and the considerable difference in tensor signature in comparison to the remaining mines.

The presented tensors in this section very clearly show the differences between the tensor components of the landmines from one another, and more importantly, tensor differences from that of clutter items. Figure 4-16 and Figure 4-17 confirm the possibility of utilizing the tensor to help discriminate mines and disregard clutter items.

4.6 Summary on Tensor Measurement

This chapter presented a systematic method capable of obtaining the unscaled magnetic dipole polarizability tensor in SI units for minimum metal anti-personnel mines and small symmetrical metallic objects. The tensors obtained experimentally, analytically and through simulation have been compared for the first time and were found to match without the need of a scaling factor. This confirmed the experimentally obtained tensor to be the correct representation of the measured object. A tensor library built using the described method would produce true object tensor values, transferrable between detectors and would act as a guide to calibrate future detectors capable of obtaining target tensors.

The reported tensors for clutter and landmines displayed variance portraying object properties such as size, shape and material. The absolute tensors for minimum metal anti-personnel mines were reported for the first time and were found to be considerably different from an example clutter set. The difference confirmed the capability of the tensor to act as a discriminatory property in order to reject clutter and reduce FARs for demining operations.

5 Coil Design

Chapter 4 confirmed the feasibility of distinguishing between different metallic objects by exploiting differences in their tensors. The thesis now shifts focus to the development of a prototype field instrument capable of measuring or deducing the tensors of buried metallic items and hence distinguishing between landmines and clutter. The electromagnetic sensor can be considered as the most important component of the detector as it needs to deliver information rich measurements of the object in order to determine the tensor correctly. The measurements need to provide the necessary fields of view to interrogate the object adequately.

This chapter summarises the selection process by which a coil array may be chosen. Candidate coil configurations were assessed against two selection criteria; (i) an analysis of their sensitivity distribution and (ii) the errors in the tensors that have been calculated from the measurements. The chapter continues with a description of the manufacturing process and the iterations performed throughout the research to arrive at the current coil. Finally, the chapter concludes with an analysis of the expected signal levels from some of the mines discussed in chapter 4 and predicts an SNR performance for the final system.

5.1 Sensitivity Analysis

At the outset of the coil design, a study was performed to identify candidate coils and select the most appropriate coil array capable of providing valuable measurements. The initial criterion by which coils were assessed was how evenly distributed the sensitivity of the coil array was in all combined transmitter-receiver directional components; i.e. xx, xy, xz, yy, yz and zz. These components correspond to the unique tensor constituents of $\overleftrightarrow{\mathbf{M}}$ in equation (3-18). The uniformity of the coil sensitivity components ensures that all tensor constituents are equally interrogated when scanning the coil over buried objects.

$$Sens = \begin{bmatrix} H_{T_x} \\ H_{T_y} \\ H_{T_z} \end{bmatrix} \cdot \begin{bmatrix} H_{R_x} \\ H_{R_y} \\ H_{R_z} \end{bmatrix} (A^2/m^2) \qquad (5\text{-}1)$$

$$
\begin{aligned}
Sens_{xx} &= H_{T_x} \cdot H_{R_x} \\
Sens_{xy} &= H_{T_x} \cdot H_{R_y} + H_{T_y} \cdot H_{R_x} \\
Sens_{xz} &= H_{T_x} \cdot H_{R_z} + H_{T_z} \cdot H_{R_x} \\
Sens_{yy} &= H_{T_y} \cdot H_{R_y} \\
Sens_{yz} &= H_{T_y} \cdot H_{R_z} + H_{T_z} \cdot H_{R_y} \\
Sens_{zz} &= H_{T_z} \cdot H_{R_z}
\end{aligned} \tag{5-2}
$$

To assess the sensitivity of coil arrays, sensitivity maps were created representing the constituents of the $\boldsymbol{H}_T \cdot \boldsymbol{H}_R$ matrix. The field values of the transmit and receive coils, $\boldsymbol{H}_T$ and $\boldsymbol{H}_R$, were calculated using the Biot-Savart Law, equation (3-14), assuming a 1A current was passed through the coils and a dyadic expansion was then performed for each transmit-receive channel as described by equation (5-1) and (5-2). The resulting six elements from the expansion represent the individual sensitivity components xx to zz for each transmit-receive coil pair, listed in equation (5-2). Alternatively, the sensitivity of the coils could have been analysed through the calculation of the induced voltage for objects of tensor values represented in Table 5-1 using equation (3-16). The former method was used to analyse coil sensitivities in this thesis.

Table 5-1: Tensors used to analyse coil sensitivities.

	$\boldsymbol{M'}_{xx}$	$\boldsymbol{M'}_{xy}$	$\boldsymbol{M'}_{xz}$	$\boldsymbol{M'}_{yy}$	$\boldsymbol{M'}_{yz}$	$\boldsymbol{M'}_{zz}$
XX Sensitivity	1	0	0	0	0	0
XY Sensitivity	0	1	0	0	0	0
XZ Sensitivity	0	0	1	0	0	0
YY Sensitivity	0	0	0	1	0	0
YZ Sensitivity	0	0	0	0	1	0
ZZ Sensitivity	0	0	0	0	0	1

The overall coil array sensitivity was then deduced by taking the root-mean-squared value of the dyadic expansions for each channel within the array to create the sensitivity maps. The coil fields and the sensitivity maps were calculated for 1 mm grid planes parallel to the coils at 5 cm, 10 cm and 15 cm. These sensitivity planes represent the sensitivity of the coil arrays at detection depths of 5 cm, 10 cm and 15 cm, with respect to the distance from the closest coil. Finally, overall array sensitivities were normalised against the array maxima to allow for the comparison of uniformity between the sensitivity components.

A large number of coil arrays were assessed at this stage; ≈ 30 arrays. Out of those arrays only 7 are displayed here, summarising the approach undertaken and the primary candidates emerging from the study. It should be stressed that these coil configurations do not represent all possible designs, but those selected at the time of the study. It is possible that better configurations may emerge in the future as research in this area progresses. The coils proposed were all designed to have receive coils which are nulled with respect to the coupling from the transmit coil; such receive coils are wound so that the signal induced on the receive coil in the absence of an object is near zero. This arrangement is necessary to maximise the dynamic range of the system, ensuring it is devoted to the object response, and not that of the background signal. The coil sizes were limited to a 30 x 30 cm footprint as it is in-line with the dimensions of current commercial systems. Larger coils would result in heavy, bulky and difficult to manoeuvre coil heads. The number of separate transmit coils was limited to two, because of the need to minimise the power drain from the battery supplying the current to these coils.

The coil designs investigated were grouped in sets where the principal design of each set was similar with slight variations to the coil arrangement. The first 3 arrays presented here, 1A-1C, are of the same set; composed of square transmit coils with figure-of-eight receive coils. All three coils contained a 30 x 30 cm transmit coil. The first array contained four figure-of-eight receive coils on two separate layers with both receive layers arranged orthogonal to one another, Figure 5-1. The other two arrays, 1B & 1C, contained only two figure-of-eight receive coils, larger in size and spanning the entire 30 x 30 cm area, Figure 5-2 and Figure 5-3 respectively. 1C had an additional transmit coil, 15 x 15 cm, in the centre. Please note, the sensitivity plots displayed throughout this study do not share the same colour bar scales.

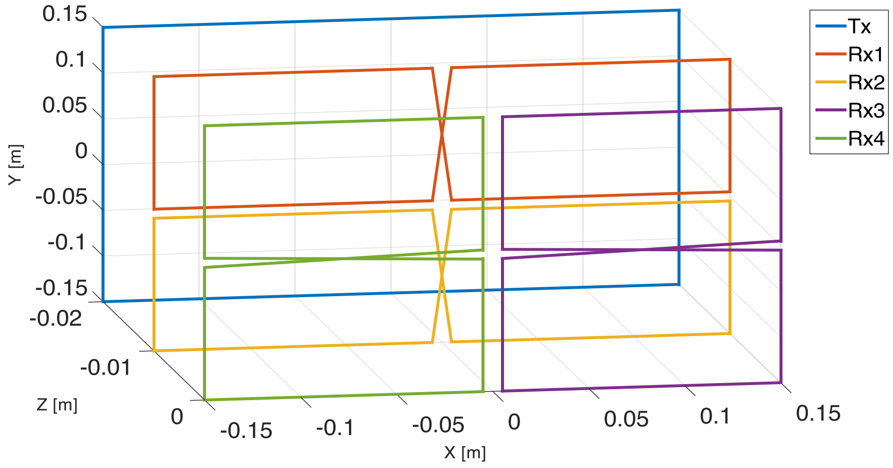

Figure 5-1: Candidate coil array 1A

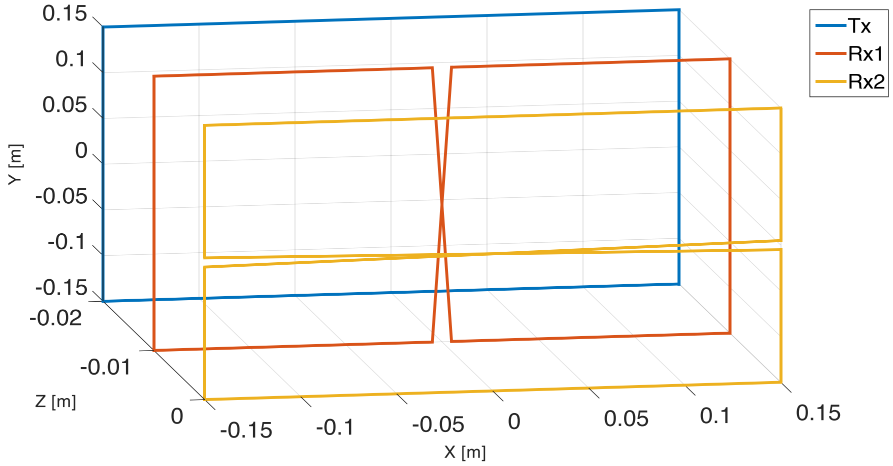

Figure 5-2: Candidate coil array 1B

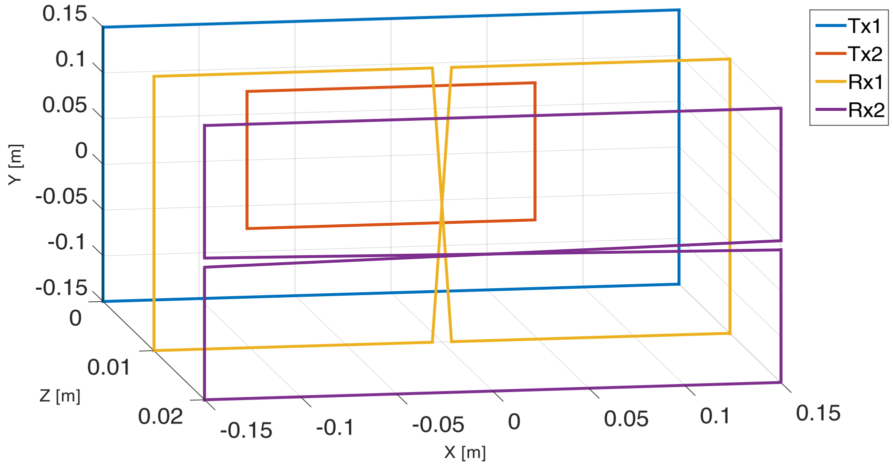

Figure 5-3: Candidate coil array 1C

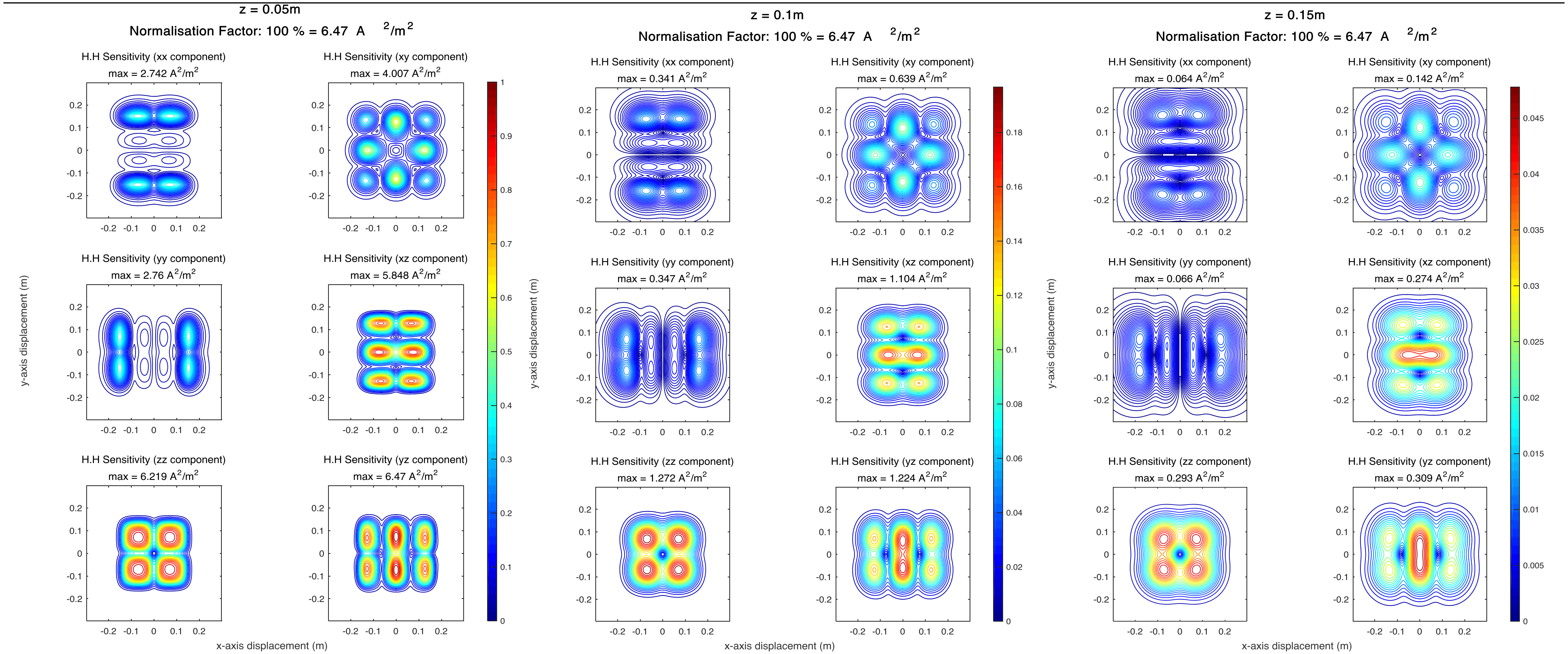

Figure 5-4: Sensitivity map of coil array 1A at 5cm (left), 10 cm (middle) and 15 cm (right) depth

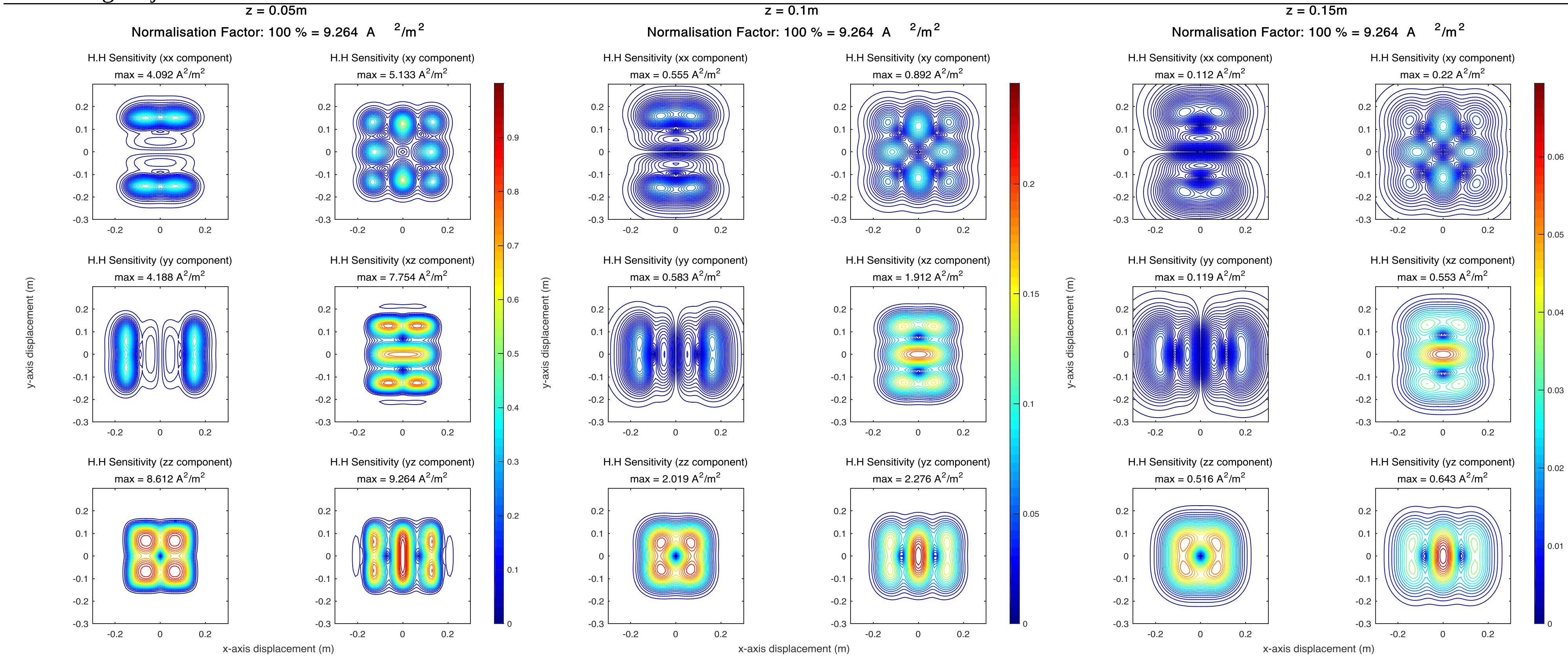

Figure 5-5: Sensitivity map of coil array 1B at 5cm (left), 10 cm (middle) and 15 cm (right) depth.

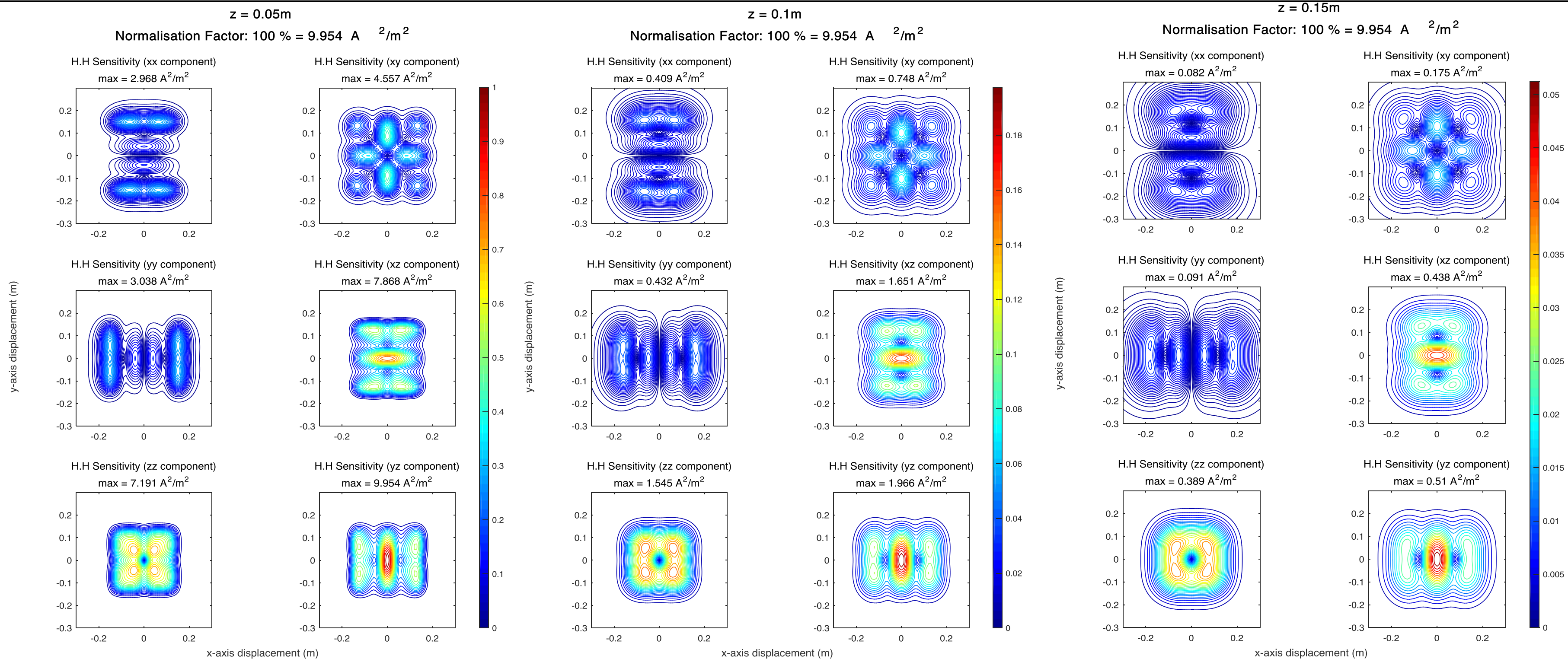

Figure 5-6: Sensitivity map of coil array 1C at 5cm (left), 10 cm (middle) and 15 cm (right) depth.

This group set was considered to be the most favourable group as it has a relatively uniform sensitivity. The coil arrangements allowed for good object location; since the signal would reverse on at least one receive coil as the object crossed from one quadrant to the next. The sensitivity is considerably worse for the xx and yy direction for all three coil arrays. This was found to be a general weakness presented by most arrays as the planar transmit coil arrangement resulted in field concentration in the zz direction and weaker xx and yy fields. All three variations were considered to be viable coil candidates at this stage and were progressed to the invert-ability study to determine the primary candidate.

To try and overcome the weakness presented by coil set 1, a number of non-planar or 3D coil configurations were proposed to create stronger fields in the xx and yy direction; coil array 2A represents such an example. While this array did present an improved uniformity, non-planar coils were dismissed due to the added size of the coils as well as the added distance to the detected object as a result of the indented coils. It was also envisaged that the flat coils could be tilted to enhance their effective interrogation of the object in the xx and yy direction.

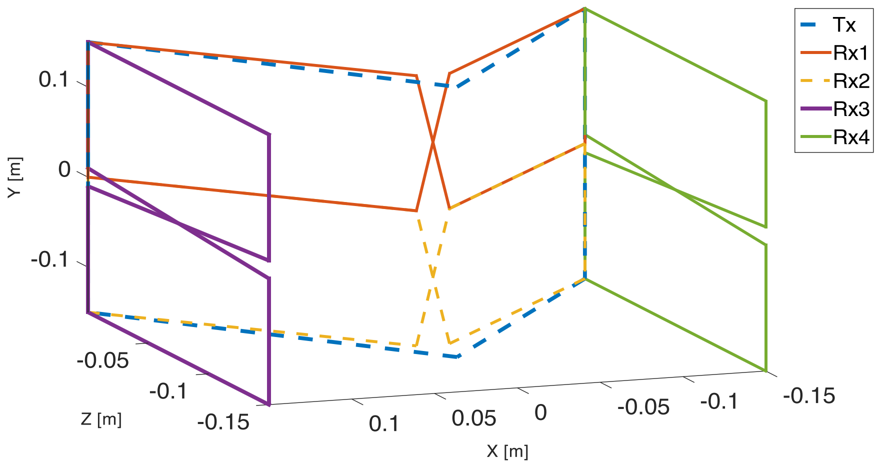

Figure 5-7: Candidate coil array 2A.

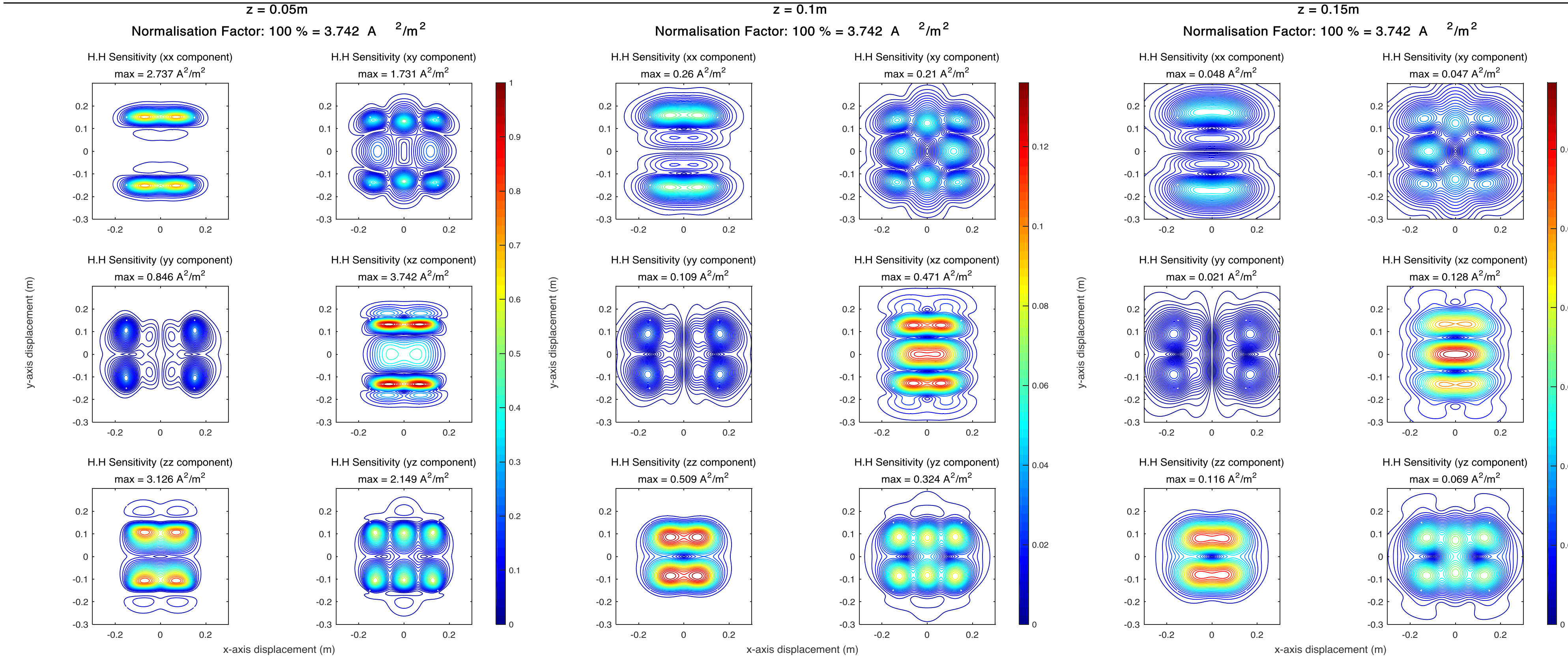

Figure 5-8: Sensitivity map of coil array 2A at 5cm (left), 10 cm (middle) and 15 cm (right) depth.

.

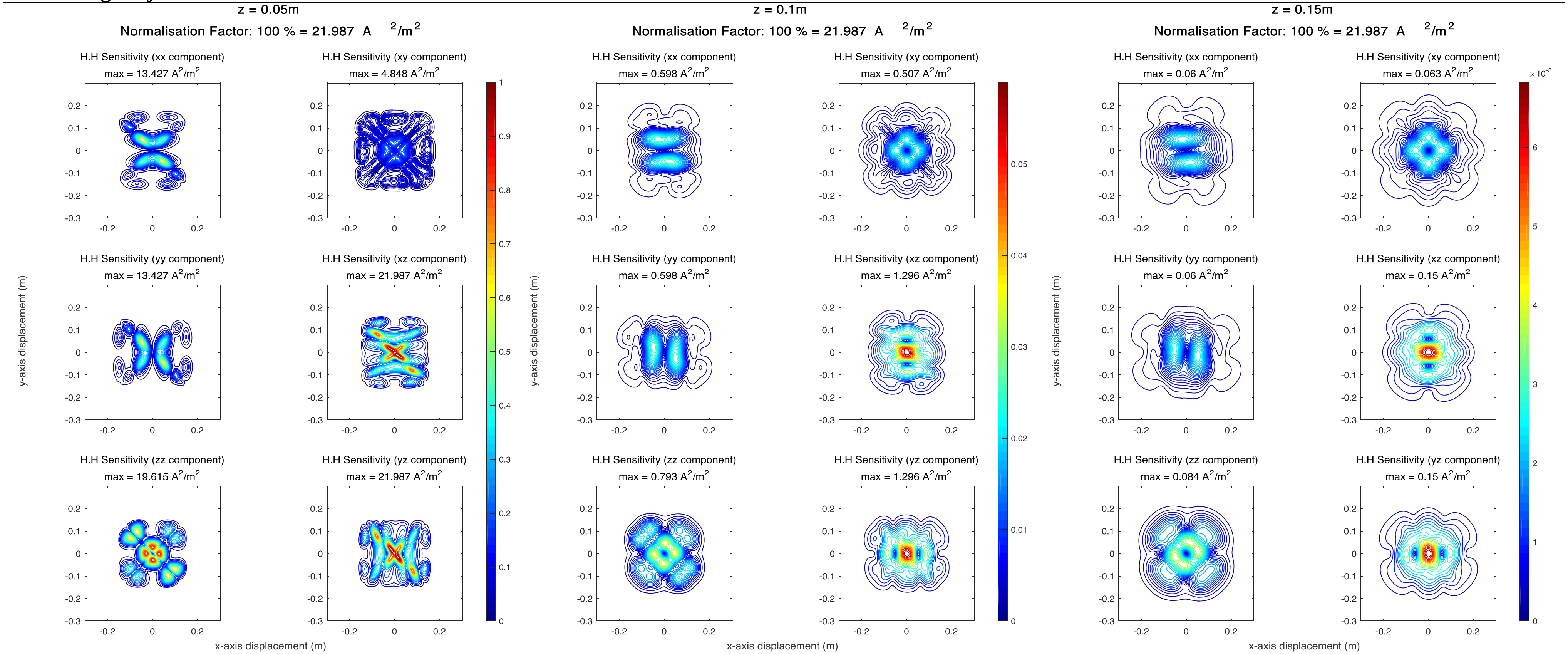

Figure 5-9: Sensitivity map of coil array 3A at 5cm (left), 10 cm (middle) and 15 cm (right) depth.

Another array set, set 3, altered the transmit coils such that they were composed of three sections with two crossover points, Figure 5-10. Array 3A is an example of set 3 and was found to present good sensitivity; however, was dismissed due to the potential strong coupling between the two transmit coils and the added difficulty in manufacturing such a geometry.

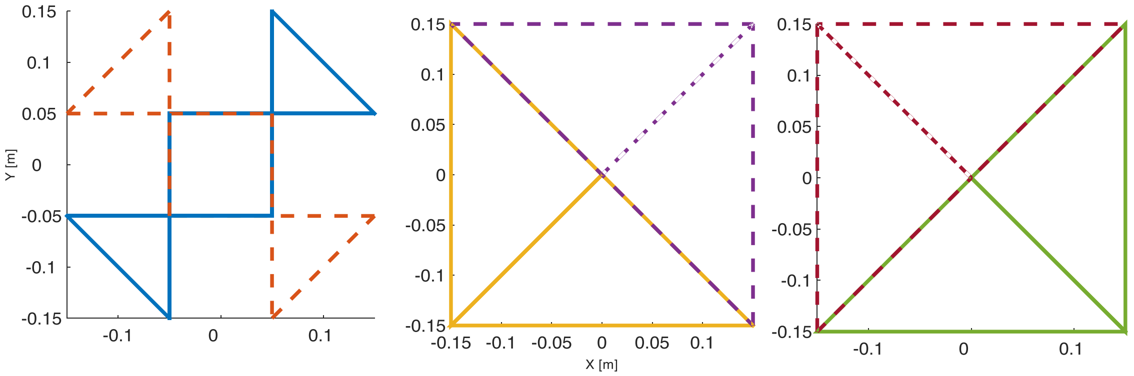

Figure 5-10: Candidate coil array 3A. Transmit coils (left), receive coil layer 1 (middle) and receive coils layer 2 (right). Layers were separated by 0.01m.

Coil arrays 4A and 4B were part of a set where different approaches were combined. Most combinations within this cross-set approach were found to not give a better uniform sensitivity than those already presented in this thesis so far.

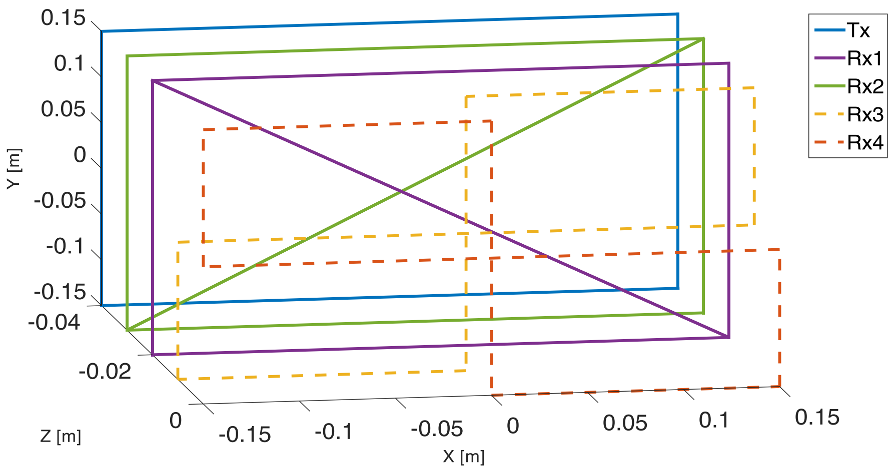

Figure 5-11: Candidate coil array 4A.

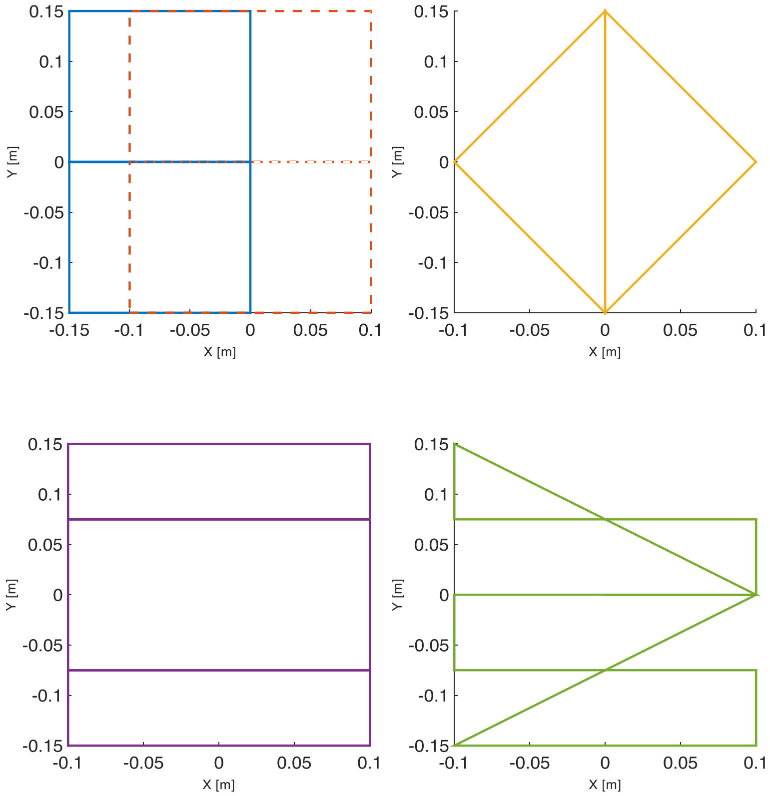

Figure 5-12: Candidate coil array 4B. Transmit coils (top-left), receive coil layer 1 (top-right), receive coil layer 2 (bottom-left) and receive coil layer 3 (bottom-right) Layers were separated by 0.01m.

This study highlighted a number of coil arrays that would provide magnetic fields capable of sufficiently interrogating buried objects. The emerging candidates were then progressed to the so called "invert-ability" analysis to identify the best coil geometry capable of performing accurate inversions in a robust manner.

5.2 Invert-ability Analysis

The invert-ability analysis was designed to determine the geometry's suitability to invert accurate tensors under adverse noise conditions. In total, 100 objects of different tensors were placed at random locations as displayed in Figure 5-13 and the different coil arrays were simulated to perform a raster scan over the upper surface of the volume. The tensors used included all the possible binary combinations of the six tensor components without and all 0 tensor, as well as a combination of 0.5, -1 and 2 values to vary the component ratios. The induced signal on the receive coil was calculated using (3-16) and in-band Gaussian noise levels of increasing magnitude were super-imposed onto the signal. The analysis then inverted the noisy signals using (3-17) and the tensor error was calculated. The tensor error was calculated using the summation of absolute values of tensor components for the original and inverted tensor. The analysis was performed for a number of the most favourable coils as deemed from the previous sensitivity analysis; however, the thesis only presents the results from coil set 1 as they were found to be the strongest candidates, Figure 5-14 to Figure 5-16.

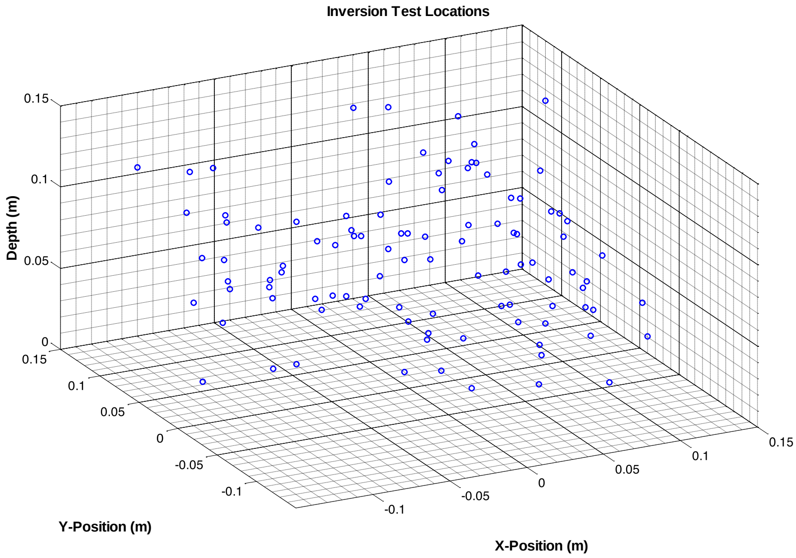

Figure 5-13: Location of test objects for invert-ability analysis.

By reviewing Figure 5-14 to Figure 5-16, 1C can quickly be dismissed as a candidate as it presented higher tensor error across all SNR levels. 1A and 1B presented similar performance, with low tensor error up to signal levels of 20 dB. A larger number of object tensors inverted with 0% error using 1A at good SNR levels (60-20dB) and below 20dB 1A displayed a considerably better performance than 1B as the majority of tensors inverted to within 10% up to 10dB SNR. The inversion of tensors using 1B did start to breakdown earlier with more tensor errors exceeding 10%.

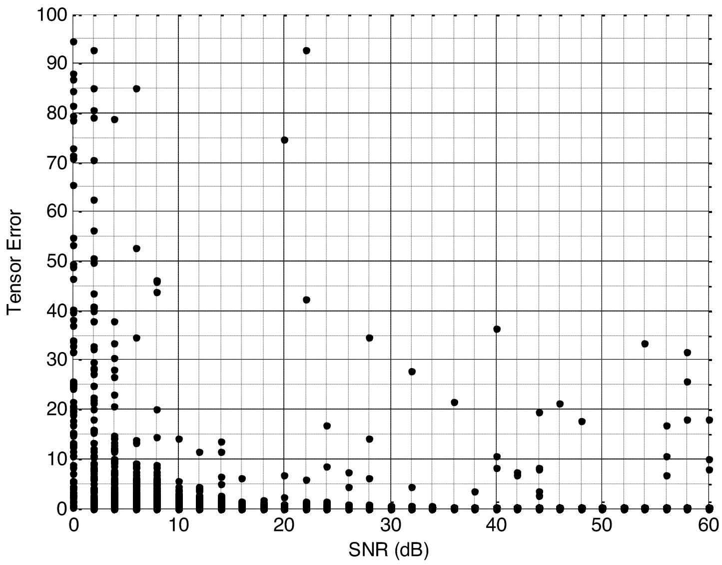

Figure 5-14: Tensor errors of inversion results using coil array 1A.

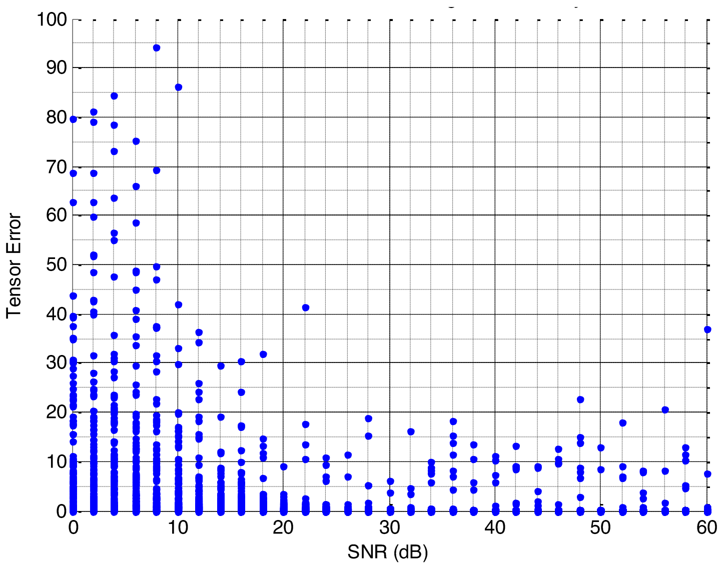

Figure 5-15: Tensor errors of inversion results using coil array 1B.

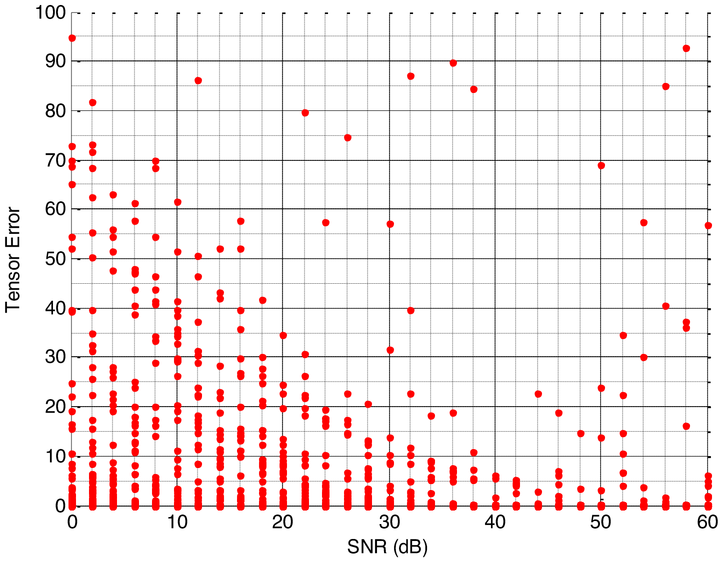

Figure 5-16: Tensor errors of inversion results using coil array 1C.

The sensitivity and invert-ability studies resulted in the selection of array 1A as it was considered the strongest candidate for the proposed application of this research. The coil array design then fed the manufacturing process to create the coil, which involved the solution to some production issues not considered thus far.

5.3 Manufacturing of Coil Array

A number of manufacturing iterations were undertaken to produce an ideal sensor head for the prototype system. Numerous outstanding decisions were yet to be made regarding the coil design that were more focused on the coil build such as wire diameter, number of turns and material of formers. This section will summarise the steps taken to fabricate the prototype coil array.

5.3.1 PCB coils

Printed Circuit Boards (PCBs) were initially considered to produce the receive coils, pictured in Figure 5-17 (a). PCBs were considered due to their accurate and reproducible track location. This was considered beneficial as the receive field, $\boldsymbol{H}_R$, could be calculated accurately using Biot-Savart Law. A medium density fibre (MDF) board was used to create the transmit coil at the time, displayed in Figure 5-17 (b), as it only needed to assess the feasibility of PCB use.

The coil impedances were measured to identify the coil characteristics such as series resistance and resonance frequency. Two 20 turn PCB receive coils were created and their resonance measured, Figure 5-18. The resonance measurements highlighted that the PCB receive coils were of relatively high impedance magnitude, 50-60 Ω at the resistive region, which in this case was below 10 kHz. The receive coils were also inductive for a relatively narrow region and more importantly were not inductive up to 20 kHz. The use of PCBs also limited the number of turns possible due to the 2D nature of track location. Finally, the PCB manufacturer advised that the coil board layout can cause issues to the etching process as it contained a large empty area in the middle with a number of fine tracks at the edges. These undesirable points quickly dismissed the PCB as a viable receiver coil option and the manufacturing direction was shifted back towards traditional wire wound coils.

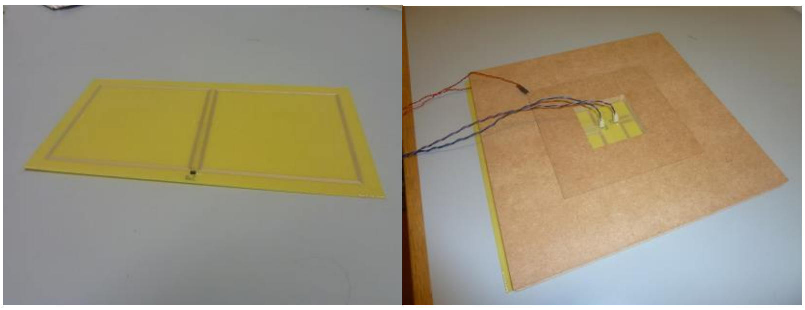

(a) (b)

Figure 5-17: (a) 20 turn PCB receive board and (b) entire coil array including a 35 turn transmit.

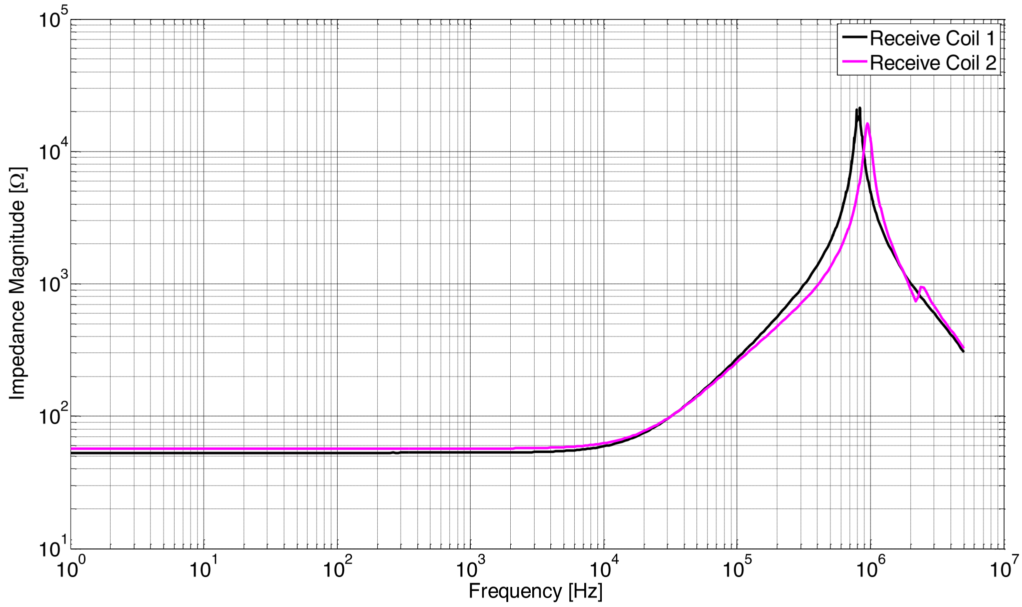

Figure 5-18: Coil Array Impedance measurement.

5.3.2 Resonance Study

With the PCB approach ruled out, the manufacturing approach returned to the more conventional wire wound coils. A study was performed to assess the effect of different wire properties on the coil resonance. Coil resonance can be calculated using (5-3), where f_R is the resonance frequency, L is the coils inductance and C is the coil capacitance.

$$f_R = \frac{1}{2\pi\sqrt{LC}}\,(\mathrm{Hz}) \qquad (5\text{-}3)$$

Coil resonance is an unfavourable property for multi-frequency applications such as the work presented in this thesis. If coil resonance occurs within the measurement region of interest, front-end amplification would be significantly reduced to ensure amplifiers do not saturate at the resonance frequencies. This in turn would hinder the SNR of non-resonant measurements. Thus the study was important to understand how different design decisions could result in a resonant frequency within the region of interest. The study involved the comparison of enamelled and polymer (PTFE) insulated wires to review the effect of insulation on the resonance frequency as well as varying the number of turns, lead length and wire thickness. To perform the study, the wooden transmit former pictured in Figure 5-17 (b) was used to create the different coils and the resonance was measured using a laboratory impedance/gain-phase analyser.

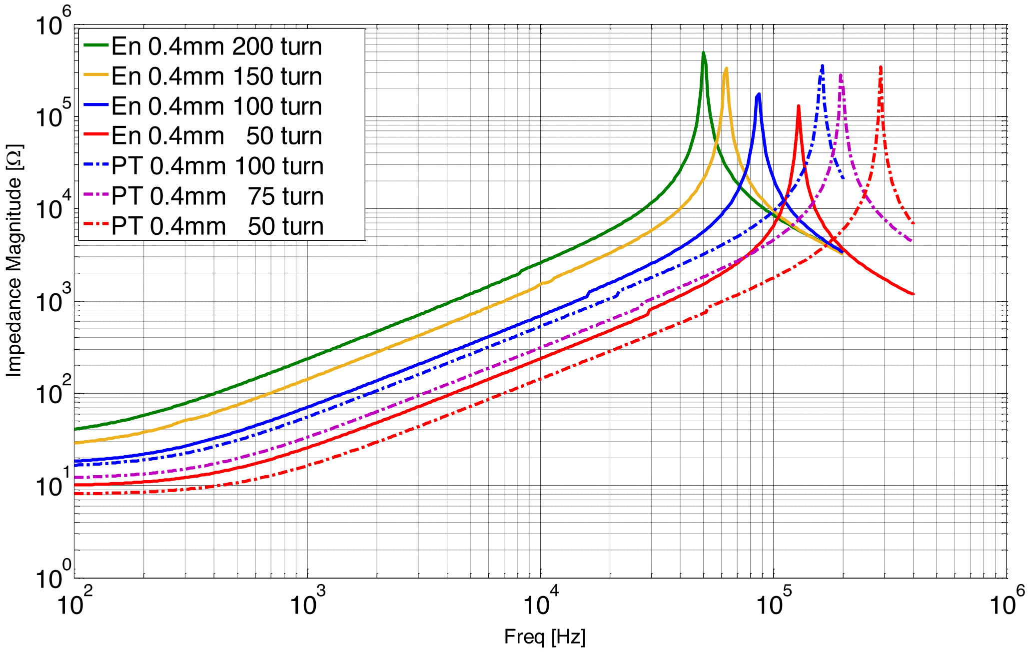

Figure 5-19: Resonance variance for 0.4 mm enamelled wire wound coils (solid lines) and 0.4 mm PTFE insulated wire (dashed lines) for different number of turns.

Figure 5-19, represents the effect of increasing the number of turns on resonance frequency for both enamelled and PTFE wound coils. As the number of turns increases the resonance decreases for both wire types. This is due to increased inductance and capacitance added by the extra turns. It is favourable to construct a coil with the maximum possible number of turns as more turns result in stronger magnetic field. However, the number of turns cannot be increased indefinitely as this would result in the resonant frequency decreasing to a point where it resides within the measurement region of interest. The frequency range of interest for this research was set to be 1 kHz-100 kHz as this was the region with the majority of information as revealed by the tensor measurements in chapter 4. The increase in turns also increases the coil series resistance and consequently reduces the maximum possible transmit current and the overall field.

Figure 5-19, also highlights the effect of different wire insulation on the resonance. The lower capacitance introduced by the thicker insulation of the PTFE wire resulted in a higher resonance when compared to enamelled wire; increasing from 87 kHz to 160 kHz for 100 turns and 130 kHz to 340 kHz for 50 turns. The increased resonance of the PTFE for the same turn number would allow for higher number of turns to be wound without the resonance dropping into the region of interest. However, the PTFE wire did occupy a much larger space for the same number of turns as the enamelled wire, making the final coil slightly heavier and significantly larger in size. This resulted in the enamelled wire being the selected wire to construct the proto-type coil.

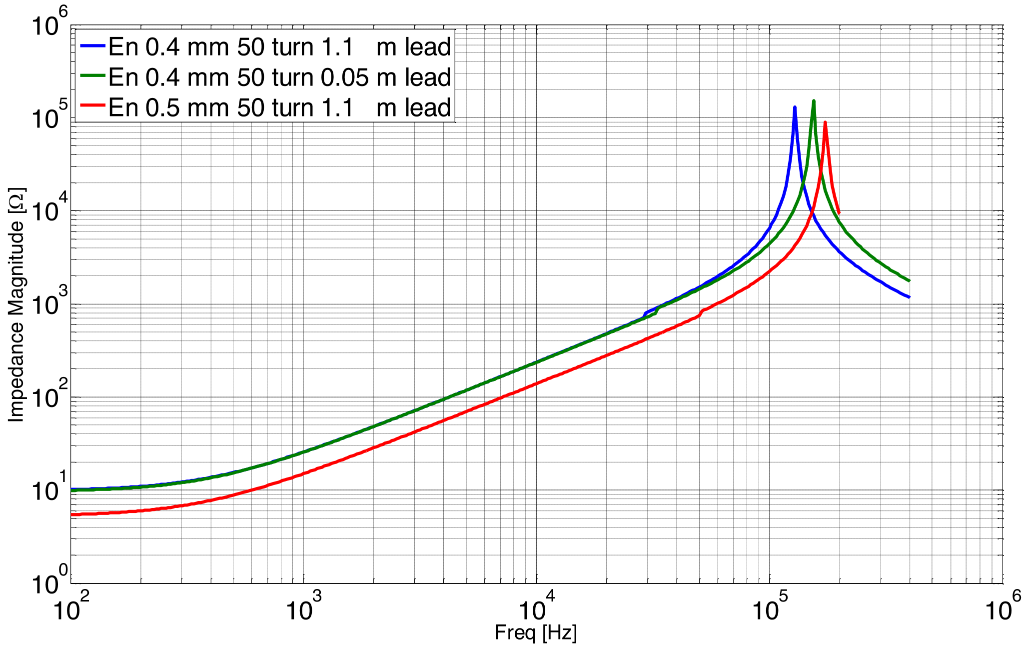

Figure 5-20: Impedance measurement of a 0.4 mm 50 turn enamelled wire wound coil with 1.1m lead (blue) and 0.05m lead (green) and 0.5 mm 50 turn enamelled wire wound coil with 1.1 m lead (red).

The final set of measurements was performed to understand the effects of lead length and wire thickness on the resonance, Figure 5-20. The increase in lead length resulted in a lower resonance frequency; a meter increase in lead length resulted in the reduction of resonance frequency by 20 kHz. This was caused due to the added capacitance introduced by the longer interconnections. The increased wire diameter resulted in an increased resonance frequency; however, this was at the cost of added weight and so was to some extent unfavourable. Since both 50 turn coils presented identical inductance, equal inductance gradient, the increase in resonance frequency can be attributed to lower capacitance of the 0.5mm wire coil. This lower capacitance could be due to a number of reasons. The enamel thickness could be thicker on the 0.5mm wire, resulting in larger spacing between wires. Alternatively, the thicker wire could have resulted in a greater number of layers with greater spacing between non-adjacent wires consequently resulting in an overall lower capacitive interaction.

The resonance study helped decide initial estimates for the number of turns and more importantly the wire of choice. The study indicated that a wire thickness in the region of 0.4 to 0.5 mm would be appropriate for the transmit coil. The choice of wire thickness was then dictated by the current rating as the transmit coil was expected to carry currents in the region of 200 to 300 mA. This current rating was chosen to make sure the final detector makes best use of battery life and would allow for continuous detector operation of similar time to that of current commercial detectors. As a result, 0.5 mm enamelled wire was chosen for the transmit as its current rating was 300 mA. Based on Figure 5-19 and Figure 5-20, it was estimated that the number of turns for the transmit coil would be in the region of 50-70 turns to ensure the resonance is above the frequency range of interest.

For the receive coil, a number of different measurements were performed for different numbers of turns, and the solution was taken to be the optimal of this set. The study thus far indicated that enamelled wire was the appropriate wire of choice. Since the receive coils would carry minimal current, current rating was not so much of a deciding factor but rather the maximum number of turns and minimal weight. Consequently, an initial wire of 0.0125mm diameter wire considered. Once initial wire estimates were agreed, formers were designed for the full coil array with dimensions capable of accommodating adjustments to wire thickness and number of turns.

5.3.3 3D Printing of Coil Formers

3D printing was the chosen means to create the final coil former due to the accuracy and repeatability of production. The formers created are also light and robust, making it an ideal manufacturing tool for the prototype coil. A model was created using SolidWorks to create the 300x300 mm transmit coil and the eight 150x150 mm parts to create the figure-of-eight receive coils, Figure 5-21. The full former was designed so that each layer would locate and connect using interlocking pegs. The transmit layer also contained a central piece which would allow a Glass Reinforced Plastic (GRP) stem to be connected as well as groves to attach bracing pieces. The central structure also contained housing for a connection board where coil wires were soldered in order to create a secure easily accessible connection point. The cost to produce the transmit coil in a single piece was considerably high as it required special machinery to print such a large volume. To reduce the manufacturing cost, the transmit coil was split into four parts to be assembled post printing, Figure 5-21 (b). The printed formers are displayed in Figure 5-22.

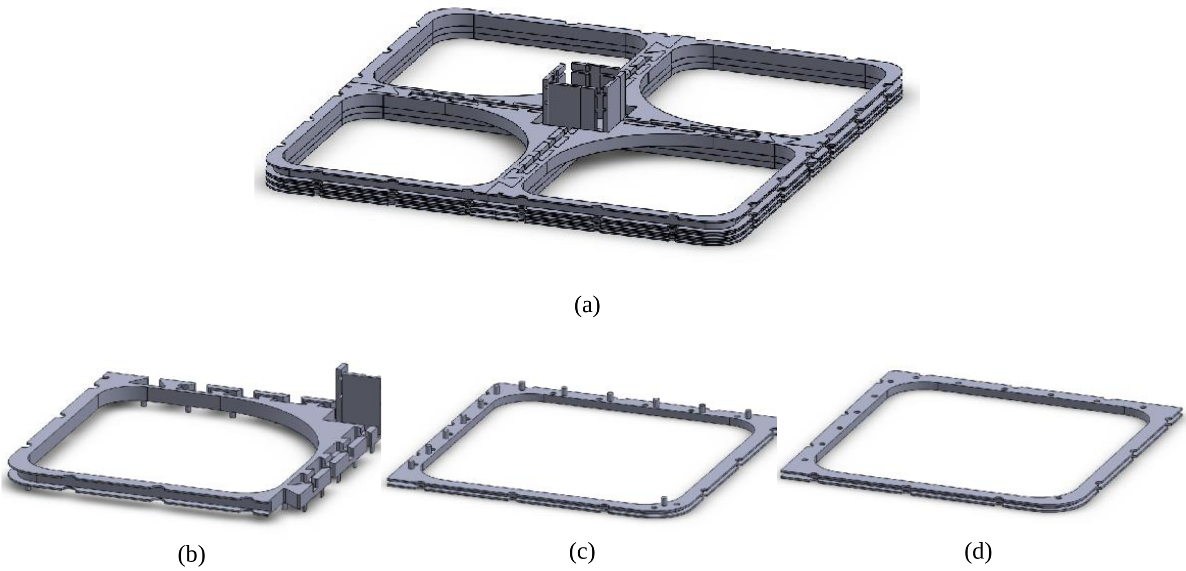

Figure 5-21: 3D model of coil array former (a) assembled. The part transmit former (b), the mid-layer receive former (c) and the bottom layer receive former (d).

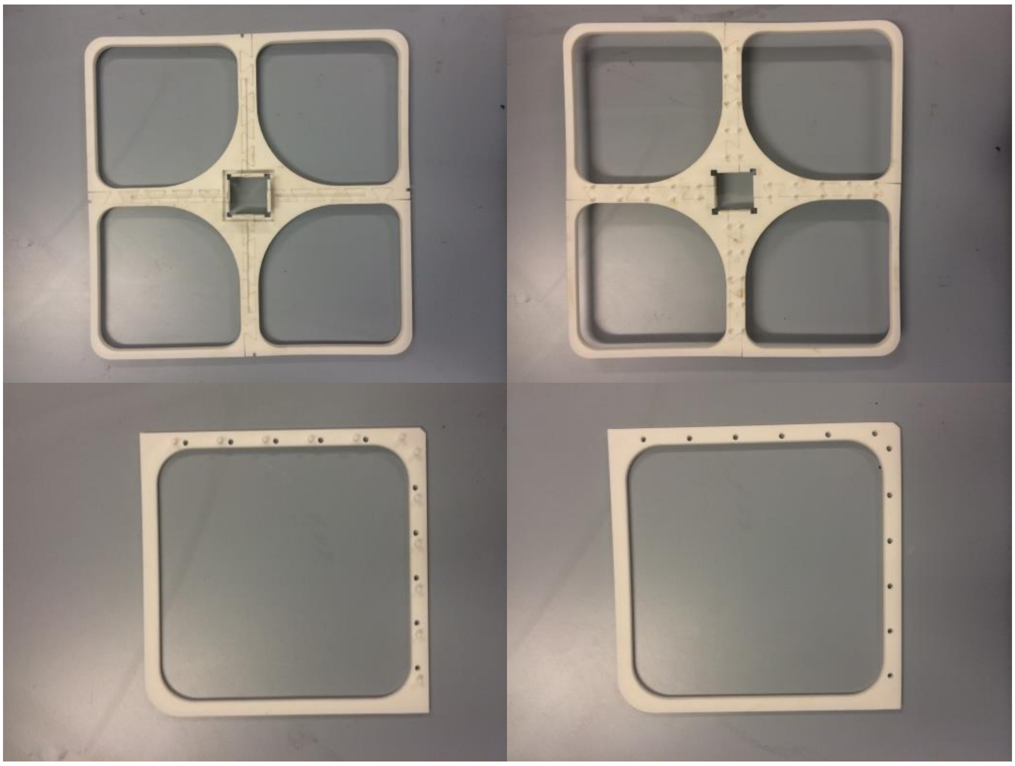

Figure 5-22: Printed Formers. Transmit coil former top-view (top-left), bottom-view (top-right), top-view of receive coil former part (bottom-left) and bottom-view (bottom-right).

5.3.4 Number of Turns

The 3D formers were used to perform a secondary resonance study to determine the optimum number of turns for the transmit and receive coil. As discussed earlier, 0.5 mm enamelled wire was chosen for the transmit coil due to primarily its current rating. The resonance was tested for 50, 60 and 70 turns, Figure 5-23. From the impedance measurements it was deemed that 60 turns was an appropriate number of turns for the transmit coil as the coil resonated at 165 kHz.

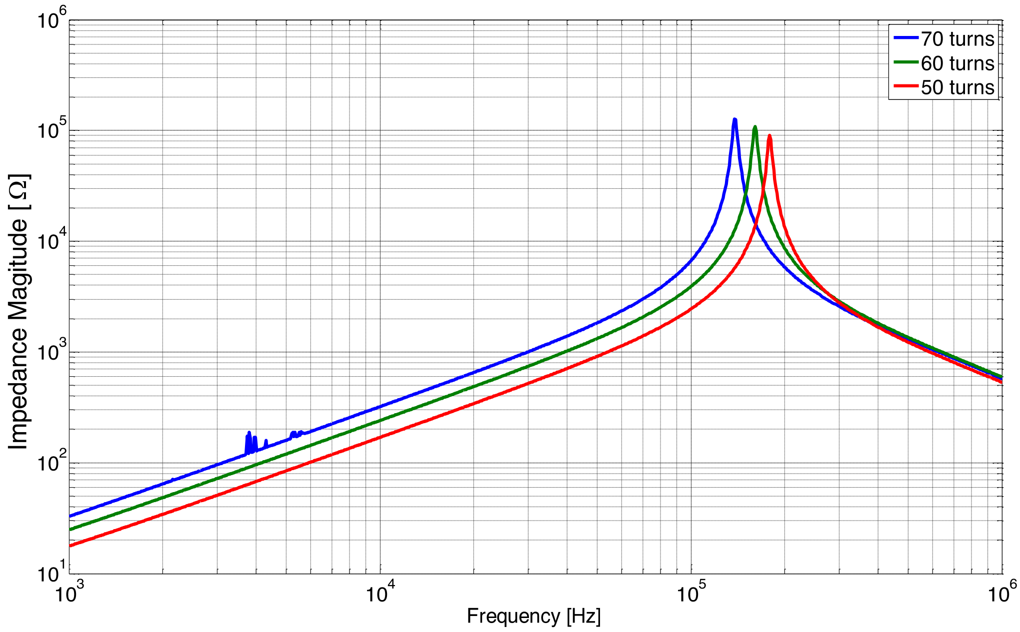

Figure 5-23: Impedance coil measurement using 0.5 mm enamelled wire and the 3D printed former for 50, 60 and 70 turns.

For the receive coil a more extensive study was performed as the earlier study in section 5.3.2, did not involve any receive coil measurements. To create the figure-of-eight arrangement, two square sections, Figure 5-21 (c) or (d), were wound in opposite arrangement and joined. 0.125mm enamelled wire was considered the likely candidate for the receive coil due to its weight. 0.25 mm and 0.2 mm wires were also considered, however were discarded due to the added weight of their increased diameter and more importantly their limited reel length. Figure 5-24 displays the impedance measurement performed to determine the ideal number of turns. Based on the measurements, it was decided that 120 turns would be an appropriate number as the coil resonated at 160 kHz.

During the winding of the receive coils using the 0.125 mm wire, some difficulty was faced due to the fragile nature of the thin wire; the wire snapped repeatedly while winding.

As a result a 0.16 mm wire was used instead for the final receive coils. The 0.16 mm wire was only marginally thicker minimising the increased weight; however, proved to be much more robust when winding the coil and rarely snapped. Final resonance measurement of the 120 turn 0.16 mm wire receive coil was performed and was found to be 195 kHz, Figure 5-25.

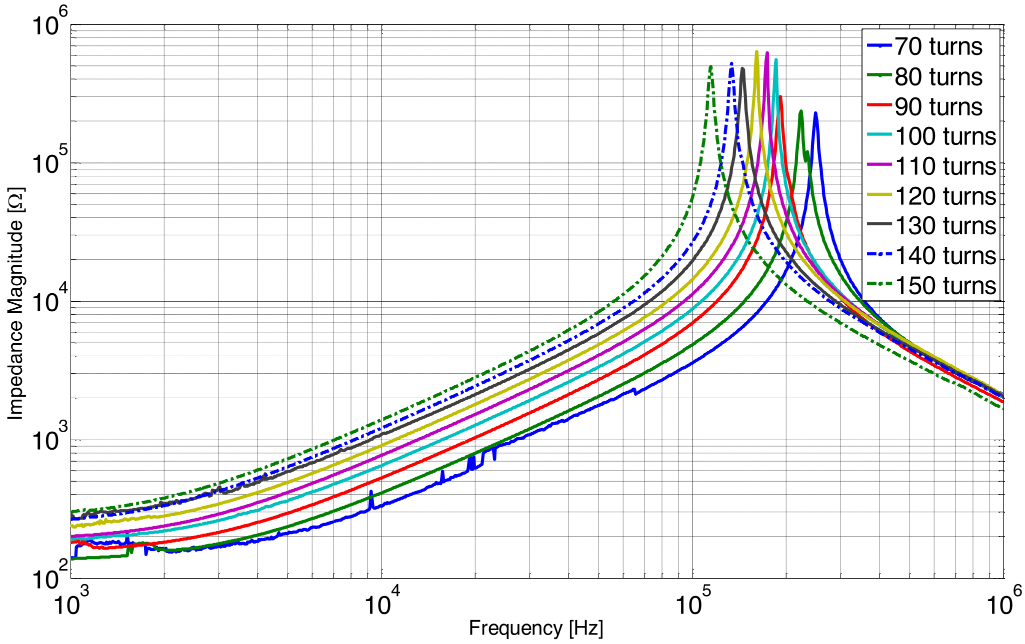

Figure 5-24: Impedance measurement for the figure-of-eight receive coil using 0.125 mm enamelled wire.

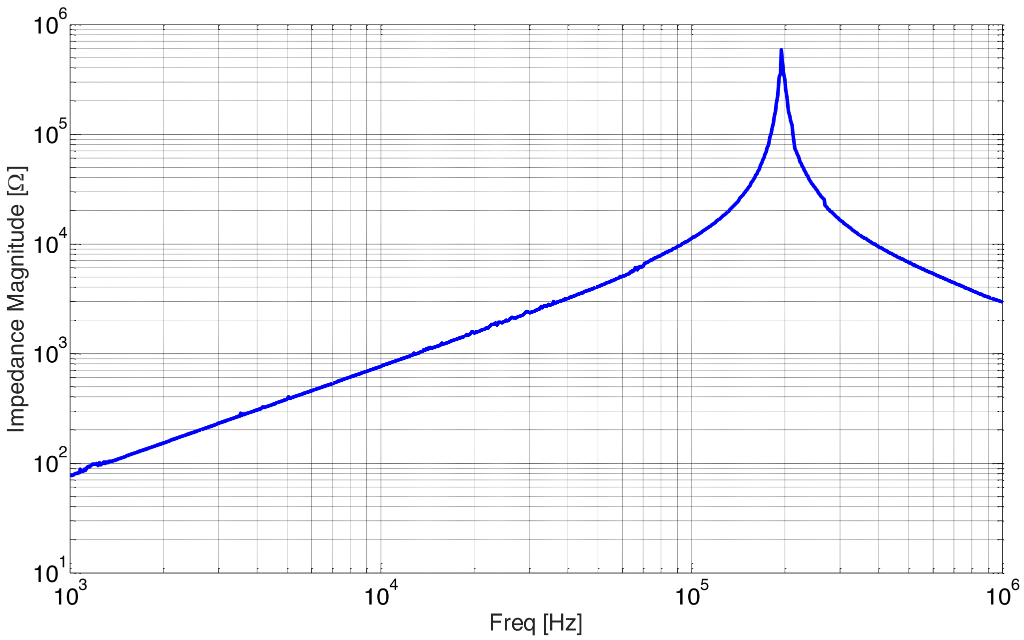

Figure 5-25: Impedance measurement of final receive coil, constructed of 120 turn using 0.16mm wire.

5.3.5 Final Coil Assembly

Once the number of turns and wire choice was made the full coil array was wound and assembled. The complete coil array was assembled and attached together using the location pegs, the wires were then soldered to the connection board and the GRP stem was attached, Figure 5-26.

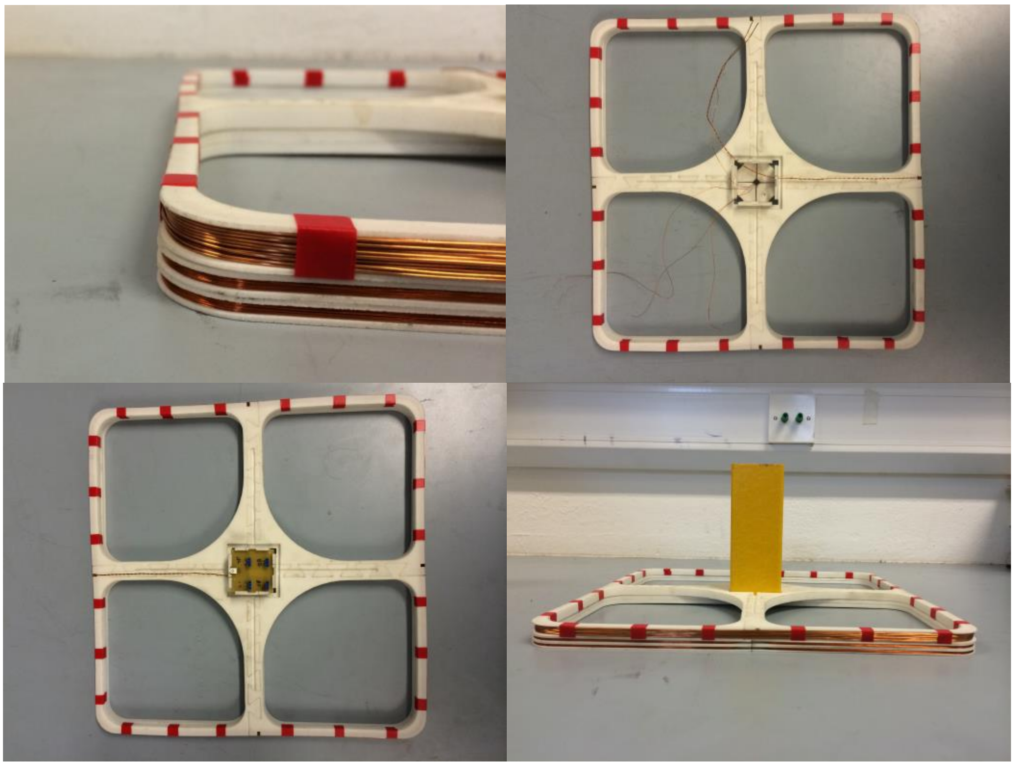

Figure 5-26: Fully assembled coil array side view (top-left), top view without connection board (top-right), with connection board (bottom-left) and a side view of the array with the GRP stem attached (bottom-right)

The fully constructed coil array underwent a final set of resonance measurements to determine the full array characteristics. The measurements were performed to understand how the coils behave in the presence of the remaining coils and involved individual coil self-impedance measurements with the remaining coils in open circuit and loaded.

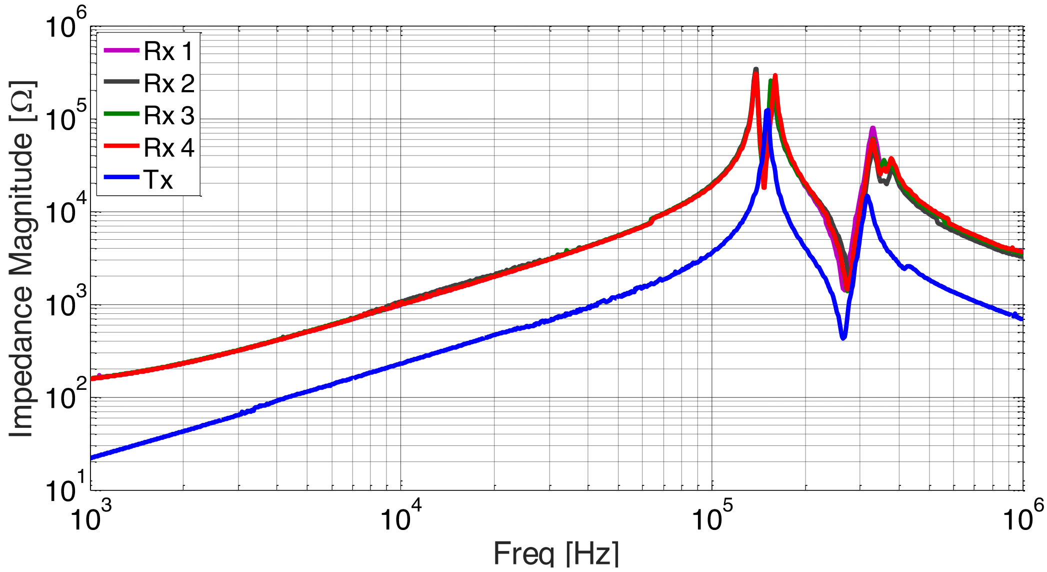

Figure 5-27: Impedance measurement of full coil array with remaining coils in open circuit.

The first set measurements performed was simply the measurement of the coil resonances with all the remaining coils in open circuit, Figure 5-27. This measurement revealed significant coupling and interaction between the receive coils. The interaction has resulted in a double resonance for the receive coils; one at a significantly lower frequency, 140 kHz, and the second at 160 kHz. The receive coils displayed near identical resonances indicating that the proximity to the transmit coil did not have a strong influence on the resonance and that the majority of cross-coupling occurred between the receive coils. This was also confirmed by the reduced effect of the receive coils on the transmit coil resonance. The transmit coil only experienced a drop in resonance frequency from 165 kHz to 152 kHz. However, the transmit impedance measurement has been clearly altered by the presence of the receive coils.

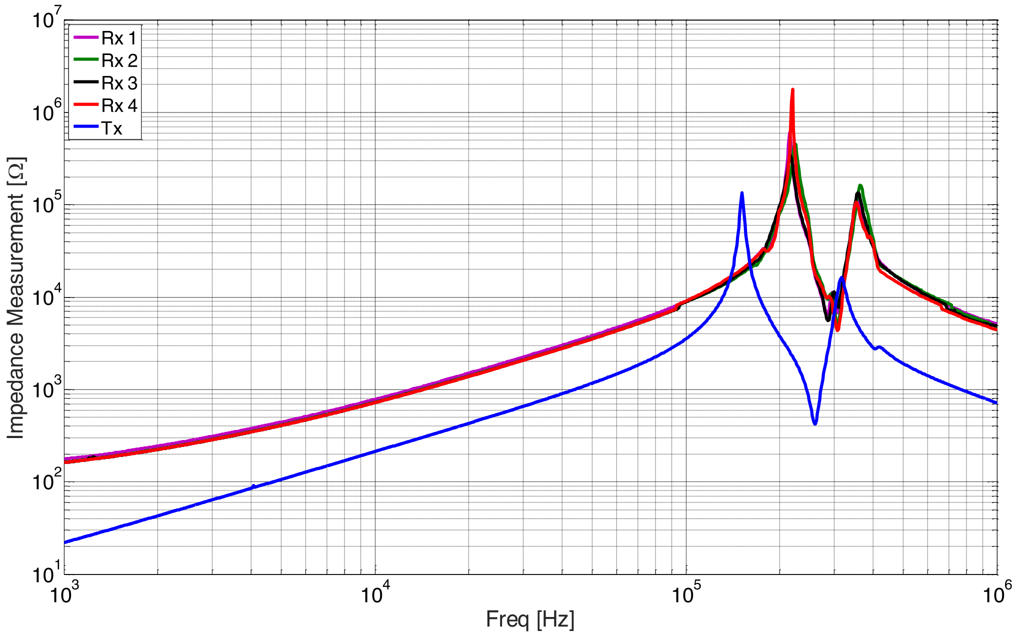

Figure 5-28: Impedance measurement of full coil array with loaded coils.

The impedance measurements in Figure 5-27 were repeated but with the remaining 4 coils loaded. To load the coils, the front-end amplification boards manufactured for the prototype system were connected to the coils and energised. Figure 5-28, reveals that the transmit coil resonance frequency remained at 152 kHz while the receive coil resonance increased to 220 kHz. The loading of the remaining coils appears to have dampened the coupling between the receive coils. This is indicated by the absence of the double resonance in Figure 5-27 and the increased resonance frequency for the receive coils. The resonance increase displayed in Figure 5-28 exceeds the stand alone receive coil resonance measurement of 195 kHz, Figure 5-25. This increase can be explained by the different lead lengths of the receive coils between the two measurements. The stand-alone impedance measurement in Figure 5-25 was performed with a longer lead length as pictured in Figure 5-29, whereas the measurements in Figure 5-28 were performed after the receive coils were attached to the connection board and consequently had shorter leads. To confirm this, the capacitance difference between the measurement scenarios was deduced from Figure 5-28 and Figure 5-27 and was found to be only 8.1 pF. Compared to a capacitance of 24.7pF for a twisted lead of 0.3m length, the lead length was considered as the likely cause for the 25 kHz increase in resonant frequency between the measurements.

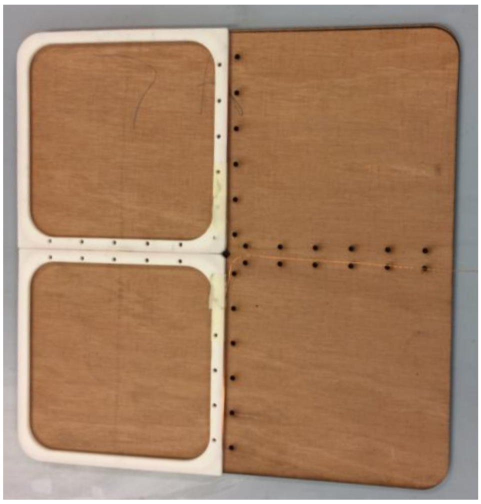

Figure 5-29: The coil former prior to installing the connection board.

These final measurements revealed a worrying aspect about the coil design. The cross-coupling between the receive coils resulted in a significant resonance change and indicated that measurements on receive coils are unlikely to be independent. This required further investigation to determine the extent of the coupling between the coils.

5.3.6 Mutual Impedance

To fully understand the interactions between the different coils, the trans-impedance between each coil combination was measured by applying a current across one coil and measuring the induced voltage across the other. The trans-impedance measurements were used to calculate mutual inductance, M_I, for each coil pair. The coil naming convention adopted in this section is indicated by the legend in Figure 5-30. The trans-impedance measurements were performed twice; once with the remaining coils in open circuit and repeated with the remaining coils loaded using the front-end amplification. The full set of trans-impedance measurements are displayed in Figure 5-31 to Figure 5-36.

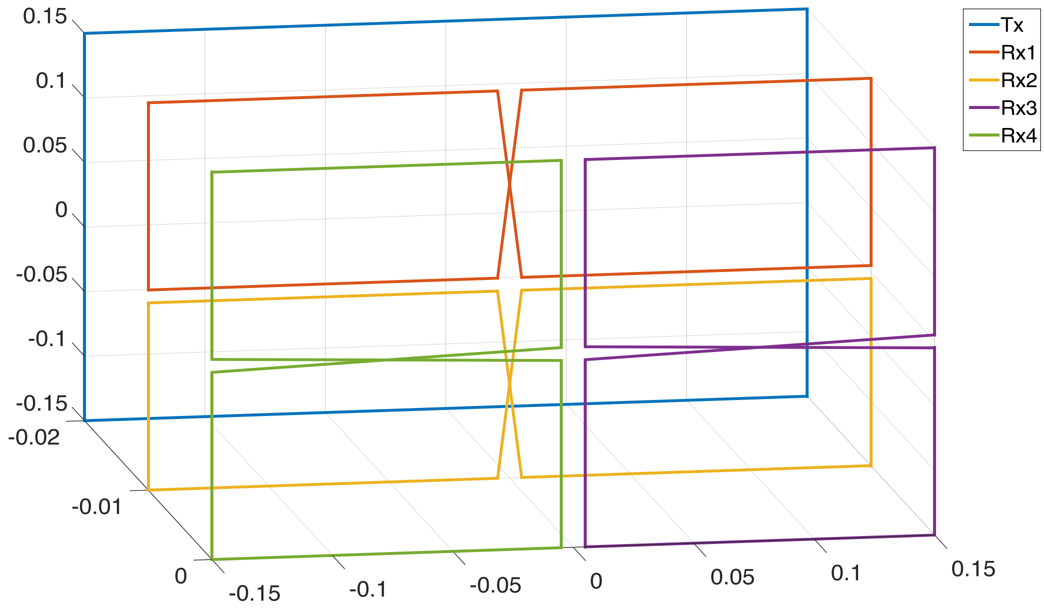

Figure 5-30: Naming of individual coils in final coil array.

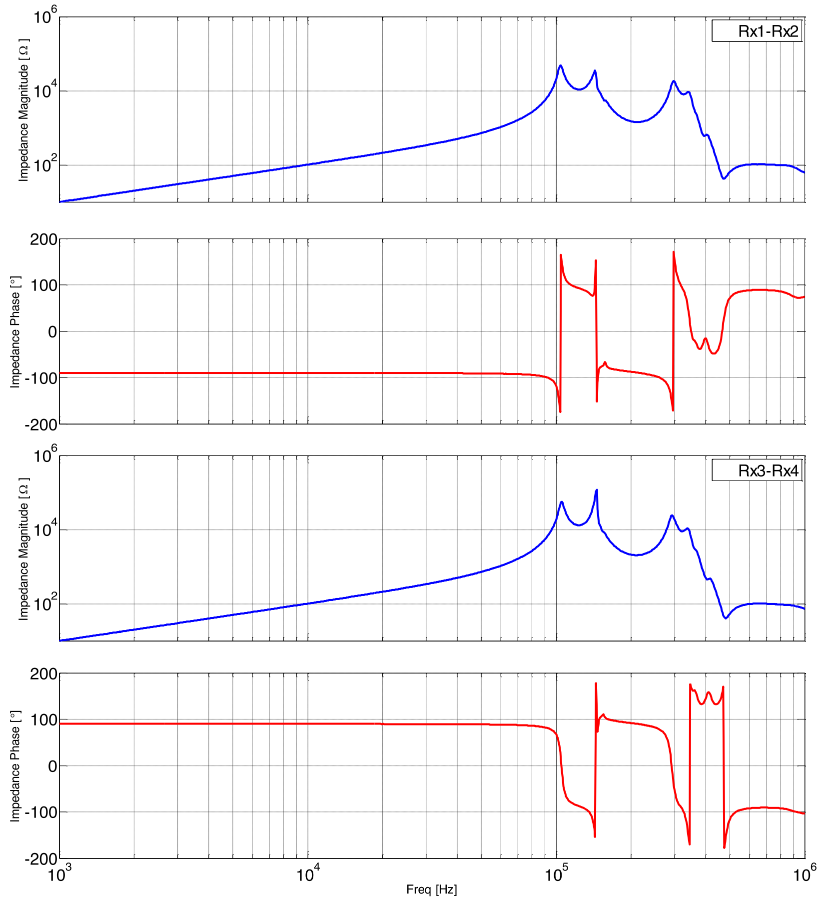

Figure 5-31: Adjacent receive coils trans-impedance with remaining coils unloaded.

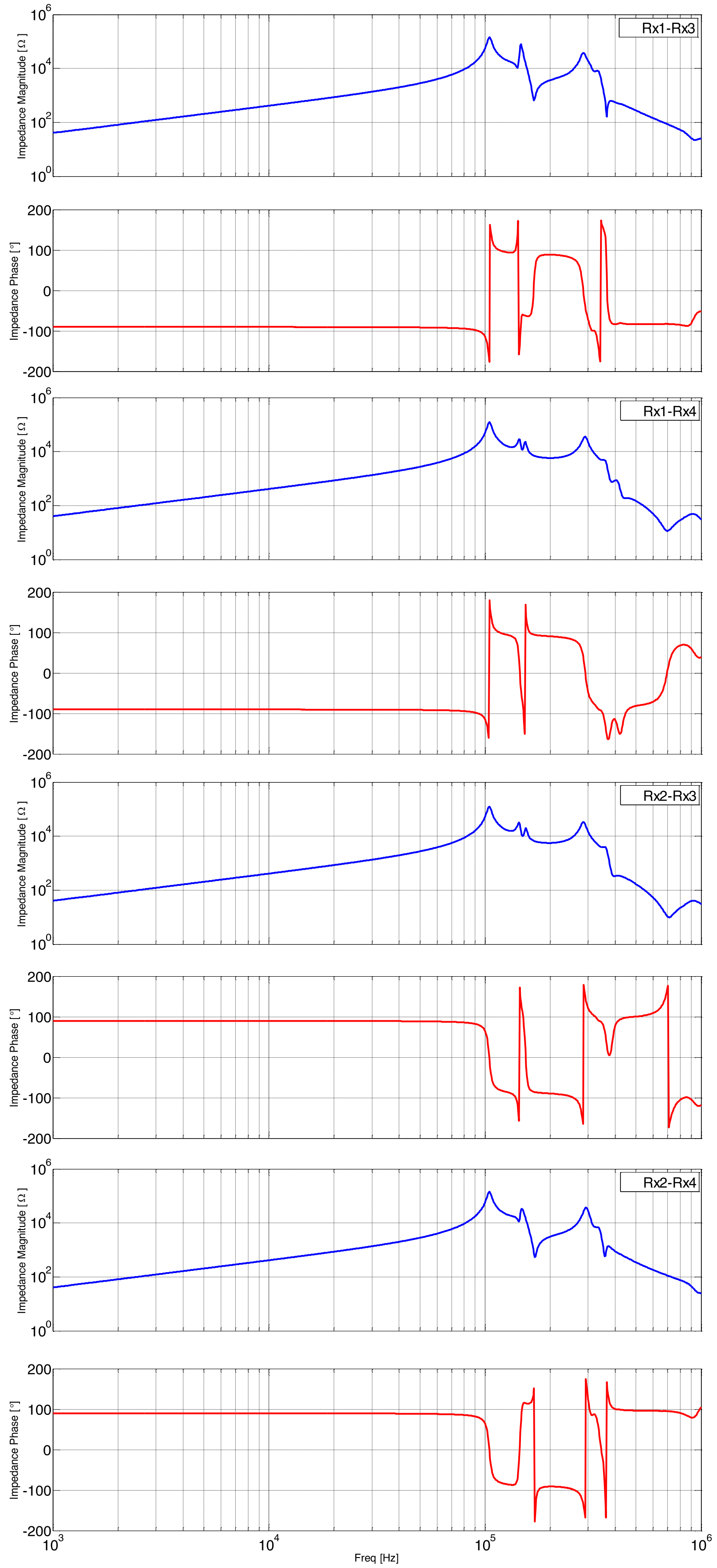

Figure 5-32: Trans-impedance between cross-layer receive coils with remaining coils unloaded.

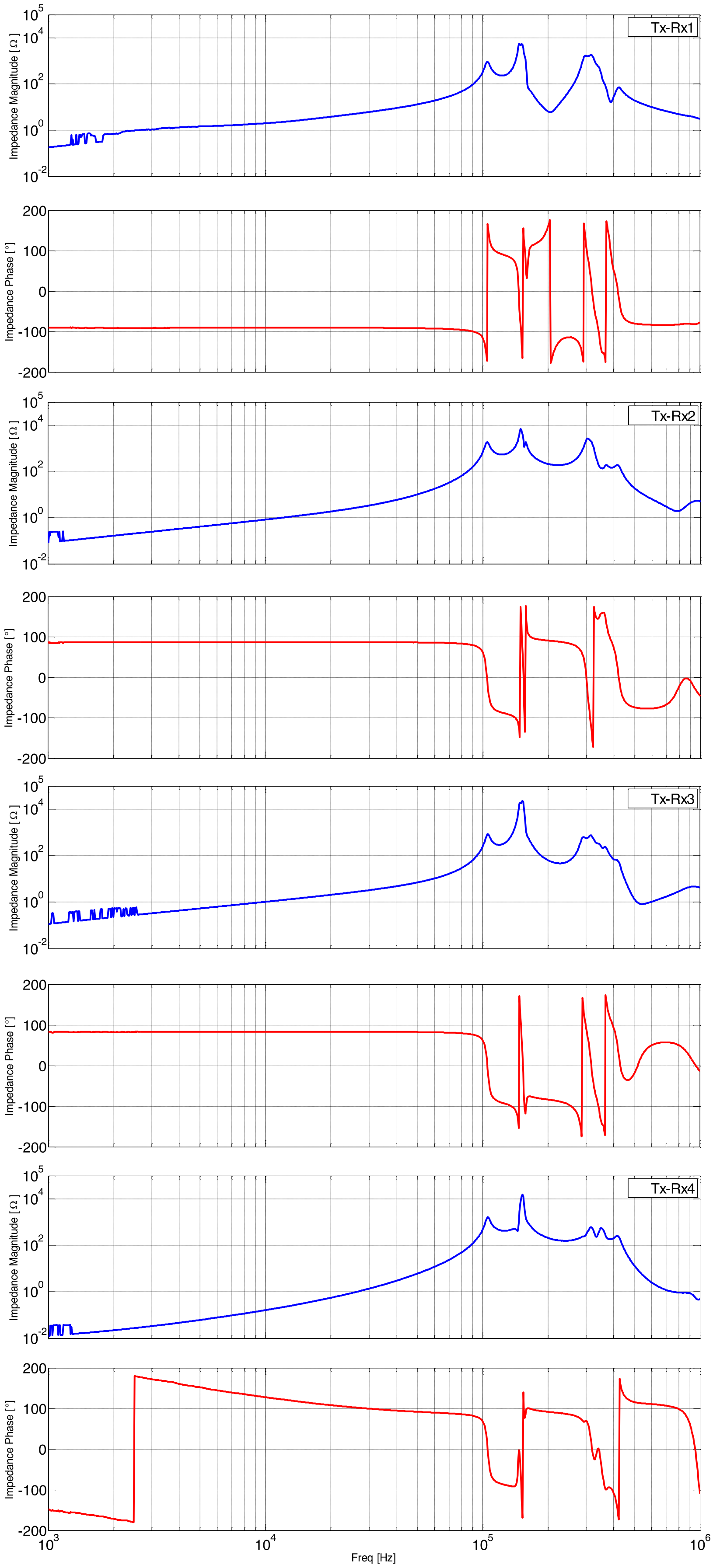

Figure 5-33: Transmit-Receive trans-impedance measurement with remaining coils unloaded.

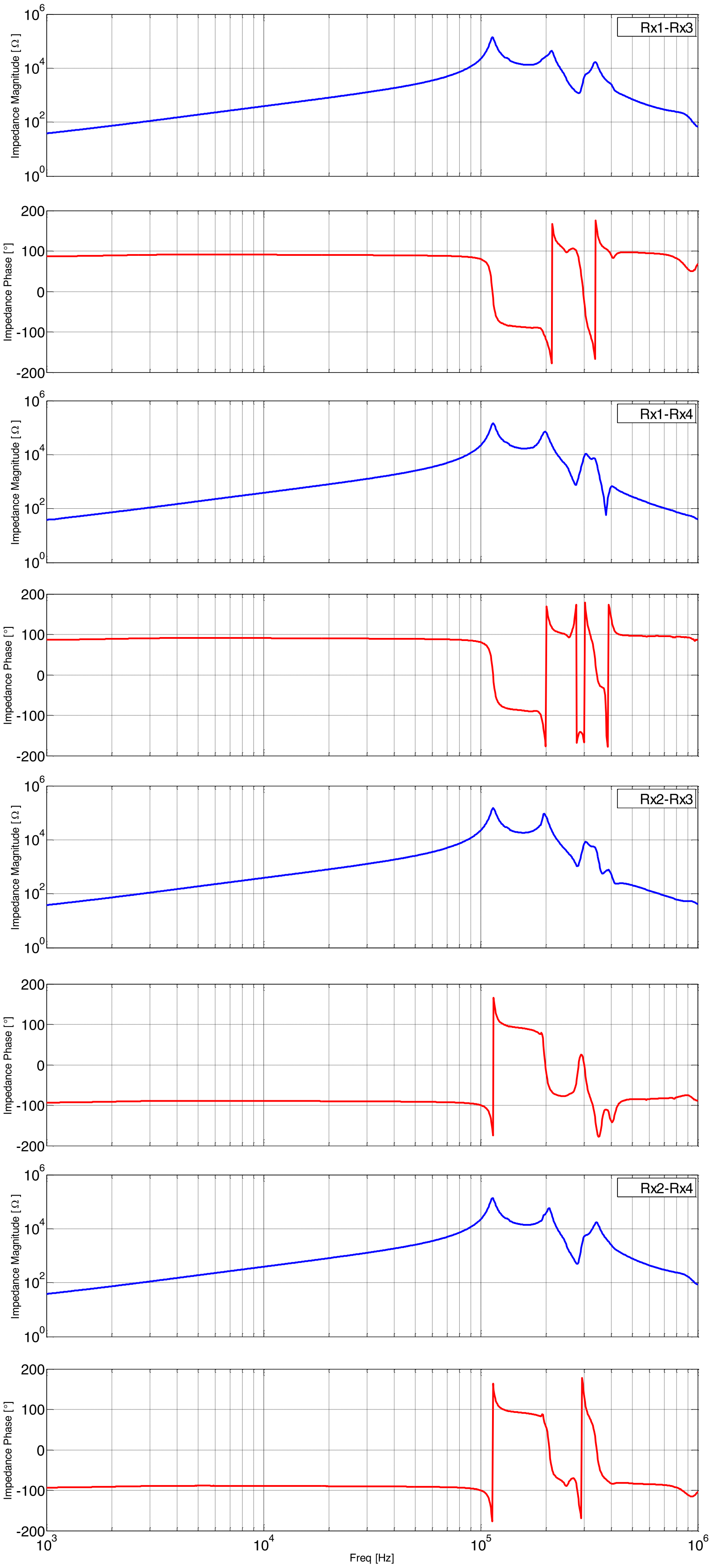

Figure 5-34: Trans-impedance between cross-layer receive coils with remaining coils loaded.

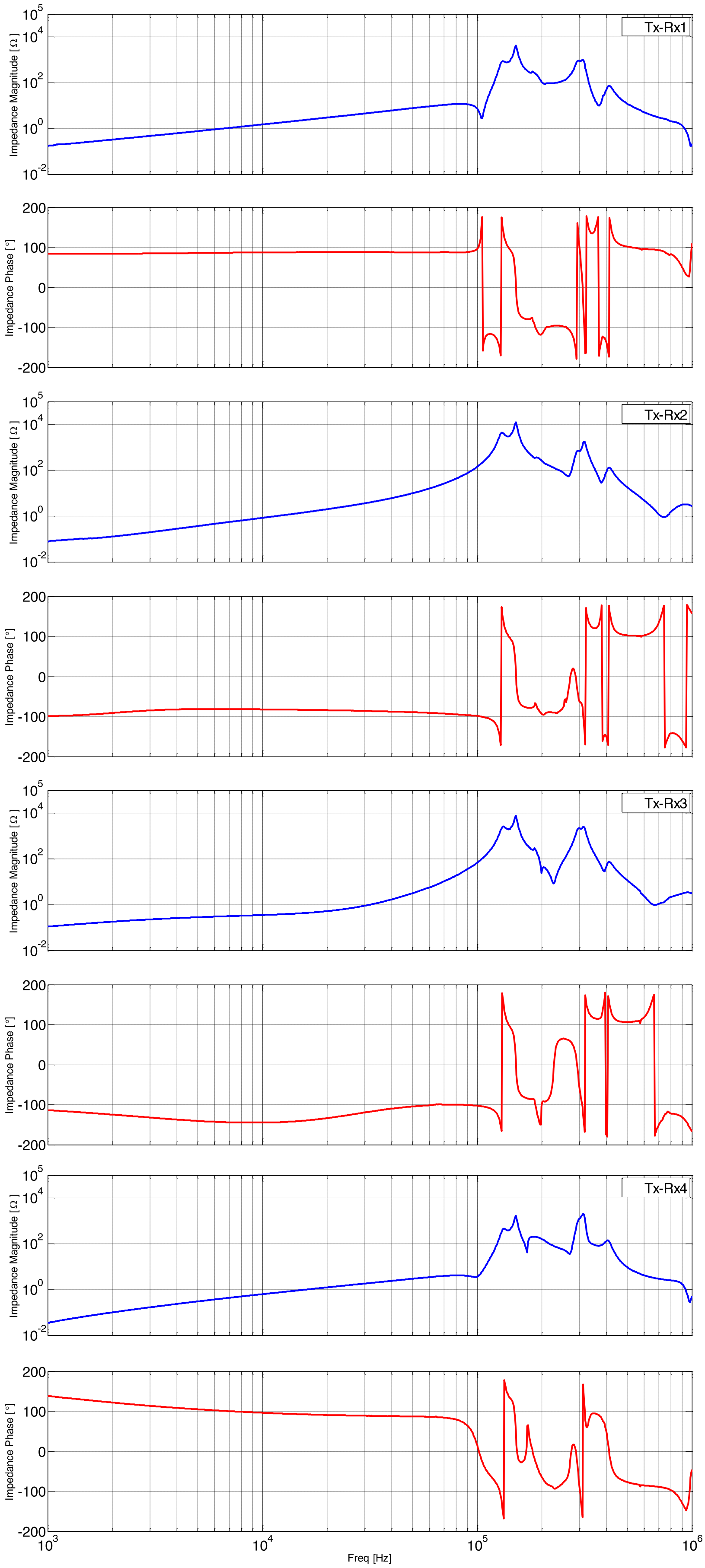

Figure 5-35: Transmit-Receive trans-impedance measurement with remaining coils loaded.

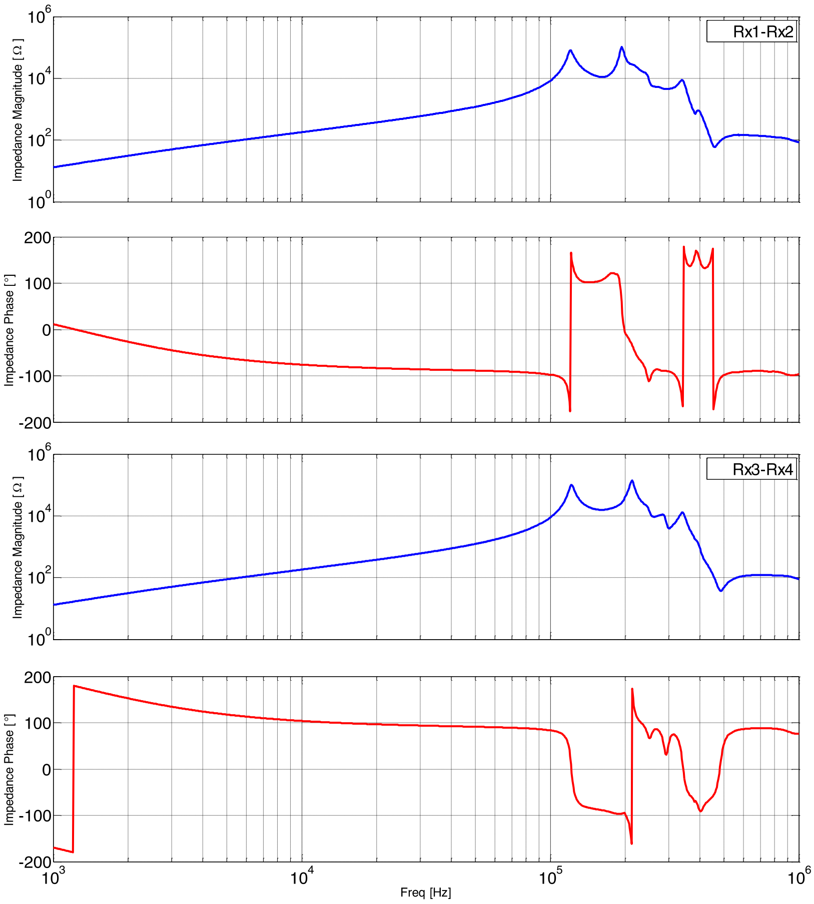

Figure 5-36: Adjacent receive coils trans-impedance with remaining coils loaded.

From these measurements, the mutual inductance, M_I, was calculated for each coil pair combination and is presented in Table 5-2.

Table 5-2: Mutual inductance between all coils.

Channel	Mutual Inductance-Open (H)	Mutual Inductance-Loaded (H)
Rx1-Rx2	1.71×10^{-3}	2.98×10^{-3}
Rx3-Rx4	1.71×10^{-3}	3.03×10^{-3}
Rx1-Rx3	7.04×10^{-3}	6.40×10^{-3}
Rx1-Rx4	6.93×10^{-3}	6.26×10^{-3}
Rx2-Rx3	6.84×10^{-3}	6.34×10^{-3}
Rx2-Rx4	6.96×10^{-3}	6.49×10^{-3}
Tx-Rx1	29.8×10^{-6}	23.7×10^{-6}
Tx-Rx2	13.5×10^{-6}	12.1×10^{-6}
Tx-Rx3	16.6×10^{-6}	16.8×10^{-6}
Tx-Rx4	1.75×10^{-6}	10.2×10^{-6}

The mutual inductance between the receive coils and the transmit coil indicates how well the receive coils were mechanically nulled with respect to the transmit. It is clear from the magnitudes that Rx4 is best nulled, Rx1 is the worst and Rx2 and Rx3 are similar. The loading of the coils has altered the mutual inductance values as represented in Table 5-2; however, the changes were not significant.

These mutual inductance values were used to create a circuit equivalent model for the entire coil array using LTSPICE. The modelling of this complex coil interaction was devised to help explain the uncharacteristic impedance measurements in Figure 5-27. The modelled circuit is represented in, Figure 5-37 and was modelled to have coupling factors between the individual coils based on the inductance values in Table 5-2. The coupling factors are displayed as at the top of the figure using the LTSPICE narrative. The transmit coill inductance, capacitance and resistance were inferred using Figure 5-23. The inductance was deduced by calculating the gradient of the inductive region. The capacitance was deduced using the resonance equation, equation (5-3), and the parallel resistance was the value of the resonance impedance. The values for the receive coils were obtained using Figure 5-25.

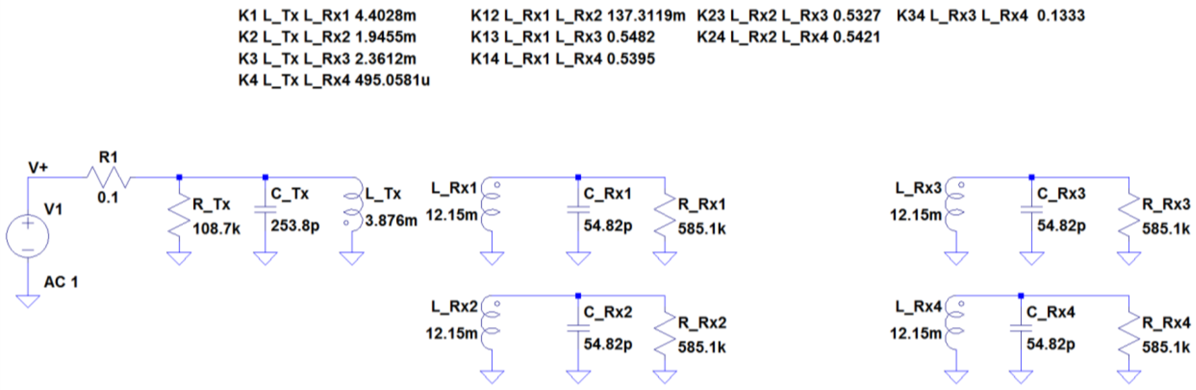

Figure 5-37: LTSPICE model of full coil array and associated mutual coupling.

The simulated impedance measurements are plotted against the real measurements from Figure 5-27 in Figure 5-38 and Figure 5-39.

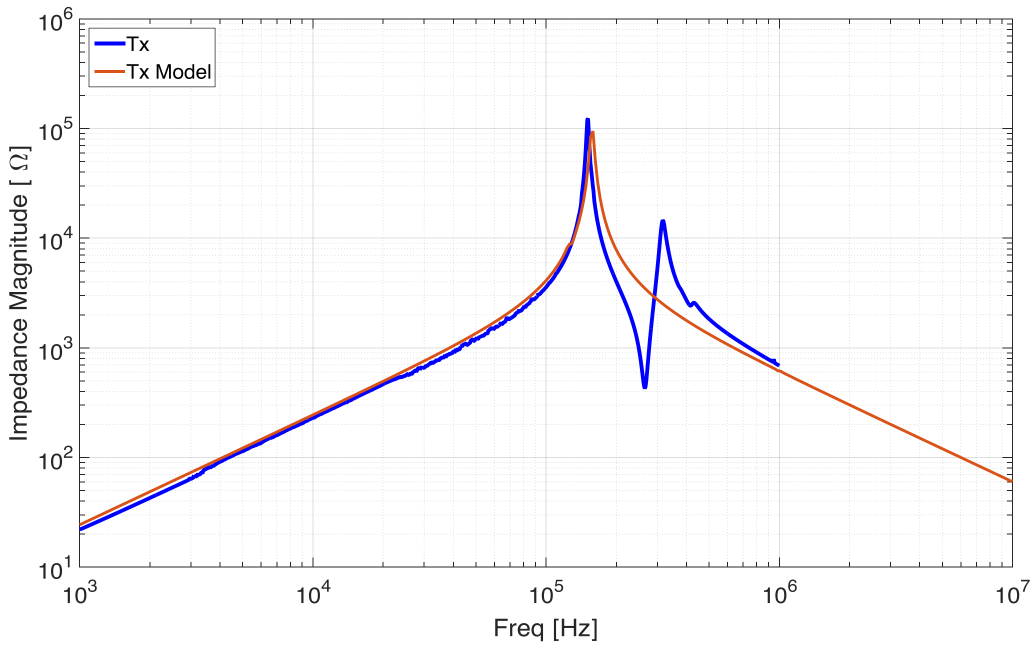

Figure 5-38: Impedance measurement of real and LTSPICE simulated transmit coil.

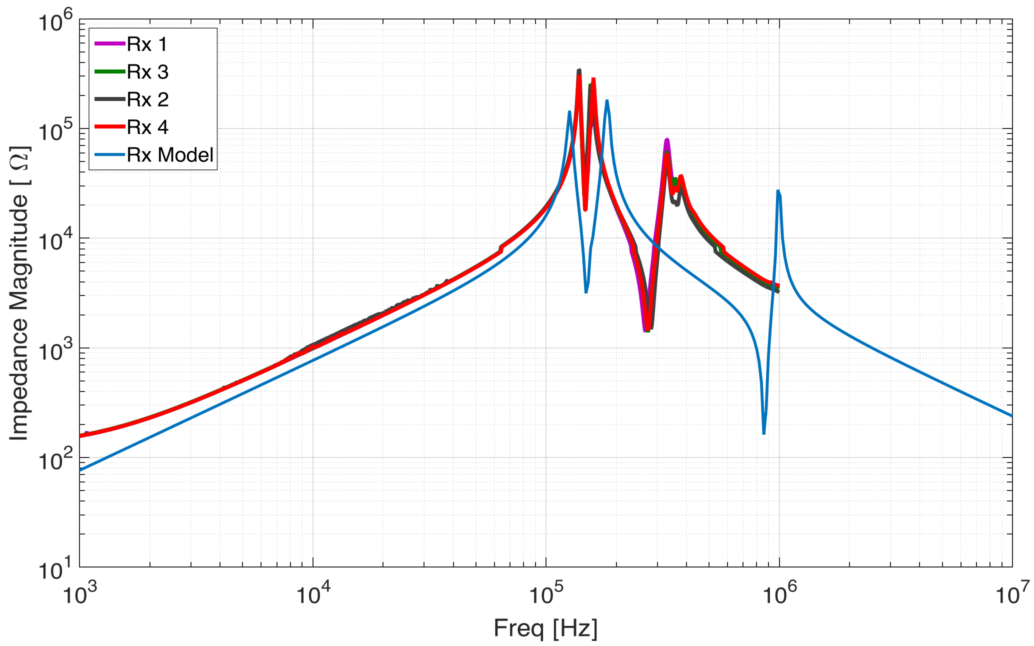

Figure 5-39: Impedance measurement of real and LTSPICE simulated receive coils.

The simulation confirmed that the mutual inductance between the coils was one cause of the abnormal impedance response and that the mutual inductance between the receive coils had significant impact on the receive coil resonance. This raised concern about the functionality of the coil as coupling between receive coils is an undesired effect. The inversion study assumed that coil measurements are independent of one another and thus the presence of significant coupling does affect the invert-ability results of the coil. This finding was overlooked during the design and selection of the coil design and prompted a re-design of the coil. This coil re-design occurred outside the scope of this thesis and is summarised in chapter 6.

5.3.7 Potting and Screening

The fully assembled coil array was then encapsulated in an epoxy resin to ensure the coils are protected and held secure with respect to one another. A mould was created to undergo the encapsulation process by first creating a positive mould pictured in Figure 5-40 (a) and consequently creating the potting mould Figure 5-40 (b). The mould was used to encapsulate the fully assembled coil with the central glass reinforced plastic (GRP) stem and bracing pieces attached. The final potted coil is pictured in Figure 5-41.

(a) (b)

Figure 5-40: (a) positive mould used to create the final potting mould (b).

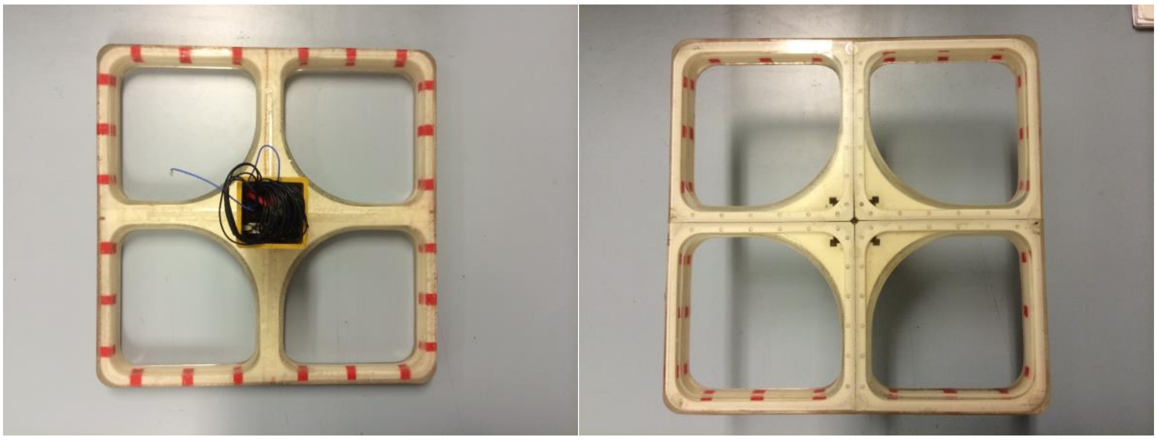

(a) (b)

Figure 5-41: Final potted coil (a) top view (b) bottom view.

The potted coil array was then screened using graphite paint to reduce the capacitive coupling of the coil with the ground and near-by surfaces. The screening was purposefully discontinued at the corners to ensure the graphite paint did not become a continuous medium through which significant eddy currents can circulate, Figure 5-42.

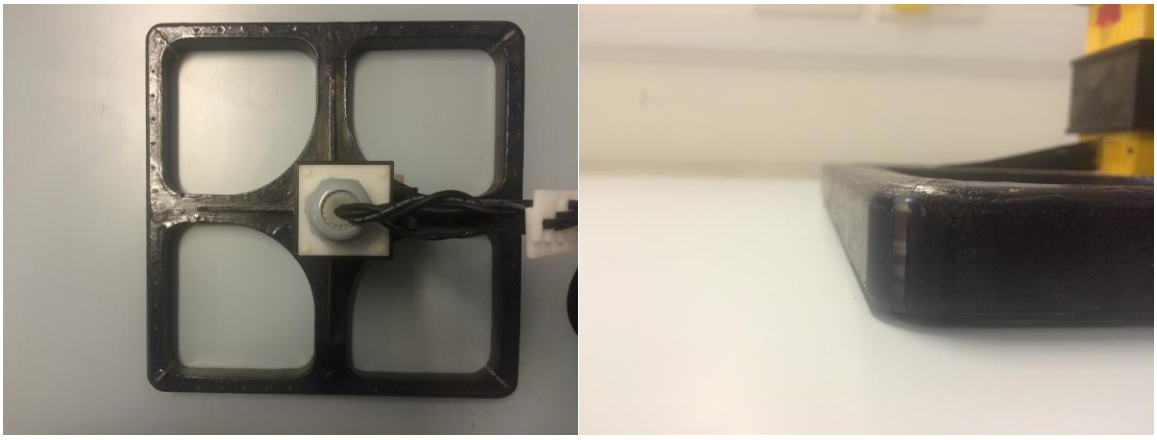

Figure 5-42: Coil array screened using graphite paint (left). The paint was discontinued at the corners to ensure minimal eddy currents did not excessively circulate through the paint (right).

5.4 Signal Analysis

At this stage of the research the necessary information to predict the expected signal levels measured by the final detector was available. The tensors of the mines measured in chapter 4 and the calculated coil fields can be used to determine the expected signal from the most challenging mines. The tensors for the Type-72A and PMA-2 landmines were used as they were considered to be the most challenging weapons; based on their small tensor magnitude and confirmed by operational individuals from the humanitarian demining community. The instrumentation noise floor can also be calculated as the amplification circuit and acquisition system had been designed at this stage separate to the research described in this thesis. This section calculated the expected SNR performance of the detector using the proposed sensor head by calculating the expected signal and noise levels, concluding with the calculation of the maximum depth the detector is capable of performing a reliable inversion.

5.4.1 Signal Calculation

The mines were simulated at buried depths of between 5 mm and 250 mm as this represented the expected depth range. Figure 5-43 and Figure 5-44 display the expected voltage levels on one receive coil from the landmines at 50 mm and 150 mm if the transmit coil current was simulated to be 300 mA and the excitation frequency to be 12 kHz. Please note the colour bar scales vary between the different plots.

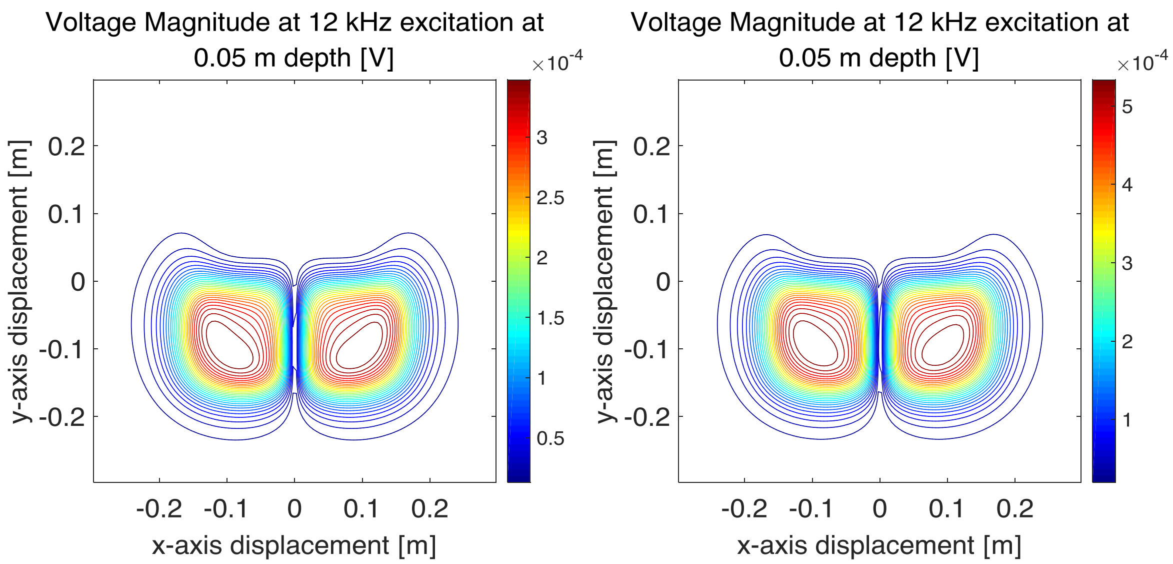

(a) (b)

Figure 5-43: Voltage levels of one receive coil at with mines simulated at 50 mmm depth for the (a) Type-72 and (b) PMA-2.

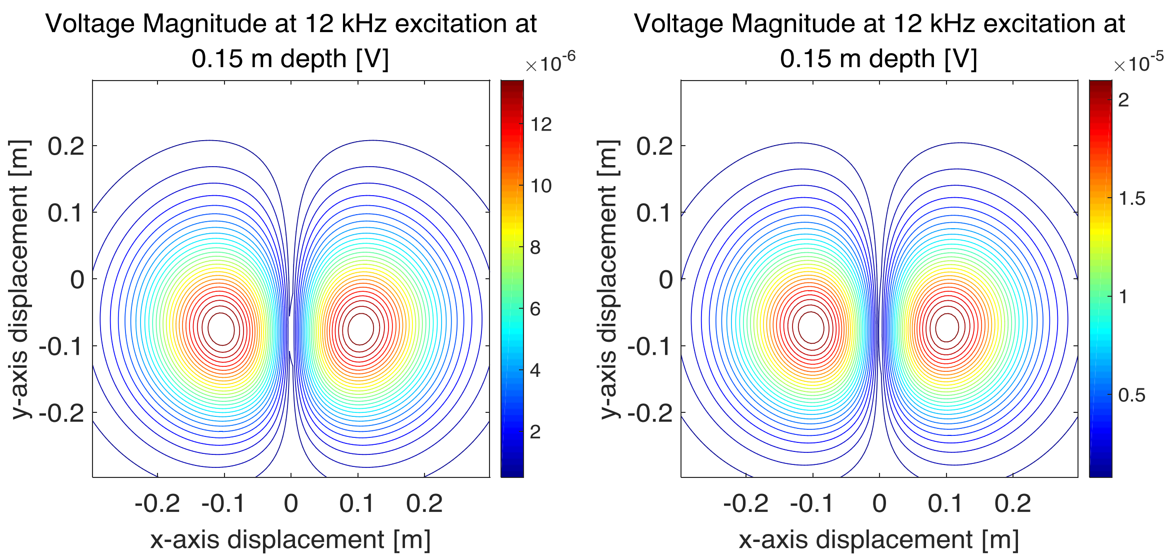

(a) (b)

Figure 5-44: Voltage levels of one receive coil at 150 mm depth for the (a) Type-72 and (b) PMA-2.

Whilst the figures above display the voltage variation over a scanned area, they do little to help predict the SNR performance of the detector. In order to achieve an SNR evaluation, the RMS value of depth layers between 5 mm and 250 mm were calculated to obtain a predicted signal levels for comparison with the expected system noise level. This RMS approach for SNR evaluation was adopted earlier in the invert-ability analysis when reporting SNR levels in section 5.2.

Figure 5-45 represents the RMS signals on the detector as the landmine depths increase. The plots display expected proportionality between the increase in frequency and signal level, equation (3-16). The voltage levels represented in Figure 5-45 assume that each frequency is excited with 300 mA. This is an unrealisable simulation due to the increased difficulty to drive high currents at high frequencies and the limited total current the wires are rated to. A more realistic excitation current has component magnitudes that decay as the frequency increases with an overall excitation current of 300mA. With these considerations in place the voltage simulation was re-run to produce signal values presented in Figure 5-46.

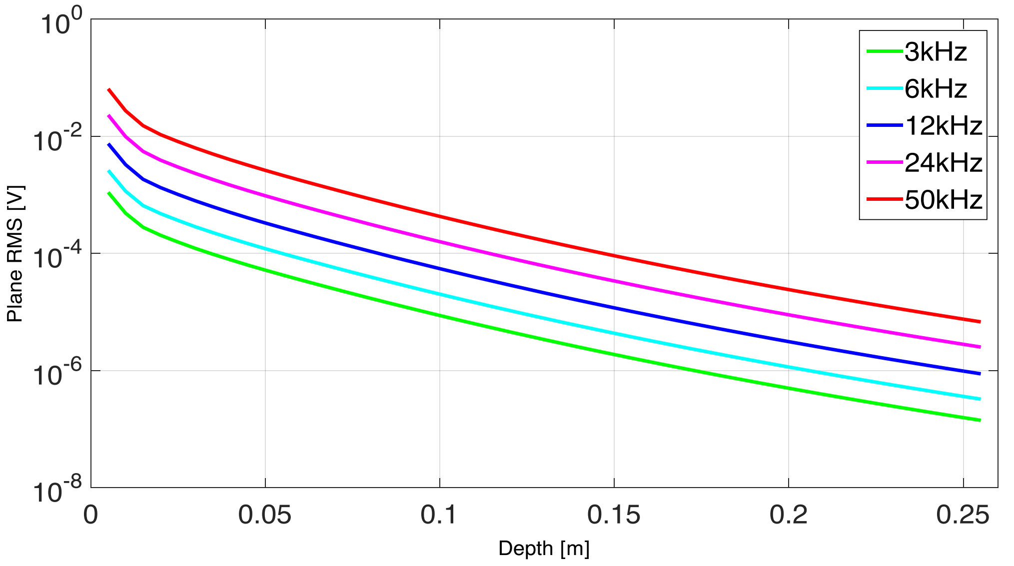

(a)

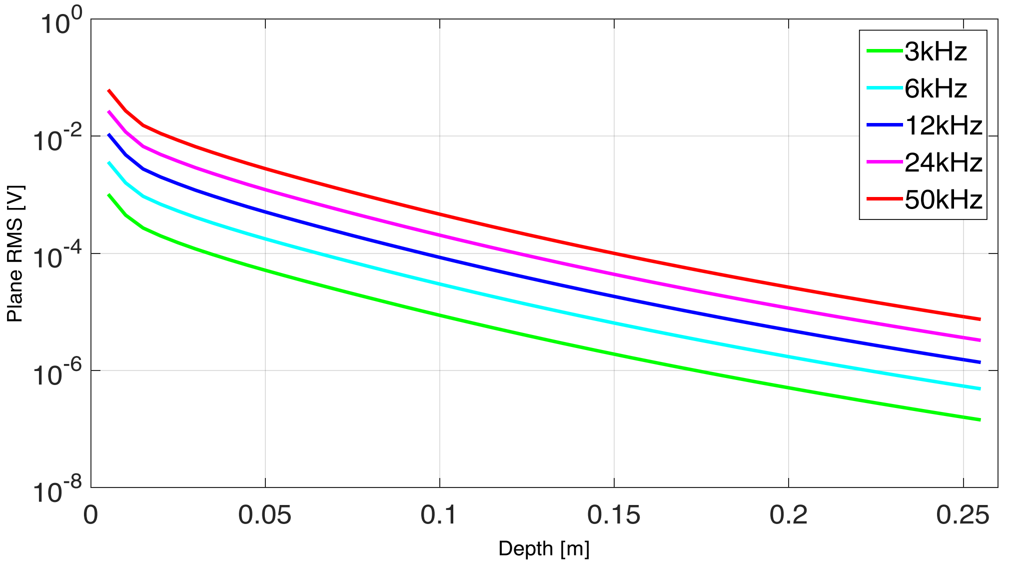

(b)

Figure 5-45: Expected signal levels from (a) Type-72 A and (b) PMA-2 mines for all excitation frequencies with varying depth.

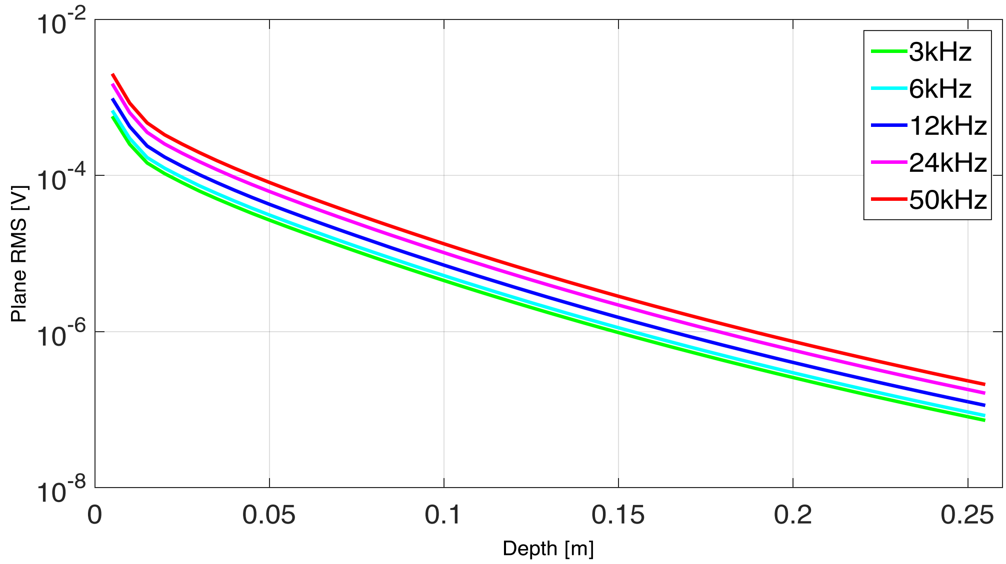

(a)

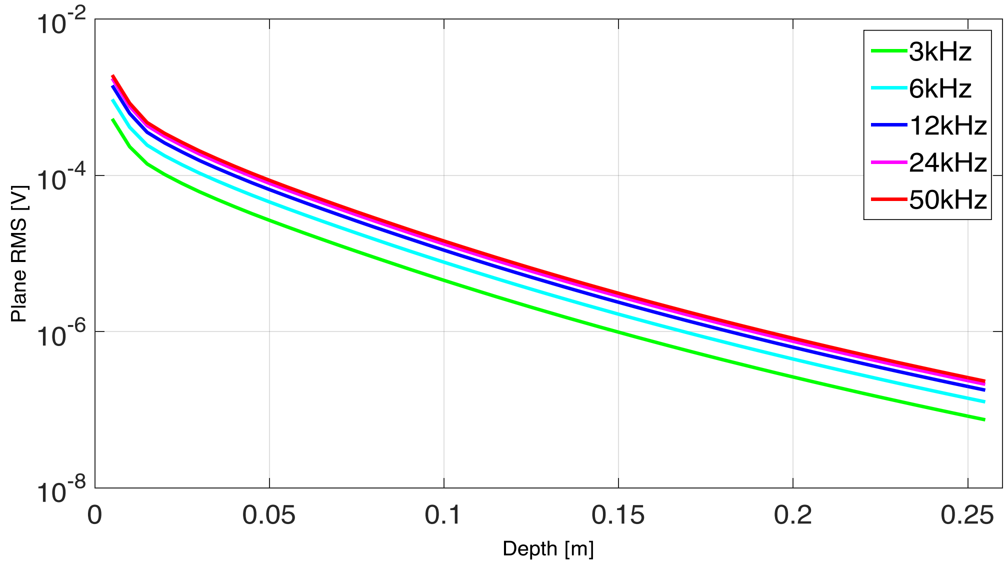

(a)

Figure 5-46: Expected signal levels from (a) Type-72 A and (b) PMA-2 mines for all excitation frequencies with varying depth. Excitation current amended to be inversely proportional to frequency and total excitation current to be no more than 300mA.

To validate these voltage calculations, calculated values were compared to measurements performed using the constructed coil array. The constructed coil was combined with front-end amplification designed and constructed by Dr. Liam Marsh and a data acquistion system, which is named here as a Multi-Frequency Impedance Analyser (MFIA). The MFIA system was designed and manufactured by Organised Technologies Ltd (OTL) to perform the analogue-to-digital (ADC) conversion, demodulate the receive signal and store the data for further processing offline. These components were designed and manufactured to achieve a portable prototype and were produced during the production of this thesis. A summary of these developments is included in chapter 6.

A suite of steel ball bearings were used to perform the validation, Figure 5-47. The ball bearings were made of 100Cr6 steel and were of the following radii; 1.99, 2.36, 2.99, 3.165, 4.36, 5.545, 5.945, 8.725 mm. The steel ball bearings were considered an appropriate validation set as their tensors can be calculated for voltage simulation using equation (4-3) and their use mirrored the study performed in [23] and described in section 2.5.4. The ball bearings were placed individually at the most sensitive location of the coil, Figure 5-48, and their distance from the coil was gradually increased while recording the measured voltage at regular intervals.

Figure 5-47: Ball bearings used comparison between measured and calculated voltage.

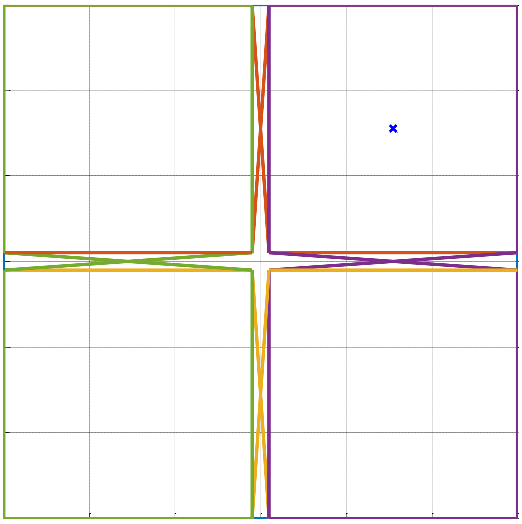

Figure 5-48: The most sensitive point along the plane of the coil.

Figure 5-49, displays the outcome of the comparison. The MFIA system presents the measurements in impedance values and so the calculated voltages were divided by the current to compare like for like values. A scaling factor of 3.14 was required to obtain the agreement displayed which was deemed to be a result of the processing carried out on the MFIA system. Overall, the plot displays good agreement between the measured and calculated; however, at distances close to the coil, the values appear to drift farther apart. This is likely to be due to the breakdown of the tensor approximation at close distances, section 3.4. The comparison confirmed that voltages calculated using tensor values are representative of expected measured values and can be used as indicative values for instrument performance studies. Thus, estimated signal levels presented in Figure 5-46 can be compared to noise levels in order to determine expected SNR performance.

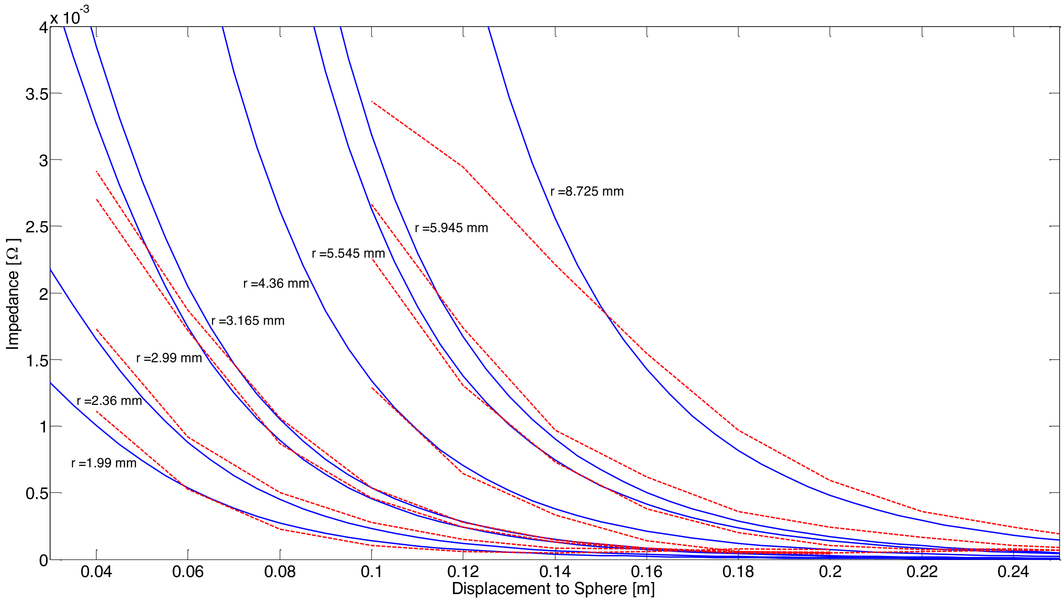

Figure 5-49: Comparison of simulated and measured steel ball bearing impedance magnitudes of increasing sizes. Simulated values are presented in blue and measured are presented in red-dashed.

5.4.2 Noise Calculation

The noise budget calculated in this section is based on the electronic components mentioned earlier in section 5.4.1; front-end amplification and the MFIA system. The calculation does not include the potential noise induced on the receive coils directly. It also does not include noise introduced by mutual coupling which has been discussed earlier in section 5.3.6. Consequently the total noise is likely to be larger than the noise level reported here which is a theoretical minimum as it is composed of instrumentation noise only.

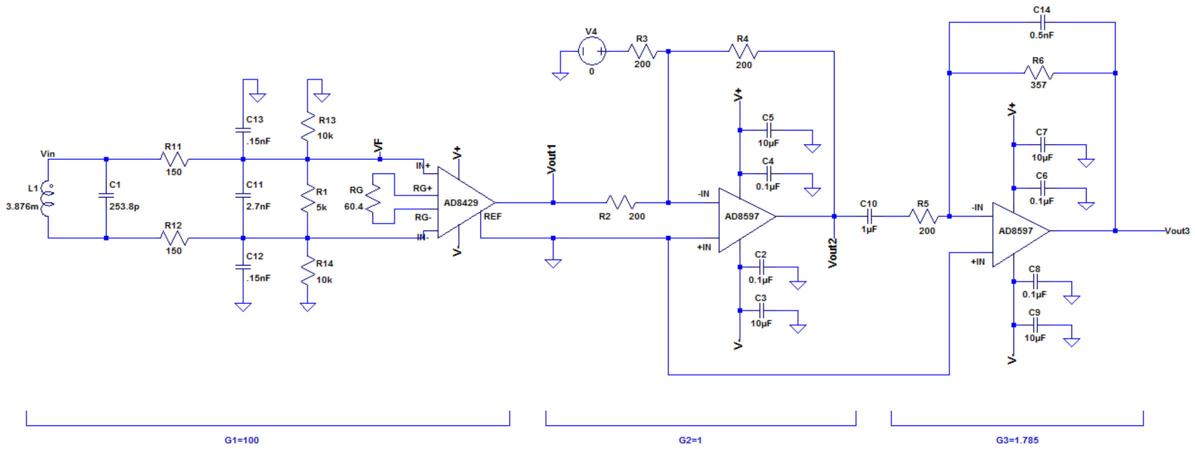

Figure 5-50: Front-end amplification schematic

The front-end amplification circuit is composed of three stages with gains of 100, 1 and 1.785, Figure 5-50. The amplifier chain also acts as a band pass filter limiting the noise introduced to the system. The large first stage gain resulted in the associated noise to be dominant in comparison to the contribution from the second and third stages and as a result, only the noise from the first stage amplification is calculated to determine the total amplification noise, Figure 5-51.

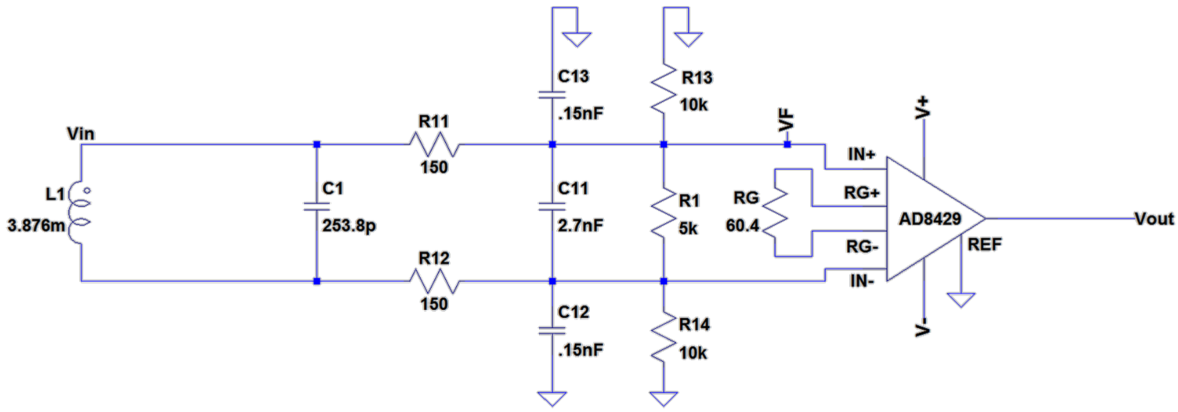

Figure 5-51: First stage of front-end amplification of receive signal

The noise model for operational amplifiers can be represented as follows [76]:

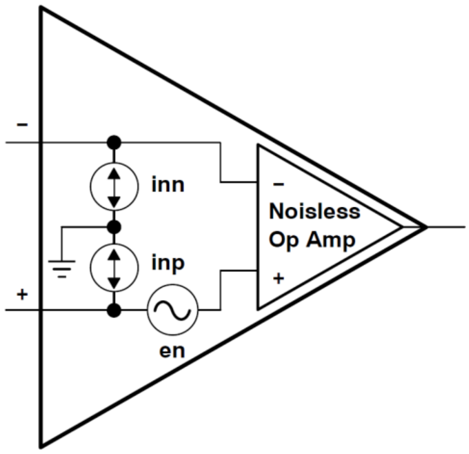

Figure 5-52: Operational amplifier noise model as represented by Texas Instruments in [76].

The operational amplifier noise can be broken down to a voltage noise source, **en**, and current noise source for the inverting and non-inverting terminals, **inn** and **inp** respectively. The datasheet for the AD8429 amplifier, used for first stage amplification, provides equation (5-4) to calculate the total voltage noise.

$$Voltage\ Noise = \sqrt{\left(\frac{en_{out}}{G}\right)^2 + (en_{in})^2 + (en_{RG})^2}\ (\mathrm{V}) \qquad (5\text{-}4)$$

where en_{out} is the output voltage noise, en_{in} is the input voltage noise, G is the gain of the amplifier and en_{RG} is the thermal noise of the gain resistor. Note that the noise calculations in this section refer to the noise with respect to the amplifier input (RTI). The gain resistor used was 60.4 Ω as displayed in Figure 5-50, resulting in a gain of 100.3 as per the datasheet. The datasheet states the output voltage noise to be $45\ \mathrm{nV}/\sqrt{\mathrm{Hz}}$ and the input noise $1\ \mathrm{nV}/\sqrt{\mathrm{Hz}}$ at a gain of 100. Thus the amplifier voltage noise density with respect to the amplifier input can be described as:

$$Voltage\ Noise\ Density = \sqrt{\left(\frac{45\times10^{-9}}{100.3}\right)^2 + (1\times10^{-9})^2 + (\sqrt{4\mathrm{kTR_G}})^2}$$

The expression $\sqrt{4kTR}$ is used to calculate the thermal noise density of resistors where k is Boltzmann's constant, $1.38{\times}10^{-23} m^2kgs^{-2}K^{-1}$, T is the temperature of the resistor in Kelvin and R is the resistor value. The gain resistor thermal noise was evaluated at 300˚K to give:

$$Voltage\ Noise\ Density$$
$$= \sqrt{\left(\frac{45\times10^{-9}}{100.3}\right)^2 + (1\times10^{-9})^2 + (4\times1.38\times10^{-23}\times300\times60.4)}$$
$$= 1.42\ \mathrm{nV}/\sqrt{\mathrm{Hz}}$$

To calculate the effect of the current noise, the circuit in Figure 5-50 was simplified to the following:

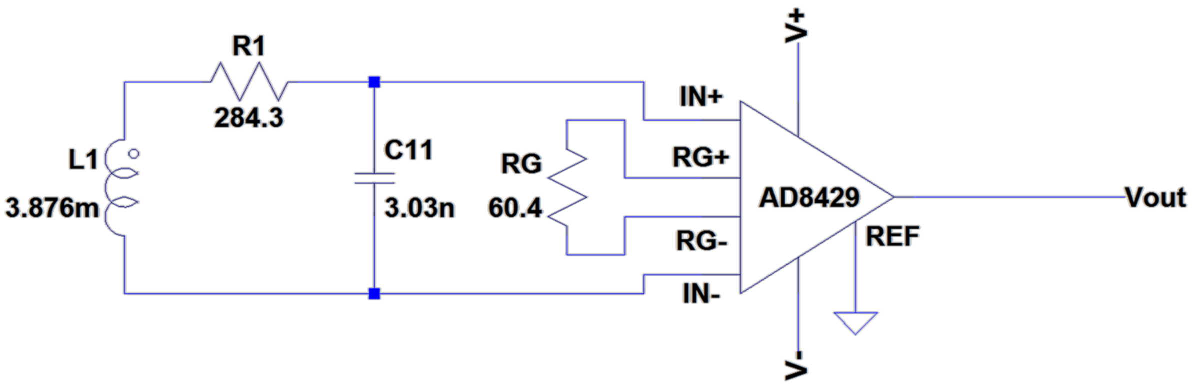

Figure 5-53: Simplified first stage amplifier circuit.

The simplified circuit allows for a straight forward calculation of the current noise. The AD8429 datasheet states that the current noise to be 1.5 pA/$\sqrt{\mathrm{Hz}}$, hence, the total current noise density can be calculated as

$$Current\ Noise\ Density = \sqrt{(inn\times R1)^2 + (inp\times R1)^2}$$
$$= \sqrt{(1.5\times10^{-12}\times284.3)^2 + (1.5\times10^{-12}\times284.3)^2}$$
$$= 603\ \mathrm{pV}/\sqrt{\mathrm{Hz}}$$

The thermal noise introduced by the resistors in the circuit is the final component to be calculated to complete the noise density analysis for the front-end amplification. The thermal noise is calculated in the same manner as the thermal noise for the gain resistor using the simplified overall resistance value in Figure 5-53.

$$Thermal\ Noise\ Density = \sqrt{4\mathrm{kTR_1}} = \sqrt{4 \times 1.38 \times 10^{-23} \times 300 \times 284.3}$$
$$= 2.17\ \mathrm{nV}/\sqrt{\mathrm{Hz}}$$

Thus, the total noise density of the amplifier circuit based on these un-correlated noise sources is combined as follows:

$$e_{amp}$$
$$= \sqrt{(Voltage\ Noise\ Density)^2 + (Current\ Noise\ Density)^2 + (Thermal\ Noise\ Density)^2}$$
$$= \sqrt{(1.10 \times 10^{-9})^2 + (603 \times 10^{-12})^2 + (2.17 \times 10^{-9})^2}$$
$$= 2.51\ \mathrm{nV}/\sqrt{\mathrm{Hz}}$$

This value was confirmed by performing a noise simulation for the first stage amplification stage using LTSPICE and was found to be 2.64 nV/$\sqrt{\mathrm{Hz}}$ as represented in Figure 5-54.

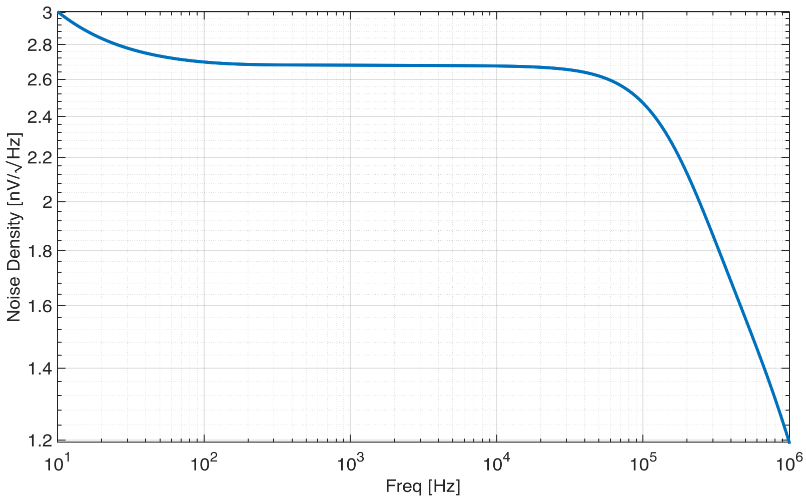

Figure 5-54: Noise Density Simulation using LTSPICE.

The noise density calculated requires multiplication by the square-root of the system bandwidth to obtain the noise value for the amplifier circuit. The bandwidth of the demodulated measurements is 50 Hz and so the total amplifier noise is

$$\mathrm{E}_{amp} = 2.51 \times 10^{-9} \times \sqrt{50} = 17.7\ \mathrm{nV}$$

Finally, quantisation noise from the MFIA system is combined with the amplifier noise to deduce the total instrumentation noise budget. The ADC used in the MFIA system was an Analog Devices AD7980BRMZ ADC converter which employs 16-bits to digitise a variable input signal range. The input range was set to 0-2.5V resulting in a representative voltage for the least significant bit of:

$$\mathrm{V_{LSB}} = \frac{\mathrm{V}_{FS}}{N_{levels}} = \frac{2.5}{2^{16}} = \ 38.1\ \mu\mathrm{V}$$

The quantisation noise, $\mathrm{E_{ADC}}$, introduced by the ADC can be calculated using the follow equation from [77] if the ADC is assumed to have an ideal transfer function [78]

$$\mathrm{E_{ADC}} = \ \sqrt{\left(\frac{2\mathrm{V_{LSB}}^2 f_B}{12 f_s}\right)}\ (\mathrm{V}) \qquad (\ 5\text{-}5\ )$$

where f_B is the system bandwidth and f_s is the sampling frequency. As mentioned earlier the bandwidth of the system is 50 Hz and the sampling frequency is set at 400 kHz.

$$\mathrm{E_{ADC}} = \sqrt{\frac{2 \times (38.1 \times 10^{-6})^2 \times 50}{12 \times 400 \times 10^3}} = 17.4\ \mathrm{nV}$$

Quantisation noise is introduced by the ADC after the signal has been fed through the amplifier chain. As a result, $\mathrm{E_{ADC}}$ needs to be divided by the amplifier gain to obtain the RTI noise before combining it to E_{amp}. The total amplifier chain provides a gain of 178.5 and hence the total instrumentation noise floor for the system is:

$$\mathrm{E}_{total} = \sqrt{(17.7 \times 10^{-9})^2 + (\frac{17.4 \times 10^{-9}}{178.5})^2} = 17.7\ \mathrm{nV}$$

The quantisation noise did not affect the overall noise value highlighting the dominating effect of the first stage amplifier noise due to the large circuit gain.

5.4.3 SNR Performance

The calculated noise value was used in conjunction with the RMS signal values calculated in 5.4.1 to produce SNR predictions of the system. Figure 5-55 represents the SNR predictions when scanning for (a) Type-72A mine and (b) PMA-2 mine. The SNR limit for healthy inversion was derived earlier during the invert-ability study, section 5.2, and was found to be around 10dB. The plot indicated favourable SNR predictions and suggests that the detector would be capable of inverting the tensors of mines accurately to depths beyond 25 cm. However, as mentioned earlier the noise values used are only related to the instrumentation and do not include any noise induced directly on the receive coils.

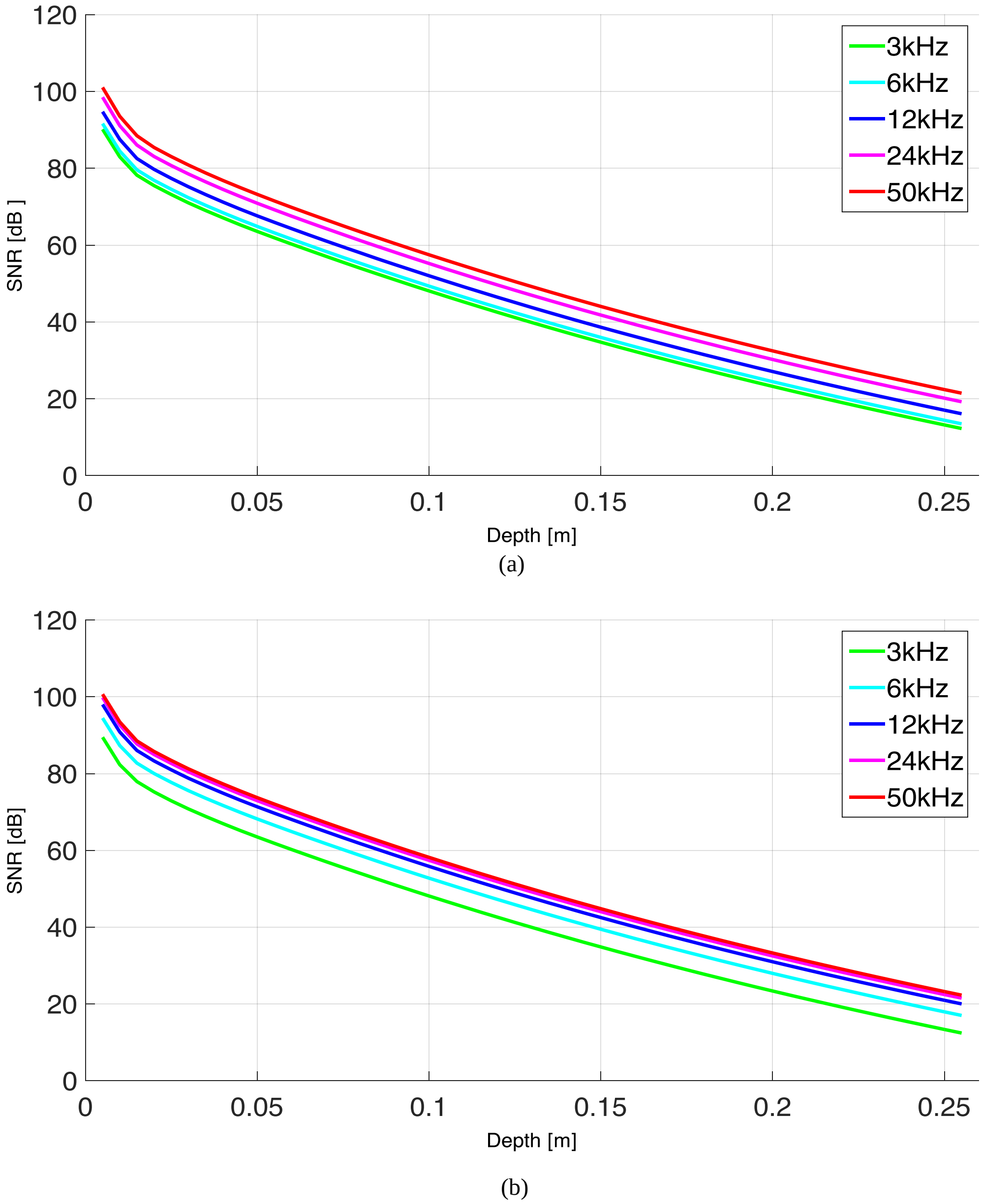

Figure 5-55: Predicted SNR with increased depth when scanning for (a) Type-72A and (b) PMA-2 mine.

To perform a more accurate SNR analysis, real noise values were measured using the constructed components described in section 5.4.1. The constructed instrument displayed a noise floor value which was present in the absence of an object and was used to estimate the SNR performance and the limit of accurate detector inversion, Figure 5-56. This SNR analysis reveals a significantly inferior performance and indicated that the detector would be capable of inverting accurate tensors for depths up to only 5 cm. An improvement of around 35 dB is required to perform accurate inversions up to a depth of 15 cm. This has been accepted by the group as a current shortfall of the system and is likely to improve through further design iterations.

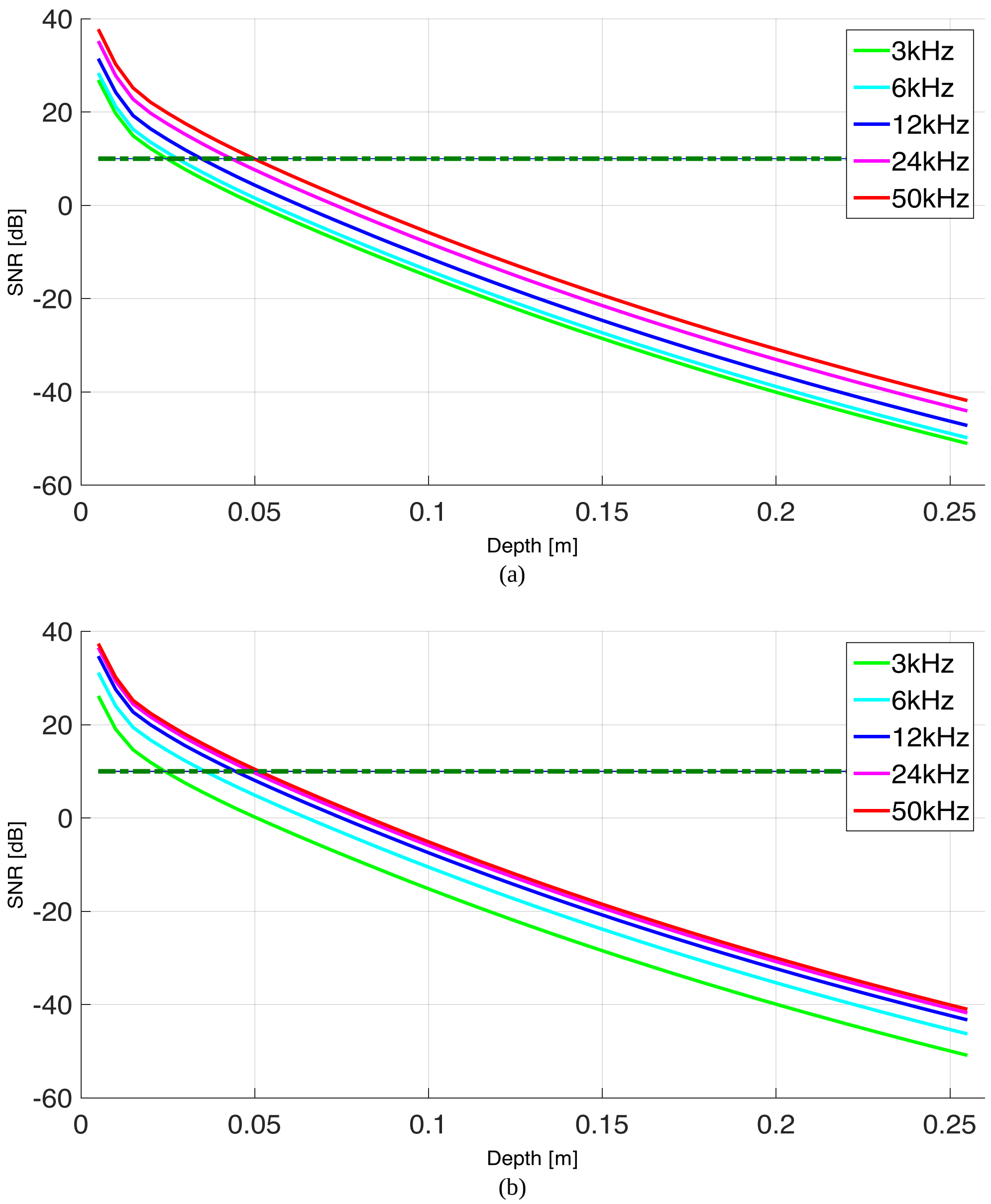

Figure 5-56: Predicted SNR with increased depth using measured noise values when scanning for (a) Type 72-A and (b) PMA-2 mine. Inversion SNR limit of 10dB is plotted in dashed green.

5.5 Coil Design Summary

This chapter described the design and manufacturing procedure followed during the duration of the research to create a sensor head for the portable landmine detector prototype. It identified a number of analytical means that were used to determine candidate coil arrays; sensitivity analysis and invert-ability analysis. The coil geometry was manufactured, potted and screened producing a prototype grade coil.

However, the final tests of the coil array revealed a number of issues with the chosen design. Firstly, the high mutual coupling discovered between the receive coils meant that the coil measurements were no longer independent. This was an assumption made during both the sensitivity analysis and the invert-ability and the absence of independent measurements negatively affects both analysis results. Secondly, the noise budget calculated for the system initially indicated healthy inversion beyond the specification of this research; however, this analysis only included the instrumentation noise. A realistic noise floor was obtained from a constructed system and indicated that accurate inversion would only be possible at much shallower depths; no further than 5 cm. The system currently needs an improvement in SNR performance of around 50 times to achieve accurate inversion at 15 cm. Note that no noise source analysis has been performed thus far. As a result this noise improvement could potentially be achievable through identification and elimination of noise sources as well as an increase of signal levels by applying a stronger transmit current.

These findings have resulted in a re-think of the coil design. Coil array 1B has become a primary candidate out the reviewed coil designs as the receive coils are nulled with respect to one another, minimising mutual coupling. However, another round of coil design is currently underway to revisit old considerations and identify new coil arrays in the light of the coupling impact.

6 Conclusion and Further Work

The final chapter concludes the work presented throughout the thesis to provide an overall summary. This chapter continues with a description of areas of further work required to progress the research in order to obtain a comprehensive tensor library and achieve a detector capable of characterising detected objects to reduce FAR during humanitarian demining.

6.1 Conclusions

Through the thesis it is clear that many elements have been completed successfully with positive results and others have progressed considerably; however, further work is required for completion. Tensor measurements were made possible through the design and construction of a measuring apparatus that is capable of determining tensors accurate to within 5% of simulated and analytical solutions. The measurements presented provided confirmation that characterisation between anti-personnel mines and clutter is possible through the spectral analysis of the magnetic polarizability dyadic tensor. Work on the coil design has produced a prototype coil that is currently being used on a portable device for field testing. However, final testing revealed hindering elements that require coil re-design.

To formally evaluate the work presented in this thesis, the objectives defined in section 1.1 are revisited with a review of each point, declaring the accomplishments achieved and referring to the relative sections supporting the claims.

- *A measurement apparatus capable of measuring the non-scaled tensor values for low metal mines and small metallic clutter.*

Through section 4.2, the thesis presented a measurement apparatus capable of measuring tensors of small symmetrical metallic objects to within 5%. The extensive validation of measured tensors performed against analytical and simulation solutions in section 4.4 confirmed that the constructed apparatus was capable of producing accurate tensor values. This validation spanned different object types to ensure the tensors measured were accurate for both simple and complicated objects. A titanium cube tensor was validated against an analytical solution based on first principals. The tensor of typical minefield clutter items, a Remington 222 shell and coins, were also validated to ensure the instrument was capable of measuring symmetrical clutter items accurately. Finally, a phantom piece for the Type-72A mine was used to validate the instrument capability of producing accurate anti-personnel mine tensors. The validated tensors were found to be nominally within 5% of the simulation or analytical solutions. Deviations larger than this value were found to be due to differences between the measurement and validation conditions. Thus based on these statements the apparatus presented in this thesis has performed well and met this objective; the measurement system is capable of producing accurate reliable tensor values for future use within the project.

- *A library of the magnetic polarizability dyadic dipole tensors for low metal mine parts and typical clutter items to help in the development of the enhanced metal detector.*

The validated measurement apparatus was used to measure the tensors of a number of objects representatives of typical clutter and low metal anti-personnel mines. In section 4.5.3, the tensors of five low-metal mine surrogates were presented, including two of the most challenging low-metal AP mines; PMA-2 and the Type-72A mines. The tensor measurements highlighted the difference in tensor spectra between the mines as a result of their varied composition and detonation mechanisms. The difference between mine tensors could potentially allow for classification between mines, provided clean signal measurement is achieved to produce accurate tensors.

Section 4.5.2, presented the tensors of typical clutter items likely to be found in mine fields contaminated with metallic content from previous conflicts. The clutter items presented are only a subset representation as they are all symmetrical due to the limitations of the measurement system. The presented tensors of clutter items were found to be considerably different from those of mines. Symmetrical clutter measured within this thesis is likely to produce tensors closer to those of AP mines than non-symmetrical clutter and since the clutter tensors measured were found to be considerably different, it can be assumed that non-symmetrical clutter is likely to present tensors different to those of mines. These findings proved the possibility of characterisation between mines and clutter using the inversion of the measured signals and deriving the tensor. Provided the measured signals when scanning for a mine are of reasonable SNR and provide enough information to invert an accurate tensor, the primary objective of this research is realisable.

Finally, the tensors for an un-circulated set of US coinage is provided in section 4.5.1, to act as a calibration metric and a comparison piece for future work in this area.

The library of magnetic polarizability dyadic dipole tensors provided in section 4.5 is diverse enough to allow for signal study and analysis of expected performance of prototype detectors. This library is already in use to help design the new sensor head for the prototype as will be discussed shortly. Thus, the objective can be regarded as successfully completed meeting the requirements of the research.

- *A sensor head optimised for inversion that is capable of detecting anti-personnel mines to depths required by mine clearance standards.*

The design and manufacturing of the sensor head was presented in chapter 5. The chapter discussed the selection process followed to create the current coil array. The criterion was aimed at producing a coil array that would obtain optimal measurements for inversion to produce accurate tensors. This was performed through the analysis of uniformity of array sensitivity and their ability to invert tensors correctly. The selected coil array was composed of a single transmit and four figure-of-eight receive coils.

3D printing was used to create a repeatable, lightweight and robust coil former. Suitable enamelled wires were used due to their minimal insulation weight and volume. The assembled coil array was encapsulated in epoxy resin to protect the array and secure the relative positions of the individual coils. The coil array was also screened using graphite paint to minimise capacitive coupling with the ground and any nearby surfaces.

Final testing of the manufactured coil array revealed strong mutual coupling between the receive coils. The coupling was discovered after the measurement of the resonant frequency of the receive coil before and after assembly was found to be considerably difference. This finding meant that the measurements of the receive coils are no longer independent measurements, which was a key assumption in the inversion study. Trans-impedance measurements and a simulation model confirmed the presence of strong mutual coupling and that it was the cause of change in resonant frequency. This prompted the need for a coil re-design with the added criteria that the receive coils are all nulled with respect to one another.

At the close of the chapter, anticipated signal levels from the coil were presented when detecting the Type-72A and PMA-2 mines. This was supported by a noise analysis of the proposed front-end amplification to determine the expected SNR performance of the final detector. The study suggested that the current sensor head and associated electronics would be capable of performing inversion at depths greater than 25 cm. However, measured noise floor indicated the inversion depth to be only around 5 cm. This falls short of the 13 cm specified by the current standards and the 15 cm specification set at the outset of this research.

Further work is required in this area to produce a suitable sensor head. However, the work presented in this research has helped the future design process and revealed further considerations; receive coil coupling and signal analysis using mine tensors. As a result, this objective cannot be deemed as a successful aspect of the research but more fittingly a considerable contribution to achieving the ideal coil design. The manufacturing decisions presented will help speed the process of constructing the new coil design and the set of new criteria should guarantee that the new coil produced is capable of performing meaningful inversions and obtaining accurate tensors.

In addition to the main objectives covered, secondary objects also include:

- *Design and implementation of front-end amplification capable of amplifying the detector signal and providing acceptable signal to noise.*

The transmit front-end amplification was designed and manufactured by Organised Technology Ltd under sub-contract and consists of a linear power amplifier aimed at driving a large current through the transmit coil while the receiver front-end amplification was designed and manufactured by Dr. Liam Marsh based on the coil design work presented in this thesis and the data acquisition system. The receive amplification circuit was designed to maximise the gain without saturation of the ADC. The gain value was based on the signal levels measured from the fully assembled coil array presented in chapter 5. The mutual coupling between the receive coils resulted in a significant background signal that varied from one coil to another and as a result the gain was limited to fewer than 178 and was varied for each channel to ensure the channels did not saturate when measuring objects of reasonable size with respect to mines. The circuit schematic of the final amplification was presented in section 5.4.2 and was used to calculate the instrumentation noise floor for the system. The calculated noise value was deemed acceptable and indicated that the main challenges for the research to improve the SNR performance lay with increasing the signal levels and decreasing the mutual coupling noise and background or interference signal.

- *Production of a multi-frequency data acquisition system.*

The design and construction of the data acquisition system was sub-contracted to Organised Technology Ltd. to perform a routine electronic design. The system was specified to be capable of generating a multi-frequency excitation signal between 1-100 kHz, perform data-acquisition, de-modulate the receive signal and store the real and imaginary responses measured to be later extracted for processing. The MFIA system produced is pictured in Figure 6-1 and was constructed to excite the transmit coil at 100, 50, 25, 12.5, 6.75, 3.38, 1.69 and 0.7 kHz. The system was designed to allow for a flexible selection of excitation frequencies with an adjustable base harmonic of 781 Hz, 390 Hz or 195 Hz and an 8 bit multiplication parameter to select the desired frequencies. The maximum selectable frequencies for each base harmonic are 200, 100 and 50 kHz respectively and are sampled at 4 samples per cycle. The initial excitation frequencies are likely to be amended to ensure a suitable range of frequencies are used to retrieve the maximum information about the measured object tensor; such as the real component cross-over frequency and imaginary component peak frequency.

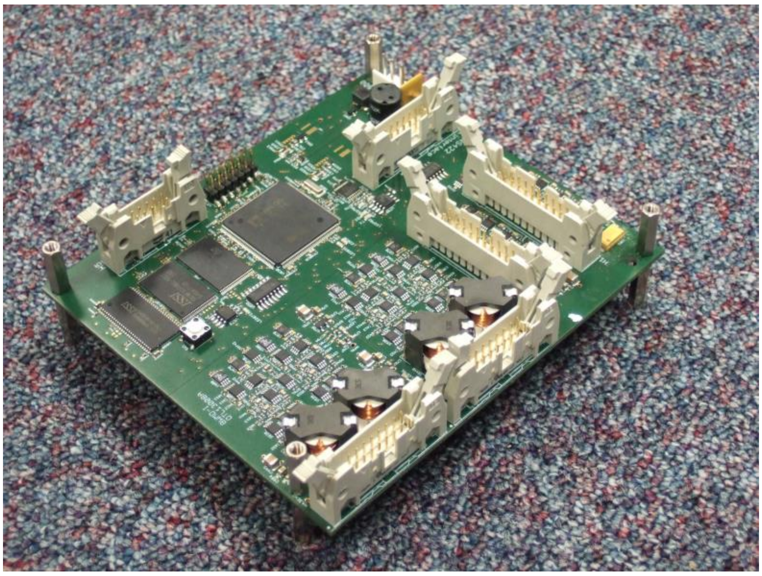

Figure 6-1: The MFIA data acquisition system.

- *implementation of an auto-nulling procedure capable of minimising the contribution of the background signal to the measured receive signal.*

The final objective of the current research was achieved through collaborative work between Dr. Liam Marsh and OTL. The MFIA system was designed with an additional excitation signal aimed to act as an injection signal into the receive amplifier chain to electrically null the background signal, Figure 6-2.

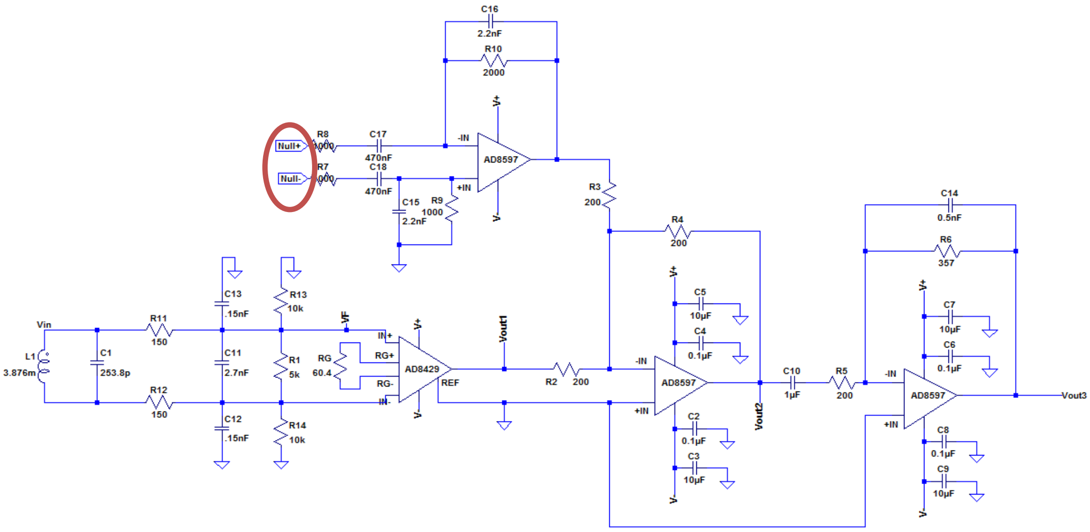

Figure 6-2: Auto-nulling signal injection point on the amplifier chain schematic.

An auto-nulling algorithm was developed by Dr. Marsh and followed an iterative approach to reduce the background signal gradually to a minimum value. The algorithm used the receive signal measured by the MFIA system to identify an appropriate nulling signal. When the auto-nulling feature is enabled the received signal phase is inverted, the magnitude scaled down and the nulling signal injected back into the amplifier chain at the injection point highlighted in Figure 6-2. This operation is performed at each iteration and the new nulling value is superimposed on to the current nulling signal. The resulting effect is that the background signal is gradually reduced to a floor level where the nulling algorithm settles at a minimum. The algorithm was found to take seconds or minutes to null depending on the magnitude of the background signal. Once the nulling algorithm has settled on a value, the auto-nulling feature can either be turned off or the scaling value significantly reduced such that the last stored nulling signal is continuously injected into the amplifier chain reducing the background signal. This ensures that any signal generated due to the presence of an object does not get eliminated by the nulling algorithm. A schematic of the algorithm is displayed in Figure 6-3.

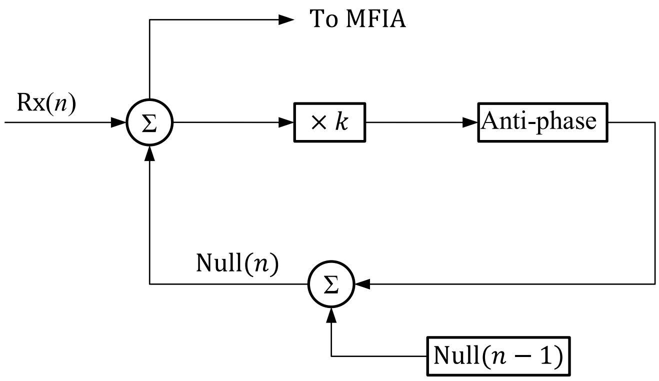

Figure 6-3: Auto-nulling algorithm, where k is a scaling factor, Null(n) is the injected nulling signal and Rx(n) is the measured background signal.

Research progress is well underway to develop a portable characterising metal detector, however; there a number of areas that need completion and others that need significant research in order to achieve a pre-production sensor capable discriminating between clutter and mines to help humanitarian demining operations.

6.2 Further Work

The work presented throughout this thesis falls into two distinct areas; one focused on the measurement of tensor values and the other focused on the development of the handheld device. In accord with this division this section will address the potential or required further work for each of these areas.

The measurement of the tensor values was achieved successfully for small symmetrical metallic objects. Investigating alternative EMI sensor design forms the main basis for future work in this area. A suite of solenoids need to be created to allow the measurement of larger objects as well as at different frequencies. The potential application of a Helmholtz arrangement could allow the tensor measurement of non-symmetrical objects. Finally, a comprehensive set of targets needs to be measured in order to build an effective tensor library. As expected, a large portion of metallic clutter found in mine fields are non-symmetrical and hence the development would allow for a significantly larger number of clutter tensors to be measuremed. The research so far has only focused on minimum metal landmines which tend to be small in size. A larger sensor head would allow for a more diverse tensor library to be created containing small and large landmines encompassing more metallic content.

The development of the final pre-production detector requires a significantly larger amount of further work. The first element that needs addressing is the re-design of the coil array. As discussed in the conclusion of chapter 5, the developed coil array experienced the unwanted effects of mutual coupling between the receive coils. The re-design process has been re-commenced and led by Dr. Marsh in collaboration with Fakultet elektrotehnike i računarstva (FER) at the University of Zagreb to design an optimised sensor head for inversion. The same criteria utilised in this research are being applied to the new design cycle with the added consideration of mutual coupling. The design process is also looking to maximise the field generated from the transmit coil to improve the signal levels and the overall SNR performance in order to perform healthy inversions for the PMA-2 and Type-72A at depths up to 15 cm.

Once the new coil design has been manufactured, the different electronic components (front-end amplification, MFIA system and auto-nulling) need to be combined to create the portable prototype. During the production of this thesis, this aspect has been progressed using the current coil array to achieve a field instrument capable of performing spectroscopic magnetic measurements of the buried objects, Figure 6-4.

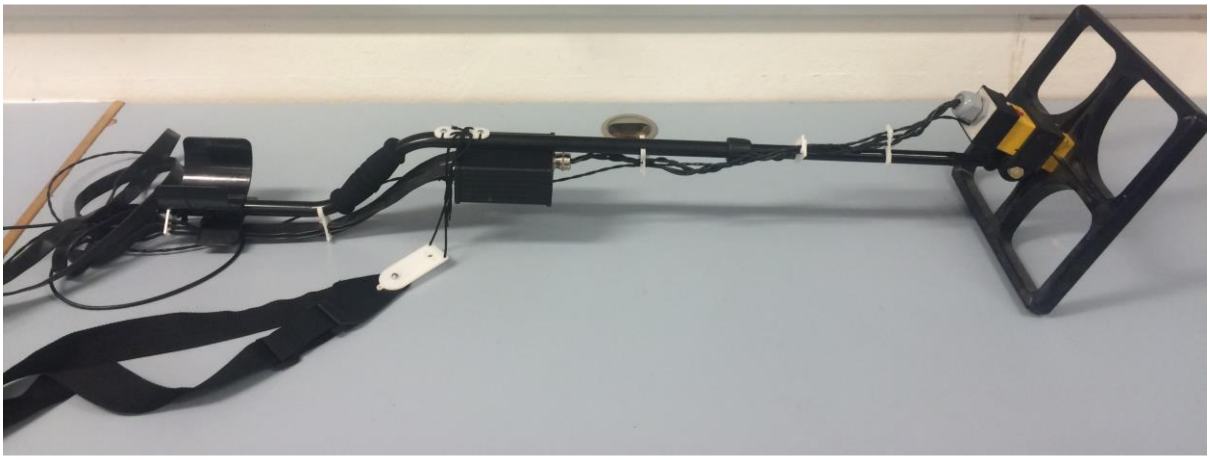

Figure 6-4: Assembled portable detector.

The pictured detector underwent a number of field trials in a mine test centre in Benkovac, Croatia to gauge an initial outlook of the system performance, Figure 6-5. The field trails were considered to be largely successful and the detector was capable of detecting the Type-72A surrogate buried at depths of up to 12 cm in cooperative soil. While this depth is shallower than the objective of 15 cm and was only achieved at a single frequency, it is still an encouraging result to achieve such depths with the mutual coupling experienced by the sensor head. An improved sensor head should allow for better nulling, both mechanically and electrically, better overall transmit field strength and ultimately a detector with improved sensitivity. The field trials also revealed an issue which should require further consideration in the future design work. Large items of clutter buried along the test lane quickly saturated the detector. A current proposal involved having a variable excitation current altering the overall sensitivity of the detector. However, literature review presented in section 2.5.3 discussed the negative impact of fine sensitivity adjustment on the repeatability of detectors which is extremely important for the inversion process.

Figure 6-5: Detector undergoing field trials in a test site in Benkovac, Croatia

Another area that requires further work to develop the full detector functionality lies within detector positioning. In order to perform inversion using the measurements captured by the portable detector the inversion process requires the relative position of each measurement. In turn, a significant area of further work needs to address this requirement and develop an accurate positioning system capable of tracking the detector movement between each measurement captured. The ALIS system already includes such capability, section 2.7.3, and thus the group is confident it is achievable. The current envisaged solution is likely to include relative image processing as implemented in ALIS as well accelerometers and gyroscopes to measure the detector movement in the X, Y and Z direction as well as the detector roll, pitch and yaw. The MFIA data acquisition system has been designed and built with the functionality to position stamp measurements with these parameters from a third-party positioning device. This area of further work is considerably independent from the remaining work presented in this thesis thus far and could be managed as a separate project.

To complete the enhanced metal detection research, the inversion of detector measurements and the characterisation of detected objects is the final area of work. Currently, it is viewed that the inversion will be performed through a simple Moore-Penrose pseudo-inversion as the inverse problem is well posed and heavily over-determined. However, this cannot be claimed with certainty until inversion is attempted; other inversion methods with optimisation may be required. As mentioned earlier the inversion requires a positioning system which is currently not in place. As a result, the potential to use temporary positioning systems such as an encoded planar arm are being considered. Finally, to achieve characterisation, the tensor library developed within this thesis and in future work would be used alongside the inverted tensors from the portable detector to assist in the discrimination between metallic clutter and AP landmines. The characterisation algorithm is to be developed; however, it is likely to follow a similar approach to that applied on a WTMD in [72].

This concludes the further work required to develop the enhanced metal detector; capable of characterising buried metallic objects in the hope of discriminating between landmines and clutter. At the outset of this thesis it was mentioned that a separate research is looking into the use of GPR to image and detect the plastic casing surrounding mines. The literature review in section 2.7 highlighted that the combination of MD and GPR has produced the most successful technical advancement in discriminating between clutter and threats. The greater research at the university aims to combine the enhanced metal detector with the parallel research investigating the use of GPR to create a detector capable of gathering a significant amount of information about buried targets in order to confidently and systematically disregard clutter when demining. The combination of the detection methodologies poses some challenges for the inversion of the metallic signal. The presence of the GPR antennas is likely to affect the signals measured by the coil as well as altering the generated field. The presence of the metal detector is also likely to affect the GPR readings and hence considerable work is likely to focus on the interaction between the two independent detection methodologies and how to minimise their effects on one another.

Despite the significant amount of further work that lies ahead of this project, this thesis has already reported on a number of novel aspects of research. For the first time the accurate unscaled tensors have been measured and verified confirming the difference between clutter and mine tensors as well as providing a source to predict signal values from prospective coils. The coil design process has been developed and refined to achieve an ideal array for inversion purposes and work is well under way with tackling a number of challenges that lay ahead such as amplification, instrumentation and field trials.

7 References

[1] International Campaign to Ban Landmines, "Landmine Monitor 2011," International Campaign to Ban Landmines, Canada 978-0-9738955-8-2, 2011, pp. iii

[2] D. J. Daniels, "Detection of buried Landmines using Ground Penetrating Radar Presentation," unpublished|.

[3] D. Guelle, A. Smith, A. Lewis, T. Bloodworth, European Commission and Joint Research Centre, "Metal Detector Handbook for Humanitarian Demining (EUR)," in *Metal Detector Handbook for Humanitarian Demining (EUR)*, European Commission, Ed., ed Italy: Joint Research Centre, 2003, p. 129.

[4] D. Guelle, A. Smith, A. Lewis, T. Bloodworth, European Commission and Joint Research Centre, "Metal Detector Handbook for Humanitarian Demining (EUR)," in *Metal Detector Handbook for Humanitarian Demining (EUR)*, European Commission, Ed., ed Italy: Joint Research Centre, 2003, pp. 15-26.

[5] Find A Better Way. (2011, January). *FABW Website*. Available: http://www.findabetterway.org.uk/

[6] UNICEF. (May 2014, May 2014). *UNICEF in Emergencies: Landmines*. Available: http://www.unicef.org/emerg/index_landmines.html

[7] Find a Better Way. (May 2014). *Find a Better Way-Landmine Facts*. Available: http://www.findabetterway.org.uk/landmine-facts/

[8] International Campaign to Ban Landmines – Cluster Munition Coalition (ICBL-CMC), "Landmine Monitor 2013," 2013.

[9] International Campaign to Ban Landmines. (2014, May). *ICBL Website*. Available: http://www.icbl.org/index.php/icbl/Treaty

[10] International Campaign to Ban Landmines. (2014, May). *International Campaign to Ban Landmines-Treaty-Basics*. Available: http://www.icbl.org/index.php/icbl/Treaty/MBT/Treaty-Basics

[11] International Campaign to Ban Landmines, "Landmine Monitor 2011," International Campaign to Ban Landmines Canada, International Campaign to Ban Landmines, 2011, p. 1.

[12] Mines Advisory Group. (2011, December). *MAG website*. Available: http://www.maginternational.org/

[13] D. Guelle, A. Smith, A. Lewis, T. Bloodworth, European Commission and Joint Research Centre, "The role of metal detectors in humanitarian demining," in *Metal Detector Handbook for Humanitarian Demining (EUR)*, European Commission, Ed., ed Italy: Joint Research Centre, 2003, pp. 27-42.

[14] International Mine Action Standards, "IMAS 1.10," in *Guide for the application of IMAS*, ed: Geneva International Centre for Humanitarian Demining, 2003, pp. 1-4.

[15] International Mine Action Standards, "IMAS 8.10," in *General Mine Action Assessment*, ed: Geneva International Centre for Humanitarian Demining, 2003, p. vi.

[16] International Mine Action Standards, "IMAS 9.10," in *Clearance Requirements*, ed: Geneva International Centre for Humanitarian Demining, 2003, pp. 1-3.

[17] GICHD. (2015). *Collaborative ORDnance Data Repository (CORD)*. Available: http://cord.gichd.org/ordnance?id=http%3A%2F%2Fcord.gichd.org%2Fontology%23Landmine4156

[18] A. Smith, "Understanding the Use of Prodders in Mine Detection," *The Journal of ERW and Mine Action*, 2014.

[19] Landmine Monitor Core Group, " Injuries that Occur in Humanitarian Demining: Landmine Monitor Report 2000," 2000.

[20] DDAS. (2011, Dec). *Accident Records by Primary Activity*. Available: http://ddasonline.com/AccidentrecordsDDAS.htm

[21] International Mine Action Standards, "IMAS 9.40," in *Guide for the Use of Mine Detecting Dogs*, ed: Geneva International Centre for Humanitarian Demining, 2008, pp. 2-3.

[22] International Mine Action Standards, "IMAS 9.50," in *Mechanical Demining*, ed: Geneva International Centre for Humanitarian Demining, 2006, pp. 2-3.

[23] A. M. Lewis, T. J. Bloodworth, D. M. Guelle, F. R. Littmann, A. Logreco, and M. A. Pike, "Systematic Test & Evaluation of Metal Detectors (STEMD) Interim Report Laboratory Tests Italy " The Institute for the Protection and Security of the Citizen, European Commission, Joint Research Centre 2006.

[24] Geneva International Centre for Humanitarian Demining, "Introduction," in *Guidebook on Detection Technologies and Systems for Humanitarian Demining*, ed Geneva: Geneva International Centre for Humanitarian Demining, March 2006, p. 3.

[25] J. MacDonald, J. R. Lockwood, J. McFee, T. Altshuler, T. Broach, L. Carin*, et al.*, "Introduction," in *Alternatives for Landmine Detection*, ed: RAND, 2003, p. 9.

[26] K. Koppetsch, "Foreword," in *Metal Detectors and PPE Catalogue 2007*, J. Glattbach, Ed., ed Geneva: Geneva International Centre for Humanitarian Demining, 2007, p. 4.

[27] Geneva International Centre for Humanitarian Demining, "Ground Penetrating Radar Systems," in *Guidebook on Detection Technologies and Systems for Humanitarian Demining*, ed Geneva: Geneva International Centre for Humanitarian Demining, March 2006, pp. 17-41.

[28] J. MacDonald, J. R. Lockwood, J. McFee, T. Altshuler, T. Broach, L. Carin*, et al.*, "Innovative Mine Detection Systems," in *Alternatives for Landmine Detection*, ed: RAND, 2003, pp. 18-29.

[29] L. Carin, "Appendix E: Ground Penetrating Radar (Paper I)," in *Alternatives for Landmine Detection*, ed: RAND, 2003, pp. 127-132.

[30] G. M. Schultz, J. Keranen, and J. S. Miller, "Analysis of Multi-Sensor EMI and GPR Array Data for Ordnance Detection," 21st EEGS Symposium on the Application of Geophysics to Engineering and Environmental Problems, 2008.

[31] P. D. Gader, M. Mystkowski, and Y. Zhao, "Landmine Detection with Ground Penetrating RadarUsing Hidden Markov ModelsPaul D. Gader, Senior Member, IEEE, Miroslaw Mystkowski, and Yunxin Zhao, Senior," *Geoscience and Remote Sensing, IEEE Transactions on*, vol. 39, pp. 1231-1244, 2001.

[32] X. Feng and M. Sato, "Pre-stack migration applied to GPR for landmine detection," *Inverse Problems*, vol. 20, pp. S99–S115, 2004.

[33] K. Koppetsch, "THE AN / PSS-14 (HSTAMIDS) / AMD-14," in *Metal Detectors and PPE Catalogue 2007*, J. Glattbach, Ed., ed Geneva: Geneva International Centre for Humanitarian Demining, 2007, pp. 132-139.

[34] United States Department of Defence, "Humanitarian Demining R&D Program:HSTAMIDS," United States Department of Defence: Humanitarian Demining R&D Program,December 2011.

[35] R. C. Doheny, S. Burke, R. Cresci, P. Ngan, and R. Walls, "Handheld Standoff Mine Detection System (HSTAMIDS) Field Evaluation in Thailand " U.S. Army Research Development and Engineering Command 2005.

[36] United States Department of Defence, "Humanitarian Demining R&D Program: Minehound ", ed, April 2013.

[37] Vallon. (2012). *MINEHOUND VMR3 (Datasheet)*. Available: http://www.vallon.de/pdf/VMR3_leaflet_10-2012.pdf?rnd=825876370cbf62719FhKFF007C57

[38] ERA Technology Ltd, "Minehound trials 2005-2006: Summary Report," 2006.

[39] D. Daniels, J. Braunstein, and M. Nevard, "Using MINEHOUND in Cambodia and Afghanistan," *the journal of ERW and mine action*, pp. 46-51, 2014.

[40] M. Sato, J. Fujiwara, T. Kido, and K. Takahashi, "ALIS Evaluation Tests in Croatia and Cambodia," presented at the Proc. of International Symposium Humanitarian Demining 2009, 2009.

[41] M. Sato, J. Fujiwara, X. Feng, Z.-S. Zhou, and T. Kobayashi, "Evaluation of a Hand-held GPR MD sensor system (ALIS)," in *Proc. of the IARP International workshop on Robotics and Mechanical Assistance in Humanitarian Demining (HUDEM2005)*, Tokyo, Japan, 2005, pp. 21-26.

[42] M. Sato, J. Fujiwara, T. Kido, and K. Takahashi, "ALIS evaluation tests in Croatia," in *Proc. SPIE 7303, Detection and Sensing of Mines, Explosive Objects, and Obscured Targets XIV*, Orlando, Florida, USA, 2009.

[43] X. Feng and M. Sato, "Landmine imaging by a Hand-held GPR and metal detector sensor (ALIS) " presented at the Proceedings. 2005 IEEE International Geoscience and Remote Sensing Symposium, 2005. IGARSS '05., 2005.

[44] A. M. Lewis "Tests and Evaluation of Dual Sensor Mine Detectorsbased on a Combination of Metal Detector and Ground Penetrating Radar (TEDS)," Joint Research Centre - European Commission (JRC/EC)2006.

[45] J. G. W. Thomas, J. Yorkey, J. Tompkins, "Comparing Reconstruction Algorthms for Electrical Impedance Tomography," *IEEE Transactoins on Biomedical Engineering*, vol. 34, pp. 843-852, 1987.

[46] F. Dicki and M. Wang, "Electrical resistance tomography for process applications," *Meas. Sci. Technol.*, vol. 7, pp. 247-260, 1996.

[47] Geneva International Centre for Humanitarian Demining, "Metal Detectors (electromagnetic induction devices)," in *Guidebook on Detection Technologies and Systems for Humanitarian Demining*, ed Geneva: Geneva International Centre for Humanitarian Demining, March 2006, pp. 11-15.

[48] P. Church, J. E. McFee, S. Gagnon, and P. Wort, "Electrical Impedance Tomographic Imaging of Buried Landmines," *Geoscience and Remote Sensing, IEEE Transactions on* vol. 44, pp. 2407-2420, Sept. 2006.

[49] G. Bouchette, S. Gagnon, P. Church, T. Luu, and J. McFee, "Electrical impedance tomography for underwater detection of buried mines," in *Detection and Sensing of Mines, Explosive Objects, and Obscured Targets XIII*, May 2008, pp. 69530O.1-69530O.12.

[50] Geneva International Centre for Humanitarian Demining, "Acoustic/Seismic Systems," in *Guidebook on Detection Technologies and Systems for Humanitarian Demining*, ed Geneva: Geneva International Centre for Humanitarian Demining,, March 2006, pp. 117-127.

[51] J. M. Sabatier and N. Xiang, "An investigation of acoustic-to-seismic coupling to detect buried antitank landmines," *Geoscience and Remote Sensing, IEEE Transactions on*, vol. 39, pp. 1146 - 1154, 2001.

[52] N. Xiang and J. M. Sabatier, "An experimental study on antipersonnel landmine detection using acoustic-to-seismic coupling," *Acoustical Society of America*, vol. 113, pp. 1333-1341, 2003.

[53] A. M. Lewis, P. Verlinde, M. Peichl, R. Ebert, V. Klein, and U. Uschkerat, "Multisensor Mine Signatures - MSMS (ITEP Project 2.5.1.2), Final Report," Joint Research Centre - European Commission (JRC/EC)2004.
[54] G. G. Skitek and S. V. Marshall, "Biot-Savart Law, Ampere’s Law, Curl Stokes’ Theorem," in *Electromagnetic Concepts and Applications*, 2nd ed: Prentice Hall, 1987, pp. 216-220.
[55] P. Lorrain, D. R. Corson, and F. Lorrain, "Magnetic fields I " in *Electromagnetic Fields and Waves*, 3rd Revised ed: W.H.Freeman & Co Ltd, 1988, pp. 329-344.
[56] F. T. Ulaby, "Magnetostatics " in *Fundamentals of Applied Electromagnetics*, 5th ed: Prentice Hall, 2006, pp. 240-260.
[57] J. D. Kraus and D. A. Fleisch, "Electromagnetics with Applications," M.-H. Book, Ed., Fifth Edition ed: McGraw-Hill Book, 1999, p. 105.
[58] F. T. Ulaby, "Maxwell's Equations for Time-Varying Fields," in *Fundamentals of Applied Electromagnetics*, 5th ed: Prentice Hall, 2006, p. 299.
[59] P. Lorrain, D. R. Corson, and F. Lorrain, "Magnetic fields VI " in *Electromagnetic Fields and Waves*, 3rd Revised ed: W.H.Freeman & Co Ltd, 1988, p. 424.
[60] T. H. Bell, B. J. Barrow, and J. T. Miller, "Subsurface Discrimination Using Electromagnetic Induction Sensors," *Geoscience and Remote Sensing, IEEE Transactions on*, vol. 39, pp. 1286-1293, June 2001.

[61] Marsh L.A., Ktistis C., Jarvi A., Armitage D.W., and P. A.J., "Three-dimensional object location and inversion of the magnetic polarisability tensor at a single frequency using a walk-through metal detector," *Meas. Sci. Technol.*, vol. 24, p. 045102, 2013.
[62] T. H. Bell, B. Barrow, and N. Khadr, "Shape-based classification and discrimination of subsurface objects using electromagnetic induction," in *Geoscience and Remote Sensing Symposium Proceedings, 1998. IGARSS '98. 1998 IEEE International*, 1998, pp. 509-513 vol.1.
[63] J. P. Fernández, B. Barrowes, A. Bijamov, T. Grzegorczyk, N. Lhomme, K. O'Neill, *et al.*, "MPV-II: an enhanced vector man-portable EMI sensor for UXO identification," 2011, pp. 801707-801707-10.
[64] A. Peyton, " Eddy Currents and Diffusion " unpublished|.
[65] Y. Das, J. E. McFee, J. Toews, and G. C. Stuart, "Analysis of an Electromagnetic Induction Detector For Real-Time Location of Buried Objects," *Geoscience and Remote Sensing, IEEE Transactions on*, vol. 38, pp. 278-288, 1990.
[66] J. P. Fernandez, B. E. Barrowes, T. M. Grzegorczyk, N. Lhomme, K. O'Neill, and F. Shubitidze, "A Man-Portable Vector Sensor for Identification of Unexploded Ordnance," *Sensors Journal, IEEE*, vol. 11, pp. 2542-2555, 2011.
[67] T. M. Grzegorczyk and B. E. Barrowes, "Real-Time Processing of Electromagnetic Induction Dynamic Data Using Kalman Filters for Unexploded Ordnance Detection," *Geoscience and Remote Sensing, IEEE Transactions on*, vol. 51, pp. 3439-3451, 2013.
[68] T. M. Grzegorczyk, B. E. Barrowes, F. Shubitidze, J. P. Fernandez, and K. O'Neill, "Simultaneous Identification of Multiple Unexploded Ordnance Using Electromagnetic Induction Sensors," *Geoscience and Remote Sensing, IEEE Transactions on*, vol. 49, pp. 2507-2517, 2011.
[69] T. M. Grzegorczyk and B. E. Barrowes, "Operation of the Pedemis Sensor at the Aberdeen Proving Ground Standardized Test Site: Single and Multi-Target Inversions," *Geoscience and Remote Sensing Letters, IEEE*, vol. 11, pp. 394-398, 2014.

[70] H. Haoping and I. J. Won, "Characterization of UXO-like targets using broadband electromagnetic induction sensors," *Geoscience and Remote Sensing, IEEE Transactions on*, vol. 41, pp. 652-663, 2003.

[71] A. M. Liam, K. Christos, J. Ari, W. A. David, and J. P. Anthony, "Three-dimensional object location and inversion of the magnetic polarizability tensor at a single frequency using a walk-through metal detector," *Measurement Science and Technology*, vol. 24, p. 045102, 2013.

[72] A. M. Liam, K. Christos, J. Ari, W. A. David, and J. P. Anthony, "Determination of the magnetic polarizability tensor and three dimensional object location for multiple objects using a walk-through metal detector," *Measurement Science and Technology*, vol. 25, p. 055107, 2014.

[73] J. Makkonen, L. A. Marsh, J. Vihonen, A. Järvi, D. W. Armitage, A. Visa, *et al.*, "KNN classification of metallic targets using the magnetic polarizability tensor," *Measurement Science and Technology*, vol. 25, p. 055105, 2014.

[74] Z. Yifei, Y. Wuliang, C. Ktistis, D. Butterworth, and A. J. Peyton, "On the Low-Frequency Electromagnetic Responses of In-Line Metal Detectors to Metal Contaminants," *Instrumentation and Measurement, IEEE Transactions on*, vol. 63, pp. 3181-3189, 2014.

[75] U. S. Mint. (July 2015, Coin Specification. Available: http://www.usmint.gov/about_the_mint/?action=coin_specifications

[76] Texas Instruments, "Noise Analysis in Operational Amplifier Circuits," 2007.

[77] R. W. Stewart. (1995, An overview of sigma delta ADCs and DAC devices. *IET Conference Proceedings*, 1-1. Available: http://digital-library.theiet.org/content/conferences/10.1049/ic_19951371

[78] Texas Instruments, "Understanding Data Converters," 1995.

Publications

Publication I

Rehim O., Davidson J., Marsh L., O'Toole M., Armitage D., and Peyton A., "Measurement system for determining the magnetic polarizability tensor of small metal targets," in *Sensors Applications Symposium (SAS), 2015 IEEE*, 2015, pp. 1-5.

The paper received the second best student paper award at the IEEE SAS 2015 conference in Zadar, Croatia.

Measurement system of magnetic polarizability tensor of small metal targets

Omar A Abdel Rehim*, John Davidson, Liam Marsh, Member, IEEE, Michael D O'Toole,
David W Armitage and Anthony J Peyton, Fellow, IEEE
School of Electronic and Electrical Engineering
The University of Manchester
Manchester, M13 9PL, UK
*Email: omar.abdelrehim@manchester.ac.uk

***Abstract*—This paper presents an apparatus to measure the spectroscopic magnetic response of small metallic objects and deduce the magnetic polarizability tensor. The measured trans-impedances of a .222 Remington rifle cartridge and titanium cube are compared to simulated results and are found to match well providing verification of the method. The eigenvalue matrix of the two objects is calculated and discussed highlighting the potential discriminatory aspect which can be used by landmine detector to provide subsurface classification and discrimination between landmines and clutter.**

Keywords—electromagentic magnetic polarizability tensor; ERW detection

I. Introduction

Buried landmines in former battlefields remain a significant humanitarian and environmental problem worldwide, posing risk of serious injury and contributes to an annual casualty rate in the thousands [1].The main challenge for landmine detectors has shifted over the last decade towards the classification of metallic content as opposed to detection. Increased sensitivity of metal detectors has meant that modern detectors are capable of detecting low-metal anti-personnel mines up to a depth of 15 cm [2]. However, landmine cleanup remains a difficult task that is extremely expensive and time consuming since most environments containing unexploded mines are cluttered with innocuous metallic content. A deminer can be faced with as many as 100 to 1000 inert metal objects for every mine [3]. Therefore it is crucial that reliable and accurate techniques are developed to enable rapid discrimination between clutter items and actual targets of interest. In the view of this, recent development has seen the introduction of ground penetrating radar (GPR) to complement the electromagnetic induction as a means of discriminating between clutter and threat objects [4]. However, recent studies have demonstrated the potential to classify metallic content by identifying the magnetic dyadic polarizability tensor of detected objects [5], [6].

Typical electromagnetic induction sensors are composed of an excitation coil which generates a primary magnetic field and a receive coil used to measure the induced fields caused by interactions with surrounding material. Eddy currents generated in the metallic content as a result of the varying primary field are dependent on a number of parameters such as size, shape, material and location. This effect is sometimes referred to as demagnetization effect or secondary field. Consequently different targets are expected to exhibit different electromagnetic responses. The object specific information is captured in the magnetic polarizability tensor and hence deducing the value from measured data would provide a means of classification.

This paper looks at the development of an instrument that provides a means of measuring and identifying the tensor values of low metal anti-personnel mines. We begin by reviewing the basic theory behind the magnetic polarizability tensor. Following this a description of the experimental set-up used to accurately and reliably obtain the electromagnetic responses of test objects is given. Simulations of object responses were run in parallel to measurements to verify the measurements and validate the experiment. Thus a description of the simulation approach and results is provided prior to reporting on experimental results. The deduced values of the tensors are then calculated and compared to one another as well as to simulation results. Finally we report on the timely relevance of exploiting the described techniques in this paper to provide a library of tensors for anti-personnel mines and clutter

II. Background

The magnetic polarizability tensor is referred to in this paper as $\overleftrightarrow{\mathbf{M}}$ and is composed of a 3x3 symmetrical complex matrix that is frequency dependent. It identifies the EMI response based on the induced dipole moment [5]. The double-arrowed accent represents the dyadic nature rather than a matrix or vector quantity [7].

$$\overleftrightarrow{\mathbf{M}}(f)=\begin{bmatrix} M'_{xx}+jM''_{xx} & M'_{xy}+jM''_{xy} & M'_{xz}+jM''_{xz} \\ M'_{yx}+jM''_{yx} & M'_{yy}+jM''_{yy} & M'_{yz}+jM''_{yz} \\ M'_{zx}+jM''_{zx} & M'_{zy}+jM''_{zy} & M'_{zz}+jM''_{zz} \end{bmatrix} \quad (1)$$

The matrix is symmetrical due to the electromagnetic reciprocity, meaning that the matrix only contains 6 unique complex numbers. In theory, the tensor can be deduced from as little as 6 incident angles of the primary field. This is provided that the angles are three orthogonal axes and their cross-diagonals to provide a full view of the object, as demonstrated in Fig. 1. However a larger number of measurement angles are normally performed to provide confidence in the measurements and the deuced tensor.

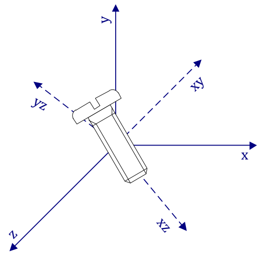

Fig. 1-Example object (screw) and the minimum number of orientations with respect to the primary field required to deduce the tensor.

The classification/discrimination process does not quite utilize $\overleftrightarrow{\mathrm{M}}$ as it is orientation specific and pre-determined knowledge of the object orientation would be required. Thus, the Eigenvalue matrix, Λ, is used instead as it provides an orientation-independent means of comparing responses. Λ isolates the three primary orthonormal axis of the object such that an external primary field aligned with one axis would result in a steady state dipole moment parallel to it [10]. It is the spectroscopic information contained in Λ that can be used as a signature to identify and discriminate between mines and clutter. $\overleftrightarrow{\mathrm{M}}$ can be deduced back from Λ to calculate the response in any orientation by applying rotational matrix *R*, [10][11], as displayed in (2):

$$\overset{\leftrightarrow}{\mathbf{M}} = R \cdot \Lambda \cdot R_T \tag{2}$$

A full derivation of the magnetic polarizability tensor theory is provided in [7] and provides the backbone equation used in this paper. Equation (3) relates $\overleftrightarrow{\mathrm{M}}$ to the measured induced voltage, V_{ind}, in the receive coil of the electromagnetic sensors:

$$V_{ind} = \frac{j\omega\mu_0}{I_R} \vec{\mathbf{H}}_T \cdot \overset{\leftrightarrow}{\mathbf{M}} \cdot \vec{\mathbf{H}}_R \tag{3}$$

where $\vec{\mathrm{H}}_\mathrm{T}$ and $\vec{\mathrm{H}}_\mathrm{R}$ are the fields incident to the object from the transmit and receive coils respectively, μ_0 is the permeability of free space and IR is the current passing through the receive coil. In practice these equations are used in reverse as the induced voltage is initially measured which provides a means of identifying $\overleftrightarrow{\mathrm{M}}$ which in turn allows the calculation of Λ.

Finally, it is worth noting that in order to approximate the secondary field (the induced voltage) using the field of the magnetic dipole moment, the primary field is assumed to be parallel across the object in question [7]. Additionally, a magnetic dipole approximation may be used to describe a current loop, where the loop dimensions are much smaller than the distance to point of interest [12].

III. Theory

In order to derive $\overleftrightarrow{\mathrm{M}}$ a system needs to be able to provide a parallel primary field at a number of incident angles. Rotating the object within a Helm-Holtz coil provides just that. The paper is to make use of the uniform field within the central region to obtain the measurements required in order to obtain $\overleftrightarrow{\mathrm{M}}$ and ultimately Λ.

Once a set of rotational voltage measurements are obtained, Λ can be obtained by one of two means. If the object is symmetrical and has an obvious primary axes, such as the example screw, the object is expected to have an eigenvalue matrix composed of a dominant component and two equal smaller values. Again in theory, only two measurements would be required to obtain the two values; one with the screw aligned with the field and one with the screw at 90˚. This simplification could go even further to obtain Λ from one measurement if the object responds equally in all directions such as a sphere. Alternatively, a full set of rotational measurements can be performed and a simple pseudo inversion process can be used to attain the values of $\overleftrightarrow{\mathrm{M}}$. The Jacobian/sensitivity matrix in the inversion is composed of the dot product of values of $\vec{\mathrm{H}}_\mathrm{T}$ and $\vec{\mathrm{H}}_\mathrm{R}$ for each angle to provide the solution for $\overleftrightarrow{\mathrm{M}}$ as:

$$\overset{\leftrightarrow}{\mathbf{M}} = \frac{1}{j\omega\mu_0} J^{-1} \cdot \frac{V_{ind}}{I_T} \tag{4}$$

where *J* is the Jacobian matrix and I_T is the current through the transmit coil. The induced voltage divided by the transmit coil current is commonly known as the trans-impedance measurement and is the recorded value obtained from the experiment discussed next.

IV. Experimental Setup

A. System Overview

The primary instrument used to perform the measurements is an impedance/gain phase analyser, Solatron SI 1260. The Solatron excites the coil with a spectroscopic sweep and captures the trans-impedance measurement for each frequency. A bespoke LabVIEW code controls the measurement process; stepping through the desired frequencies providing the required excitation values and recording the trans-impedance measured by the Solatron. This data is then passed onto MATLAB to perform the post-processing; inversion and tensor calculation. Basic front-end amplification is used to provide a stronger driving current (≈1.2A) and amplify the induced voltage from the receive coil. A system overview is represented in Fig. 2.

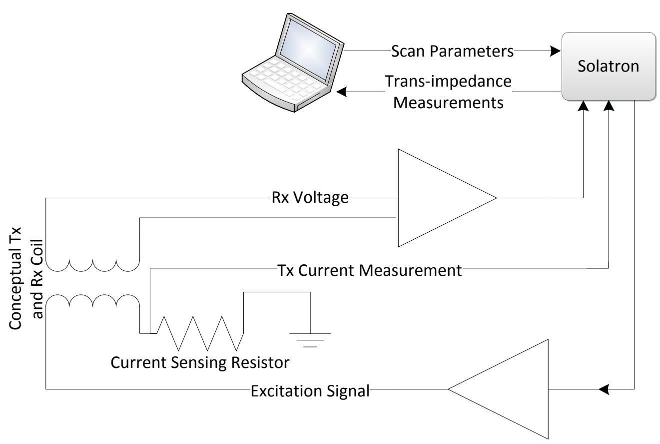

Fig. 2-System overview highlighting the flow of signals and measurements to and from the Solatron and the workstation.

B. The coil

The helm-holtz coil constructed in order to take the measurements is pictured in, Fig. 3(b). The coil is composed of an inner 120 turn transmit coil, visualized in red in Fig. 3(a), and two outer 60 turn receive coils wound in a gradiometer arrangement, displayed in green in Fig. 3(a) and red in Fig. 3(b). The coil dimensions are as follows; a=202.0 mm, b=105.0 mm, H=220.0 mm, d=107.0 mm and D=149.0 mm, with a wire wall thickness of 1.75 mm for the transmit coil and 1.66mm for the receive. The z-axis is considered to be along the centre of the coil.

The coil was designed to provide maximum sensitivity (larger number of turns) while ensuring the resonance of the coil is well above the region of interest. The frequency range investigated within this paper is 1-100 kHz as this contains the majority of the useful information required for classification.

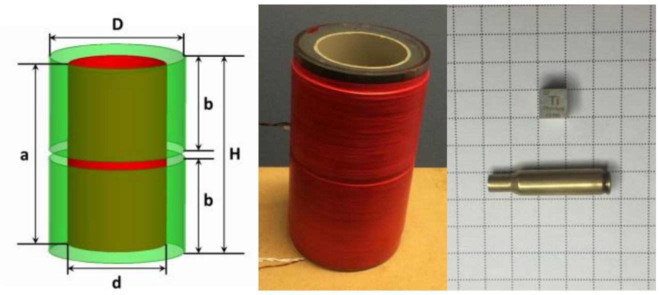

(a) (b) (c)

Fig. 3-(a) Coil schematic,(b) constructed coil and (c) test objects used (Titanium cube and .222 Remington shell) on 1 cm grid.

C. Test Objects

Fig. 3(c) displays the two test pieces measured within this paper; a .222 Remington rifle cartridge and a titanium cube. The .222 cartridge is made out brass, exact alloy unknown, with a primer assumed to be of the same material (not shown). As for the cube, it is made of 10 mm3 of pure titanium.

D. Experimental Procedure

A mechanical arrangement was used to position the test objects at the most sensitive part of the gradiometer along the z-axis. The arrangement enabled manual rotation for defined angular orientations. In this paper, rotations were performed about the y-axis in 15° steps. Due to the parallel field provided by the Helm-Holtz coil, the measurements obtained when rotating about the x-axis would yield identical results. At each angular orientation a full frequency sweep was performed from 1-100 kHz and stored. The object was then manually rotated and the process repeated until a full 360° rotation was performed.

E. Calibration

The raw trans-impedance measurements needed to be calibrated against the response of a ferrite object. This was due to the introduction of phase shifts as a result of the front-end amplification as well as an uneven amplification across the frequency range. In order to do so, trans-impedance measurements of a ferrite rod, 6x20 mm, were performed. Ferrite should provide a flat response across the frequency spectrum in terms of magnitude and induce no phase shift. This information was used to effectively cancel out the distortion introduced due to amplification.

F. Post-Processing and Field Measurement

The calibration and experimental measurements are passed through to MATLAB to perform the post processing and calculate the tensor/Eigenvalue matrix. The process simply performs the calibration initially to provide a view of the trans-impedance response of the object. As will be seen later this information can be used to deduce information about the object material, size and symmetry. This is then passed through the inversion process to deduce the tensor values and effectively Λ. As highlighted in section III, this requires knowledge of the field values from of the transmit and receive coils, $\vec{H}_T$ and $\vec{H}_R$ respectively. To do so a hall probe was lowered into the centre of the coil to measure the magnetic flux density while passing a unit current through the transmit and receive coils in turn.

V. Simulation

Simulations were performed using the commercial FEM (Finite Element Method) solver, Ansys Maxwell v16. The simulation geometry comprised of an outer free-space region, the coil arrangement as shown in Fig. 3(a) and the test object positioned nominally at the most sensitive region of the gradiometer. A series of simulations involved geometrical rotations of the test object about its centre in 15˚ increments from 0˚ to 345˚ over the frequency sweep range 1 kHz to 10 kHz in 1 kHz steps and thereafter in 5 kHz steps up to 100 kHz. The geometry of the .222 Remington case was simplified as three stacked geometrical primitives; a long and thin tapered cone, a smaller fatter cone and a simple cylinder representing the outer main body, shoulder and neck respectively of the cartridge. Subtraction of smaller sized primitives enabled the creation of a simplified cartridge shell of 0.5 mm wall thickness. Typical total meshing levels was in the order of 700 k tetrahedral elements and solution times for all frequencies and rotations was in the order of 72 hrs running on Intel Xeon ES-2620 (2 GHz) and required approximately 40 GBytes of physical RAM. An example H-field plot of the cartridge shell in the coil arrangement for a simulation of 20 kHz excitation current and angular orientation of 0˚ to the z-axis is shown in Fig. 4.

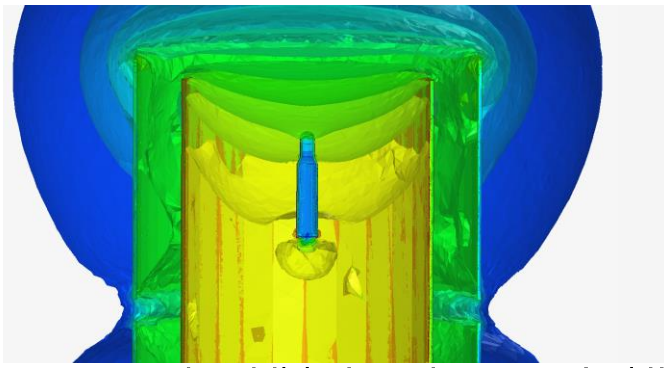

Fig. 4-Cross-sectional upper half of gradiometer showing an example H field perturbation due to the modelled .222 Remington rifle cartridge. Midpoint of the cartridge is at the simulated rotational centre and the most sensitive part of the gradiometer.

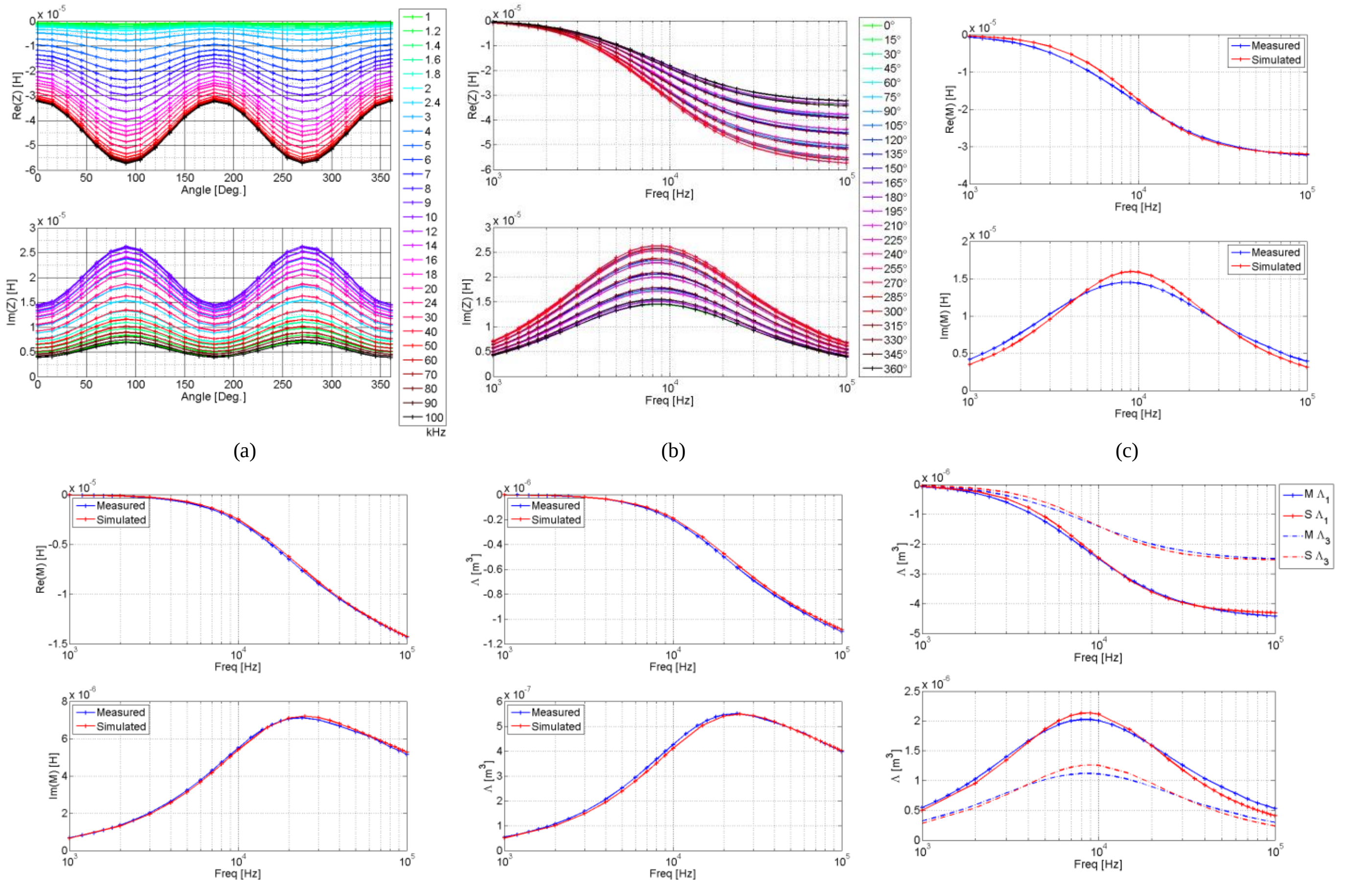

Fig. 5-.222 Remington cartridge calibrated trans-impedance measurement divided by ω, displayed per frequency (a), per angle of rotation (b) and compared to simulated at 0˚ (c). (d) is the comparison between measured and simulated data for the Titanium cube at 0˚. The calculated eigenvalues for the titanium cube (e) and the .222 Remington rifle cartridge (f) for both the measured (blue) and simulated (red) results.

VI. Results and Discussion

A. *Trans-Impedance Measurements*

The calibrated trans-impedance measurements obtained from the .222 Remington cartridge are presented in Fig. 5. The plots highlight expected results such as the sinusoidal shaped response in (a) which is a result of the geometrical shape of the cartridge. The frequency response displayed in (b) elucidates a number of object specific information such as the material and size. The lack of a positive real response at low frequencies alludes to the lack of ferritic composition in the material. The location of the peak frequency of the imaginary response can be viewed as a function of conductivity. This will be discussed further when comparing the eigenvalues of the cube and cartridge. The smooth measurement transition as the object is rotated can be viewed as a merit to the quality of measurements and they proved to be very reproducible (within 5%).

The measurements were compared with simulated results at 0˚and were found to match very well, Fig. 5(c). However some slight discrepancies are visible. This is assumed to be down to a number of aspects. Firstly, the simulation lacked the exact material properties of the cartridge; mainly the conductivity of the alloy used was unknown. Secondly, there were a number of subtle simplifications to the simulated cartridge such as the absence of the extractor groove and primer. Finally, the cartridge was modelled to have a thicker wall to reduce the number of elements created by the simulation. To confirm these assumptions were the cause of the difference, the titanium cube measurements were compared and were found to agree much better as illustrated in Fig. 5 (d).

B. *Eigenvalue matrix*

Finally, the Eigenvalue matrix was deduced from the measured and simulated results using the inversion technique described in the theory. The calculated eignevalues from the titanium cube and .222 cartridge for both measured and simulated results are shown in Fig. 5 (e) and (f).Only one eigenvalue is reported for the titanium cube as it responds equally in all directions (the three primary axis) and as result has the same eigenvalue in all three directions. Two eigenvalues are reported for the .222 cartridge; the dominant value (along the length of the cartridge) and a smaller eigenvalue which is identical for the remaining two axes due to its shape. These statements in their own right are discriminatory properties highlighted by the eigenvalue matrix. The identification of the shape of the object alone could provide a means of disregarding clutter.

The peak frequency for the eigenvalue imaginary spectrum provides significant information about the material properties. The conductivity of the materials is significantly different; brass has/is assumed to have a conductivity of 1.5×10^7 S/m, while titanium has a considerably lower conductivity of 1.8×10^6 S/m. This is reflected in the peak position in Fig. 5 (e) and (f) where the .222 Remington rifle cartridge displays a peak at around 8 kHz and the titanium cube is around 25 kHz. Finally, the magnitude of the eigenvalue matrix is considerably different highlighting the difference in size. However, the magnitude is a function of the conductivity, permeability and size of the object. Thus it cannot be used as a measure of size, unless prior knowledge of the material is present. Fig. 5(e) and (f) illustrate the potential information that can be deduced about the object. It can be referred to as an object signature and can deliver a discriminating dimension to metal detectors.

VII. Conclusions and Further work

The magnetic dipole polarizability tensor is of great interest in order to identify subsurface targets detected during mine clearance. The instrument described in this paper is capable of performing clean reliable measurements to obtain tensor values of small metal targets. The agreement with simulation results without the need of scaling validates the true tensor values obtained rather than assessing them comparatively. Looking forward the instrument is ready to be used to start measuring the magnetic responses of low-metal metal mines and typical clutter items to provide a library of signatures that can be used by detectors to identify and discriminate. The instrument can also be used to understand the effects of ageing on the response of a mine as well as recognizing the degree to which surrogates reflect the true response of a mine.

Acknowledgment

The authors would like to thank Find A Better Way for their financial support of this research under the SEMIS programme. The authors would also like to thank Christos Ktistis and Bachir Dekdouk, formerly of the University of Manchester, for their contribution to this work.

References

[1] "Landmine Monitor 2013," Intl. Camp. to Ban Landmines. Nov. 2013

[2] A. M. Lewis, T. J. Bloodworth, D. M. Guelle, F. R. Littmann, A. Logreco, and M. A. Pike, "Systematic Test & Evaluation of Metal Detectors (STEMD) Interim Report Laboratory Tests Italy," The Inst. for the Protection and Security of the Citizen, Euro. Com. Joint Research Centre, 2006.

[3] MacDonald, J., J. R. Lockwood, J. McFee, T. Altshuler, T. Broach, L. Carin, R. Harmon, C. Rappaport, W. Scott, and R. Weaver , "Alternatives for Landmine Detection", RAND, p. 9, 2003.

[4] K. Koppetsch, J. Glattbach, "Metal Detectors and PPE Catalogue 2007," Geneva Intl. Ctr. for Humanitarian Demining, 2007, p. 4.

[5] Bell, T.H., Barrow, B.J., Miller, J.T. Subsurface Discrimination Using Electromagnetic Induction Sensor. GeoSci. and Rem. Sens. IEEE Trans. vol. 39 No 6, 1286 - 1293 doi: 10.1109/36.927451, 2001.

[6] Makkonen J *et. al*. KNN classification of metallic targets using the magnetic polarizability tensor Meas. Sci. Technol. vol. 25 055105 doi:10.1088/0957-0233/25/5/055105, 2014.

[7] Marsh L A *et. al*. Three-dimensional object location and inversion of the magnetic polarisability tensor at a single frequency using a walk-through metal detector Meas. Sci. Technol. vol. 24 045102 doi:10.1088/0957-0233/24/4/045102, 2013.

[8] Norton S. J., Won I. J. Identification of Buried Unexploded Ordnance From Broadband Electromagnetic Induction Data. GeoSci. and Rem. Sens. IEEE Trans. vol. 39 No 10, 2253 - 2261 doi: 10.1109/36.957288, 2001.

[9] Marsh L A *et. al*. Determination of the magnetic polarizability tensor and three dimensional object location for multiple objects using a walk-through metal detector Meas. Sci. Technol. vol. 24 045102 doi:10.1088/0957-0233/24/4/045102

[10] Fernandez, J.P *et al* A Man-Portable Vector Sensor for Identification of Unexploded Ordnance IEEE Sens. Jr. vol. 11 No. 10, 2542 – 2555 doi: 10.1109/JSEN.2011.2118200

[11] Zhao Y. *et al* On the Low-Frequency Electromagnetic Responses of In-line Metal Detectors To Metal Contaminants Instr. and Meas. IEEE Trans. vol. PP No. 99 doi: 10.1109/TIM.2014.2324791

[12] Ulaby F T, Michielssen E and Umberto R 2010 Fundamentals of Applied Electrodynamics ed A Gilfillan (Englewood Cliffs, NJ: Prentice-Hall) p 261

Publication II

Abdel-Rehim O., Davidson J., Marsh L., O'Toole M. and Peyton A., " Magnetic Polarizability Tensor Spectroscopy for Low Metal Anti-personnel Mine Surrogates,"

Paper accepted on 16th February 2016 for publication in IEEE Sensors Journal.

Magnetic Polarizability Tensor Spectroscopy for Low Metal Anti-personnel Mine Surrogates

Omar A Abdel-Rehim, John L Davidson, Liam A Marsh, Member, IEEE, Michael D O'Toole and Anthony J Peyton, Fellow, IEEE

***Abstract*— The magnetic dipole polarizability tensor is an object specific property possessing information about the size shape and material. This information could be used by electromagnetic induction sensors typically used for demining operations to discriminate between buried mines and clutter, reducing False Alarm Rates, improving demining throughput and safety. The paper presents a methodology capable of obtaining the spectroscopic tensors of small metallic objects and low metal anti-personnel mine surrogates. The experimental results are validated against simulated and analytical solutions to ensure the obtained tensor truly represents the absolute object tensor. Absolute tensors for a number of typical clutter items and mine surrogates are presented, with significant variance observed between those of mine and clutter.**

***Index Terms*— electromagnetic induction; magnetic polarizability tensor; metal detection; landmine**

I. Introduction

ANTI-PERSONNEL mines remain a global challenge with contaminated land estimated to be 300 km^2 world-wide [1]. Annual casualty rates remain above 4,000 of which 42% are children [1]. Mine clearance operations typically utilize metal detectors to detect and locate buried mines through electromagnetic induction (EMI) of mine metallic components, followed by manual excavation to remove and disarm the threat [2]. Some anti-personnel mines have been designed to use the smallest amount of metal in their construction to impede their detectability. These types of mines are known as *minimum metal mines* and typically contain only a few metallic components limited to the necessary parts. Fig. 1 shows a cross-sectional schematic view of a typical anti-personnel mine with the metallic components highlighted in red, green and blue. While some anti-personnel mines can contain a spring and lock ball arrangement to form the detonation mechanism, highlighted in blue, minimum metal mines substitute these components and may utilize a non-metallic diaphragm to reduce their metallic content. As a result, minimum metal mines can contain metallic content that is composed of only a firing pin and the detonator casing, highlighted in red in Fig. 1. The safety pin is removed when arming the mine and so does not contribute to the EMI response measured by metal detectors.

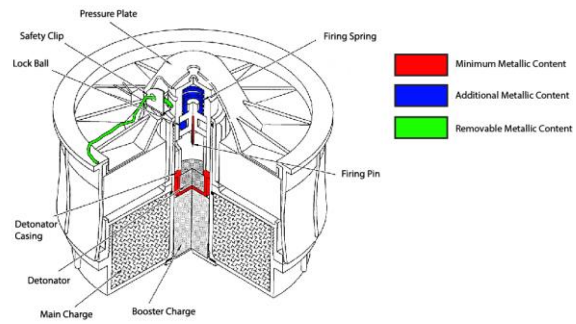

Fig. 1. Metallic content in anti-personnel mines. Figure adapted from [3].

The use of metal detectors has been successful at locating the mines, however presents an imperative weakness. Most mined areas are regions of previous conflicts with significant metal contamination. Thus the use of metal detector can result in a significantly high False Alarm Rate (FAR) and deminers can be found to excavate up to 100 innocuous objects for every mine [4]. This poses overheads on clearance operations; hindering throughput, increasing clearance costs and compromising the deminer's safety. Recent research efforts have seen the introduction of dual sensor detectors, utilizing Ground Penetrating Radar (GPR) to reduce the FAR [5]-[7], yielding impressive results. However, GPR also has challenges distinguishing clutter, especially when faced with water pockets and has poor ground penetration in certain soil conditions such as wet clay [8]. Another line of research has investigated the potential to deduce information about the detected object from the EMI response. The magnetic dipole polarizability tensor has been the focus of the research approach and has proved successful in the identification of buried unexploded ordnance, UXOs [9] as well as the classification of detected objects in an airport style walk-through metal detector [10]. For the sake of conciseness the magnetic polarizability tensor will be referred to as simply tensor throughout this paper.

Paper was submitted for review on 19/08/2015. The authors would like to thank the Find a Better Way (FABW) charity (http://www.findabetterway.org.uk/) for financial support of this research under the research programme, SEMIS Scanning electromagnetic mine imaging systems – Grant number: 2011/002

O. A. Abdel-Rehim is with the Electrical and Electronic Engineering School, The University of Manchester, Manchester, UK, M13 9PL (e-mail: omar.abdelrehim@manchester.ac.uk).

J. L. Davidson is with the Electrical and Electronic Engineering School, The University of Manchester, Manchester, UK, M13 9PL (e-mail: J.Davidson-2@manchester.ac.uk).

L. A. Marsh is with the Electrical and Electronic Engineering School, The University of Manchester, Manchester, UK, M13 9PL (e-mail: Liam.Marsh@manchester.ac.uk).

M. D. O'Toole is with the Electrical and Electronic Engineering School, The University of Manchester, Manchester, UK, M13 9PL (e-mail: Michael.OToole@manchester.ac.uk).

A. J. Peyton is with the Electrical and Electronic Engineering School, The University of Manchester, Manchester, UK, M13 9PL (e-mail: A.Peyton@manchester.ac.uk).

The tensor is an object specific property that depends on the shape, size, orientation and material. While a robust utilization of the polarizability tensor has not yet been applied into field devices to reduce FARs in humanitarian demining, work in research continues to report improved results of utilizing the property to reduce FARs [11], [12]. This paper reports on an apparatus capable of measuring and reporting the spectroscopic tensors of minimum metal anti-personnel mines and clutter items. The apparatus would provide capable metal detectors with a tensor library for the classification of mines and innocuous objects.

The paper initially defines the magnetic dipole polarizability tensor in Section II, describing its composition, its properties and how target features are represented within the tensor. In Section III, the paper describes the apparatus used to obtain the measurement and the experimental procedure. Section IV describes the simulation method used to simulate object responses. The tensors obtained for a number of objects are verified against simulation results as well as analytical solutions in section V. Sections VI presents the tensors of a number of clutter items and minimum metal mine surrogates. Finally section VII concludes with a discussion on the tensor potential for discrimination and a description of further work.

II. The Tensor

A. Dipole Model

In order to discuss the tensor we must first introduce the dipole model approximation and how it can represent metallic target responses. It has been a popular and useful approach to represent metallic responses as point dipoles for classification [9]. The approximation stipulates that the primary field from the EMI sensor is effectively parallel across the object. The dipole model has been shown to adequately represent the object response for time and frequency domain systems provided that the previous statement is observed [13]. This dipole approximation is presented in equation (1), where the representative induced dipole, $\vec{\boldsymbol{m}}$, is defined in terms of the object's tensor, $\overleftrightarrow{\boldsymbol{M}}$, and the incident primary field of the EMI sensor, $\vec{\boldsymbol{H}}_T$ [14]:

$$\vec{\boldsymbol{m}} = \overleftrightarrow{\boldsymbol{M}} \cdot \vec{\boldsymbol{H}}_T \tag{1}$$

The derived theory has been presented in numerous papers previously for time and frequency domain systems [15]-[19]. Thus it is the intention of this paper to present the key equations and call upon [19] for the complete derivation.

The induced voltage measured by an EMI sensor can be represented in terms of the induced dipole, $\vec{\boldsymbol{m}}$, as follows [19]:

$$V_{ind} \approx \frac{j\omega\mu_0}{I_R} \vec{\boldsymbol{m}} \cdot \vec{\boldsymbol{H}}_R \tag{2}$$

where μ_0 is the magnetic permeability of free space. Here, I_R refers to current passing through the receive coil, $\vec{\boldsymbol{H}}_R$ is the field of the receive coil and ω refers to the frequency at which the magnetic field is varying.

By substituting for equation (1) in (2), we obtain the expression for the induced voltage in terms of the object tensor and the fields of the EMI sensor coil [19]. This provides the capability of calculating the measured response provided we know the object's tensor and the sensor coil geometry.

$$V_{ind} \approx \frac{j\omega\mu_0}{I_R} \vec{\boldsymbol{H}}_T \cdot \overleftrightarrow{\boldsymbol{M}} \cdot \vec{\boldsymbol{H}}_R \tag{3}$$

The tensor is composed of a 3x3 matrix displayed in equation (4) that is frequency dependent. It describes the object response to an incident primary field in all axial directions and cross-diagonals as displayed in Fig. 2.

$$\overleftrightarrow{\boldsymbol{M}}(f) = \begin{bmatrix} M'_{xx} + jM''_{xx} & M'_{xy} + jM''_{xy} & M'_{xz} + jM''_{xz} \\ M'_{xy} + jM''_{xy} & M'_{yy} + jM''_{yy} & M'_{yz} + jM''_{yz} \\ M'_{xz} + jM''_{xz} & M'_{yz} + jM''_{yz} & M'_{zz} + jM''_{zz} \end{bmatrix} \tag{4}$$

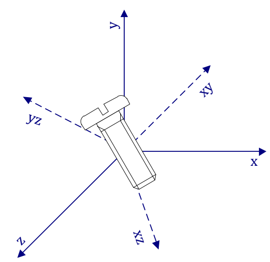

Fig. 2. Representation of the tensor components for a screw in an arbitrary orientation.

It is symmetrical in nature due to electromagnetic reciprocity; containing only 6 unique complex values. The frequency dependency is implicitly represented through the complex nature of the tensor.

It is evident from Fig. 2 that the tensor is orientation dependent; a change in orientation would result in different tensor components. This may seem as a favorable property; however, in order to perform classification of objects, orientation independence is required to ensure that the same tensor would be obtained for an object regardless of its orientation. Therefore, the eigenvalue matrix of the tensor, $\boldsymbol{\Lambda}$, is used instead for classification. The eigenvalues are the responses induced when the primary field is aligned with each principle axis of the object in turn [13]. The principal axes for an object are orthogonal to one another and an external magnetic field pointing along one of the axis would induce a

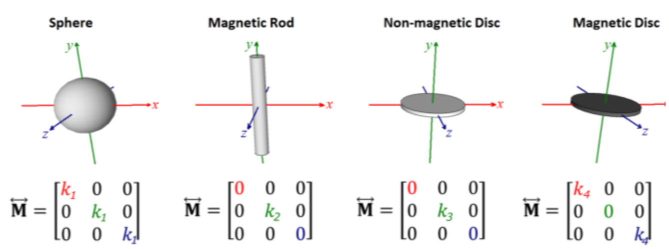

Fig. 3. Example single frequency tensor components for a sphere, magnetic rod of negligible diameter, non-magnetic and magnetic discs of negligible thickness [19].

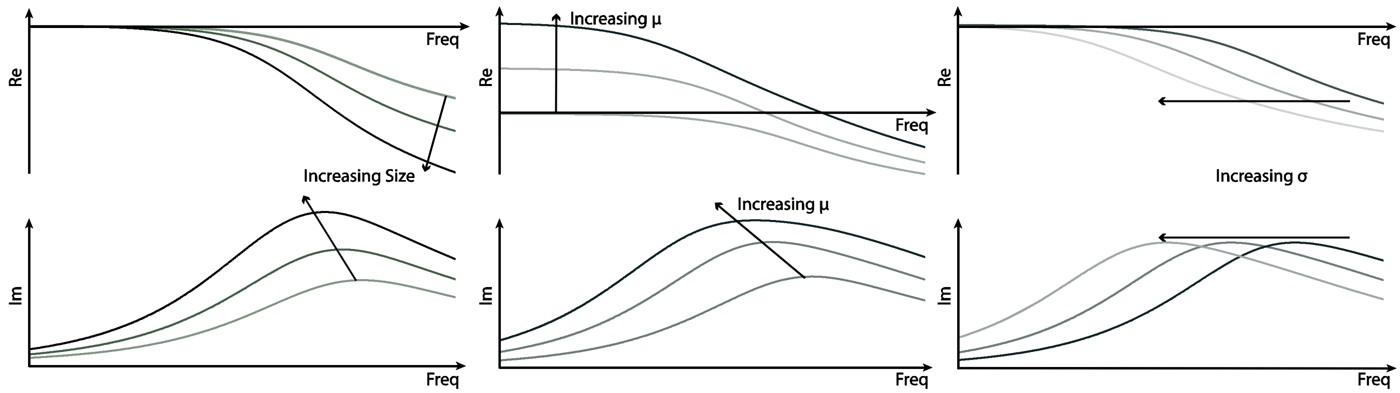

Fig. 4. The variance in the spectroscopic complex tensor with a change in object properties; increasing object size (a), increasing object permeability μ (b) and increasing object conductivity σ (c).

steady-state dipole moment parallel to it [11]. The orientation information is retained through the rotational matrix R as displayed in equation (5)

$$\overleftrightarrow{\boldsymbol{M}} = R \cdot \boldsymbol{\Lambda} \cdot R_T \tag{5}$$

where $\boldsymbol{\Lambda}$ is a diagonal matrix:

$$\boldsymbol{\Lambda}(f) = \begin{bmatrix} \boldsymbol{\Lambda}'_{xx} + j\boldsymbol{\Lambda}''_{xx} & 0 & 0 \\ 0 & \boldsymbol{\Lambda}'_{yy} + j\boldsymbol{\Lambda}''_{yy} & 0 \\ 0 & 0 & \boldsymbol{\Lambda}'_{zz} + j\boldsymbol{\Lambda}''_{zz} \end{bmatrix} \tag{6}$$

B. Object Properties

The means by which object properties can be inferred from the tensor involves the consideration of a number of tensor features. Some shape characteristics of the object can be inferred in terms of relative object dimensions by comparing the relative tensor components as show in Fig. 3.

The complex nature of the tensor implicitly describes the phase shift exhibited between the primary (transmit) field and the induced dipole or secondary field. This depends on a number of object attributes, mainly the object's electromagnetic properties [13]. Consequently, the spectroscopic tensor can reveal information about the object's material and size.

Fig. 4 represents the effects of object properties on the spectroscopic tensor. The real and imaginary tensor components represent the reactive and resistive response of the object. The imaginary response is linked to the eddy currents induced in the object and varies with frequency as the skin depth in the object varies. As shown in Fig. 4(a), as the object size increases, both tensor components increase. This is accompanied by a shift of the imaginary peak frequency to lower frequencies. The real tensor component also experiences an increase in gradient. These changes are due to the increased object interaction with the primary field which impacts on the generated eddy currents and the degree of field diversion or concentration. Fig. 4(b) shows that an increase in material magnetic permeability shifts the real response up, resulting in a positive real tensor at lower frequencies and crossing over to negative values at higher frequencies, reaching an asymptote that is dependent on the outer shape of the object. For ferrous objects this asymptote occurs at very high frequencies, well above MHz, which are generally beyond the range of practical measurement. The increase in permeability concentrates the primary field through the object; strengthening the field and increasing the real tensor component to a positive value. This in turn results in stronger eddy currents which result in an increase in imaginary tensor magnitude. The imaginary tensor also displays a slight shift in the peak frequency to lower frequencies which is due to the reduced skin depth caused by the increase in permeability. Fig. 4(c) shows that an increase in object conductivity results in the shift of the imaginary tensor to a lower frequency. The shift to lower frequency is also displayed by the real tensor. This is a direct result of the skin depth variation with conductivity. These linked variations of the tensor to the object properties, make the tensor a capable property for characterization and discrimination.

C. Inverse Problem

The inversion process forms an important operation carried out within this paper. In practice the induced voltage is measured and the tensor is the property to be derived. Hence, equation (3) is simply re-arranged to express the relation in terms of the tensor $\overleftrightarrow{\boldsymbol{M}}$:

$$\overleftrightarrow{\boldsymbol{M}} = \frac{I_R}{j\omega\mu_0}\left(\vec{\boldsymbol{H}}_T \cdot \vec{\boldsymbol{H}}_R\right)^{-1} \cdot V_{ind} \tag{7}$$

This is commonly known as an inverse problem with respect to tomography principles. Strictly, only six measurements are required for a valid data set for inversion. However, this assumes the six measurements are for all the field projections shown in Fig. 2 and are noise-free. Additionally, if the principal axes of the object are known then as few as three measurements would produce a meaningful tensor from the inversion process. In practice a much larger dataset is provided to the inversion, taking numerous fields of view to ensure the correct tensor is obtained. This is achieved by either moving the detector with respect to the object or moving the object with respect to the detector in such a way as to acquire a suitable set of projections for data inversion. This paper adopts the later approach which is described in the next section.

III. Experimental Setup

A. System Overview

The primary instrument used to perform the measurements was an impedance/gain phase analyzer (Solatron SI 1260). The analyzer excited a purpose-built solenoid coil with discrete fixed frequencies and captured the trans-impedance values. A bespoke LabVIEW code controlled the measurement process, stepping through the desired frequencies, providing the required excitation values and recording the trans-impedance measured by the impedance analyzer. This data was then processed using MATLAB to perform the inversion and tensor calculation. Front-end amplification was used to provide a stronger driving current (≈1.2A) and amplify the induced voltage from the receive coil. A system schematic is represented in Fig. 5.

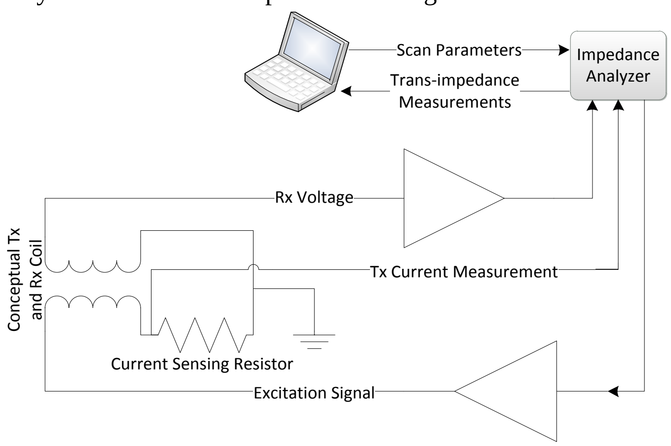

Fig. 5. System schematic showing the flow of signals and measurements to and from the impedance analyzer, front-end amplification and the sensing

B. The coil

The solenoid coil constructed in order to take the measurements is pictured in Fig. 6. The coil was composed of an inner 120 turn transmit coil, visualized in green in Fig. 6(a), and two outer 60 turn receive coils wound in a reverse opposition arrangement, displayed in red in Fig. 6(a) and 6(b). The coil dimensions were as follows; a=202 mm, b=105 mm, H=220 mm, d=107 mm and D=149 mm, with a wire wall thickness of 1.75 mm for the transmit coil and 1.66 mm for the receive. The measured self-resonance of the constructed coil was 650 kHz for the transmit and 950 kHz for the receive. The z-axis is considered to be along the center of the coil.

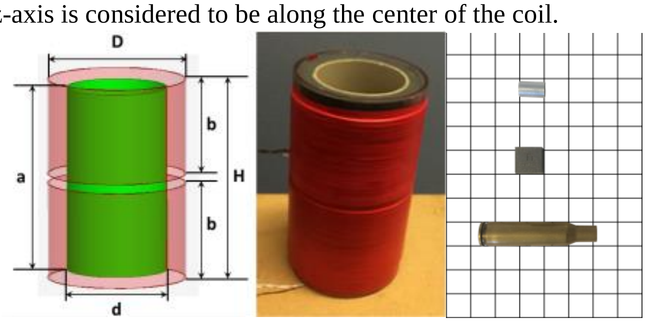

(a) (b) (c)

Fig. 6. (a) Coil schematic, (b) constructed coil and (c) validation objects used on a 1cm grid. The objects pictured from top to bottom are a Type-72A Chinese mine phantom, Titanium cube and .222 Remington shell.

The coil was designed to provide maximum sensitivity (larger number of turns) while ensuring the resonance of the coil was well above the maximum frequency of interest. The frequency range investigated within this paper is 1-100 kHz as this contains the majority of the useful information required for classification.

C. Experimental Procedure

A mechanical arrangement was used to position the small metallic objects and mines at the most sensitive part of the gradiometer along the z-axis. The arrangement enabled manual rotation for defined angular orientations. In this paper, rotations were performed about the y-axis in 15° steps. At each angular orientation a full frequency sweep was performed from 1-100 kHz and stored.

D. Calibration

The raw trans-impedance measurements required calibration against the response of a ferrite object. This was due to the introduction of phase shifts as a result of the front-end amplification as well as an uneven amplification across the frequency range. In order to do so, trans-impedance measurements of a NiZn ferrite rod, 6x20 mm, were performed. This ferrite provides a flat response across the frequency spectrum in terms of magnitude and induce no phase shift. This information was used to effectively cancel out the errors introduced due to amplification.

E. Post-Processing and Field Measurement

The experimental measurements were finally passed to MATLAB to perform the post processing and calculate the eigenvalue tensor. Equation (3) was implemented to deduce the tensor values, and subsequently Λ through Equation (5). This operation required the field values for the transmit and receive coils, $\vec{\boldsymbol{H}}_T$ and $\vec{\boldsymbol{H}}_R$ respectively. The field strengths were derived from flux density measurements obtained using a Hall probe. Further details regarding the apparatus can be found in [20].

It is worth noting at this point the limitations of the measurement system presented. The system and procedure only allow the correct tensor inversion for small symmetrical metallic objects. Asymmetrical objects would need to be rotated about two planes; (i) to establish a principle axis and (ii) to measure the tensor components perpendicular to this axis. Secondly, the system is only capable of measuring small metallic objects to uphold the uniform parallel field through the object.

IV. Simulation

Simulations were performed using the commercial FEM (Finite Element Method) solver, Ansys Maxwell v16. The simulation geometry comprised of an outer free-space region, the coil arrangement as shown in Fig. 6(a) and the test object positioned nominally at the most sensitive region of the gradiometer. A series of simulations involved geometrical rotations of the test object about its centre in 15˚ increments from 0˚ to 345˚ over the frequency sweep range 1 kHz to 10 kHz in 1 kHz steps and thereafter in 5 kHz steps up to

100 kHz. The geometry of the .222 Remington case was simplified as three stacked geometrical primitives; a long and thin tapered cone, a smaller fatter cone and a simple cylinder representing the outer main body, shoulder and neck respectively of the cartridge. Subtraction of smaller sized primitives enabled the creation of a simplified cartridge shell of 0.5 mm wall thickness. Thinner wall thickness would have introduced a larger number of finer meshing elements. Consequently, the developed simplified geometry of the shell represented an appropriate level of trade-off between absolute accuracy of modelling and practicable computational time requirements for the FEM simulation. Typical total meshing levels at each rotational position was in the order of 700k tetrahedral elements and solution times for all frequencies and rotations was in the order of 72 hrs running on Intel Xeon ES-2620 (2 GHz) and required approximately 40 GBytes of physical RAM. An example H-field plot of the cartridge shell in the coil arrangement for a simulation of 20 kHz excitation current and angular orientation of 0˚ to the z-axis is shown in Fig. 7.

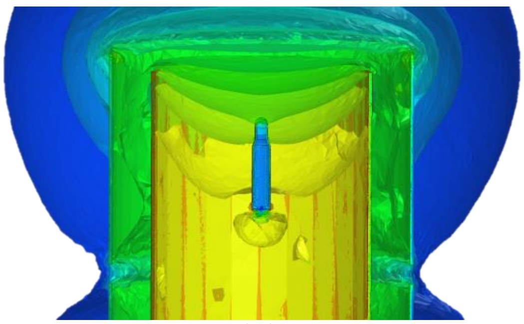

Fig. 7. Cross-sectional upper half of gradiometer showing an example H field perturbation due to the modelled .222 Remington rifle cartridge. Midpoint of the cartridge is at the simulated rotational centre and the most sensitive part of the gradiometer.

V. Experimental Validation

Validation of the experimental and tensor calculation methodologies was achieved using the objects shown in Fig. 6(c). The validation involved comparison of experimentally derived eigenvalue tensors with simulation and analytical solutions where possible. A 1 cm titanium cube was the first validation piece used as it is a well-defined object that can be accurately simulated. An analytical solution for the tensor can be calculated for the cube as it is deemed to have the same tensor structure of a sphere, Fig 3; composed of equal diagonal tensor components. This is a result of the symmetrical shape of the cube along all three axes. This was confirmed by rotating the cube through the coil and the response measured was found to be equal for all orientations. Consequently, a volume equivalent sphere was used to calculate the analytical solution for the tensor of the cube. There is abundance in literature reporting the tensor for a sphere as in [14], [15] which can be calculated using equation (8) and (9)

$$\overleftrightarrow{\boldsymbol{M}} = -2\pi a^3(k' + jk'')\begin{pmatrix}1 & 0 & 0\\ 0 & 1 & 0\\ 0 & 0 & 1\end{pmatrix} \tag{8}$$

$$(k + jk'') = \frac{[\mu_0(1+k^2a^2)+2\mu]\,sinh(ka) - (2\mu+\mu_0)ka\cdot cosh(ka)}{[\mu_0(1+k^2a^2)-\mu]\,sinh(ka) + (\mu-\mu_0)ka\cdot cosh(ka)} \tag{9}$$

Here, $\mu = \mu_0\mu_r$ is the magnetic permeability of the sphere, σ is the conductivity, ω is the frequency of excitation and $k = \sqrt{i\sigma\mu\omega}$.

Fig. 8(a) displays the spectroscopic real and imaginary eigenvalue tensor for the cube. Note only one eigenvalue is plotted as all three values were equal. The comparison shows good agreement for all three solutions. The measured and simulated tensors match within 1.75%, for both the real and imaginary components. The calculated tensor matches well for the real component, within 2.5%, however with a slight disagreement for the imaginary component at higher frequencies; increasing from 3% to 30% for frequencies above 20 kHz. This is due to the use of a spherical equation to calculate the tensor. At high frequencies the eddy currents are pushed to the limits of the object and hence the precise shape has more influence on the eddy current distribution, the skin depth and ultimately the imaginary component of the tensor. Nevertheless, the strong agreement between all three solutions for the titanium cube gives confidence in the adopted method. In particular, the agreement with the analytical solution confirms that the obtained tensor is the correct tensor value. Such tensor calculation allows for the development of a tensor library which is transferrable between detectors and can act as a powerful calibration tool.

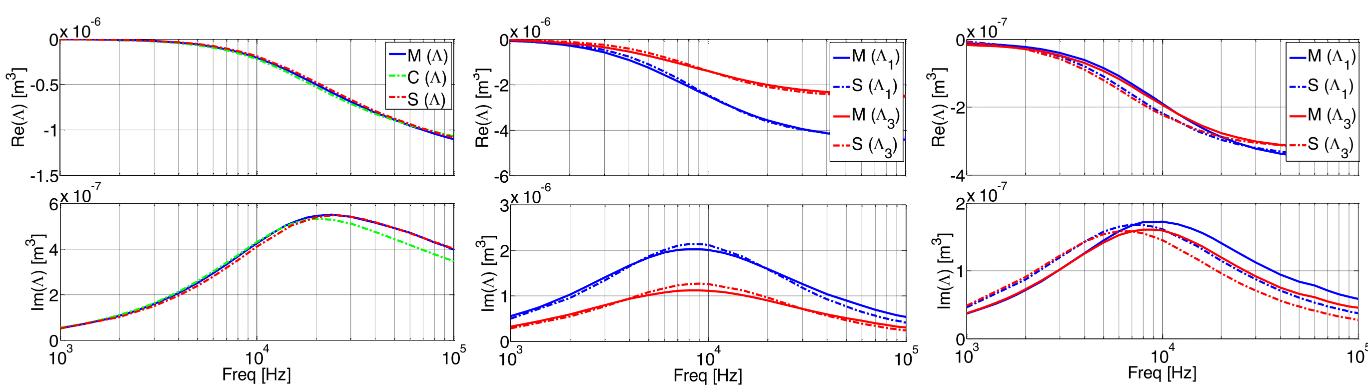

Fig. 8. Validation of eigenvalue calculation and tensor methodology applied to; (a) titanium cube, (b) .222 Remington cartridge and (c) Type-72A phantom. The solid lines are eigenvalues of tensors derived from experimental data, M, whereas the dashed lines are derived from simulation, S, or analytical solution, C.

The apparatus was then validated for a .222 Remington cartridge shell to ensure the method holds for complex shapes. The Remington shell is representative of a typical clutter piece that could be found in a mined area of previous conflict. The measured tensor was compared to only that of simulation as an analytical solution does not exist. Fig. 8(b) represents the eigenvalues obtained from measurement and simulation. Note that two eigenvalues are reported here since the cartridge presents two equal smaller eigenvalues, Λ3, along the non-axial direction with a dominant eigenvalue along the axial direction, Λ1. This re-affirms the possible shape characterization through the tensor. As for the titanium cube, a relatively good agreement is observed; within 2.5% for the real and 7% for the imaginary tensor components. The small discrepancy between experimental and simulation can be attributed to a number of reasons. Firstly, the simulation was performed using a conductivity value of a typical brass alloy since the exact material composition of the cartridge was unknown. Secondly, the simulation also performed a number of subtle simplifications to the cartridge shape such as the absence of the extractor groove and primer. Finally, the wall thickness was simulated to be slightly thicker to reduce the required meshing.

A third validation exercise followed, using a phantom piece for a Type-72A mine, Fig 8 (c). The phantom piece is usually used in the field to calibrate metal detectors prior to clearance operations and was considered a suitable validation piece to represent a typical mine tensor. Once again, agreement is observed but with some discrepancy of around 13% in the quadrature tensor. The exact material properties were again absent for the simulation. However, by observing the effects of increased conductivity in Fig. 4, the observed discrepancy can be attributed to a mismatch of conductivity between that used for simulation and that of the phantom measurement.

The validation exercise confirmed the apparatus is capable of accurately obtaining the absolute tensor values for small metallic objects that embody both clutter and mine targets. The paper now moves on to reporting on the measured tensors for a number of clutter items and mine surrogates.

VI. Tensors

A. Clutter Items

Fig. 9 represents the clutter items measured along with the tensors obtained. The set of clutter items was chosen to represent potential clutter faced during demining operations. Even on a cursory examination of Fig. 9, the difference between each item tensor is clear; the change in peak imaginary frequency, the positive or lack of real component and the variance in tensor ratios and values.

The first tensors presented in Fig. 9 are that of an uncirculated US nickel (5-cent) and dime. The tensors reveal the difference in material and size as discussed in Fig 4. The US nickel and dime have bulk compositions by weight of 25%Ni-75%Cu and 8.33%Ni-91.77%Cu respectively and weigh 5g and 2.268g [21]. The higher copper content of the dime results in a lower peak imaginary frequency due to the increased overall conductivity [22]. The difference in physical coin size is clearly evident from the tensors with the US nickel having larger magnitude in eigenvalues compared with the physically smaller dime. Again, only two tensors are displayed here; the dominant eigenvalue tensor, Λ_1, is along the axial direction and the repeated tensor is Λ_3. This tensor ratio is expected as the coins reflect the shape of a non-magnetic disc displayed in Fig. 3.

The third clutter tensor displayed is of a steel nail. A metallurgical assessment of the steel was not made, but by observing the tensor it is clear that the nail is composed of a material with relative permeability greater than 1 such as ferrous steel. This is deduced from the positive real component as discussed earlier in Fig. 4. The nail tensor also exhibits larger tensor values than the coins despite being smaller in size which can also be credited to the increased permeability as emphasized in Fig. 4. The extreme unidirectional shape of the nail results in two near negligible tensors, Λ_3, in comparison to the dominant axial tensor, Λ_1. This is clearly shown by the near zero components for the real and imaginary eigenvalue tensor Λ_1. The tensor structure of the nail is representative of the magnetic rod discussed in Fig. 3. Note if the nail was bent in one or two planes then no near zero tensors would have been measured.

The .222 Remington cartridge shell is also unidirectional in shape as discussed earlier. However, the ratio is not as extreme as the nail and the non-axial tensor, Λ_3, is of some magnitude. The ratio of Λ_1 to Λ_3 is not linearly representative of the object's relative dimensions as the tensor ratio is roughly 2:1, whereas the object's relative dimensions are around 5:1. The lack of a positive real component indicates that the cartridge material is non-magnetic with relative permeability around 1. The material of the cartridge is known to be a brass alloy and hence the statement complies with brass properties.

Finally, the safety pin of an L109A1 grenade is the last clutter item presented in this paper. The grenade pin was measured in the arrangement presented in Fig. 9, with the pin and ring coplanar. Since the pin is able to freely move with respect to the ring, the tensor becomes variable in nature as it is will vary depending on the orientation of the pin with respect to the ring. However, the combined material will remain constant regardless of the arrangement. The metallic composition of the pin appears to be ferritic. The peak frequency is not visible in the frequency range measured, which indicates to a rather non-conducting material relative to the other objects. These tensor characteristics will be present regardless of the ring-pin arrangement, with only the tensor ratio varying as the pin is moved with respect to the ring. The pin should introduce a unidirectional property to the tensor increasing the ratio of the components, between Λ_1 and Λ_3. However, the tensor seems to not display a very unidirectional ratio, indicating that the ring is the dominant metallic component. This means that the tensor variation would be considerably less if the ring and the pin were of similar magnitude of response. These aspects make the tensor presented still viable to characterize the pin.

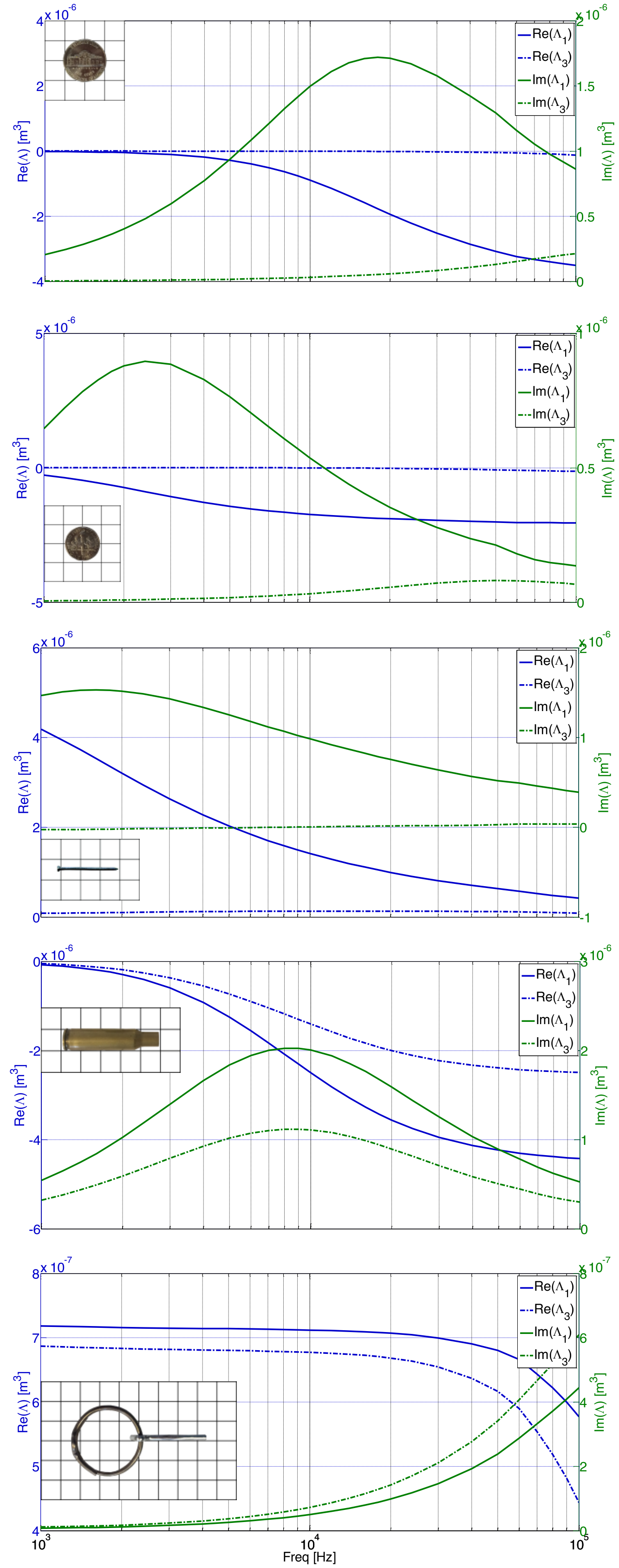

Fig. 9. Experimentally obtained tensors for clutter items; uncirculated US nickel, uncirculated US dime, a nail, .222 Remington cartridge shell and a grenade safety pin (top to bottom). Note that the clutter items are represented on a 1cm grid and are to scale with respect to one another. Blue plots are real tensor components plotted against the left axis and green plots are imaginary plotted against the right axis.

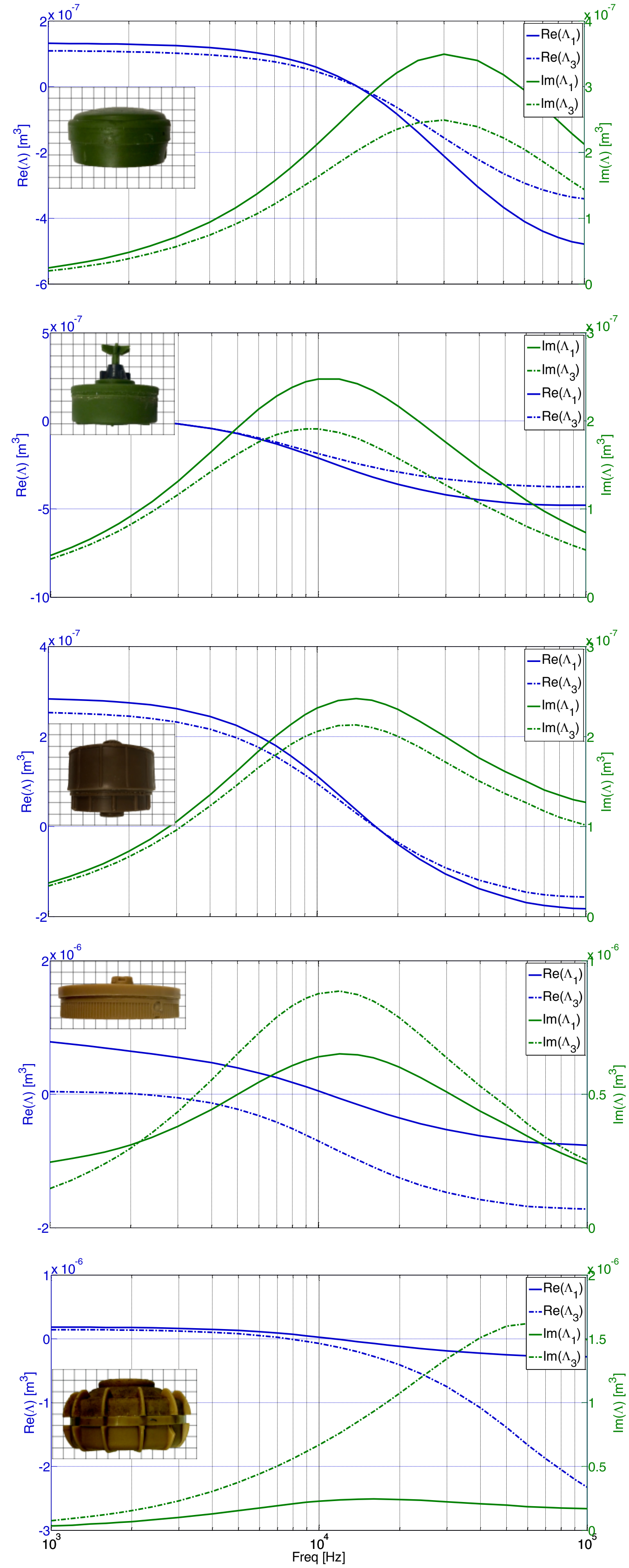

Fig. 10. Experimentally obtained tensors for minimum metal mine surrogates; Type-72A, PMA-2, R2M2, M-409 and TS-50 (from top to bottom). Note that the mines pictures are to scale with respect to one another and represented on 1 cm grid. Blue plots are real tensor components plotted against the left axis and green plots are imaginary plotted against the right axis.

B. Anti-personnel Mine Surrogates

A number of minimum metal anti-personnel landmine surrogates were obtained from Fenix Insight Ltd. to perform tensor measurements. Fig. 10, reports on the tensors obtained from a Type-72A Chinese landmine, a Yugoslavian PMA-2 landmine, a South-African R2M2 landmine, a Belgian M409 and an Italian TS-50. The variance between mine types here is not as high as that displayed for clutter items. This is expected as mine parts are relatively similar with a similar set of components. However, there is still a significant amount of difference between the tensors to differentiate between the mines.

Comparing the magnitude of the tensors it is clear that the PMA-2 has the lowest metallic content followed by the Type-72A. These mines are generally considered to be amongst the most difficult mines to detect due to their low metallic content. The tensors of the Type-72A, R2M2, M409 and the TS-50 reveal a metallic composition of ferritic content. The M409 is slightly different as the ferritic component appears to have an influence in only one direction. This is interpreted from the positive real value for Λ_1 only and not for the repeated Λ_3. This can be attributed to the two cylindrical torsion springs highlighted in the plan X-ray scan of the M409 mine shown in Fig. 11(a). The spring material was confirmed to be ferritic by the manufacturer and so the two spring formations effectively act as two magnetic rods, strengthening the field in one direction significantly more than the other two. This type of spring arrangement is not included in the other tested mines as displayed by the X-ray of the smaller PMA-2 presented in Fig. 11(b).

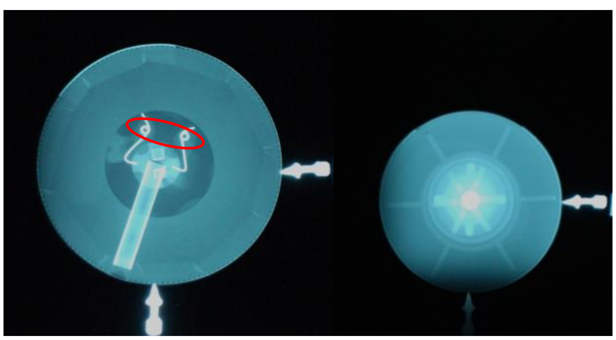

(a) (b)

Fig. 11. Plan X-ray projections of (a) M409 and (b) PMA-2. Scaling between the two landmines is approximate.

The TS-50 mechanism for detonation is more complex, containing several additional metallic components. This is reflected in the larger values of tensor and the considerable difference in tensor signature in comparison to the remaining mines. The presented tensors in this section very clearly show the differences between the tensor components of the landmines from one another, and more importantly, tensor differences from that of clutter items. Fig. 9 and Fig. 10 confirm the possibility of utilizing the tensor to help discriminate mines and disregard clutter items.

VII. Conclusion & Future work

The paper presented a systematic method capable of obtaining the absolute magnetic dipole polarizability tensor of minimum metal anti-personnel mines and small symmetrical metallic objects. The tensors obtained experimentally, analytically and through simulation have been compared for the first time and were found to match without the need of a scaling factor. This confirmed the experimentally obtained tensor to be the correct representation of the measured object. A tensor library built using the described method would produce true object tensor values, transferrable between detectors and would act as a guide to calibrate future detectors capable of deducing target tensors.

The reported tensors for clutter and landmines displayed variance portraying object properties such as size, shape and material. The absolute tensors for minimum metal anti-personnel mines were reported for the first time and were found to be considerably different from an example clutter set. The difference confirmed the capability of the tensor to act as a discriminatory property in order to reject clutter and reduce FARs for demining operations.

Investigating alternative EMI sensor design forms the main basis for future work to this paper. The solenoid used in this paper presents two limitations; a measurement frequency range of 1-100 kHz and a maximum object dimension of 100 mm. These limitations are due to the self-resonant frequencies of the coils and the limited central void space. A suite of solenoids needs to be created to allow the measurement of larger objects as well as at different frequencies. The potential application of a Helmholtz arrangement could allow the tensor measurement of non-symmetrical objects. Finally, a comprehensive set of targets needs to be measured in order to build an effective tensor library.

To utilize the tensor for the characterization of objects, field detectors need to identify individual items and accurately measure their tensors. In practical demining operations, a number of field challenges need to be addressed in order to correctly discriminate between metallic clutter and landmines. Sufficient lateral spacing needs to exist between multiple targets to ensure individual tensors are obtained. Secondly, incorporative soil or soil of high magnetic content can pose challenging conditions for accurate tensor measurement. These are topics of ongoing research aimed at overcoming these issues. In [11] and [18], the topic of lateral spacing has been visited displaying the capability of multi-object inversion provided reasonable separation is observed, while further research is required to assess the effect of soil conditions on tensor measurements. The development of a tensor inverting field instrument forms the ultimate goal of this research as it will realize the reduction of FARs through the use of the magnetic dipole polarizability tensor.

References

[1] "Landmine Monitor 2012," Int'l Campaign Ban Landmines, Nov., 2012.

[2] A. M. Lewis, T. J. Bloodworth, D. M. Guelle, F. R. Littmann, A. Logreco, M. A. Pike, "Systematic Test & Evaluation of Metal Detectors (STEMD) Interim Report Laboratory Tests Italy," The Inst. For Protection & Security of the Citizen. EU Comm. Jnt. Research Cent., 2006.

[3] GICHD. (2015, July). *Collaborative ORDnance Data Repository (CORD)*. [Online] Available: http://cord.gichd.org/ordnance?id=http%3A%2F%2Fcord.gichd.org%2Fontology%23Landmine4156

[4] J. MacDonald, J. R. Lockwood, "Alternatives for Landmine Detection," RAND Corp., 2003.

[5] R. C. Doheny, S. Burke, R. Cresci, P. Ngan, and R. Walls, "Handheld standoff mine detection system (HSTAMIDS) field evaluation in Thailand (Invited Paper)," *Proc. SPIE* 5794, Detection and Remediation Technologies for Mines and Minelike Targets X, 889 (July 08, 2005); doi:10.1117/12.617920.

[6] D. J. Daniels, P. Curtis, R. Amin, N. Hunt, "MINEHOUND production development", *Proc. SPIE* 5794, Detection and Remediation Technologies for Mines and Minelike Targets X, 488 (July 08, 2005); doi:10.1117/12.601888.

[7] M. Sato, K. Takahashi, "Hand-held dual-sensor ALIS and its evaluation tests", *Proc. SPIE* 6953, Detection and Sensing of Mines, Explosive Objects, and Obscured Targets XIII, 695311 (April 14, 2008); doi:10.1117/12.777236.

[8] D. Daniels, "A review of GPR for landmine detection," *Sensing and Imaging: An International Journal*, vol. 7, pp. 90-123, 2006.

[9] J. P. Fernandez, B. E. Barrowes, T. M. Grzegorczyk, N. Lhomme, K. O'Neill, and F. Shubitidze, "A Man-Portable Vector Sensor for Identification of Unexploded Ordnance," *Sensors Journal, IEEE*, vol. 11, pp. 2542-2555, 2011.

[10] J. Makkonen, L. A. Marsh, J. Vihonen, A. Järvi, D. W. Armitage, A. Visa, *et al.*, "KNN classification of metallic targets using the magnetic polarizability tensor," *Measurement Science and Technology*, vol. 25, p. 055105, 2014.

[11] J. P. Fernández, B. Barrowes, A. Bijamov, T. Grzegorczyk, N. Lhomme, K. O'Neill, *et al.*, "MPV-II: an enhanced vector man-portable EMI sensor for UXO identification," *Proc. SPIE 8017*, Detection and Sensing of Mines, Explosive Objects, and Obscured Targets XVI, 801707 (May 23, 2011); doi:10.1117/12.884085

[12] T. M. Grzegorczyk and B. E. Barrowes, "Operation of the Pedemis Sensor at the Aberdeen Proving Ground Standardized Test Site: Single and Multi-Target Inversions," *Geoscience and Remote Sensing Letters, IEEE*, vol. 11, pp. 394-398, 2014.

[13] T. H. Bell, B. J. Barrow, and J. T. Miller, "Subsurface Discrimination Using Electromagnetic Induction Sensors," *IEEE Transactions on Geoscience and Remote Sensing*, vol. 39, pp. 1286-1293, June 2001.

[14] Z. Yifei, Y. Wuliang, C. Ktistis, D. Butterworth, and A. J. Peyton, "On the Low-Frequency Electromagnetic Responses of In-Line Metal Detectors to Metal Contaminants," *Instrumentation and Measurement, IEEE Transactions on*, vol. 63, pp. 3181-3189, 2014.

[15] Y. Das, J. E. McFee, J. Toews, and G. C. Stuart, "Analysis of an Electromagnetic Induction Detector For Real-Time Location of Buried Objects," *Geoscience and Remote Sensing, IEEE Transactions on*, vol. 38, pp. 278-288, 1990.

[16] Y. Zhang, L. Collins, H. Yu, C. Baum, and L. Carin, "Sensing of unexploded ordnance with magnetometer and induction data: Theory and signal processing," *IEEE Trans. Geosci. Remote Sens.*, vol. 41, no. 5, pp. 1005–1015, May 2003

[17] S. J. Norton and I. J. Won, "Identification of buried unexploded ordnance from broadband electromagnetic induction data," *Geoscience and Remote Sensing, IEEE Transactions on*, vol. 39, pp. 2253-2261, 2001.

[18] T. M. Grzegorczyk, B. E. Barrowes, F. Shubitidze, J. P. Fernandez, and K. O'Neill, "Simultaneous Identification of Multiple Unexploded Ordnance Using Electromagnetic Induction Sensors," *Geoscience and Remote Sensing, IEEE Transactions on*, vol. 49, pp. 2507-2517, 2011.

[19] L. A. Marsh, C. Ktistis, A. Järvi, D. W. Armitage, and A. J. Peyton, "Three-dimensional object location and inversion of the magnetic polarizability tensor at a single frequency using a walk-through metal detector," *Measurement Science and Technology*, vol. 24, p. 045102, 2013.

[20] O. A. A. Rehim, J. L. Davidson, L. A. Marsh, M. D. O'Toole, D. W. Armitage, and A. J. Peyton, "Measurement system for determining the magnetic polarizability tensor of small metal targets," in *Sensors Applications Symposium (SAS), 2015 IEEE*, 2015, pp. 1-5

[21] U. S. Mint. (July 2015), Coin Specification. [Online] Available: http://www.usmint.gov/about_the_mint/?action=coin_specifications

[22] C. Y. Ho, M. W. Ackerman, K. Y. Wu, T. N. Havill, R. H. Bogaard, R. A. Matula, *et al.*, "Electrical Resistivity of Ten Selected Binary Alloy Systems," *Journal of Physical and Chemical Reference Data*, vol. 12, pp. 183-322, 1983.

Omar A. Abdel-Rehim received an Hons MEng degree with industrial placement in Electronic System Engineering from the University of Manchester in 2011. He then went onto study his PhD at the University of Manchester, joining the Sensing, Imaging and Signal Processing research group within the school of EEE.

John L. Davidson graduated with a BSc (Hons) in Engineering Physics in 1993 from Sheffield Hallam University (SHU) and later received his PhD in Mössbauer Spectroscopy from SHU in 1997. As a research fellow at the University of Southampton from 1998 to 2002, he developed an interest in electrostatics and electromagnetics. In 2002 he joined the University of Manchester initially working in the area of Electrical Impedance Tomography applied to industrial and medical problems, and more recently, in the area of electromagnetics. He has authored and co-authored more than thirty scientific publications and in 2008 was awarded the Beloe Fellowship award from the Worshipful Company of Scientific Instrument Makers. His current research interests include electromagnetic modelling, inverse problems and magnetic induction sensor development.

Liam A. Marsh graduated with a first class MEng (Hons) in Electrical Engineering and Electronics in 2007 from UMIST. He later received his PhD in Electromagnetic Tomography and People Screening from the University of Manchester in 2011. He subsequently joined the Sensing, Imaging and Signal Processing research group of the University of Manchester's School of Electrical and Electronic Engineering as a Research Associate; his current research interests include the development of electromagnetic sensor systems and inverse problems.

Michael O'Toole received the MEng degree in Integrated Engineering from the University of Reading in 2006 and the PhD from the Wolfson School of Mechanical and Manufacturing Engineering, Loughborough University in 2011.

He has been a research associate at the University of Manchester since 2011, first working in the School of Computer Science on simulation and analysis tools for non-smooth mechanical systems. He moved to the School of Electrical and Electronic Engineering in 2012 working on magnetic induction systems for non-destructive inspection in the food industry. His research interests include signal processing, and sensor and instrumentation design, with particular emphasis towards bio-impedance spectroscopy and magnetic induction systems for non-destructive testing.

Anthony J. Peyton graduated with a first B.Sc. in Electrical Engineering and Electronics from UMIST, 1983 and later received his Ph.D. in medical instrumentation from UMIST in 1986. He was appointed as Principal Engineer at Kratos Analytical Ltd to 1989, developing precision electronic instrumentation systems for mass spectrometers, from which an interest in electromagnetic instrumentation developed. He returned to UMIST as a Lecturer and worked with the Process Tomography Group. He moved to Lancaster University in 1996 taking up post of Senior Lecturer. Promoted to reader in Electronic Instrumentation in July 2001 and Professor in May 2004. Since December 2004 he has been Professor of Electromagnetic Tomography Engineering at the University of Manchester. His main research interests currently are in the area of instrumentation, applied sensor systems and electromagnetics.